Applications of Multinuclear Solid-State NMR Spectroscopy to the Characterisation of Industrial Catalysts

Andrew Gordon McLaughlin Rankin

University of
St Andrews

This thesis is submitted in partial fulfilment for the degree of PhD
at the
University of St Andrews

October 2017

1. Candidate's declarations:

I, Andrew Gordon McLaughlin Rankin, hereby certify that this thesis, which is approximately 59000 words in length, has been written by me, and that it is the record of work carried out by me, or principally by myself in collaboration with others as acknowledged, and that it has not been submitted in any previous application for a higher degree.

I was admitted as a research student in October 2013 and as a candidate for the degree of PhD in October 2014; the higher study for which this is a record was carried out in the University of St Andrews between 2013 and 2017.

Date Signature of candidate

2. Supervisor's declaration:

I hereby certify that the candidate has fulfilled the conditions of the Resolution and Regulations appropriate for the degree of PhD in the University of St Andrews and that the candidate is qualified to submit this thesis in application for that degree.

Date Signature of supervisor

3. Permission for publication:

In submitting this thesis to the University of St Andrews I understand that I am giving permission for it to be made available for use in accordance with the regulations of the University Library for the time being in force, subject to any copyright vested in the work not being affected thereby. I also understand that the title and the abstract will be published, and that a copy of the work may be made and supplied to any bona fide library or research worker, that my thesis will be electronically accessible for personal or research use unless exempt by award of an embargo as requested below, and that the library has the right to migrate my thesis into new electronic forms as required to ensure continued access to the thesis. I have obtained any third-party copyright permissions that may be required in order to allow such access and migration, or have requested the appropriate embargo below.

The following is an agreed request by candidate and supervisor regarding the publication of this thesis:

PRINTED COPY

Embargo on all or part of print copy for a period of 2 years on the following ground:

(a) Publication would preclude future publication

ELECTRONIC COPY

Embargo on all or part of electronic copy for a period of 2 years on the following ground:

(a) Publication would preclude future publication

Date Signature of candidate

Date Signature of supervisor

ABSTRACT AND TITLE EMBARGOES

An embargo on the full text copy of your thesis in the electronic and printed formats will be granted automatically in the first instance. This embargo includes the abstract and title except that the title will be used in the graduation booklet.

If you have selected an embargo option please indicate below if you wish to allow the thesis abstract and/or title to be published. If you do not complete the section below the title and abstract will remain embargoed along with the full text of the thesis.

a)	I agree to the title and abstract being published	YES
b)	I require an embargo on abstract	NO
c)	I require an embargo on title	NO

Date: 08/03/18

signature of candidate: A. Rankin signature of supervisor: S. Ashbrook

Acknowledgements

I would like to express my sincere thanks to my supervisor, Sharon Ashbrook. Her patient advice, support, and enthusiasm throughout the last four years have been invaluable, and for that I am truly grateful. I am grateful also to Daniel Dawson for all his help in the solid-state NMR lab, particularly his ability to get probes to tune simply by waving his hands over them, as well as for his unique style, which I will not soon forget. Special thanks go also to Paul Webb for his help with all things catalyst related. His encouraging words and enthusiastic approach to science kept me going even when things did not quite go to plan.

Thank you to all the members of the Ashbrook group for making sure lab and office life was never boring - I've probably eaten my own weight in cake during the course of all of our group meetings. Thanks go to Henri Colaux for teaching me some choice phrases in French and for sharing an appreciation for Monty Python. Thank you to Dave McKay for helping me to understand a little about DFT calculations, for good conversations, and for keeping the coffee flowing. Thanks to Giulia Bignami for all her help with X-ray diffraction, materials chemistry and citrus fruits, and for always sparing a moment to talk. I am grateful to Arantxa Fernandes for keeping me on track in the ^{17}O enrichment lab, and to Bonifác Légrády for putting up with my hand wavy explanations and bad jokes, and for his contribution to some of the experiments presented in Chapter 6. Thanks also to everyone in the Sasol St Andrews Lab who patiently and kindly answered questions, prepared samples and performed measurements for me. I am grateful to Lyndon Emsley at EPFL and his postdoctoral researchers Brennan Walder and Jasmine Viger-Gravel for all their help in Switzerland with those tricky DNP experiments. Thanks also go to Subhradip Paul and Jeremy Titman for their assistance on the DNP NMR spectrometer in Nottingham, and to Dinu Iuga for help on the 20.0 T (850 MHz) instrument at Warwick.

Thank you to all the friends in St Andrews that I have made over the years. A special mention goes to Laurence Taylor and Ciaran Lahive - you are some men for two men indeed. Thank you to all the regulars at darts and dominoes on Wednesdays - it was

nice to have something to look forward to in the middle of the week. Thanks also to everyone at All Saints' Scottish Episcopal Church for helping to take my mind off NMR for a few hours on a Sunday morning. Special mentions go to Claire, Mark, Alex, Ian, Dorian, Sibyl and Seamus. Many thanks to Kenny MacDonald (and his cat), Helen Rendall, David Killilea and Federico Mazzola - it was a pleasure to share a house with you all over the years. Thanks too, to friends further afield. To James Foster for being just a phone call away when I needed him, and to Alex Radevic for always having time for a coffee in Glasgow.

I am incredibly grateful to my family for all the support I received during my PhD studies. Many thanks to my Mother for her continued faith and encouragement, to Lisa and Douglas for being the kind of siblings every brother should have, and Kiera the dog for being a gentle and welcoming friend. To my late Father, who saw me begin this journey, thank you. You gave me the strength to persist through the toughest moments.

It was wonderful. There I really, I really believed in the spin, there are the states, count them! Each one, I suppose, seeks God in his own way.

Isidor I. Rabi

Abstract

This thesis describes applications of advanced multinuclear solid-state nuclear magnetic resonance (NMR) experiments to the characterisation of industrially-relevant catalyst materials. Experiments on γ-Al_2O_3 introduce the use of solid-state NMR spectroscopy for the investigation of disordered solids. The existence of Al(V) sites on the surface of this material is demonstrated, showing that removal of adsorbed H_2O may facilitate a rearrangement effect in γ-Al_2O_3 that promotes the formation of these Al environments. A range of aluminium oxide-based supported metal catalysts has been investigated. Studies of these systems by ^{1}H and ^{27}Al solid-state NMR spectroscopy indicate that a metal-support interaction (MSI) exists between surface cobalt oxide crystallites and the γ-Al_2O_3 support, and is strongest for materials containing small, well dispersed Co oxide crystallites. It is shown that the hygroscopic nature of γ-Al_2O_3 allows the extent of the MSI to be visualised by ^{1}H MAS NMR, by observing the extent of the proton-metal oxide interaction resulting from the presence of adventitious adsorbed H_2O. The surface/bulk chemistry of Co spinel aluminate materials is also investigated. ^{1}H, ^{29}Si, ^{27}Al and ^{17}O solid-state NMR techniques are used to gain insight into the structural nature of silicated alumina catalysts. The combination of isotopic enrichment and dynamic nuclear polarisation (DNP) surface-enhanced NMR spectroscopy can provide a definitive and fully quantitative description of the surface structure of Si-γ-Al_2O_3 (1.5 wt% Si), and the role of adventitious surface water is highlighted. Analysis of silicated aluminas prepared by "sequential grafting" and "single shot" approaches shows that silica growth on γ-Al_2O_3 follows two distinct morphologies. ^{17}O gas exchange enrichment is also shown to be successful in facilitating ^{17}O solid-state NMR studies of these materials. It is demonstrated that double (^{29}Si and ^{17}O) enrichment of Si-γ-Al_2O_3 (1.5 wt% Si) can facilitate access to ^{29}Si-^{17}O 2D correlation experiments, even at low silica loading. An exploratory investigation of Ti-alumina model catalysts has also been carried out using ^{1}H, ^{27}Al and ^{17}O solid-state NMR spectroscopy. These studies indicate that Ti-γ-Al_2O_3 and Ti-Al M50 may be structurally distinct materials.

Publications

A. G. M. Rankin, P. B. Webb, D. M. Dawson, J. Viger-Gravel, B. J. Walder, L. Emsley and S. E. Ashbrook, *J. Phys. Chem. C*, 2017, **121**, 22977.

Table of Contents

Chapter 1. Introduction

1.1 Catalysis and Catalysts

The term "catalyst" was first used in 1835 to refer to a chemical species that is capable of promoting a chemical reaction *via* "catalytic contact",[1] *i.e.* the catalyst can be added to a reaction to speed up the rate without itself being consumed in the process. Since the beginning of the 20th century, catalysts have played a major role in the chemical industry, and over 95% of chemicals today are produced by processes containing at least one catalytic step. Generally, catalysts can be divided into two types: homogeneous, operating in the same phase as the one where the reaction occurs, and heterogeneous, where the two phases are different.[2] The catalytic materials dealt with in this work are of the second, heterogeneous, type.

As mentioned above, chemical production and processing is highly reliant on catalysis. In particular, the transportation fuels sector is attempting to move towards fuel sources based on alternatives to crude oil, as it is a finite resource. Several methods exist for the production of such liquid fuels from natural gas, coal or biomass with one of the key examples being Fischer-Tropsch (F-T) synthesis. The process was developed in the 1920s by Franz Fischer and Hans Tropsch in Mülheim an der Ruhr, Germany.[3] Their aim was to develop a method by which coal could be converted into synthetic crude oil ("syncrude"), because in Germany there was a desire not to be reliant on natural petroleum as a fuel source at that time.[4] Fischer and Tropsch's efforts were well-received, and in 1934 F-T technology was commercialised by Ruhrchemie A. G.[5] A F-T production facility can be divided into three main components: generation of synthesis gas ("syngas") by gasification of coal or natural gas conversion; F-T synthesis, where syngas is converted into hydrocarbons, and product upgrading, where specific final products are produced.[6] In industry, F-T technology is classified as either high temperature F-T (HTF-T) or low temperature F-T (LTF-T), with the difference between the two being the operating conditions and product compositions. HTF-T processes typically produce higher mass % of olefins (alkenes) than their low-temperature counterparts.[7] Fischer-Tropsch reactions are catalysed by transition

metals, such as cobalt, iron or ruthenium, loaded onto oxide supports such as TiO_2, SiO_2 or Al_2O_3. These types of catalysts are discussed in more detail in Chapters 5 and 6.

Fluid catalytic cracking (FCC) also plays an important role in the commercial production of modern fuels. The process was developed in the 1940s by researchers working for the Standard Oil Company.[8] It involves the conversion of heavy olefins into more valuable products such as light olefins, middle distillates and petrol (also called gasoline). FCC is a versatile process and, as such, is capable of converting the products of F-T reactions into these kind of high value products.[9] As its name suggests, the FCC process utilises a solid catalyst that is made to behave like a fluid *via* the addition of hot vapour and liquid fed into the cracking column. This allows it to move easily through the reactor vessel and in combination with heat, 'cracks' apart large molecules of crude oil into smaller ones.[9] The FCC process utilises aluminosilicates such as zeolites and silicon-modified aluminas as catalysts, due primarily to their thermal stability, pore geometry and acid site strength, which enables product selectivity to be controlled in complex reactions. Solid acids are also attractive because they are convenient to handle in reactors, can be used at high temperatures and possess similar fundamental chemistry to solution-based acids.[10] These types of catalysts are also used in the dehydrative conversion of methanol/dimethyl ether (DME) to hydrocarbons, a key industrial process for the production of light olefins and petroleum,[11] and the Claus process for sulfur recovery from the gaseous H_2S found in raw natural gas.[12] Further detail on Si-alumina catalysts is given in Chapter 6.

1.2 Studying Catalysts by NMR Spectroscopy

The choice of catalyst can have a significant impact on the nature of the products that are produced in a reaction, so it is not surprising that there is currently a significant interest in the analysis and characterisation of such materials. Several studies have included characterisation by means of catalytic testing, X-ray techniques, vibrational

Table 1.1. *Summary of the nuclear magnetic properties – the spin quantum number, I, natural abundance, Larmor frequency, ν_0 (at 9.4 T), relative receptivity (to ^{1}H), and nuclear electric quadrupole moment, Q (for spin I > 1/2) – of some nuclei commonly found in heterogeneous catalysts.*[13]

Nucleus	Spin I	Natural Abundance (%)	ν_0 at 9.4 T / MHz	Receptivity Relative to ^{1}H[a]	Q / fm^2
^{1}H	1/2	99.99	400.13	1.00	-
^{2}H	1	0.01	61.42	1.11×10^{-6}	0.27
^{13}C	1/2	1.07	100.61	1.70×10^{-4}	-
^{14}N	1	99.64	28.92	1.00×10^{-3}	2.04
^{15}N	1/2	0.36	40.56	3.79×10^{-6}	-
^{17}O	5/2	0.04	54.24	1.10×10^{-5}	−2.56
^{19}F	1/2	100.00	376.50	8.33×10^{-1}	-
^{23}Na	3/2	100.00	105.84	9.26×10^{-2}	10.4
^{25}Mg	5/2	10.00	24.49	2.68×10^{-4}	19.94
^{27}Al	5/2	100.00	104.26	2.06×10^{-1}	14.66
^{29}Si	1/2	4.69	79.50	3.67×10^{-4}	-
^{31}P	1/2	100.00	161.98	6.63×10^{-2}	-
^{39}K	3/2	93.26	18.67	4.75×10^{-4}	5.85
^{47}Ti	5/2	7.44	22.557	1.56×10^{-4}	30.2
^{49}Ti	7/2	5.41	22.563	2.04×10^{-4}	24.7
^{51}V	7/2	99.75	105.25	3.83×10^{-1}	−5.2
^{59}Co	7/2	100.00	94.94	2.79×10^{-1}	42
^{87}Rb	3/2	27.83	130.92	4.88×10^{-2}	13.35
^{89}Y	1/2	100.00	19.60	1.19×10^{-4}	-
^{93}Nb	9/2	100.00	97.94	4.89×10^{-1}	−32
^{109}Ag	1/2	48.16	18.62	4.94×10^{-5}	-
^{183}W	1/2	14.31	16.67	1.07×10^{-5}	-
^{195}Pt	1/2	33.83	86.02	3.51×10^{-3}	-
^{207}Pb	1/2	22.1	83.68	2.01×10^{-3}	-

[a]Receptivity is defined as $\gamma^3 N(I(I + 1))$, where γ is the gyromagnetic ratio of the nucleus and N is the natural abundance.[13]

infrared and Raman) spectroscopy and electron microscopy.[14-17] However, many researchers have realised that solid-state nuclear magnetic resonance (NMR) spectroscopy is ideally suited to the study of heterogeneous catalysts,[18-20] as it has been demonstrated to be an effective probe of the local structure of materials. Advantages include no requirement for long range order, sensitivity to small changes in local environments, element specificity and a lack of restriction based on crystallite size.[21] Notable examples include Maciel and co-workers, who in the 1980s provided valuable insight into the surface chemistry of silica-based materials. They were able to demonstrate that the composition and concentration of surface hydroxyl (SiOH) groups could be determined *via* ^{1}H and ^{29}Si MAS NMR spectroscopy. These investigations also revealed that the reactivity of such sites varied considerably, depending on whether they were subjected to heat treatment or chemical modification.[22-24] In the 1990s, the Maciel research group also undertook NMR spectroscopic studies of a number of aluminium oxide- and hydroxide-based materials. In these studies, they were able to use ^{1}H MAS NMR techniques to demonstrate the presence of Al_2OH groups on the surface of bohemite (γ-AlOOH), a precursor to the widely used γ-Al_2O_3 catalyst.[25,26] The Hunger research group have also pursued the characterisation of catalyst materials by solid-state NMR spectroscopy, with a particular focus on zeolites. For example, by using one- and two-dimensional ^{23}Na NMR experiments, they were able to characterise sodium cations localised at crystallographically distinct cation sites in dehydrated faujasite zeolites.[27] In that study, they demonstrated the potential of ^{23}Na solid-state NMR spectroscopy for obtaining valuable information on cation distributions and coordination properties in zeolites and related materials.[27]

The majority of heterogeneous catalysts are composed of one or more elements that possess an NMR-active nucleus. These include "conventional" ones, such as ^{13}C, ^{29}Si and ^{31}P,[28] as well as more "exotic" nuclei such as ^{51}V and ^{93}Nb.[29] Details of some of these nuclei and their nuclear magnetic properties are provided in Table 1.1. The nuclei most extensively studied in this work, and their applications to heterogeneous catalyst characterisation, are outlined in more detail below.

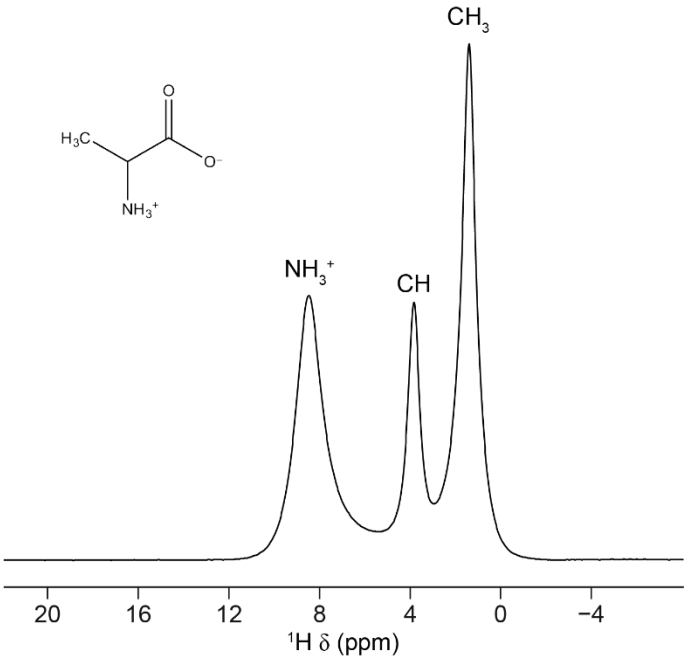

Figure 1.1. *^{1}H (14.1 T, 55 kHz MAS) NMR spectrum of L-alanine (structure shown above), with resonance assignments for each of the three H environments.*

1.2.1 ^{1}H

^{1}H (spin I = 1/2) is a nucleus with high natural abundance (99.99%) and very high γ. This makes ^{1}H NMR spectroscopy very sensitive, although techniques such as fast magic angle spinning (MAS)[30] or homonuclear decoupling[31] are required to compensate for large dipolar interactions in order to acquire high resolution spectra (these techniques are addressed in more detail in Chapters 2 and 3). The standard chemical shift range for ^{1}H is from 20 to −5 ppm, as demonstrated in the ^{1}H MAS NMR spectrum of L-alanine in Figure 1.1., although resonances from H species in paramagnetic compounds may lie outside of this range.[32] Additional details about the interactions that affect spectra are given in Chapter 2.

Hydrogen is present in, and is an important part of the structural chemistry of many heterogeneous catalysts. In particular, the hydroxyl groups of aluminosilicates (*e.g.* SiOH and AlOH) are key to the success of these materials as catalysts, providing a source of Brønsted acidity on the surface.[10] Table 1.2 gives chemical shift ranges for the main types of hydroxyl groups that are present in aluminosilicate materials. Many

Table 1.2. *^{1}H chemical shift ranges for the main types of hydroxyl groups present in aluminosilicate materials[22-26,33-37] These values are approximate and may vary slightly depending on the material studied.*

^{1}H δ (ppm)	Hydroxyl Group Abbreviation	Hydroxyl Group Type
−0.5-1	MeOH	Isolated Metal/cation (*e.g.*, Al, Mg) OH groups in large cavities or on particle surfaces
1-2.5	SiOH	Isolated (non-H bonded) silanol groups on particle surfaces or at lattice defects
2.5-3.5	Al_2OH	Isolated (non-H bonded) bridging aluminol groups on particle surfaces or in cavities
3.5-6.5	H_2O	Adsorbed H_2O on particle surfaces
6.5-12.5	AlOH	H-bonded aluminol groups on particle surfaces
9.5-16	SiOH	H-bonded silanol groups on particle surfaces

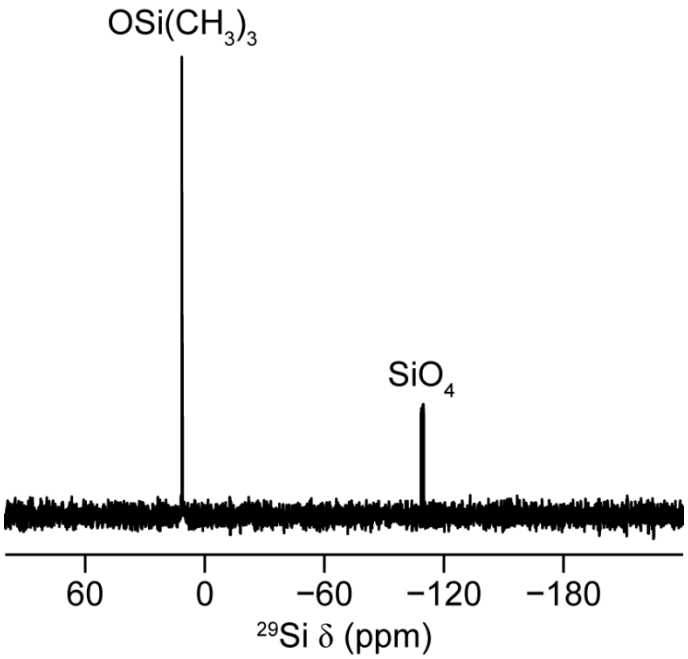

Figure 1.2. *^{1}H-^{29}Si (9.4 T, 10 kHz MAS and τ_{CP} = 1 ms) CP NMR spectrum of powdered octakis(trimethylsiloxy)silsesquioxane (Q8M8) with resonance assignments for each type of Si environment present.*

catalysts also readily adsorb molecules onto their surfaces. Examples include pyridine, acetone[37] and H_2O, the last of which adsorbs onto the surface as a result of the hygroscopic nature of the material.[33] In both cases, such molecules can be useful probes of the surface chemistry of catalysts, as has been highlighted both in the literature[38,39] and, in the case of H_2O, Chapter 6 of this work.

1.2.2 ^{29}Si

^{29}Si (spin I = 1/2) is the only NMR-active isotope of the element silicon and has a low natural abundance (4.69%) and medium/low γ. Silicon-containing materials are used extensively in industrial processes, with some of the most commonly-utilised catalysts being derived from zeolites and aluminosilicates.[40] As a result, ^{29}Si NMR spectroscopy has been widely employed as a characterisation technique in this field, primarily for materials in the solid state.[41]

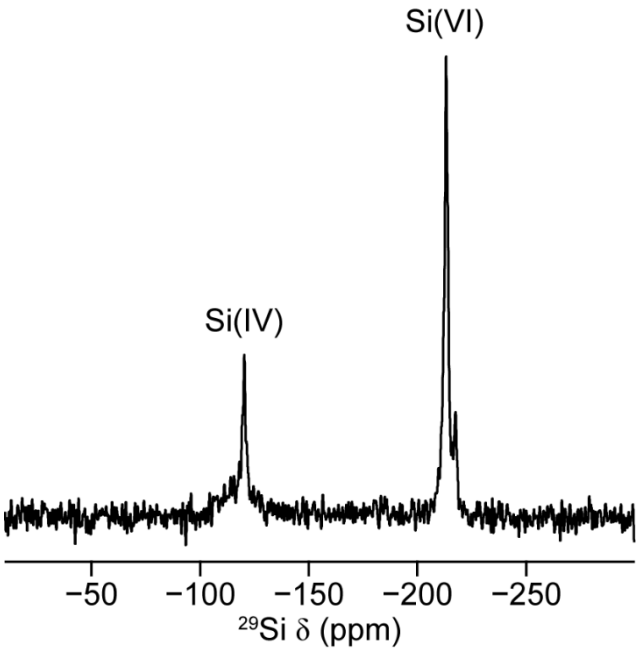

Figure 1.3. *[29]Si (14.1 T, 18 kHz MAS) NMR spectrum of a silicon phosphate material, accompanied by resonance assignments for the two types of Si coordination environment present.*

The standard chemical shift range for ^{29}Si is from 30 to −230 ppm, and for a given Si species, this is influenced greatly by its local environment, where the two principal factors are coordinating element and coordination number.[42] In the first instance, this is demonstrated *via* the ^{1}H-^{29}Si cross polarisation (CP) NMR spectrum of powdered octakis(trimethylsiloxy)silsesquioxane (Q8M8) in Figure 1.2, where resonances at 11.5 and −110 ppm are observed. These correspond to $OSi(CH_3)_3$ and SiO_4 species, respectively.[43] The second case, a variation in coordination number, can commonly be observed in inorganic materials, such as catalysts, where silicon is bonded to oxygen. Typically, the chemical shift of Si sites of this nature varies by approximately 50 ppm going from Si(IV) to Si(V) to Si(VI).[44] Examples of catalyst materials containing more than one Si-O coordination environment have been documented in the literature,[28,45,46] and an example is also shown in Figure 1.3, where the ^{29}Si NMR spectrum of a silicon phosphate material reveals the presence of both Si(IV) and Si(VI) species with a significant shift difference between them.

Si species in most silicates consist of tetrahedral (Si(IV)) units that are polymerised to varying extents. It is common practice to describe these environments using "Q" notation, where Q denotes a Si bonded to four O atoms, and a superscript number from

Table 1.3. *Examples of the typical ^{29}Si chemical shift variation between silicates and aluminosilicates.*[47]

Silicate	^{29}Si δ (ppm)	Q^4 Aluminosilicate	^{29}Si δ (ppm)
Q^1	−80	4Al	−84
Q^2	−87	3Al	−88
Q^3	−98	2Al	−95
Q^4	−109	1Al	−100
-	-	0Al	−107

0 to 4 is then used to indicate how many other Q species are attached to a particular unit. For example, in a silicate material, Q^4 represents a Si that is bonded *via* O to four other Si species. Each additional Si connection moves the ^{29}Si chemical shift to more negative ppm values, with a variation of ~10 ppm occurring for each additional Si-O-Si linkage present.[44] To describe the Si species in aluminosilicates however, an addition to the above notation is required. In this case, the notation takes the form of Q^n(mAl), where n represents a superscript number in the same manner as above, and m denotes the number, from 0 to n, of aluminium units that a particular Si species is bonded to through O. For example, Q^4(3Al) represents a Si that is bonded *via* O to three Al species and one additional Si(IV) unit. Each additional Al connection moves the ^{29}Si chemical shift to higher ppm values, with a variation of ~5 ppm occurring for each additional Si-O-Al linkage present.[47] Table 1.3 provides a summary of this for the case of Q^4(mAl) species. However, one factor that must be considered when acquiring ^{29}Si spectra though, is that this nucleus usually possesses long T_1 relaxation times (sometimes on the order of hours).[44] This means that extended experimental times are necessary in order to acquire high-resolution spectra. Techniques such as paramagnetic doping and ^{1}H-^{29}Si CP (the second of which is discussed further in Chapter 3) can be used to shorten experiment times.[44,48]

1.2.3 ^{27}Al

^{27}Al (spin I = 5/2) is a nucleus with 100% natural abundance, medium γ and a moderate quadrupole moment. As with silicon, aluminium is ubiquitous in industry and Al-containing materials are routinely employed as heterogeneous catalysts.[40] As ^{27}Al is a quadrupolar nucleus, the peak position (of the central transition) is shifted away from

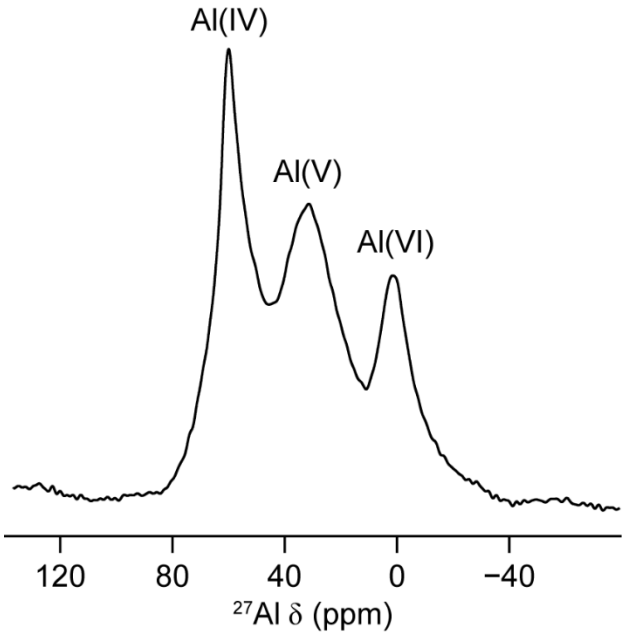

Figure 1.4. *^{27}Al (14.1 T, 14 kHz MAS) NMR spectrum of zeolite USY, with resonance assignments for the three types of Al-O coordination environment present.*

the isotropic chemical shift (δ_{iso}), typically to more negative ppm values. Fortunately, δ_{iso} can be experimentally determined, providing that quadrupolar parameters such as C_Q and η_Q are known.[49] A detailed explanation of these parameters and their use is provided in Chapters 2 and 3.

The standard chemical shift range for ^{27}Al is from −30 to 110 ppm and is strongly dependent on the coordinating elements and coordination number. In the case of Al-O species, ^{27}Al NMR spectroscopy is an excellent probe of coordination number, as there are well-defined chemical shift ranges for tetrahedral (Al(IV)), pentahedral (Al(V)) and octahedral (Al(VI)) environments. Al(IV) resonances are observed from 80-50 ppm, Al(V) resonances from 40-30 ppm and those of Al(VI) from 15 to −10 ppm.[44,50] This is illustrated in Figure 1.4, where these three types of environment are observed in the ^{27}Al NMR spectrum of "ultrastable" zeolite Y (designated USY, and produced by steam treatment of zeolite Y), a material employed as a catalyst in processes such as FCC.[10]

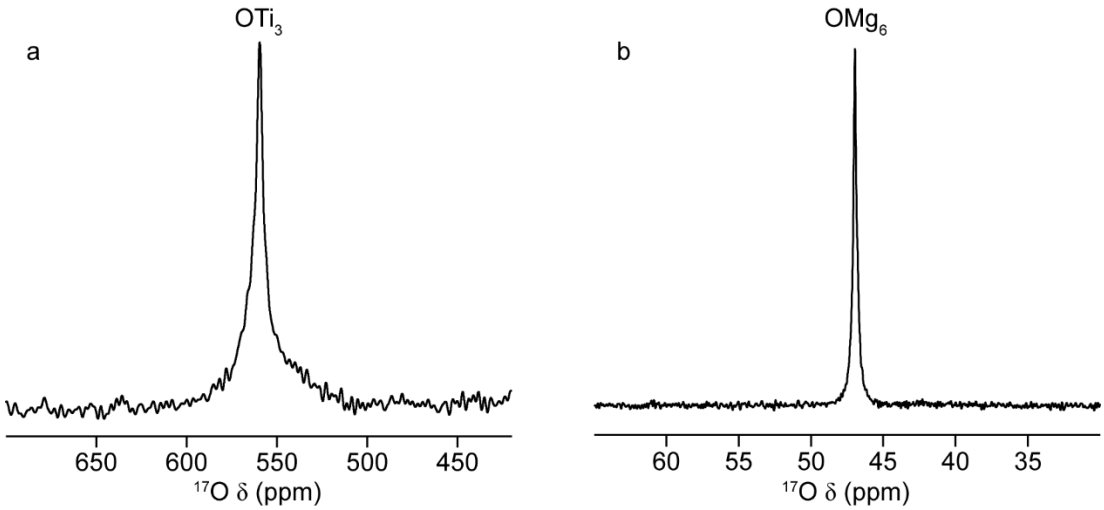

Figure 1.5. *^{17}O (14.1 T, 14 kHz MAS) NMR spectra of ^{17}O enriched (a) TiO_2 (anatase) and (b) MgO, along with resonance assignments for the O environments present in each material.*

1.2.4 ^{17}O

^{17}O (spin I = 5/2) is the only NMR-active isotope of the element oxygen. It is a nucleus with medium/low γ, a small quadrupole moment and very low natural abundance (0.04%). As with ^{27}Al, ^{17}O is a quadrupolar nucleus, and so the peak position of the central transition is shifted away from its isotropic chemical shift (δ_{iso}) in the same manner. Like ^{27}Al, experimental determination of δ_{iso} can be undertaken if the quadrupolar parameters (C_Q and η_Q) are known.[49] The standard chemical shift range for ^{17}O is from −40 to 1140 ppm, and each type of chemical environment possesses its own distinctive subrange.[51] This makes ^{17}O NMR spectroscopy an attractive technique for the study of materials such as catalysts, where oxygen is an integral component of the chemical structure.[40,44] The sensitivity of ^{17}O to the local environment is well illustrated in Figure 1.5, where ^{17}O spectra of two catalyst materials, TiO_2 (anatase)[52] and MgO[53] are shown. The spectra reveal that the resonances for each type of species (OTi_3 and OMg_6, respectively) possess distinctly different δ values.

Given what has been outlined above, it would not be unreasonable to expect ^{17}O NMR spectroscopy to be a popular and widely-used technique in materials characterisation. However, as has already been mentioned, ^{17}O has a very low natural abundance

(0.04%), which makes performing NMR experiments with this nucleus very challenging. In order to overcome this hurdle, isotopic enrichment strategies have been developed, and these can be divided into two categories. The first involves the synthesis of the material to be studied using ^{17}O-enriched reagents, such as $H_2{}^{17}O$. This is particularly relevant for materials where synthetic routes are well documented and can be carried out on a small scale; examples include zeolites,[54] minerals[55] and metal-organic frameworks.[56] In the second category, ^{17}O enrichment is carried out "post synthetically", with the primary method for achieving this being *via* gas exchange treatment. In brief, this is accomplished by heating the material under vacuum in an atmosphere of $^{17}O_2$ gas for a period of several hours. Isotope exchange then occurs, resulting in a material that is ^{17}O enriched. This method has been successfully applied to ^{17}O NMR spectroscopic studies of heterogeneous catalysts, both in the literature[57,58] and in Chapter 6 of this work, where it is described in more detail.

1.3 Thesis Overview

This thesis describes the applications of solid-state NMR spectroscopy to the characterisation of a variety of industrial catalysts.

Chapter 2 outlines the theoretical background of solid-state NMR spectroscopy and the signal enhancement technique known as dynamic nuclear polarisation (DNP).

Chapter 3 describes the solid-state NMR and DNP NMR experimental methods and techniques that have been utilised in this thesis.

Chapter 4 describes the solid-state NMR and DNP NMR spectroscopic details for the experiments that have been undertaken in this thesis. Information regarding the samples that have been studied in this thesis are also provided. Details of ^{17}O enrichment procedures are also given.

In Chapter 5, the investigation of alumina-supported cobalt oxide catalysts by solid-state NMR spectroscopy is detailed. Information regarding the insight that has been

gained into the influence of metal oxide loading and crystallite size on the metal-support interaction in this type of catalyst, *via* the study of the Co-Al_2O_3 and Co-$CoAl_2O_4$ systems, is outlined.

Chapter 6 describes efforts to understand the structural nature of the silicated alumina type of catalyst. It outlines the insight into the surface chemistry and interatomic interactions that has been gained through multinuclear solid-state NMR techniques. This includes the application of DNP NMR spectroscopy to the study of model catalysts, which has facilitated the acquisition of additional valuable one and two-dimensional experiments. Efforts to acquire structural information from ^{17}O NMR experiments *via* isotopic enrichment are also detailed. Insight is provided into the growth morphology of silica on catalytically-relevant oxide materials, by combining information obtained from NMR and X-ray-photoelectron spectroscopies. Multinuclear solid-state NMR spectroscopic approaches for elucidating the structure of titanium-modified alumina catalysts are also outlined. This includes efforts to acquire information about the structural location of Ti species from ^{17}O NMR experiments *via* isotopic enrichment.

In Chapter 7, an overall summary of the conclusions for this work is given. The outlook for each experimental project is also briefly outlined.

1.4 References

1. J. J. Berzelius, *Årsberättelse om framstegen i fysik och kemi,* 1835, **1**, 1.
2. A. P. G. Kieboom, J. A. Moulijin, P. W. N. M. van Leeuwen and R. A. Santen, in *Catalysis: An Integrated Approach*, Elsevier Science B.V., Amsterdam, Second Edn., 1999.
3. *US Pat.* US1746464A, 1930.
4. A. N. Stranges, *Stud. Surf. Sci. Catal.*, 2007, **163**, 1.
5. D. Leckel, *Energy Fuels*, 2009, **23**, 2342.
6. A. P. Steynberg, *Stud. Surf. Sci. Catal.*, 2004, **152**, 1.
7. A. de Klerk, *Green Chem.*, 2008, **10**, 1249.

8. *US Pat.* US2451804A, 1940.
9. J. Scherzer, in *Fluid Catalytic Cracking: Science and Technology*, Eds. J. S. Magee and M. M. Mitchell, Elsevier, Amsterdam, The Netherlands, First Edn., 1993.
10. H. Hattori and Y. Ono, *Solid Acid Catalysis: From Fundamentals to Applications*, CRC Press, Boca Raton, First Edn., 2015.
11. N. Hazari, E. Inglesia, J. A. Labinger and D. A. Simonetti, *Acc. Chem. Res*., 2012, **45**, 653.
12. M. A. Fahim, T. A. Alsahhaf and A. Elkilani, *Fundamentals of Petroleum Refining*, Elsevier, Amsterdam, First Edn., 2010.
13. R. K. Harris, E. D. Becker, S. M. C. de Menezes, R. Goodfellow and P. Granger, *Pure Appl. Chem.*, 2001, **73**, 1795.
14. M. I. Zaki, G. A. M. Hussein, S. A. A. Mansour, H. Ismail and G. A. H. Mekhemer, *Colloids Surf. A*, 1997, **127**, 47.
15. R. Ferwerda and J. H. van der Maas, *J. Phys. Chem.*, 1995, **99**, 14764.
16. D. Jaumain and B-L. Su, *Catal. Today*, 2002, **73**, 187.
17. A. Y. Khodakov, W. Chu and P. Fongarland, *Chem. Rev.*, 2007, **107**, 1692.
18. J. F. Haw, I-S. Chuang, B. L. Hawkins and G. E. Maciel, *J. Am. Chem. Soc.*, 1983, **105**, 7206.
19. J. Klinowski, *Chem. Rev.*, 1991, **91**, 1459.
20. E. Papulovskiy, D. F. Khabibulin, V. V. Terskikh, E. A. Paukshtis, V. M. Bondareva, A. A. Shubin, A. S. Andreev and O. Lapina, *J. Phys. Chem. C*, 2015, **119**, 10400.
21. D. C. Apperley, R. K. Harris and P. Hodgkinson, *Solid-State NMR: Basic Principles & Practice*, Momentum Press, New York, First Edn., 2012.
22. D. W. Sindorf and G. E. Maciel, *J. Am. Chem. Soc.*, 1983, **105**, 5529.
23. D. W. Sindorf and G. E. Maciel, *J. Phys. Chem.*, 1983, **87**, 5516.
24. C. E. Bronnimann, R. C. Zeigler and G. E. Maciel, *J. Am. Chem. Soc.*, 1988, **110**, 2023.
25. G. Piedra, J. J. Fitzgerald, N. Dando, S. F. Dec and G. E. Maciel, *Inorg. Chem.*, 1996, **35**, 3474.

26. J. J. Fitzgerald, G. Piedra, S. F. Dec, M. Seger and G. E. Maciel, *J. Am. Chem. Soc.*, 1997, **119**, 7832.
27. M. Hunger, G. Engelhardt, H. Koller and J. Weitkamp, *Solid State Nucl. Magn. Reson.*, 1993, **2**, 111.
28. T. R. Krawietz, P. Lin, K. E. Lotterhos, P. D. Torres, D. H. Barich, A. Clearfield and J. F. Haw, *J. Am. Chem. Soc.*, 1998, **120**, 8502.
29. O. B. Lapina, D. F. Khabibulin, A. A. Shubin and V. V. Terskikh, *Prog. Nucl. Magn. Reson. Spectrosc.* 2008, **53**, 128.
30. Y. Nishiyama, Y. Endo, T. Nemoto, H. Utsumi, K. Yamauchi, K. Hioka and T. Asakura, *J. Magn. Reson.*, 2011, **208**, 44.
31. P. K. Madhu, *Solid State Nucl. Magn. Reson.*, 2009, **35**, 2.
32. V. I. Bakhmutov, *Solid-State NMR in Materials Science Principles and Applications*, CRC Press, Boca Raton, 2012.
33. D. R. Kinney, I-S. Chuang and G. E. Maciel, *J. Am. Chem. Soc.*, 1993, **115**, 6786.
34. M. Hunger, S. Ernst, S. Steuernagel and J. Weitkamp, *Microporous Mater.*, 1996, **6**, 349.
35. M. Hunger, *Catal. Rev.-Sci. Eng.*, 1997, **39**, 345.
36. X. Xue and M. Kanzaki, *J. Am. Ceram. Soc.*, 2009, **92**, 2803.
37. Y. Jiang, J. Huang, W. Dai and M. Hunger, *Solid State Nucl. Magn. Reson.*, 2011, **39**, 116.
38. J. H. Lunsford, W. Rothwell and W. Shen, *J. Am. Chem. Soc.*, 1985, **107**, 1540.
39. B. Alonso, I. Klur and D. Massiot, *Chem. Commun.*, 2002, **1**, 804.
40. P. A. Wright, *Microporous Framework Solids*, Royal Society of Chemistry, Cambridge, First Edn., 2008.
41. G. Engelhardt and H. Koller, in *NMR Basic Principles and Progress*, Springer-Verlag, Berlin, First Edn. 1994, Volume 31, pp. 1-29.
42. J. M. Thomas and J. Klinowski, *Adv. Catal.*, 1985, **33**, 199.
43. W. Kolodziejski and J. Klinowski, *Solid State Nucl. Magn. Reson.*, 1992, **1**, 41.
44. K. J. D. MacKenzie and M. E. Smith, *Multinuclear Solid-State NMR of Inorganic Materials*, Pergamon, Oxford, First Edn., 2002.

45. C. Lejeune, C. Coelho, L. Bonhomme-Coury, T. Azaïs, J. Maquet and C. Bonhomme, *Solid State Nucl. Magn. Reson.*, 2005, **27**, 242.
46. C. Coelho, T. Azaïs, L. Bonhomme-Coury, J. Maquet, D. Massiot and C. Bonhomme, *J. Magn. Reson.*, 2006, **179**, 114.
47. E. Lippmaa, M. Magi, A. Samoson, G. Engelhardt and A. R. Grimmer, *J. Am. Chem. Soc.*, 1980, **102**, 4889.
48. S. Inagaki, I. Kawamura, Y. Sasaki, K. Yoshida and A. Naito, *Phys. Chem. Chem. Phys.*, 2013, **15**, 13523.
49. A. P. M. Kentgens, *Geoderma*, 1997, **80**, 271.
50. M. E. Smith, *Appl. Magn. Reson.*, 1993, **4**, 1.
51. S. E. Ashbrook and M. E. Smith, *Chem. Soc. Rev.*, 2006, **35**, 718.
52. X. Sun, M. Dyballa, J. Yan, L. Li, N. Guan and M. Hunger, *Chem. Phys. Lett.*, 2014, **594**, 34.
53. A. V. Chadwick, I. J. F. Poplett, D. T. S. Maitland and M. E. Smith, *Chem. Mater.*, 1998, **19**, 4756.
54. D. Freude, T. Loeser, D. Michel, U. Pingel and D. Prochnow, *Solid State Nucl. Magn. Reson.*, 2001, **20**, 46.
55. S. E. Ashbrook and D. M. Dawson, *Nucl. Magn. Reson.*, 2016, **45**, 1.
56. P. He, J. Xu, V. V. Terskikh, A. Sutrisno, H-Y. Nie and Y. Huang, *J. Phys. Chem. C*, 2013, **117**, 16953.
57. L. Peng, H. Huo, Y. Liu and C. P. Grey, *J. Am. Chem. Soc.*, 2007, **129**, 335.
58. C. A. Klug, S. Kroeker, P. M. Aguiar, M. Zhou, D. F. Stec and I. E. Wachs, *Chem. Mater.*, 2009, **21**, 4127.

Chapter 2. Nuclear Magnetic Resonance

"These atomic frequencies in the magnetic field are so characteristic for each element and its isotopes that they are more undisturbed and regular than the balance-wheel, pendulum and vibrating quartz-crystal in our modern chronometers…"[1]

In 1952, the Nobel Prize in Physics was jointly awarded to Felix Bloch and Edward Purcell for their discovery of nuclear magnetic resonance (NMR).[1,2,3] Since that time, NMR has revolutionised the fields of natural sciences and medicine, proving itself to be an essential part of modern scientific analysis. In this chapter, the essential principles of NMR are introduced, along with the rapidly emerging signal-enhancement technique known as dynamic nuclear polarisation (DNP).

2.1 NMR Theory

2.1.1 The Vector Model and Zeeman Interaction

The spin angular momentum of atomic nuclei (**I)**, is a quantum mechanical property with corresponding spin quantum number, I, which can be zero or any positive integer multiple of 1/2. The magnitude of **I** is given by

$$|\mathbf{I}| = \hbar\sqrt{I(I+1)} \ . \qquad (2.1)$$

The projection of **I** onto a specific axis, by convention the *z*-axis, is given by $m_I\hbar$, where m_I is the azimuthal quantum number and takes values from +I to –I in integral steps, resulting in 2I + 1 degenerate states. Nuclei with non-zero spin ($I \geq 1/2$) possess a magnetic dipole moment, **μ**, which is given by

$$\boldsymbol{\mu} = \gamma\mathbf{I} \ , \qquad (2.2)$$

where γ is the gyromagnetic ratio of the nucleus. The component of **μ** along the z-axis, μ_z, is, therefore

$$\mu_z = \gamma m_I\hbar \ . \qquad (2.3)$$

In the presence of an external magnetic field the *z*-axis is defined as the direction of

the magnetic field vector, $\mathbf{B}_0$, having magnitude B_0. The Zeeman interaction[4,10] is the interaction between the nuclear magnetic moment and the external field and the energy of this is given by

$$E_{m_I} = -\mu_z B_0 = -\gamma m_I \hbar B_0 \ . \qquad (2.4)$$

The selection rule for observable transitions in NMR is $\Delta m_I = \pm 1$, and so these transitions are degenerate and occur with energy difference

$$\Delta E = \gamma \hbar B_0 \ . \qquad (2.5)$$

The frequency of such transitions can be defined as

$$\omega_0 = 2\pi\nu_0 = \Delta E / \hbar = -\gamma B_0 \ , \qquad (2.6)$$

where this frequency is referred to as the Larmor frequency and has units of rad s^{-1} (ω_0) or Hz (ν_0). On the macroscopic scale at thermal equilibrium, the population of these energy levels can be described by the Boltzmann distribution

$$N_{upper} / N_{lower} = e^{-\Delta E / k_B T} \ , \qquad (2.7)$$

and thus, from Equation 2.5, for I = 1/2

$$N_{upper} / N_{lower} = e^{-\gamma \hbar B_0 / k_B T} \ . \qquad (2.8)$$

For ^{1}H in a magnetic field of 14.1 T at 300 K, the population ratio of the upper state to the lower state is 1000000 : 1000096 and so the population difference, ΔN_{eq} (N_{upper} / N_{lower}), results in the bulk magnetisation vector, $\mathbf{M}_0$

$$\mathbf{M}_0 = 1/2 \ \gamma \hbar \Delta N_{eq} \ . \qquad (2.9)$$

The fact that the populations are almost equal ($\Delta N_{eq} / N \cong 0$, where N is the total number of nuclei) means that NMR spectroscopy is an inherently insensitive technique, with only one nucleus in 10416 contributing to $\mathbf{M}_0$ in this particular example. ^{1}H has one of the highest known gyromagnetic ratios and 99.9% natural abundance and so receptivity is lower for virtually all other nuclei, often by several orders of magnitude, due to the exponential dependence of $\mathbf{M}_0$ on γ and the lower

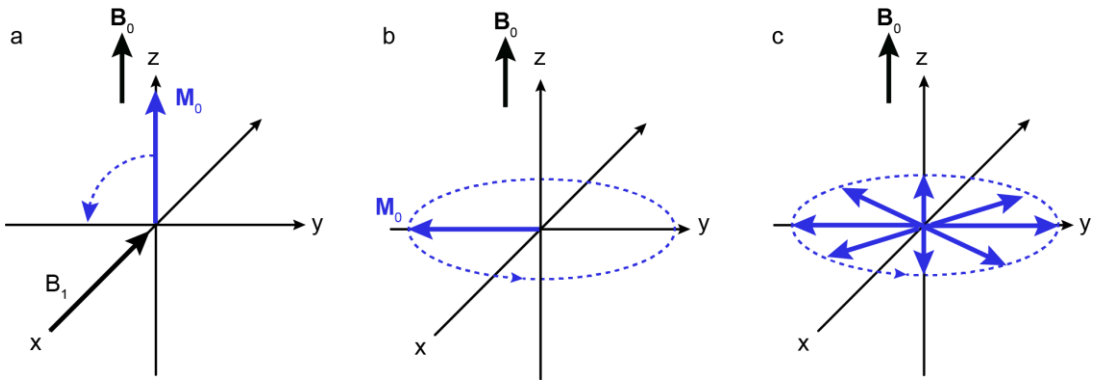

Figure 2.1. *(a) Application of a 90$_{-x}$° B_1 pulse of sufficient duration results in nutation of* $\mathbf{M}_0$ *in the yz plane until it is in the xy plane. (b) Then* $\mathbf{M}_0$ *precesses around* B_0 *at the Larmor frequency with nuclei in magnetically different environments having different frequencies. (c) Transverse relaxation eventually results in magnetisation being completely dephased in the xy plane.*

natural abundance of many other NMR-active nuclei.

In the laboratory frame, $\mathbf{M}_0$ is aligned along the *z*-axis defined by B_0; the presence of the magnetic field though results in precession of $\mathbf{M}_0$ around the *z*-axis at the Larmor frequency. In NMR spectroscopy an oscillating radiofrequency field, B_1 (commonly called a pulse), with frequency ω_{rf} (close to ω_0) is applied to the sample under analysis. B_1 can be considered as two counter-rotating magnetic fields having frequencies of $+\omega_{rf}$ and $-\omega_{rf}$. Since the mathematics of the precession of $\mathbf{M}_0$ in the laboratory frame are complex, it is more convenient to consider a set of axes rotating at ω_{rf} such that $\mathbf{M}_0$ is aligned along the *z*-axis, which appears to be stationary with respect to the *x*- and *y*-axes. The result is that the $+\omega_{rf}$ component of B_1 appears to be stationary with respect to the rotating frame, while the counter-rotating component rotates at $-2\omega_{rf}$ and therefore does not interact with $\mathbf{M}_0$.

In the rotating frame B_1 is a static field and is normally applied orthogonally to B_0. The application of a B_1 field along the *x*-axis causes nutation of magnetisation in the *yz* plane, and this continues provided that the B_1 field is present, as shown in Figure 2.1. The extent of nutation can be measured by the flip angle, β, where τ_P is the pulse duration

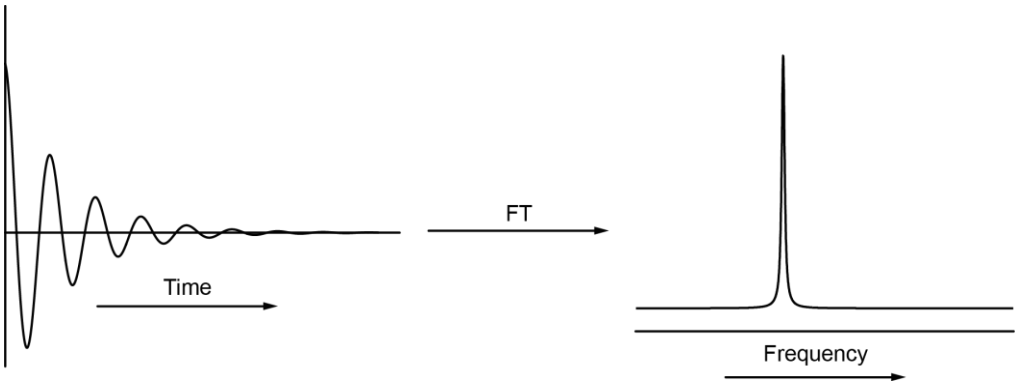

Figure 2.2. *Schematic representation of the conversion of time-domain data to frequency-domain data, via Fourier transformation.*

$$\beta = \omega_1 \tau_P \ , \tag{2.10}$$

and, therefore,

$$\omega_1 = -\gamma B_1 \ . \tag{2.11}$$

The pulse does not have to be applied along the *x*-axis, meaning that a phase, ϕ, needs to be specified. The phase describes the direction along which the pulse is applied and, as a result, B_1 pulses are usually described by β_ϕ notation. Once the pulse has been applied, the nuclear magnetic moments precess around the *z*-axis, now with a component in the *xy* plane. This component can be recorded in the *xy* plane in the form of a free induction decay (FID). Conversion of this time-domain FID to an NMR spectrum in the frequency domain is achieved *via* a Fourier transformation (FT):

$$S(\omega) = \int_{-\infty}^{\infty} s(t) \exp(-i\omega t)\, dt \ . \tag{2.12}$$

This process is illustrated in Figure 2.2. Quadrature detection[8] is usually employed during acquisition of the FID and involves the measurement of two distinct components to generate a complex signal that distinguishes the sign of the resonance offset, Ω, in order to produce an unambiguous frequency-domain spectrum *via* a FT. Two orthogonal detectors are utilised, allowing for the acquisition of two components that are 90° out of phase with one another; one component is a cosine and the other is a sine function of the offset frequency. These two components are considered to be

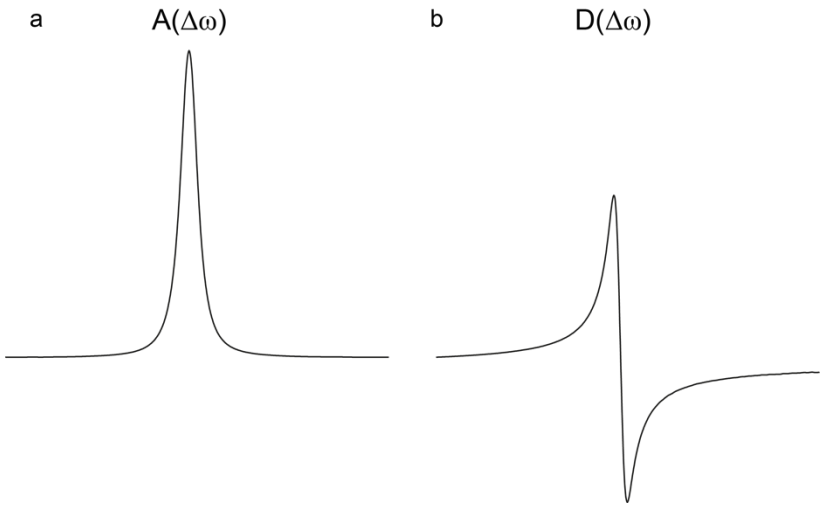

Figure 2.3. *Examples of (a) absorptive (real) and (b) dispersive (imaginary) lineshapes.*

real and imaginary components of a single complex signal.

In general, the FID contains cosine and sine functions of the offset frequency, Ω, that decay at a rate proportional to $1/T_2$

$$S(\omega) = [\cos \Omega t + i \sin \Omega t]\exp(-t/T_2) \ . \qquad (2.13)$$

Fourier transformation of the FID results in a frequency-domain spectrum that contains absorptive (real), A(Δω), and dispersive (imaginary), D(Δω), components

$$S(\omega) = A(\Delta\omega) + iD(\Delta\omega) \ , \qquad (2.14)$$

with

$$A(\Delta\omega) = 1/T_2 \ / \ (1/T_2)^2 + (\Delta\omega)^2 \ , \qquad (2.15)$$

and

$$D(\Delta\omega) = (\Delta\omega) \ / \ (1/T_2)^2 + (\Delta\omega)^2 \ , \qquad (2.16)$$

where $\Delta\omega = \omega - \Omega$. Generally, the real part of a frequency-domain spectrum contains a combination of absorption and dispersion signals, so it must be "phase corrected" to

obtain a pure absorption lineshape. Examples of absorptive and dispersive lineshapes are shown in Figure 2.3.

2.1.2 Density Operator Formalism

Whilst the vector model provides a convenient way of considering simple NMR experiments, for more complex ones a more rigorous approach is required. The density operator formalism is a useful tool for dealing with complex experiments and higher-order spin systems.[5] In a given sample, there is a set of spin systems which may be each represented by a wavefunction $\Psi(t)$, described as a linear combination of elements of an orthogonal basis set $|i\rangle$, where $c_i(t)$ are time-dependent coefficients

$$\Psi(t) = \sum_i c_i(t) |i\rangle \ . \qquad (2.17)$$

The elements, $\rho_{i,j}(t)$, of the corresponding density matrix, ρ, are products of the expansion coefficients of the wavefunction

$$\rho_{i,j}(t) = \langle i|\rho(t)|j\rangle = \overline{c_i(t)c_j(t)^*} \ , \qquad (2.18)$$

with the overbar donating an ensemble average and * a complex conjugate. The time evolution of the density operator is given by the Liouville-von Neumann equation

$$d\rho(t) / dt = -i[H(t),\rho(t)] \ . \qquad (2.19)$$

If the Hamiltonian is time independent (or is made to be so), then it can be solved by

$$\rho(t) = \exp(-iHt)\ \rho(0)\ \exp(iHt) \ , \qquad (2.20)$$

where $\rho(0)$ is the density operator at time zero. This formalism is utilised by simulation programs such as SIMPSON[6] when simulating pulses and delays in a NMR experiment.

2.1.3. Coherence

When considering a collection of non-interacting spin I = 1/2 nuclei, each one can be described by a superposition of states, $|\alpha\rangle$ and $|\beta\rangle$, corresponding to the two Zeeman levels. The complex superposition coefficients, $c_\alpha(t)$ and $c_\beta(t)$, describe the

contribution to these states and have phases ϕ_α and ϕ_β, respectively, at t = 0. Therefore, the wavefunction is

$$|\Psi\rangle = c_\alpha e^{i\phi_\alpha}|\alpha\rangle + c_\beta e^{i\phi_\beta}|\beta\rangle . \quad (2.21)$$

The corresponding density matrix is

$$\rho(t) = \begin{pmatrix} c_\alpha^2 & c_\alpha c_\beta e^{i(\phi_\alpha - \phi_\beta)} \\ c_\alpha c_\beta e^{-i(\phi_\alpha - \phi_\beta)} & c_\beta^2 \end{pmatrix}, \quad (2.22)$$

where the diagonal elements, c_α^2 and c_β^2, refer to the populations of the $|\alpha\rangle$ and $|\beta\rangle$ states, respectively. The off-diagonal elements are considered to have phase coherence if they possess the same relative phases for each spin and therefore have non-zero magnetisation. Coherence is generated by individual spins that experience the same interaction with the applied rf field.[7]

The application of a pulse results in rotation of the axis along which polarisation is aligned, so if an operator gains a phase of $-p\phi$ *via* a *z*-rotation through angle ϕ, then it will have coherence order p. Therefore, changing the coherence order can only be accomplished with a pulse. Coherence order p = 0 corresponds either to zero-quantum or z-magnetisation (*i.e.*, a population state), p = ±1 to single-quantum and p = > ±1 to multiple-quantum (MQ) coherences. The coherence order has to be controlled during a pulse sequence and the coherence transfer pathway diagram indicates the desired coherence at each point. A coherence transfer pathway always begins at p = 0 and ends at p = −1 (*i.e.*, observable magnetisation), if quadrature detection[8] is employed. Whilst not directly observable, MQ coherences are used in advanced NMR experiments, such as those described in Chapter 3.

2.1.4 Relaxation

Magnetisation in the *xy* plane is lost rapidly (on the order of 1-1000 ms) by dephasing of spin coherence. This occurs due to the fact that each nucleus experiences a slightly different magnetic field and so precess at a slightly different rate. Dephasing is also known as transverse or spin-spin relaxation[4] and is characterised by the exponential

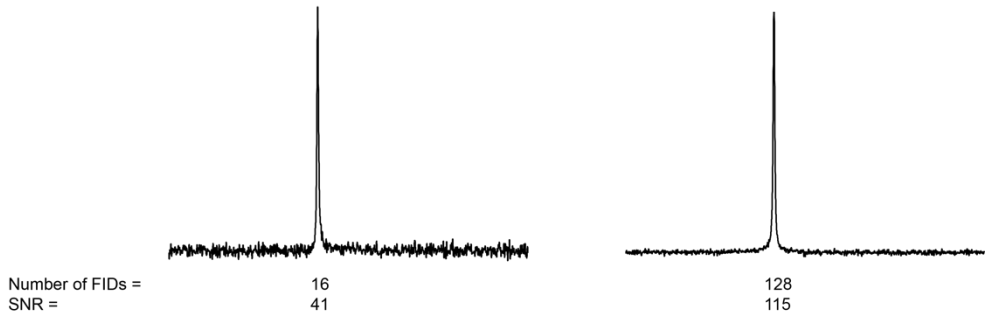

Figure 2.4. *The effect of signal averaging on the ^{13}C MAS NMR spectrum (9.4 T, 14 kHz MAS) of the CH_3 site (δ = 20.5 ppm) of L-alanine.*

time constant, T_2. The overall magnetization returns to thermal equilibrium *via* longitudinal or spin-lattice relaxation. This is characterised by the exponential time constant, T_1, which can be on the order of a few ms up to several hours depending on the sample and nucleus being studied. Generally, for solids, $T_1 > T_2$.

When studying nuclei that have low receptivity, Fourier transformation of a single FID can often result in a spectrum with a considerable level of thermal "noise". It is, therefore, common practice to carry out "signal averaging", where multiple FIDs are acquired and summed prior to the Fourier transform. The signal intensity increases linearly with the number of combined FIDs, N, and the intensity of the noise increases with √N. The signal-to-noise ratio (SNR) is therefore increased by √N for each combined FID (or "transient"). An example is given in Figure 2.4.

To avoid distortion of a spectrum due to incomplete T_1 relaxation after the first FID is acquired, a "recycle interval" is required to ensure that thermal equilibrium is reached before the next transient is obtained. This delay must be at least $5 \times T_1$ of the slowest relaxing component of the spectrum, in order to obtain the full signal after the second excitation. Even for samples with very short T_1 values, the recycle interval must be longer than a minimum value in order to avoid damaging the probe.

2.2 Interactions in NMR

2.2.1 The Chemical Shielding Interaction

In any given material, electrons can be found around a nucleus, generating a magnetic field, $\mathbf{B}'$. In an isolated nucleus this aligns opposite to $\mathbf{B}_0$ and reduces the effective

magnetic field at the nucleus

$$\mathbf{B} = \mathbf{B}_0 - \mathbf{B}' = \mathbf{B}_0 (1 - \sigma) \ , \tag{2.23}$$

where σ is the field-independent shielding constant. Therefore,

$$\nu_{obs} = -\gamma \mathbf{B_0} (1 - \sigma) / 2\pi \ . \tag{2.24}$$

Although σ is always positive for isolated atoms, it can be either positive or negative for a molecule, due to the presence of regions of magnetic shielding and deshielding caused by currents arising from delocalised electrons. Obtaining an absolute σ value experimentally is difficult and so the chemical shift, δ, is normally determined relative to a standard reference frequency. The magnitude of $\mathbf{B}'$ is very small compared to $\mathbf{B}_0$ so δ is usually given in ppm

$$\delta = 10^6 (\nu - \nu_{ref}) / \nu_{ref} \approx 10^6 (\sigma_{ref} - \sigma) \ , \tag{2.25}$$

where ν_{ref} is the reference frequency for the particular nucleus under study, and is determined using either a primary (δ = 0) or secondary (δ relative to primary) reference material. As δ is related to $\nu - \nu_{ref}$ it has the opposite sign to σ and so is a deshielding parameter; increased δ means a more deshielded nucleus (higher resonance frequency).[9]

For a non-spherically symmetric electron distribution (*i.e.*, as is found in most systems), the shielding is described by a tensor, **σ**, and as such, a set of axes can be defined in such a way that the shielding tensor is diagonalised within this frame

$$\boldsymbol{\sigma}^{\mathbf{PAS}} = \begin{pmatrix} \sigma_{11} & 0 & 0 \\ 0 & \sigma_{22} & 0 \\ 0 & 0 & \sigma_{33} \end{pmatrix} \ , \tag{2.26}$$

where this is known as the principal axis system (PAS), and σ_{11}, σ_{22} and σ_{33} are the principal components of the tensor. σ_{11} corresponds to the direction of least shielding, with the highest frequency, while σ_{33} corresponds to the direction of highest shielding, with the lowest frequency. The corresponding principal values of the chemical shift tensor are δ_{11}, δ_{22} and δ_{33}. According to the Haeberlen convention,[10] the chemical shift can be described by the isotropic component, δ_{iso}, anisotropy, $\Delta\delta_{cs}$, and the asymmetry

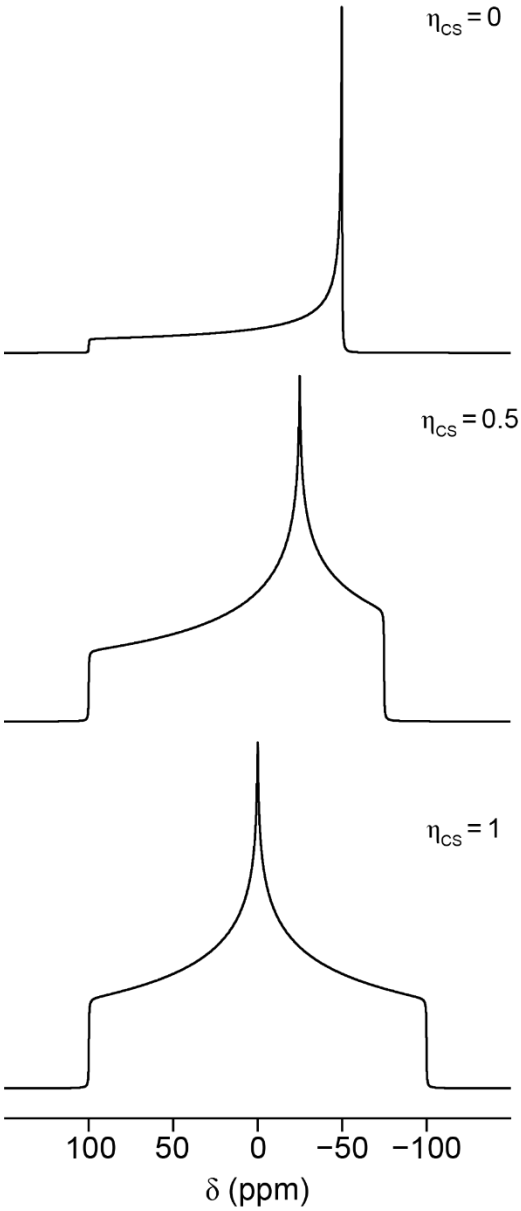

Figure 2.5. *Simulated powder pattern lineshapes (9.4 T, static) for a spin I = 1/2 nucleus with $\Delta\delta_{cs}$ = 100 ppm and η_{cs} of 0, 0.5 and 1, respectively.*

parameter, η_{cs}

$$\delta_{iso} = 1/3\ (\delta_{11} + \delta_{22} + \delta_{33})\ , \qquad (2.27)$$

$$\Delta\delta_{cs} = \delta_{33} - \delta_{iso}\ , \qquad (2.28)$$

and

$$\eta_{cs} = (\delta_{22} - \delta_{11}) / \Delta\delta_{cs} \ . \qquad (2.29)$$

Alternatively, in the Herzfeld-Berger convention,[11] the chemical shift tensor can be described in terms of its span and skew

$$\Omega = \delta_{11} - \delta_{33} \ , \qquad (2.30)$$

and

$$\kappa = 3(\delta_{22} - \delta_{iso}) / \Omega \ , \qquad (2.31)$$

respectively.

To convert from the PAS to the laboratory frame, rotation around the polar angles, θ and ϕ (or Euler angles α, β and γ) is required, which leads to δ being orientation dependent in this frame. It has an isotropic (δ_{iso}) and an orientation-dependent anisotropic component

$$\delta = \delta_{iso} + (\Delta \delta_{cs} / 2) [(3\cos^2 \theta - 1) + \eta_{cs} (\sin^2 \theta \cos 2\phi)] \ . \qquad (2.32)$$

In liquid samples the orientation of the molecules changes rapidly, such that the anisotropic component is averaged to zero and only the isotropic shift is observed. In solid samples though, there are no such effects. For a single crystal, the spectrum will contain a peak shifted from its isotropic position but, for a powdered sample containing crystallites with a variety of random orientations, a range of shifts leads to a powder-pattern lineshape, illustrated in Figure 2.5.

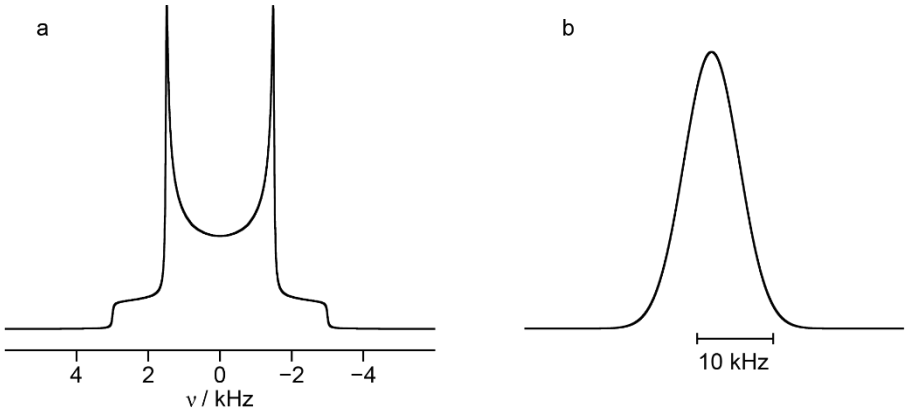

Figure 2.6. *(a) A simulated Pake doublet for an isolated heteronuclear pair of spin I = 1/2 nuclei with* ω_D^{PAS} *= 3 kHz. (b) A simulated Gaussian-type lineshape for a spin I = 1/2 nucleus, resulting from dipolar coupling between many nuclei.*

2.2.2 Dipolar Coupling

As nuclei possess magnetic dipoles, a nuclear spin generates a magnetic field that interacts with any other nuclei that are close in space. In the case of a simple two-spin system, the first nucleus, I, is separated from the second, S, by a distance, r_{IS}. The internuclear vector, $\mathbf{r}_{IS}$, is oriented at an angle θ_{IS} to B_0. The magnitude of the dipolar coupling is

$$\omega_D = \omega_D^{PAS}\, 1/2\, (3\cos^2\theta_{IS} - 1) \ , \qquad (2.33)$$

with

$$\omega_D^{PAS} = -(\mu_0 / 4\pi)\, \gamma_I \gamma_S \hbar / r^3_{IS} \ , \qquad (2.34)$$

where γ_I and γ_S are the gyromagnetic ratios of I and S, respectively.[4] The dipolar interaction tensor is, by definition, axially symmetric with $\eta_D = 0$. In static powder samples dipolar coupling between an isolated spin pair leads to the formation of a powder pattern lineshape known as a Pake doublet, as shown in Figure 2.6(a). This is $2\omega_D^{PAS}$ wide for heteronuclear dipolar coupling ($I \neq S$) and $3\omega_D^{PAS}$ for homonuclear ($I = S$) dipolar coupling. In practice however, dipolar coupling occurs simultaneously between many nuclei rather than isolated spin pairs, which results in a Gaussian-type lineshape, as shown in Figure 2.6(b).

2.2.3 Scalar Coupling

The scalar, or J coupling,[4] arises from magnetic interaction between nuclei, mediated by the electrons that are involved in chemical bonding. The J coupling Hamiltonian is

$$H_J = 2\pi \cdot \mathbf{I} \cdot \mathbf{J} \cdot \mathbf{S} , \tag{2.35}$$

where **J** is an anisotropic tensor describing the interaction. When the *z*-axis is defined as the direction of $\mathbf{B}_0$, the J coupling Hamiltonian becomes

$$H_J = 2\pi J I_z S_z , \tag{2.36}$$

where J is the isotropic J coupling, which is equal to the average of the diagonal elements of the J coupling tensor. The magnitude of the isotropic J coupling between two spins, I and S, is given by the scalar coupling constant, J_{IS}. In solid-state NMR, the magnitude of scalar coupling is usually small in comparison to the other interactions, and so it is not usually resolved. It can, however, be utilised in certain "through-bond" correlation experiments, examples of which are detailed in Chapter 3. The experimental determination of J couplings in the solid-state has become a topic of interest recently.[12,13]

2.2.4 The Quadrupolar Interaction

Nuclei with I > ½, while also being affected by the dipolar and shielding interactions, have a non-spherical charge distribution that results in a nuclear quadrupole moment, **Q**, that interacts with the electric field gradient (EFG) generated at the nucleus.[9] The EFG can be described by the tensor, **V**, which is diagonalised in the PAS as

$$\mathbf{V}^{PAS} = \begin{pmatrix} V_{xx} & 0 & 0 \\ 0 & V_{yy} & 0 \\ 0 & 0 & V_{zz} \end{pmatrix} , \tag{2.37}$$

where $|V_{zz}| \geq |V_{yy}| \geq |V_{xx}|$, and the cross-section of the tensor that is perpendicular to V_{zz} can be described by the asymmetry parameter, η_Q, where

$$\eta_Q = (V_{xx} - V_{yy}) / V_{zz} . \tag{2.38}$$

The asymmetry parameter is normalised by V_{zz} such that $0 \leq \eta_Q \leq 1$; a value of 0 indicates axial symmetry around the *z*-axis, whereas a value of 1 indicates axial symmetry around the *x*-axis. The quadrupolar coupling constant, C_Q, is given in units of Hz and is dependent on the nuclear quadrupole moment and the magnitude of **V**, V_{zz}

$$C_Q = eQV_{zz} / h \ . \tag{2.39}$$

C_Q and η_Q can be combined to give the quadrupolar product as follows

$$P_Q = C_Q (1 + \eta_Q^2 / 3)^{1/2} \ . \tag{2.40}$$

The quadrupolar interaction results in a perturbation of the Zeeman energy levels, and the magnitude of this depends on the quadrupolar splitting parameter, ω_Q, which is usually quoted in units of rad s^{-1}

$$\omega_Q = (\omega_Q^{PAS} / 2) (3\cos^2 \theta - 1 + \sin^2 \theta \cos 2\phi) \ , \tag{2.41}$$

$$\omega_Q^{PAS} = 3\pi C_Q / 2I (2I - 1) \ , \tag{2.42}$$

where θ and ϕ define the orientation of the PAS relative to the laboratory frame. Observable single-quantum (SQ) transitions have first- ($E^{(1)}_{|m_I\rangle}$) and second-order ($E^{(2)}_{|m_I\rangle}$) quadrupolar contributions to the energy levels, given by

$$E_{|m_I\rangle} - E_{|-m_I\rangle} = E^{(1)}_{|m_I\rangle} - E^{(1)}_{|-m_I\rangle} + E^{(2)}_{|m_I\rangle} - E^{(2)}_{|-m_I\rangle} \ , \tag{2.43}$$

For simple axial symmetry, that is, $\eta_Q = 0$, first- and second-order quadrupolar contributions will be

$$E^{(1)}_{|m_I\rangle} - E^{(1)}_{|-m_I\rangle} = \pm (2m_I - 1) \omega_Q^{PAS} d^2_{0,0} (\theta) \ , \tag{2.44}$$

and

$$E^{(2)}_{|m_I\rangle} - E^{(2)}_{|-m_I\rangle} = (\omega_Q^{PAS})^2 / \omega_0 [A^0(I,m_I) + A^2(I,m_I)\, d^2_{0,0} (\theta) + A^4(I,m_I)\, d^4_{0,0} (\theta)] \ , \tag{2.45}$$

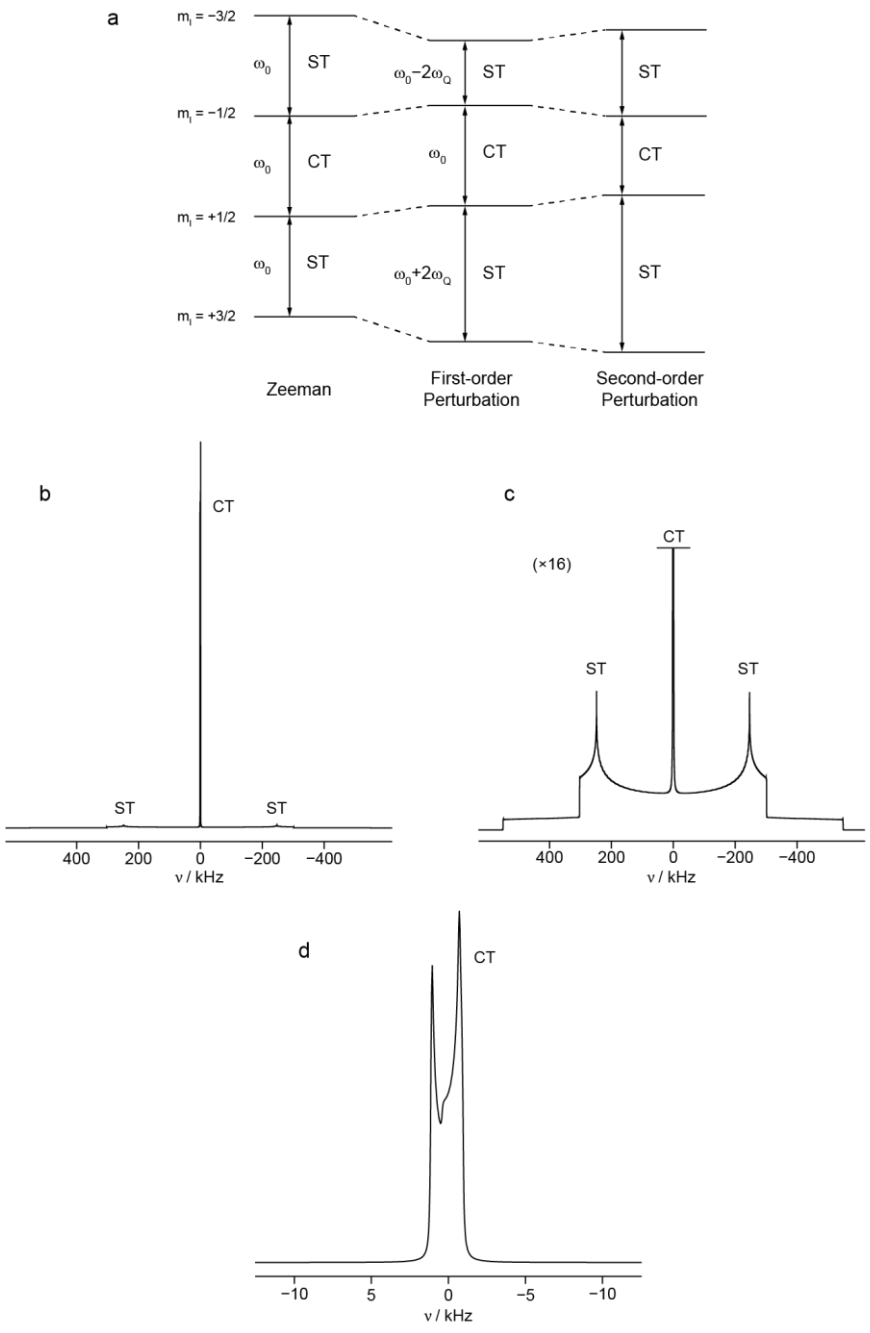

Figure 2.7. *(a) Schematic energy level diagram for a nucleus with spin I = 3/2. (b) Simulated static quadrupolar lineshape for a spin I = 3/2 nucleus in an axially-symmetric environment and affected by only the first-order quadrupolar interaction. (c) A (×16) expansion of (b), revealing the broad satellite-transition (ST) lineshape. (d) The central transition (CT) of a spin I = 3/2 nucleus in an axially-symmetric environment and experiencing second-order quadrupolar broadening. Simulation parameters include:* $B_0 = 14.1$ *T;* $\nu_0 = 150.3$ *MHz;* $C_Q = 1.1$ *MHz and* $\eta_Q = 0.1$.

where $A^0(I,m_I)$, $A^2(I,m_I)$ and $A^4(I,m_I)$ are spin- and transition-dependent coefficients for the isotropic chemical shift, second-rank anisotropic broadening and fourth-rank anisotropic broadening, respectively. Values for these coefficients are given in Appendix C. The terms $d^2_{0,0}(\theta)$ and $d^4_{0,0}(\theta)$ are Wigner reduced rotation matrix elements and are given by

$$d^2_{0,0}(\theta) = 1/2\,(3\cos^2\theta - 1) \tag{2.46}$$

and

$$d^4_{0,0}(\theta) = 1/8\,(35\cos^4\theta - 30\cos^2\theta + 3)\,. \tag{2.47}$$

For nuclei with half-integer spin quantum number, the first-order perturbation only affects the satellite transitions; when Q or V_{zz} is larger, a second-order perturbation must be considered, and this affects all transitions.[9] This is illustrated in Figure 2.7. Nuclei with integer spin quantum number have no central transition, meaning that all single-quantum transitions are affected by the first-order perturbation. For a single crystallite a doublet with peak spacing of $2\omega_Q$ is observed, giving rise to a Pake doublet in a powdered sample. The $+I \leftrightarrow -I$ transitions however remain unaffected by the first-order interaction.[9]

2.2.5 Paramagnetic Interactions

Electrons, having spin S = 1/2, are able to interact with atomic nuclei. Where the electrons are paired, as in the case of diamagnetic solids, only the indirect effects of electron-nuclear interactions are observed. In paramagnetic materials, however, unpaired electrons are present and interact with the parent nucleus, bonded nuclei nearby and other non-bonded nuclei within a radius of ~100 Å. The γ of an electron is ~660 times higher than that of ^{1}H, and so the magnitude of the interaction between a nucleus and an unpaired electron is usually very large. This interaction has four main contributions: a through-space (dipolar) interaction causing an isotropic shift and anisotropic broadening of the NMR lineshape; a through-bond orbital polarisation resulting in an additional isotropic shift; a bulk susceptibility leading to further anisotropic broadening; and relaxation enhancement that leads to very fast T_1 and T_2 relaxation in many cases. The isotropic and anisotropic shift contributions are referred

to as the paramagnetic shift and paramagnetic shift anisotropy (PSA), respectively.[14] Commonly, T_1 and T_2 relaxation time constants for electrons are significantly faster than their nuclear counterparts, and so on the NMR timescale, the nuclear magnetic moment, $\boldsymbol{\mu}_N$, interacts with the thermally-averaged electronic magnetic moment, $\bar{\boldsymbol{\mu}}_e$

$$\bar{\boldsymbol{\mu}}_e = \frac{\mu_B^2 S(S+1)}{3k_B T}\mathbf{g}\cdot\mathbf{g}\cdot\mathbf{B}_0 \,, \tag{2.48}$$

where μ_B is the Bohr magneton, k_B is the Boltzmann constant and **g** is the electron g tensor. The interaction Hamiltonian is

$$H = \bar{\boldsymbol{\mu}}_e\cdot\mathbf{D}_{eN}\cdot\boldsymbol{\mu}_N \,. \tag{2.49}$$

The dipolar interaction tensor, $\mathbf{D}_{eN}$, has components

$$D_{ij} = \frac{1}{r^3}\left(\delta_{ij} - 3e_i e_j\right) \,, \tag{2.50}$$

where the electron and the nucleus are separated by distance, r, δ_{ij} is the Kronecker delta function ($\delta_{ij} = 1$ if $i = j$ and 0 if $i \neq j$) and e_i and e_j (i, j = x, y or z) indicate the x, y and z components of the vector between the electron and the nucleus. When **g** is isotropic, $\bar{\boldsymbol{\mu}}_e$will be aligned with $\mathbf{B}_0$ and $\mathbf{g}\cdot\mathbf{g}\cdot\mathbf{D}_{eN}$ will be traceless and axially symmetric. The nucleus experiences a thermally-averaged electron spin, and so this interaction will result in a powder-pattern lineshape rather than a Pake doublet. Generally, though, **g** is not isotropic and $\mathbf{g}\cdot\mathbf{g}\cdot\mathbf{D}_{eN}$ is not traceless, resulting in a dipolar-induced isotropic shift referred to as the pseudocontact shift, in addition to anisotropic broadening.[14]

In addition to interacting with the nucleus, the unpaired electron spin density can induce spin polarisation of the nuclear orbitals. This is referred to as the Fermi contact or hyperfine interaction, and has the Hamiltonian

$$H = \frac{\mu_0}{4\pi}\frac{8\pi}{3}\gamma_e\gamma_N \mathbf{I}\cdot\mathbf{S}\,\delta(r) \,, \tag{2.51}$$

where γ_e and γ_N are the gyromagnetic ratios of the electron and nucleus, respectively, I and S are their respective spins, and $\delta(r)$ is the Dirac delta function ($\delta(r) = 1$ if $r = 0$

and 0 elsewhere). The wavefunctions of the s orbitals of the nucleus have finite value at r = 0, and so polarisation of these orbitals induces a contact shift of frequency

$$\nu_c = \frac{A\gamma_N B_0}{\hbar}\langle S_z\rangle , \tag{2.52}$$

where A/ħ is the hyperfine coupling constant in Hz and $\langle S_z\rangle$ is the expectation value of the z component of the electronic magnetic moment. This is thermally averaged by the fast electronic relaxation and has a value of

$$\langle S_z\rangle = \frac{\mu_B J(J+1) g_J (g_J - 1) B_0}{3k_B T} , \tag{2.53}$$

where the Landé g factor, g_J is

$$g_J = \frac{3J(J+1) - L(L+1) + S(S+1)}{2J(J+1)} . \tag{2.54}$$

J is the total angular momentum quantum number for the electron state, L is the orbital angular momentum and S is the spin angular momentum. The contact shift is usually very large (thousands of ppm) for the nucleus of the directly affected atom, and smaller contact shifts (tens to thousands of ppm) may be observed for the nuclei of nearby atoms that are bonded to the directly affected atom. The transfer of spin polarisation between atoms is similar mechanistically to the scalar coupling, and the magnitude of ν_c decreases rapidly as the number of bonds between the nucleus and the unpaired electron increases. In addition to the shifts and anisotropic broadening arising from the contact and pseudocontact interactions, both of these interactions can contribute to transverse and longitudinal relaxation, leading to values on the order of a few ms for T_1 and on the μs - ms timescale for T_2.[14]

In addition to the interactions described above, the bulk magnetic susceptibility (BMS) may also be relevant.[15] However, predicting the effects of the BMS on an experimental spectrum is highly complex and so this term is usually not considered when analyzing NMR spectra of paramagnetic materials.

The presence of paramagnetic species within a sample can result in large isotropic shifts, anisotropic broadening and very rapid relaxation, making NMR studies of

paramagnetic materials challenging. However, as outlined in Chapter 5, significant insight into these type of materials can still be obtained *via* solid-state NMR.

2.3 Dynamic Nuclear Polarisation

NMR spectroscopy, whilst extremely valuable, is also an inherently insensitive technique. As a result, in recent years there has been a drive towards the development of sensitivity enhancement methods in order to counteract this limitation.[16-18] Principal amongst these is the rapidly emerging method referred to as dynamic nuclear polarisation (DNP). DNP enhances the NMR signal by the transfer of polarisation from electrons (as mentioned above, γ for an electron is ~660 times higher than that of ^{1}H) to nearby nuclei *via* microwave (mw) irradiation of electronic-nuclear transitions.[19] It has found extensive applicability in the fields of biological[20] and materials NMR spectroscopy,[18] including in Chapter 6 of this work. What follows is a brief overview of the theory of DNP. Information on the practical aspects of DNP NMR experiments is outlined in Chapter 3.

2.3.1 DNP Theory

DNP was first proposed theoretically by Overhauser[21] in 1953, and this was swiftly followed that same year by experimental observation of the effect by Carver and Slichter.[22] This first example involved the enhancement of the ^{7}Li signal from powdered lithium and Overhauser DNP, as it became known, was subsequently applied to experiments involving metals such as Rb and Na.[23] Solomon and Bloembergen[24] went on to demonstrate that the effect was also observable between nuclear spins and this Nuclear Overhauser Effect (NOE) continues to be used for distance measurements in solution-state NMR.[7] Whilst Overhauser DNP continues to be developed in the present day,[25] the two primary mechanisms that are utilised in solid-state DNP NMR are the solid effect (SE) and the cross effect (CE).[26]

2.3.2 The Solid Effect

The SE was first documented in 1958[27,28] and is the dominant mechanism for radicals where the electronic anisotropy is smaller than the nuclear Larmor frequency. Polarising agents employed are usually radicals with high molecular symmetry such as 1,3-bisdiphenylene-2-phenylallyl (BDPA) or derivatives of trityl. The SE can be described using a two-spin system featuring one electron and one nucleus.[19,26] Here, electronic-nuclear dipolar coupling can be considered as a perturbation of the Zeeman Hamiltonian, which leads to mixing of the Zeeman states. This allows normally forbidden "flip-flop" transitions to occur, generating enhanced ^{1}H polarisation. This two-spin system has the approximate Hamiltonian

$$H = \omega_{0e}S_z - \omega_{0n}I_z + DS_zI_+ + D^*S_zI_- , \tag{2.55}$$

where I and S are the nuclear and electronic spin operators, respectively, ω_{0n} is the Nuclear Larmor frequency, ω_{0e} is the electronic Larmor frequency, and D is the electronic-nuclear dipolar term

$$D = \frac{-3\gamma_S\gamma_I}{4r_{IS}^3}\sin\theta\cos\theta\, e^{-i\phi} , \tag{2.56}$$

where r_{IS}, θ and ϕ are the polar coordinates of the electronic-nuclear vector. The mixing of eigenstates means that microwave irradiation can facilitate double- and zero-quantum transitions, with intensity proportional to

$$q^2 = \left|\frac{D}{2\omega_{0n}}\right|^2 . \tag{2.57}$$

The zero-quantum transition will generate a negative enhancement, whereas the double-quantum transition will give a positive one. Signal enhancement is usually denoted by ε and is usually given as an integer number, *e.g.*, "ε ^{1}H = 70".[18] The mixing coefficient is proportional to B_0^{-2}, meaning that ε scales in the same way. Therefore, the SE becomes less efficient as the B_0 field strength increases. For this reason, SE radicals are most commonly used for dissolution DNP. An overview of this technique can be found in the work of Jähnig *et al.*[29]

2.3.3 The Cross Effect

In contrast to the SE, the CE involves allowed transitions (*i.e.*, 2S + 1I) where the electronic anisotropy is on the order of, or larger than, the nuclear Larmor frequency.[19,26] It can be described by a three-spin system featuring two electrons and one nucleus, which has the Hamiltonian

$$H = H_Z + H_{E\text{-}N} + H_{E\text{-}E} , \tag{2.58}$$

where

$$H_Z = \omega_{0e1} S_{1z} - \omega_{0e2} S_{2z} - \omega_{0n} I_z , \tag{2.59}$$

$$H_{E\text{-}N} = (A_1 S_{1z} + A_2 S_{2z}) I_z + (B_1 S_{1z} + B_2 S_{2z}) I_x , \tag{2.60}$$

and

$$H_{E\text{-}E} = d(3 S_{1z} S_{2z} - \mathbf{S}_1 \cdot \mathbf{S}_2) + 2J \mathbf{S}_1 \cdot \mathbf{S}_2 , \tag{2.61}$$

where the first term describes the electronic dipolar coupling, d, and the second term the exchange coupling, J.[30] If $|\omega_{0e1} - \omega_{0e2}| = \omega_{0n}$, known as the matching condition, then the central energy levels will be degenerate and electronic-nuclear polarisation transfer can be achieved by saturating one of the electronic transitions. Nitroxide radicals such as TEMPO[31,32] and biradicals such as TOTAPOL[33] and TEKPol[34] are efficient CE polarising agents. The anisotropy scales inversely with respect to B_0, and ε is therefore proportional to B_0^{-1}. The CE is the dominant mechanism for polarisation transfer at higher field (B_0 = 9.4 T and higher) solid-state DNP NMR. The practicalities associated with preparing for, and performing, these types of experiments, are outlined in Chapter 3.

2.4 References

1. E. Hulthén, "Presentation Speech of the Nobel Prize in Physics 1952" in *Nobel Lectures, Physics 1942-1962*, Elsevier, Amsterdam, 1964.
2. E. M. Purcell, H. C. Torrey and R. V. Pound, *Phys. Rev.*, 1946, **69**, 37.
3. F. Bloch, W. W. Hansen and M. Packard, *Phys. Rev.*, 1946, **70**, 474.

4. P. J. Hore, *Nuclear Magnetic Resonance*, Oxford University Press, Oxford, 1995.
5. C. P. Slichter, *Principles of Magnetic Resonance*, Springer-Verlag, Berlin, 1990.
6. M. Bak, J. T. Rasmussen and N. Ch. Nielsen, *J. Magn. Reson.*, 2000, **147**, 269.
7. J. Keeler, *Understanding NMR Spectroscopy*, Wiley, Chichester, 2nd Edn., 2010.
8. D. J. States, R. A. Haberkorn and D. J. Ruben, *J. Magn. Reson.*, 1982, **48**, 286.
9. D. C. Apperley, R. K. Harris and P. Hodgkinson, *Solid-State NMR: Basic Principles & Practice*, Momentum Press, New York, 2012.
10. U. Haeberlen, in *Advances in Magnetic Resonance*, Ed. J. S. Waugh, Academic Press, New York, 1976.
11. J. Herzfeld and A. E. Berger, *J. Chem. Phys.*, 1980, **73**, 6021.
12. P. Florian, F. Fayon and D. Massiot, *J. Phys. Chem. C*, 2009, **113**, 2562.
13. D. Massiot, F. Fayon, M. Deschamps, S. Cadars, P. Florian, V. Montouillout, N. Pellerin, J. Hiet, A. Rakhmatullin and C. Bessada, *C. R. Chimie*, 2010, **13**, 117.
14. V. I. Bakhmutov, *Solid-State NMR in Materials Science Principles and Applications*, CRC Press, Boca Raton, 2012.
15. A. Kubo, T. P. Spaniol and T. Terao, *J. Magn. Reson.*, 1998, **133**, 330.
16. T. Theis, M. Truong, A. M. Coffey, E. Y. Chekmenevc and W. S. Warren, *J. Magn. Reson.*, 2014, **248**, 23.
17. J. H. Lee, Y. Okuno and S. Cavagnero, *J. Magn. Reson.*, 2014, **241**, 18.
18. A. J. Rossini, A. Zagdoun, M. Lelli, A. Lesage, C. Copéret and L. Emsley, *Acc. Chem. Res.*, 2013, **46**, 1942.
19. Q. Z. Ni, E. Daviso, T. V. Can, E. Markhasin, S. K. Jawla, T. M. Swager, R. J. Temkin, J. Herzfeld and R. G. Griffin, *Acc. Chem. Res.*, 2013, **46**, 1933.
20. A. B. Barnes, G. De Paëpe, P. C. A. van der Wel, K-N. Hu, C.-G. Joo, V. S. Bajaj, M. L. Mak-Jurkauskas, J. R. Sirigiri, J. Herzfeld, R. J. Temkin and R. G. Griffin, *Appl. Magn. Reson*., 2008, **34**, 237.
21. A. Overhauser, *Phys. Rev*., 1953, **92**, 411.
22. T. R. Carver and C. P. Slichter, *Phys. Rev*., 1953, **92**, 212.

23. T. R. Carver, *Phys. Rev.*, 1956, **102**, 975.
24. I. Solomon and N. Bloembergen, *J. Chem. Phys.*,1956, **25**, 261.
25. E. Ravera, C. Luchinat and G. Parigi, *J. Magn. Reson.*, 2016, **264**, 78.
26. A. Zagdoun, *PhD Thesis*, École Normale Supérieure de Lyon, 2014.
27. A. Abragam, *C. R. Hebd. Seances Acad. Sci*., 1958, **246**, 2253.
28. E. Erb, J. L. Motchane and J. Uebersfeld, *C. R. Hebd. Seances Acad. Sci.*, 1958, **246**, 2253.
29. F. Jähnig, G. Kwiatkowski and M. Ernst, *J. Magn. Reson.,* 2016, **264**, 22.
30. T. V. Can, Q. Z. Ni and R. G. Griffin, *J. Magn. Reson.*, 2015, **253**, 23.
31. V. S. Bajaj, C. T. Farrar, M. K. Hornstein, I. Mastovsky, J. Vieregg, J. Bryant, B. Eléna, K. E. Kreischer, R. J. Temkin and R. G. Griffin, *J. Magn. Reson.*, 2003, **160**, 85.
32. M. Rosay, J. C. Lansing, K. C. Haddad, W. W. Bachovchin, J. Herzfeld, R. J. Temkin and R. G. Griffin, *J. Am. Chem. Soc.*, 2003, **125**, 13626.
33. C. Song, K-N. Hu, T. M. Swager and R. G. Griffin, *J. Am. Chem. Soc.*, 2006, **128**, 11385.
34. A. Zagdoun, G. Casano, O. Ouari, M. Schwarzwälder, A. J. Rossini, F. Aussenac, M. Yulikov, G. Jeschke, C. Copéret, A. Lesage, P. Tordo and L. Emsley, *J. Am. Chem. Soc.*, 2013, **135**, 12790.

Chapter 3. Experimental Methods

In this chapter, the techniques and experiments used in NMR spectroscopy for the study of solid samples are outlined. Additionally, information on the practical considerations for performing solid-state DNP NMR experiments is also provided.

3.1 Essential Methods

3.1.1 Magic Angle Spinning

In the solution state, rapid molecular motion results in the complete averaging of anisotropic interactions to their isotropic value, resulting in sharp NMR spectral resonances.[1] In solid samples however, where motion does not exist on this timescale, the static NMR spectrum contains a broad lineshape that often conceals important chemical information.[2] To overcome this problem, Andrew *et al.*[3] and Lowe[4] independently developed a technique now referred to as magic angle spinning (MAS), where macroscopic rotation of a solid can be used to mimic the molecular "tumbling" that occurs in liquids. To perform MAS, the sample under study is packed into a rotor that is sealed with a cap with lid bearing "fins", allowing it to be rotated by a flow of "drive" gas, around an axis at an angle of 54.736° relative to B_0. The spinning speed that can be achieved is limited by the speed of sound in the rotation medium, mass of the rotor and mass of the sample. The original sample spinner developed by Andrew *et al.* was limited to speeds of several hundred Hz, whereas contemporary studies have described the use of spinning speeds of up to 110 kHz,[5] using commercially available hardware.

MAS is effective because many of the interactions that affect spectral resolution have a similar orientation dependence. The magnitudes of the CSA and dipolar coupling are both proportional to $3\cos^2\theta-1$. Therefore, if the sample is rotated around an axis inclined at an angle θ_R relative to B_0, then θ, the angle describing the orientation of the spin interaction tensor, will vary with time as rotation occurs. If θ_R is set to be 54.736° (the "magic" angle) then the average orientation, assuming rapid rotation, will be 54.736°.

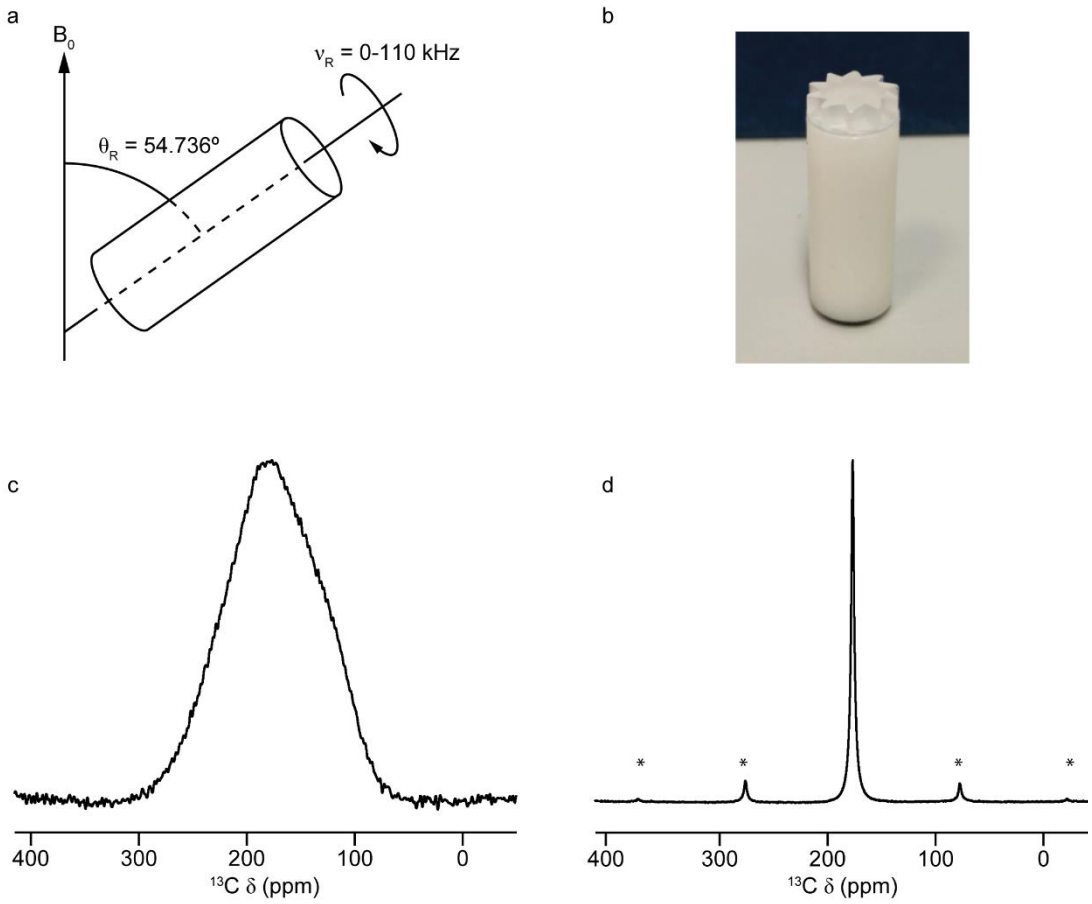

Figure 3.1. *(a) Schematic representation of the experimental setup for MAS. (b) Photograph of a 7 mm rotor used for spinning solid samples at a maximum MAS rate of 7 kHz. (c)* ^{13}C *(9.4 T) NMR spectrum of a static sample of 1[*^{13}C*]-glycine. (d)* ^{13}C *(9.4 T, 10 kHz MAS) NMR spectrum of 1[*^{13}C*]-glycine. * denotes a spinning sideband.*

If the MAS rate, ν_R, is sufficiently rapid, the anisotropic interactions are averaged to zero and only the isotropic terms remain.[6] A schematic representation of MAS is shown in Figure 3.1(a), along with a photograph of a rotor used for sample spinning in Figure 3.1(b). Table 3.1 lists the maximum sample volumes and MAS rates that are possible for different rotor sizes. If the MAS rate is insufficient (*i.e.* in comparison to the magnitude of the interaction that is to be averaged), then spinning sidebands will be present in the NMR spectrum. These are additional resonances that are separated by multiples of the spinning frequency from the isotropic resonance. This is shown in Figure 3.1(c) and (d), where the resolution of the ^{13}C NMR spectrum of 1[^{13}C]-glycine is greatly enhanced with MAS, but spinning at a rate of 10 kHz does not completely

Table 3.1. *The maximum sample volumes and MAS rates, ν_R, that are possible for different rotor sizes (measured by outer diameter).*

Outer Diameter / mm	Approximate Sample Volume / μl	Maximum ν_R / kHz
7	300-500	7
4	50-90	14
3.2	20-40	24
2.5	14	35
1.9	10	42
1.3	1.5	67
1	0.8	80
0.75	0.4	110

average the anisotropic interactions, as evidenced by the presence of spinning sidebands. In the case of a resonance broadened principally by CSA, at slow MAS rates the sideband manifold resembles the powder pattern lineshape observed for a static solid. By increasing the spinning speed, the isotropic resonance becomes more readily identifiable. This is illustrated in Figure 3.2, where the ^{119}Sn NMR spectrum of SnO_2 is shown under both static and variable MAS conditions. So far, the effect of MAS on NMR spectra of spin I = 1/2 nuclei has been considered, but the technique can also be used when performing experiments with quadrupolar nuclei. However, in some cases, MAS is only able to partially average the quadrupolar interaction. As outlined in Chapter 2, when C_Q is large, the CT is affected by a second-order quadrupolar interaction, which cannot be averaged by MAS alone. Under MAS, the second-order perturbation to a transition $E^{(2)}_{|m_I\rangle} - E^{(2)}_{|-m_I\rangle}$ (where E denotes energy), with $\eta_Q = 0$, is given by

$$E^{(2)}_{|m_I\rangle} - E^{(2)}_{|-m_I\rangle} = (\omega_Q{}^{PAS})^2 / \omega_0 [A^0(I,m_I) + A^2(I, m_I)\, d^2_{0,0}(\theta)\, d^2_{0,0}(\theta_R) + A^4(I, m_I)\, d^4_{0,0}(\theta)\, d^4_{0,0}(\theta_R)] \quad (3.1)$$

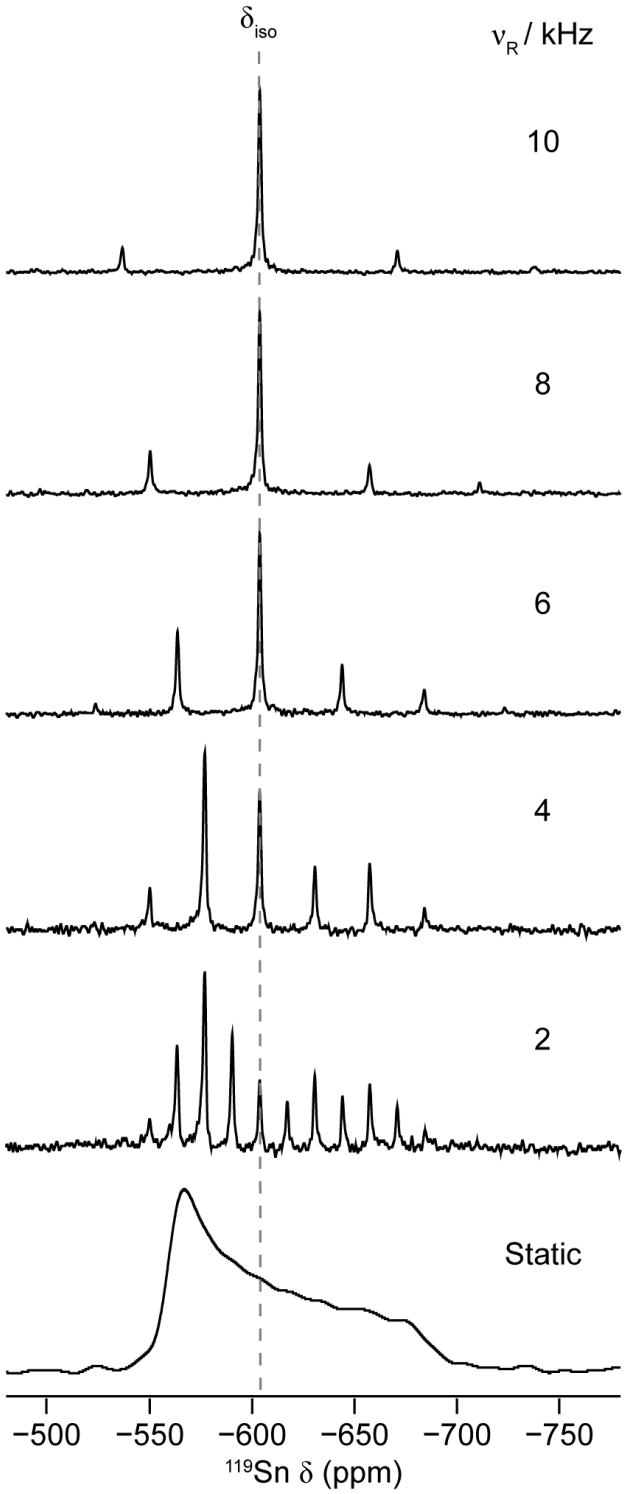

Figure 3.2. *^{119}Sn (9.4 T) NMR spectra of SnO_2 acquired at several different MAS rates. The isotropic resonance is broadened by the CSA interaction. $\delta_{iso} = -604$ ppm, $\Omega = 126$ ppm and $\kappa = 1$ ($\delta_{11} = \delta_{22} = -563$ ppm, $\delta_{33} = -687$ ppm).*

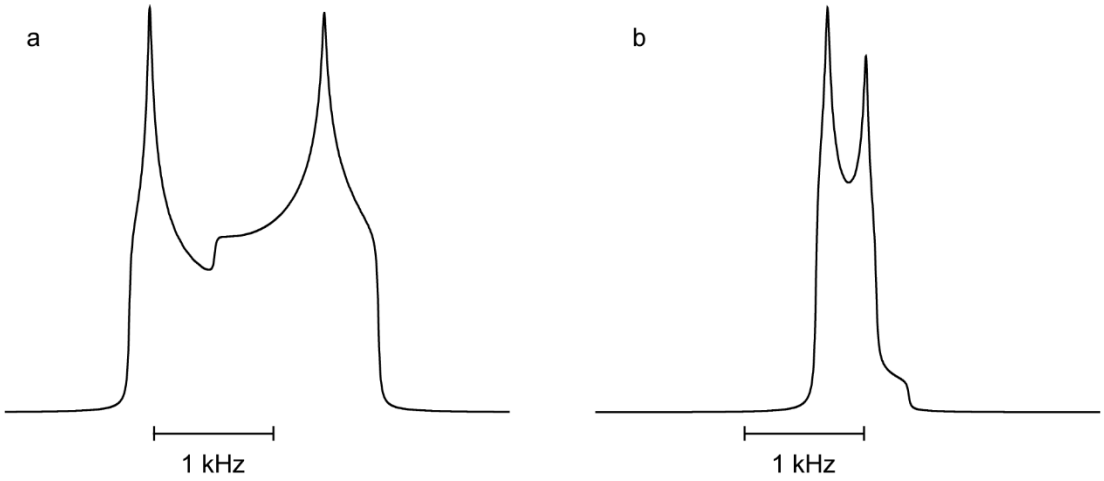

Figure 3.3. *Simulated quadrupolar lineshapes for the CT of a spin I = 3/2 nucleus under (a) static and (b) 14 kHz MAS conditions. Simulation parameters include: B_0 = 9.4 T; ν_0 = 105.8 MHz; C_Q = 1.2 MHz and η_Q = 0.2.*

where

$$d^2_{0,0}(\theta_d) = 1/2\,(3\cos^2\theta_d - 1) \tag{3.2}$$

and

$$d^4_{0,0}(\theta_d) = 1/8\,(35\cos^4\theta_d - 30\cos^2\theta_d + 3)$$

$$\theta_d = \theta, \theta_R. \tag{3.3}$$

$A^0(I, m_I)$, $A^2(I, m_I)$ and $A^4(I, m_I)$ are spin- and transition-dependent coefficients for the isotropic chemical shift, second-rank anisotropic broadening and fourth-rank anisotropic broadening, respectively. Values for these coefficients are given in Appendix C. The terms $d^2_{0,0}(\theta)$, $d^4_{0,0}(\theta)$, $d^2_{0,0}(\theta_R)$ and $d^4_{0,0}(\theta_R)$ are Wigner reduced rotation matrix elements.[7] Under MAS, the angle, θ_R = 54.736°, as the orientation dependence of $d^2_{0,0}(\theta)$ is the same as that for the CSA and the dipolar coupling, the second-rank anisotropic quadrupolar broadening is averaged to zero. The fourth-rank anisotropic broadening, however, is only equal to zero at values of θ_R = 30.56 or 70.12° meaning that it cannot be removed by MAS.[6] This is demonstrated in Figure 3.3, which shows simulated CT static and MAS spectra for a spin I = 3/2 nucleus. For I = 3/2, with η_Q = 0, under MAS the quadrupolar contribution to the CT frequency is given by

$$E^{(2)}_{|1/2\rangle} - E^{(2)}_{|-1/2\rangle} = (\omega_Q^{PAS})^2 / \omega_0 [-2/5 - 8/7\, d^2_{0,0}(\theta)\, d^2_{0,0}(\theta_R) + 54/35\, d^4_{0,0}(\theta)\, d^4_{0,0}(\theta_R)] \quad , \qquad (3.4)$$

where $A^0(3/2, 1/2) = -2/5$, $A^2(3/2, 1/2) = -8/7$ and $A^4(3/2, 1/2) = 54/35$. When $\theta_R = 54.736°$, Equation 3.4 reduces to

$$E^{(2)}_{|1/2\rangle} - E^{(2)}_{|-1/2\rangle} = (\omega_Q^{PAS})^2 / \omega_0 [-2/5 + 54/35\, d^4_{0,0}(\theta)\, d^4_{0,0}(54.736)] \quad . \qquad (3.5)$$

Although anisotropic broadening is still present under MAS, CT lineshapes can still yield useful information about the system under study.[6] Additionally, there are techniques that can be employed to remove the fourth-rank anisotropic broadening. Examples of such methods will be outlined later in this chapter.

3.1.2 Direct Polarisation

The most straightforward NMR experiments involve directly acquiring the FID of the chosen nucleus. These are known as direct polarisation (DP) or direct excitation experiments.[6] The simplest of these is the single pulse experiment, which involves the application of a radiofrequency pulse (with flip angle $\beta = 90°$) to generate maximum polarisation in the transverse plane (as explained in Chapter 2) and subsequent acquisition of the FID. Before signal collection begins, there is a short waiting time, τ_D, known as the "dead time" or "pre-acquisition delay". Its purpose is to ensure that the detected signal does not contain any remnants of the pulse itself (known as "ringing"), that can cause distortion of the final NMR spectrum.[8] However, it may be the case that the effects of ringing cannot be completely supressed, or that important data points are lost from the FID during τ_D. In such situations the spin echo experiment can be employed.[9] Here, a $90°_x$ pulse is applied as before, but then after a short delay, τ, a $180°_x$ pulse is then used. This second pulse inverts the magnetisation around the x axis and is followed by a second τ period. The result is that $\mathbf{M}_0$ becomes aligned again along the y axis. By utilising this approach, spectral distortions and loss of information can be avoided.[8] Pulse sequences for the single pulse and spin echo experiments are shown in Figure 3.4.

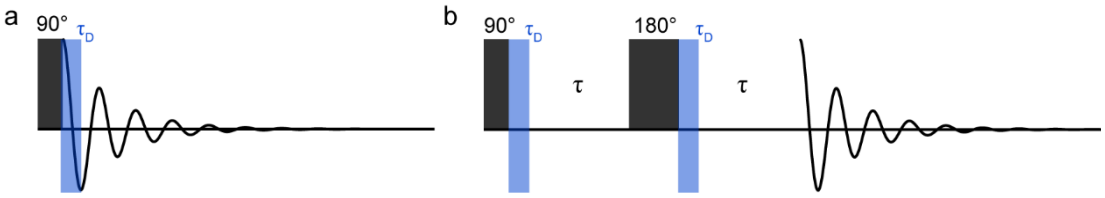

Figure 3.4. *Pulse sequences for the (a) single pulse and (b) spin echo NMR experiments. The dead time, τ_D is highlighted in blue. The interpulse delay, τ, is also shown in (b).*

3.1.3 Cross Polarisation

Another type of experiment that is extensively utilised in solid-state NMR spectroscopy is cross polarisation (CP). This phenomenon was first observed in 1962 by Hartmann and Hahn[10] and was subsequently applied to the study of solid samples by Pines *et al.* ten years later.[11] In the CP experiment, controlled reintroduction of the heteronuclear dipolar interaction (defined in Chapter 2) enables magnetisation transfer from a nucleus, I (for example, ^{1}H or ^{19}F), to a second nucleus, S, typically of low natural abundance (such as ^{13}C or ^{29}Si). For CP to be effective, the Hartman-Hahn match condition[10] must be met

$$-\gamma_I B_{1I} = -\gamma_S B_{1S} \, . \qquad (3.6)$$

When MAS is used it causes the dipolar interaction to become time dependent and so, in a rotating sample, the revised Hartman-Hahn match condition becomes relevant[12,13]

$$-\gamma_I B_{1I} = -\gamma_S B_{1S} \pm n\nu_R \, , \qquad (3.7)$$

where n is an integer number, typically 1 or 2. S nuclei with slow longitudinal relaxation require long recycle intervals between each transient, resulting in long experimental times. Through CP they can receive magnetisation from an I nucleus with faster relaxation. This means that the appropriate recycle interval depends on the I nucleus, resulting in faster spectral acquisition. Combined with the transfer of magnetisation, this can result in a signal enhancement when compared to direct polarisation of the S nucleus,[6] as shown in Figure 3.5(a).

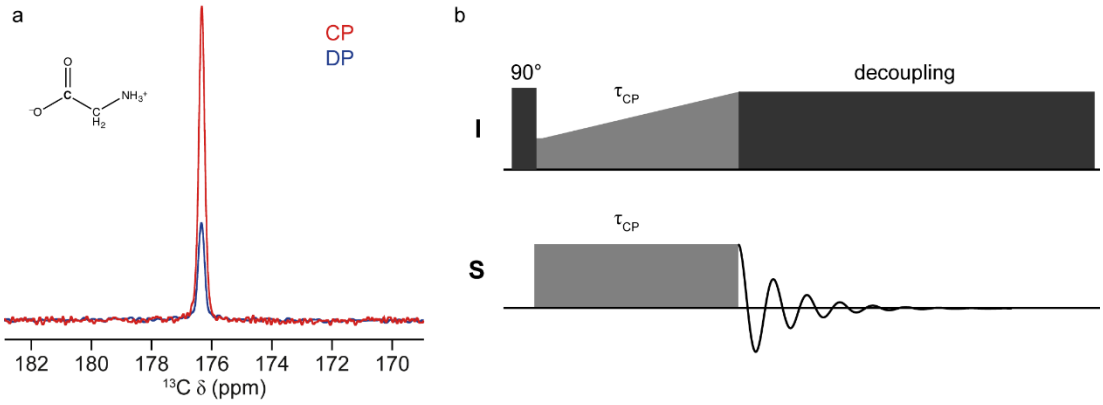

Figure 3.5. *(a) ^{13}C (9.4 T, 14 kHz MAS) DP (blue) and CP (red, τ_{CP} = 0.5 ms) MAS NMR spectra of the C=O resonance of glycine (structure also shown). (b) Schematic depicting the pulse sequence for the CP experiment.*

Here, ^{13}C DP and CP MAS NMR spectra of the C=O resonance of glycine are compared. It can be seen that the application of CP results in increased sensitivity when compared with the equivalent DP spectrum (signal averaging was carried out for 16 transients in both experiments). The theoretical maximum gain in signal intensity over that of a DP experiment is given by

$$M_S^{CP} / M_S^{DP} = \gamma_I / \gamma_S \, 1/1 + \varepsilon \,, \qquad (3.8)$$

where

$$\varepsilon = S(S + 1)N_S / I(I + 1)N_I \,, \qquad (3.9)$$

where N_S and N_I are the number of S and I spins present, respectively. In the case where $\varepsilon \ll 1$ and I = S = 1/2, Equation 3.8 can be approximated as

$$M_S^{CP} / M_S^{DP} = \gamma_I / \gamma_S (1 - N_S / N_I) \,. \qquad (3.10)$$

For a typical ^{1}H-^{13}C system, $N_S / N_I \approx 150$ and $\gamma_I / \gamma_S \approx 4$. This results in a theoretical maximum signal enhancement of a factor of four. In the spectra in Figure 3.5(a), CP has resulted in signal enhancement by a factor of 3.3.

Dipolar interactions occur through space and so the duration of the CP pulses, known

as the contact time, τ_{CP}, can be varied in order to allow for magnetisation transfer to nuclei that are more distant in space, thus providing information on the spatial proximity of I and S nuclei.[6] The pulse sequence for the CP experiment is shown in Figure 3.5(b). It begins with a 90° pulse on the I nucleus. The resulting magnetisation is then transferred during the contact time to the S nucleus. During this time, low-power pulses are applied to both spins to "lock" them along the axis in the rotating frame (preventing them from dephasing) whilst magnetisation transfer occurs. A "ramped" pulse is often applied to one set of spins to satisfy the match condition for more crystallites throughout the spin-locking period (spin I in Figure 3.5(b)).[6] Additionally, heteronuclear decoupling is applied during the acquisition period to improve spectral resolution.[14] Decoupling is discussed in more detail in the next subsection.

So far, CP has been outlined for the case of two spin I (and S) = 1/2 nuclei. However, it is possible to perform the experiment with I = 1/2 and S = >1/2 (quadrupolar) nuclei. Where magnetisation transfer occurs between I = 1/2 and the CT of a quadrupolar nucleus, S, the Hartmann-Hahn match condition has to be modified in order to take into account the effective gyromagnetic ratio[15]

$$\omega_{1I} = (S + 1/2)\omega_{1S} , \qquad (3.11)$$

where $\omega_{1I} = -\gamma_I B_{1I}$ and $\omega_{1S} = -\gamma_S B_{1S}$. Additionally, under MAS, the efficiency of the spin lock of the S magnetisation is dependent on the magnitude of the adiabaticity parameter[15,16]

$$\alpha = \omega_{1S}^2 / \omega_Q^{PAS} \omega_R . \qquad (3.12)$$

If $\alpha \ll 1$ (the "sudden" limit), the signal amplitude (often following a small initial drop in intensity), remains unchanged by MAS as a function of spin lock duration. For the case where $\alpha \gg 1$ (the "adiabatic" limit), a time dependence is introduced in the spin locked state, resulting in oscillatory behaviour of the signal amplitude as function of

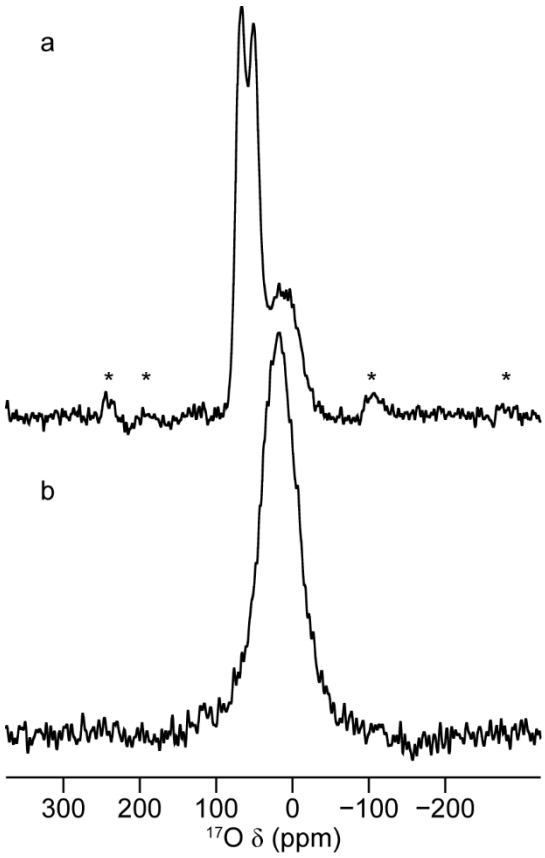

Figure 3.6. *^{17}O (14.1 T, 14 kHz MAS) (a) DP and (b) CP (from ^{1}H, τ_{CP} = 0.4 ms) NMR spectra of ^{17}O-enriched γ-Al_2O_3. * denotes a spinning sideband.*

spin lock duration, and with maximum signal obtained when $\tau = n\tau_R$.[16] In both of these conditions, the spin lock behaviour of the S magnetisation is generally favourable enough to facilitate spectral acquisition using the CP experiment. The intermediate case, $\alpha \approx 1$, results in rapid loss of spin lock efficiency and, as such, is usually unfavourable for successful spectral acquisition.[16] Owing to these factors, CP between spin I = 1/2 and quadrupolar nuclei is generally not effective as a signal enhancement technique.[17] However, it has found application as a tool for "spectral editing". In 1988, Walter *et al.*[18] were amongst the first to successfully utilise CP for this purpose. By means of a ^{1}H-^{17}O CP experiment, they were able to demonstrate that the surface oxygen sites in a variety of ^{17}O-enriched inorganic solids (including amorphous SiO_2 and $Mg(OH)_2$) could be selectively observed. In a later study from the same research group,[19] the ^{1}H-^{17}O CP experiment was applied to the investigation of ^{17}O-enriched aluminium oxides and hydroxides, where it was found that CP was particularly effective for the observation of AlOH species. Figure 3.6 demonstrates the

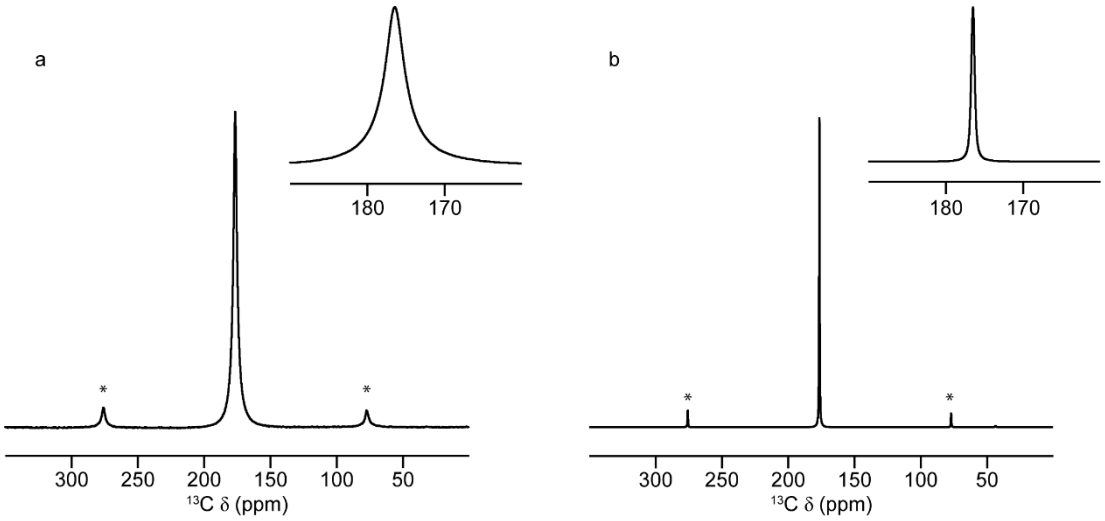

Figure 3.7. *^{13}C (9.4 T, 10 kHz MAS) DP NMR spectra of 1[^{13}C]-glycine (a) without ^{1}H decoupling and (b) with ^{1}H TPPM decoupling. Expansions of the isotropic resonances are also shown inset. * denotes a spinning sideband.*

efficacy of this approach by comparing the ^{17}O DP and ^{1}H-^{17}O CP NMR spectra of ^{17}O-enriched γ-Al_2O_3. It can be seen that the CP NMR spectrum contains only one resonance, corresponding to surface oxygen species. By contrast, resonances for both surface and bulk environments are seen in the conventional NMR spectrum. In 1989, Morris and Ellis[20] showed that ^{1}H-^{27}Al CP experiments could be utilised to probe the structures of α- and γ-Al_2O_3. They demonstrated that CP could reveal Al(IV) and Al(VI) Brønsted acid sites that were close to the surface of the oxides. CP-based experiments involving quadrupolar nuclei have been extensively used to investigate the surface chemistry of a variety of functional materials.[21-24] Furthermore, as discussed later in this chapter, CP is an integral part of DNP NMR spectroscopy, a valuable surface-selective technique.

3.1.4 Decoupling

3.1.4.1 Heteronuclear Decoupling

As previously discussed, heteronuclear dipolar couplings between nuclei can exert a broadening effect on solid-state NMR spectral lineshapes. In order to remove these and to improve spectral resolution, decoupling can be employed.[25] The first decoupling method to be developed was the continuous wave (CW) approach. This is the simplest

of the decoupling schemes in use and involves applying an rf pulse to spin I throughout the acquisition period (of spin S) of the pulse sequence.[25] By continuously irradiating the spins in this way, the heteronuclear dipolar coupling is averaged to zero. The cw approach suffers from sensitivity loss over a wide frequency range, as its efficiency is highly dependent on offset,[26] and so several other sequences have been introduced to provide improved performance. Some of the most commonly used in solid-state NMR spectroscopy are TPPM (two pulse phase modulation)[27] and SPINAL (small phase incremental alternation)[28] sequences. They employ a number of repeating pulses in combination with a phase cycle in order to compensate for resonance offsets and pulse inefficiencies. For example, the TPPM involves a train of pulses with flip angle β = ~170°, with the phase alternating between ϕ and $-\phi$, applied to S spins. The difference between ϕ and $-\phi$ is usually small, and is indicated by the notation TPPM-ϕ, in the name of the decoupling scheme (*e.g.*, TPPM-15).[27] Many additional schemes have been developed to yield further improvements in this area, some examples of which include XiX (X-inverse-X),[29] PISSARRO (phase-inverted supercycled sequence for attenuation of rotary resonance)[30] and eDROOPY (experimental decoupling is robust for offset or power inhomogeneity).[31] The resolution improvement that is provided by heteronuclear decoupling is well illustrated in Figure 3.7. Here, the application of ^{1}H decoupling *via* the TPPM scheme results in a noticeable decrease in the linewidth of the C=O resonance, from ~320 Hz to ~50 Hz, in the ^{13}C MAS NMR spectrum of 1[^{13}C]-glycine. Decoupling of quadrupolar nuclei can also be carried out. In this case, it is advisable to employ low power CW decoupling to avoid recoupling the dipolar interaction.[32]

3.1.4.2 Homonuclear Decoupling

Homonuclear decoupling is an important technique in solid-state NMR spectroscopy. This is because, in powdered solids, strongly dipolar-coupled ^{1}H spins typically give rise to broad, featureless spectra. Therefore, dipolar decoupling is required in order to obtain high-resolution ^{1}H NMR spectra.[6] In solids, magic angle spinning (MAS) alone is usually not sufficient even at the highest rotation rates available, and so in order to carry out homonuclear dipolar decoupling the application of rf pulses is usually required. Since the early work of Lee and Goldburg[33] and Waugh and co-workers,[34-36]

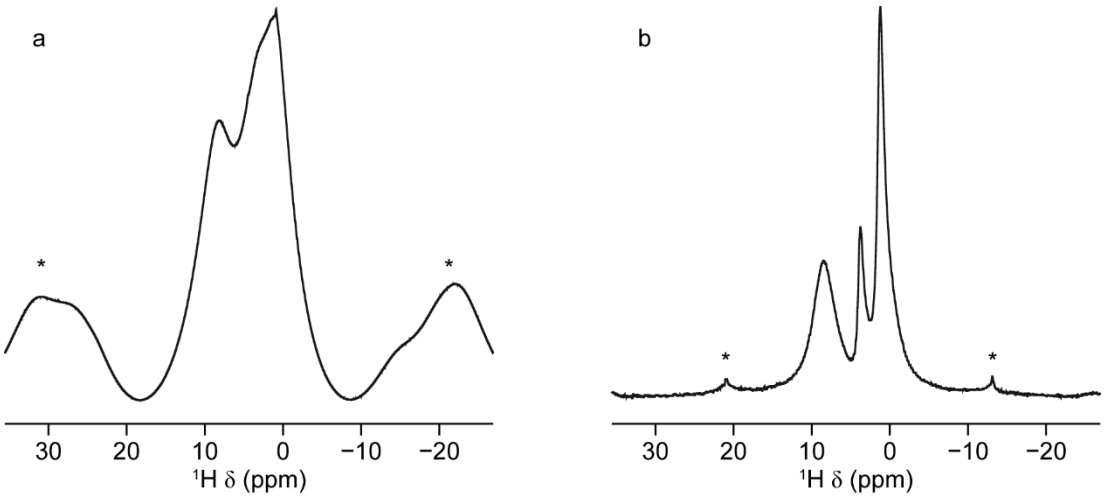

Figure 3.8. *^{1}H (9.4 T, 9.091 kHz MAS) NMR spectra of L-alanine (a) without and (b) with eDUMBO-1_{22} homonuclear decoupling during acquisition. In (b), a scaling factor of 0.50 has been applied to correct the chemical shift axis. * denotes a spinning sideband.*

there has been considerable development in the field of homonuclear dipolar decoupling, and current schemes are able to achieve efficient decoupling through a combination of rf-based pulse sequences and magic-angle spinning (MAS) - the so-called combined rotation and multiple-pulse spectroscopy (CRAMPS) approach.[37] Two types of decoupling sequences have become the preferred methods for acquiring high-resolution ^{1}H NMR spectra in the solid state. The first type includes the phase-modulated[38] and frequency-switched[39] Lee−Goldburg sequences. These were developed using a theoretical model based on the original Lee−Goldburg experiment[33] where the spin system is subjected to a rotation about the magic angle in the rotating frame under the influence of off-resonance rf irradiation. The second group, the "decoupling using mind-boggling optimisation" (DUMBO) sequences, were developed using an optimisation strategy that aimed to provide the most efficient narrowing of spectral lines, *versus* either simulation[40] or experiment (eDUMBO).[41-43] DUMBO sequences are generally analogous to Lee−Goldburg approaches, with the exception that there are four, rather than two, rotations. Additionally, DUMBO sequences include a low-amplitude phase modulation that is designed to further improve line narrowing. This improvement in line narrowing is illustrated in Figure 3.8, which shows ^{1}H MAS NMR spectra of L-alanine with and without the application of eDUMBO-1_{22} decoupling during acquisition.[41,44,45] In (b), the spectral resolution is

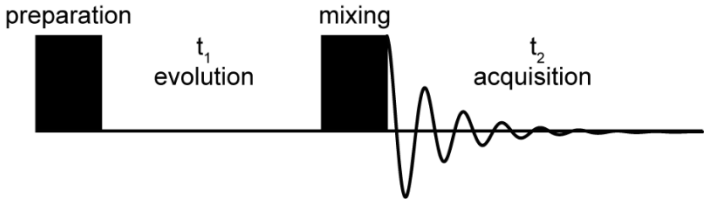

Figure 3.9. *Pulse sequence for a generic 2D NMR experiment.*

comparable to that of Figure 1.1, where fast MAS was employed. There are some considerations that should be noted when utilising homonuclear decoupling. The first is that the optimisation process is multi-step, and must be carefully followed to ensure optimal results. The second is that because chemical shifts evolve around an effective field, a scaling factor must be applied in order to provide "meaningful" δ values.[40] Additionally, care should be taken to set the transmitter offset such that any artefact peaks do not interfere with "true" resonances.[43]

3.2 Advanced Experiments

3.2.1 Two-Dimensional NMR Spectroscopy

So far, one-dimensional (1D) experiments in solid-state NMR spectroscopy have been outlined. Often, though, it is not sufficient simply to know whether certain species are present, or if two nuclear species are spatially close to one another, but it can be important also to know exactly which of each type of species are close to which of another. It is possible to utilise nuclear spin interactions to gain insight into this question by employing two-dimensional (2D) NMR experiments.[6] A pulse sequence for a generic 2D NMR experiment is shown in Figure 3.9. It proceeds as follows: there is a preparation step where magnetisation is generated, which is then allowed to evolve in a time, t_1. This is then followed by a mixing step where magnetisation transfer occurs between spins, followed by signal (FID) acquisition in a time, t_2. The amplitude of the signal that is obtained is modulated by the evolution in t_1 and so, if this time is systematically increased across a series of experiments, then it is possible to indirectly follow magnetisation evolution during the t_1 period.

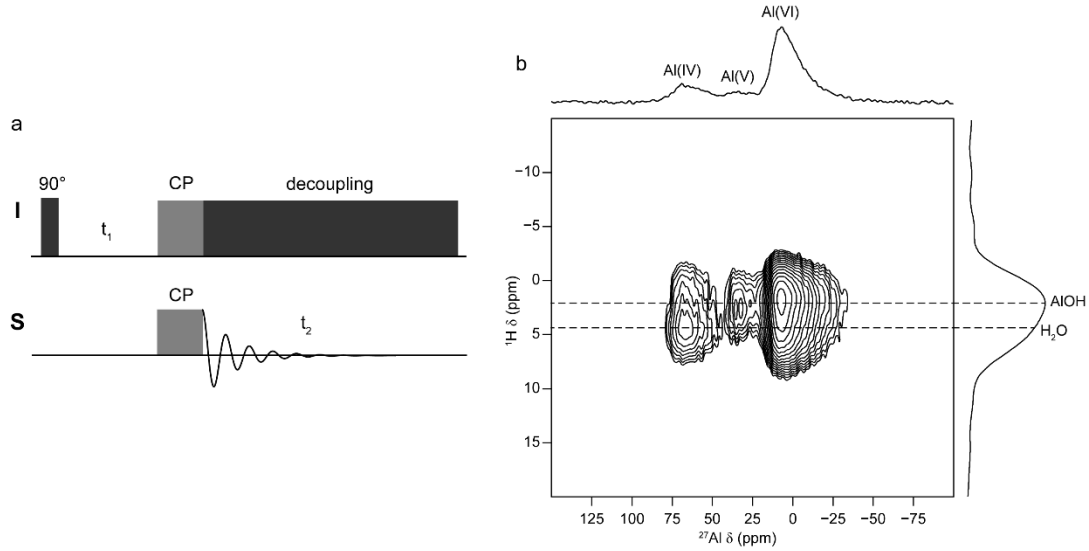

Figure 3.10. *(a) Pulse sequence for a CP HETCOR experiment. (b) ^{1}H-^{27}Al (9.4 T, 14 kHz MAS, τ_{CP} = 0.8 ms) CP HETCOR spectrum of partially dehydrated γ-Al_2O_3. Assignments for Al and H resonances are shown next to the projections of each dimension.*

Fourier transforming the data then results in a 2D spectrum that shows spins between which magnetisation has been transferred.[6] There are two types of 2D correlation experiments: heteronuclear (where magnetisation is transferred between two different nuclear species) and homonuclear (where transfer occurs between the same type of nuclear species), and these are described in more detail below.

3.2.1.1 Heteronuclear Correlation Experiments

To perform a heteronuclear correlation experiment, it is necessary to apply rf pulses to both nuclei in order to enable magnetisation transfer. Experiments can be designed such that this process occurs *via* either the J coupling (through bond) or the dipolar interaction (through space). Cross peaks then reveal which spins are connected through bonds or are in close proximity.[6] One example of a 2D heteronuclear correlation experiment is the CP HETCOR experiment, where the basic pulse sequence can be considered as a derivative of that for CP, and is shown in Figure 3.10(a). The experiment begins with creation of I spin coherences which evolve during t_1. It is possible, if desired, to insert a homonuclear decoupling scheme during this period.[41] Magnetisation is then transferred from I to S using a CP step and subsequent

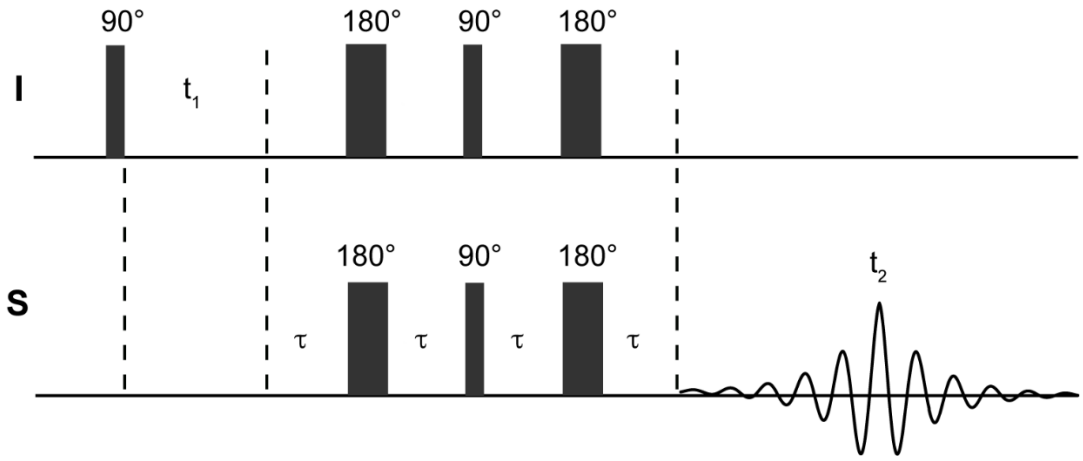

Figure 3.11. *Pulse sequence for the R-INEPT experiment. The sequence above is for a scalar (through-bond) experiment. A dipolar (through-space) experiment can be created by modifying the sequence to include blocks of dipolar recoupling on the I spin during the τ periods. A prior cross polarisation component can also be added to the pulse sequence if required.*

signal acquisition occurs during t_2.[6] In this basic experiment it is possible, as for a 1D CP experiment, to vary the contact time in order to probe the variation in spatial proximity of I and S nuclei.[46] An example of a CP HETCOR spectrum is shown in Figure 3.10(b), a ^{1}H-^{27}Al 2D correlation spectrum of a sample of γ-Al_2O_3 dehydrated *in vacuo* at 150 °C for ~24 h. It reveals that Al(VI) and Al(V) environments are close in space primarily to AlOH species on the surface of the material, whereas Al(IV) mainly correlates to residual adsorbed H_2O.

Another example of a heteronuclear correlation sequence is the INEPT (insensitive nuclei enhanced by polarisation transfer) experiment. It was initially designed for use in solution-state experiments to enhance weak NMR signals of low-γ nuclei through the use of magnetisation from high-γ nuclei.[47,48] A modified version is usually used in solids that includes a refocusing step, in order to obtain purely absorptive (*i.e.* in-phase) lineshapes.[49] The intensity of the signal that is detected depends on the magnitude of the equilibrium magnetisation and the transfer efficiency. Nuclei with high γ have larger equilibrium magnetisation and so generate higher sensitivity in the experiment. Fyfe *et al.* demonstrated the feasibility of using INEPT in the solid state to study scalar (through-bond) connectivity involving quadrupolar nuclei in the 1990s[50] and since that time, it has become a popular experiment.[51,52]

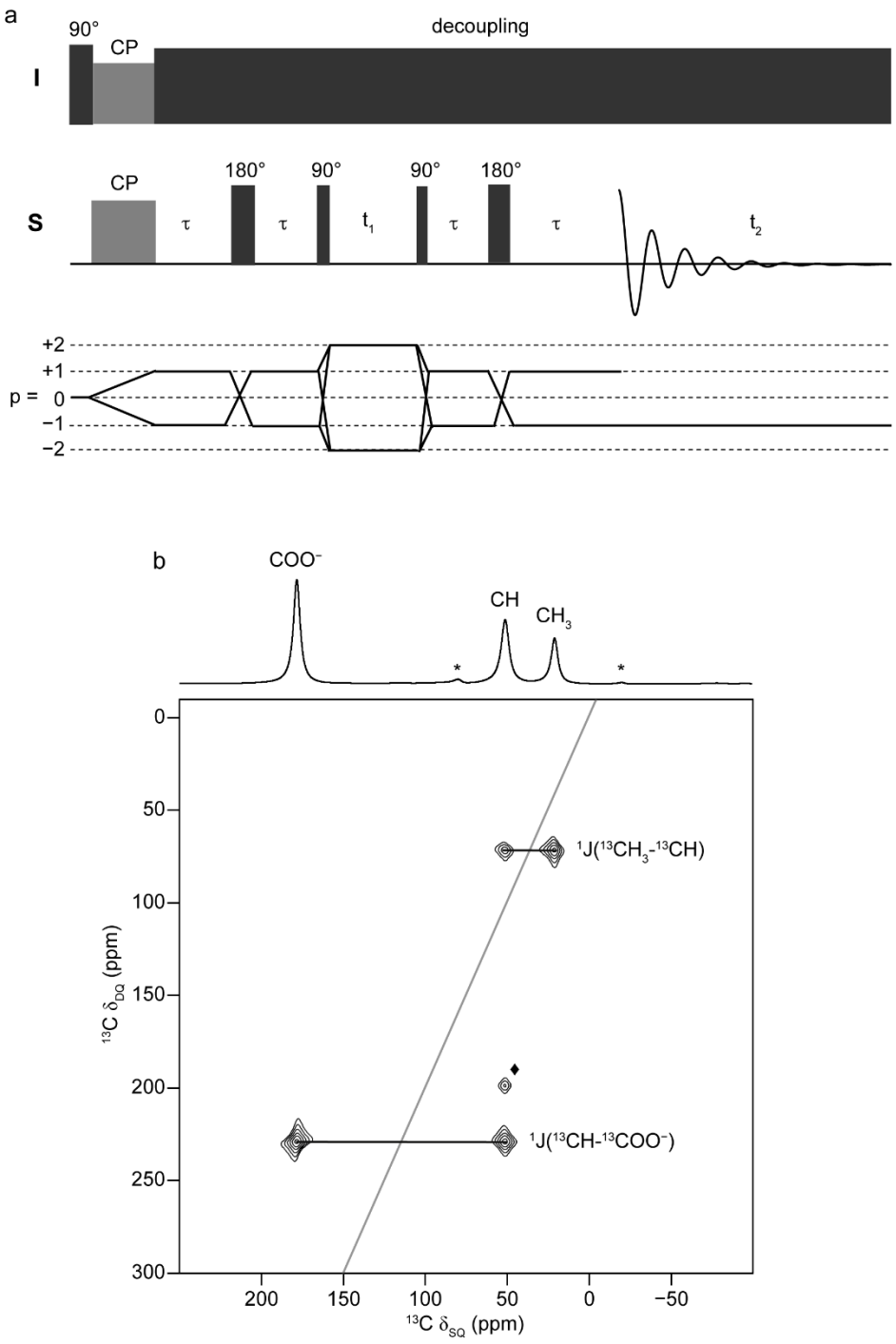

Figure 3.12. *(a) Pulse sequence and coherence pathway for a refocused INADEQUATE experiment. In this version, CP is used to enhance initial ^{13}C magnetisation. (b) ^{13}C-^{13}C (9.4 T, 10 kHz MAS, τ = 3 ms) refocused INADEQUATE spectrum (with CP from ^{1}H, where τ_{CP} = 0.5 ms) of U[^{13}C]-L-alanine. Solid black lines indicate correlations between directly bonded ^{13}C species. The solid grey line denotes the $\delta_{DQ} = 2\delta_{SQ}$ autocorrelation diagonal. ♦ indicates a relayed anti-phase peak resulting from two nuclei that are not covalently bonded, but share a common coupling partner.*[59] ** denotes a spinning sideband.*

It has also been adapted to probe through-space (dipolar) connectivity between heteronuclei by incorporating dipolar recoupling schemes.[53] Gan described the use of methods such as REDOR as applied to the HMQC experiment,[54] but they are also applicable to INEPT as well.[55] Indeed, the INEPT experiment, in both scalar and dipolar forms, has previously been utilised for the study of aluminosilicate-based materials with notable success.[56] It has also been used for this purpose, in combination with DNP, in Chapter 6 of this work. The pulse sequence for the refocused INEPT (R-INEPT) experiment is shown in Figure 3.11.

3.2.1.2 Homonuclear Correlation Experiments

It is also possible to probe proximities between the same type of nuclear species. This can prove to be useful in cases where a material is comprised of a complex mixture of polymorphs or phases. By utilising 2D correlation experiments, it is possible to identify homonuclear pairs in such mixtures, thus providing valuable information regarding, for example, phase identity.[57] Homonuclear 2D experiments can be designed to probe both scalar and dipolar couplings between species. Although scalar couplings are less evident in the solid state than in the solution state (owing to the additional interactions present), their relationship to connectivity in molecular systems is an important one. One example of this type of experiment is the incredible natural abundance double quantum transfer experiment (INADEQUATE). The pulse sequence is shown in Figure 3.12(a). Although it is primarily used for solution-state experiments, a version that has been adapted for use in solid-state NMR spectroscopy is also available, incorporating a refocusing step to produce purely in-phase lineshapes.[58] During the delay, τ, the magnetisation evolves, influenced by J couplings, to create double-quantum coherences between coupled spins. The 180° pulse then refocuses any evolution resulting from chemical shifts and the τ period is rotor synchronised, in order to avoid signal modulation by MAS. Double-quantum coherences evolve during t_1 then are converted to observable coherences before the signal is acquired.[58] Figure 3.12(b) shows the ^{13}C-^{13}C refocused INADEQUATE spectrum of U[^{13}C]-L-alanine. Correlations are observed between those ^{13}C species that are directly bonded to one another (*i.e.* $^{1}J(^{13}C\text{-}^{13}C)$). The experiment can also be used to explore more distant couplings (for example, $^{2}J(^{13}C\text{-}^{13}C)$) by increasing the

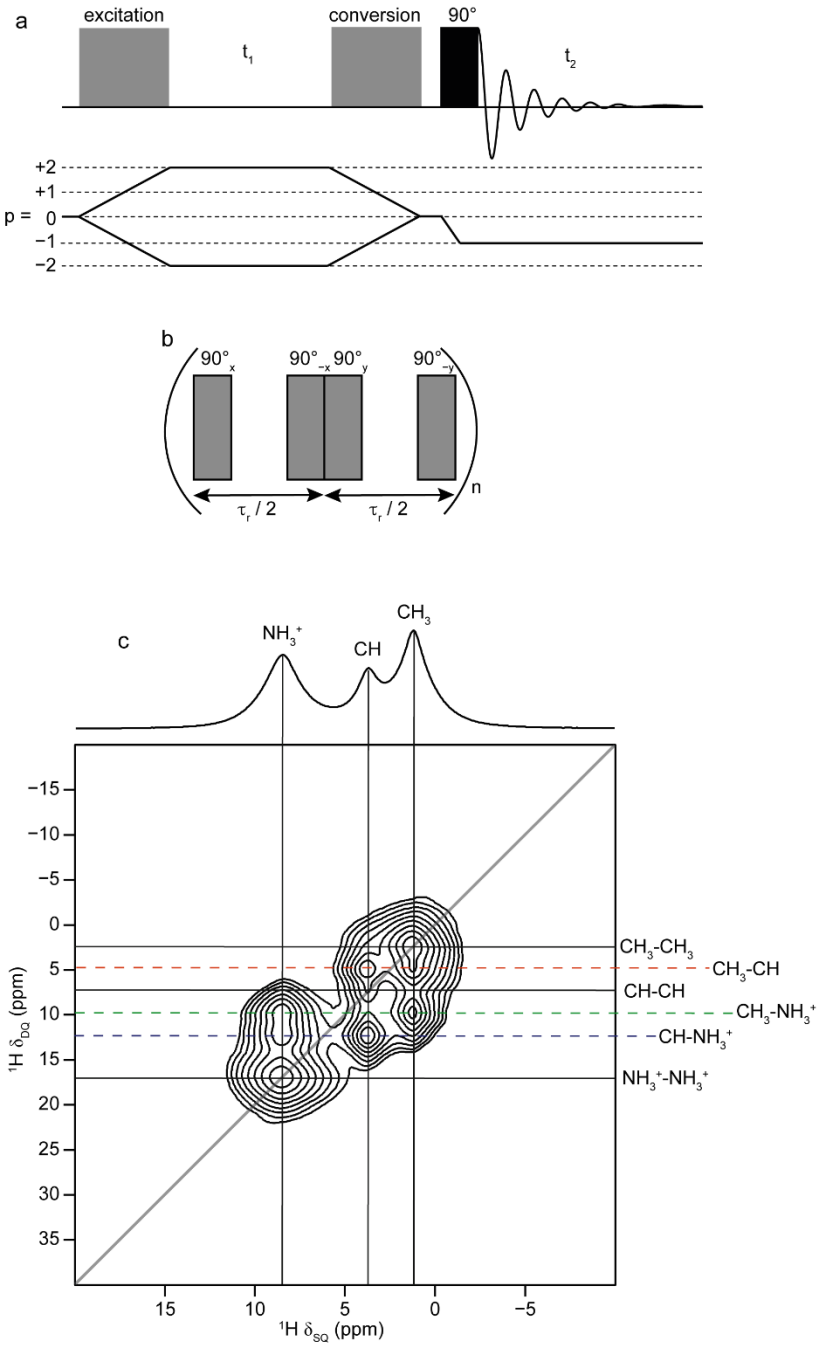

Figure 3.13. *(a) Pulse sequence and coherence transfer pathway for a generic homonuclear SQ-DQ correlation experiment. (b) The BABA scheme employed for excitation and conversion of DQ coherences where τ_r = rotor period and n = number of BABA blocks used. (c) ^{1}H-^{1}H (9.4 T, 40 kHz MAS) SQ-DQ BABA spectrum of* L*-alanine, where n = 1. Solid black lines denote DQ coherences between two protons of the same type (e.g., CH-CH). Dashed coloured lines indicate DQ coherences between two different types of protons (e.g., CH_3-CH). The solid grey diagonal line denotes the $\delta_{DQ} = 2\delta_{SQ}$ autocorrelation diagonal.*

length of the τ period. In the case of U[^{13}C]-L-alanine, however such resonances are expected to be present at ~1% of the intensity of ^{1}J(^{13}C-^{13}C) ones.[59] As a result, they are not observed in the spectrum in Figure 3.12(b). ^{29}Si-^{29}Si refocused INADEQUATE experiments have been utilised in the study of silicated alumina catalysts, in combination with DNP, in Chapter 6 of this work.

Several different approaches exist for conducting homonuclear through-space correlations experiments for solids. The generic sequence for this kind of experiment is shown in Figure 3.13. It proceeds as follows: double-quantum (DQ) coherences are generated by an excitation scheme and evolve during t_1. They are converted to a population state by a conversion scheme (which is often the same as the excitation scheme), before being converted to transverse SQ magnetisation by a 90° pulse.[60] Several types of excitation/conversion schemes exist that can be used in a SQ-DQ correlation experiment. One example is the back-to-back (BABA) sequence developed by Spiess and co-workers.[61,62] The scheme, shown in Figure 3.13(b), consists of two 90° pulses with different phases which are applied at half rotor period intervals ($\tau_r/2$) to prevent refocusing of the dipolar coupling. This means that the basic component fits into one whole rotor period, and the recoupling approach can be used at high MAS rates. This gives it good applicability for studying ^{1}H-^{1}H and ^{19}F-^{19}F dipolar interactions.[63] Figure 3.13(c) shows a ^{1}H-^{1}H SQ-DQ BABA correlation spectrum of L-alanine. It can be seen that all three types of proton (CH_3, CH and NH_3^+) are close in space to each other, from the presence of "off-diagonal" ($\delta_{DQ} \neq 2\delta_{SQ}$) resonances resulting from DQ coherences between two different types of ^{1}H species (*e.g.*, CH_3-CH). Alternative excitation/conversion schemes can also be used for DQ correlations.[64-67]

3.2.2 Carr-Purcell Meiboom-Gill

Studies of some NMR-active nuclei can be challenging due to low sensitivity resulting from low natural abundance and/or low-γ. The Carr-Purcell Meiboom-Gill (CPMG) pulse sequence,[68,69] named for the researchers who developed it, can be used to enhance the peak height signal-to-noise ratio of solid-state NMR spectra. The pulse sequence is shown in Figure 3.14(a). It consists of an "echo train" of successive 180° pulses, which continually refocus the magnetisation in the transverse plane. The signal

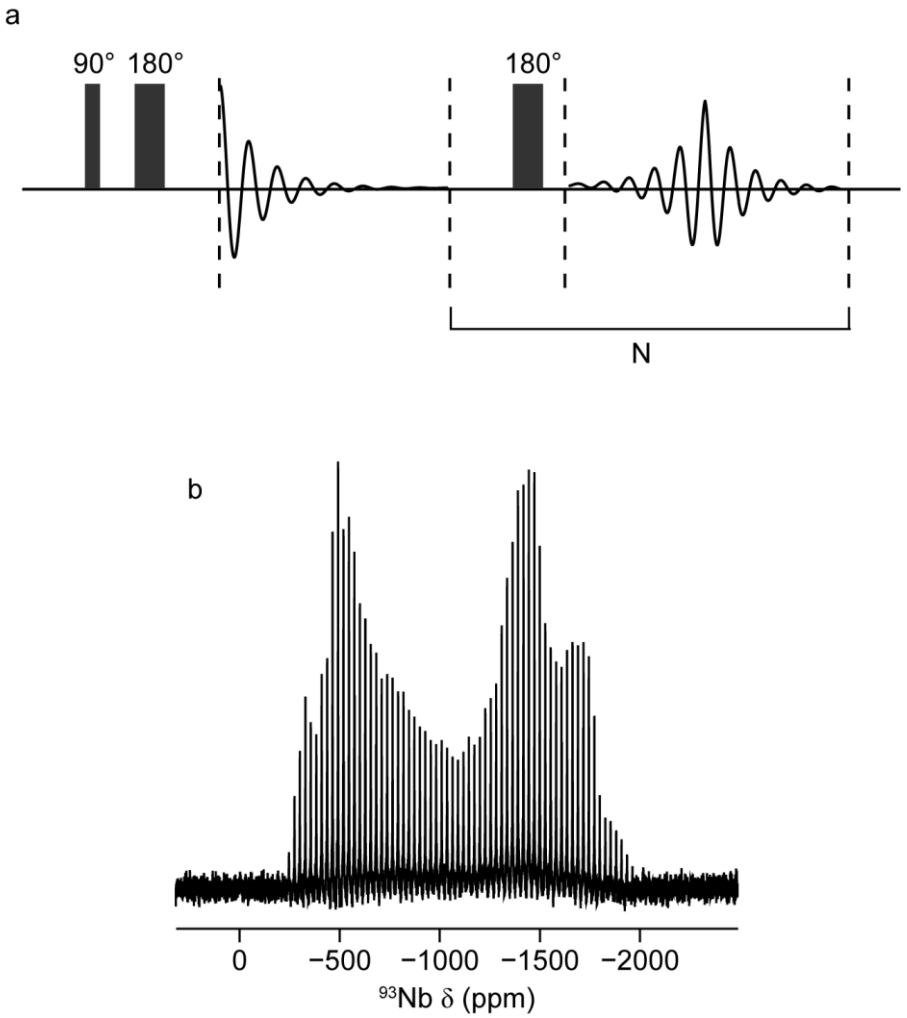

Figure 3.14. *(a) Pulse sequence for a CPMG experiment, where N = number of echoes. (b)* ^{93}*Nb (14.1 T) CPMG spectrum of a static sample of* $K_7Na[Nb_6O_{19}]$*.*

intensity in the resulting NMR spectrum is therefore concentrated into sharp "spikelets", with intensities that resemble the conventional powder pattern lineshape. The lineshape resolution is dependent on the spikelet separation, which is the inverse of the echo separation. CPMG can be used under both static and MAS conditions.[70] In the latter case, it is necessary to ensure that the echo interval is rotor synchronised. CPMG can also be useful for the study of nuclei that exhibit large quadrupole interactions, resulting in broad powder pattern lineshapes.[71] An example of this is shown in Figure 3.14(b), where the ^{93}Nb (spin I = 9/2) CPMG spectrum of the polyoxometalate $K_7Na[Nb_6O_{19}]$ is shown. The application of CPMG allows for the acquisition of the complete CT lineshape with a high level of sensitivity.

3.2.3 Techniques for Studying Quadrupolar Nuclei

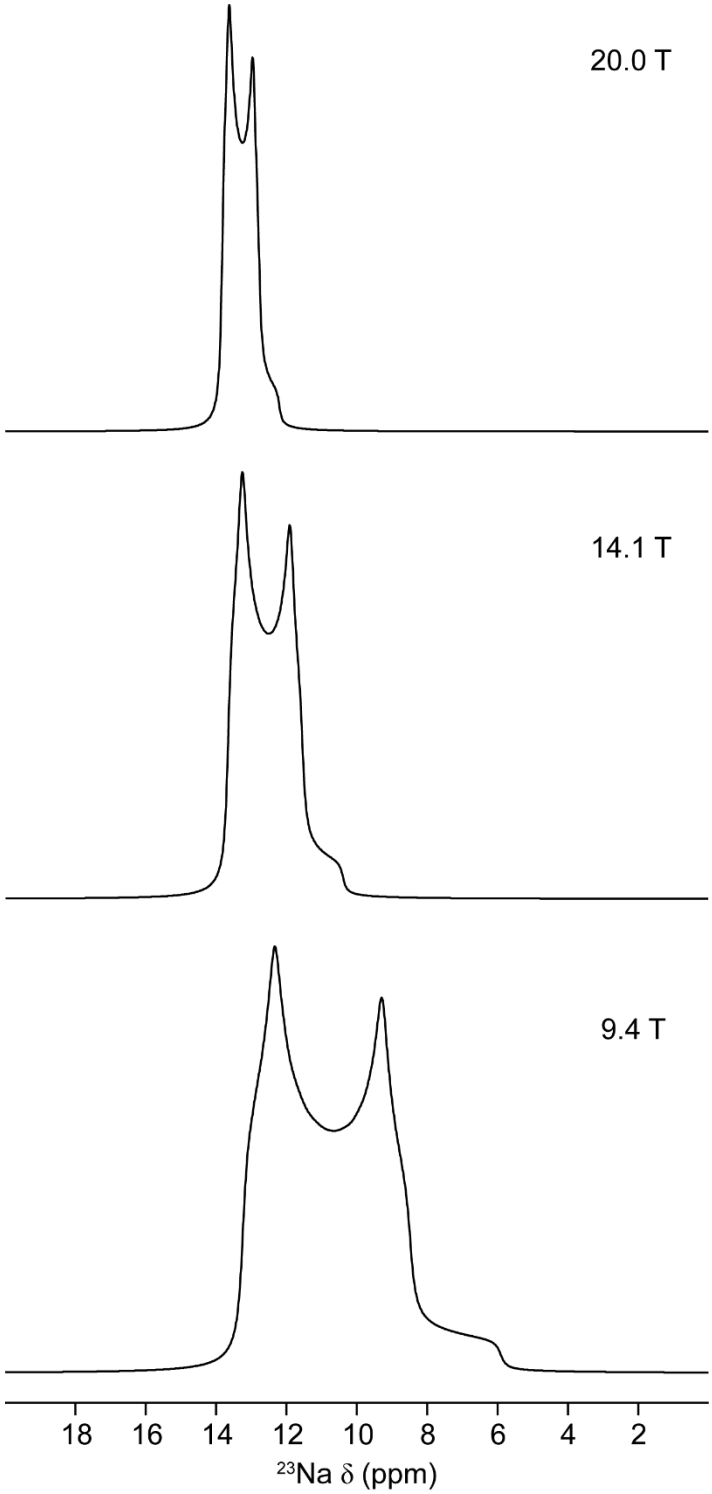

Figure 3.15. *Simulated quadrupolar lineshapes for the ^{23}Na CT (spin I = 3/2) at different B_0 field strengths. Simulation parameters include: ν_R = 14 kHz; δ_{iso} = 14 ppm; C_Q = 1.2 MHz and η_Q = 0.2.*

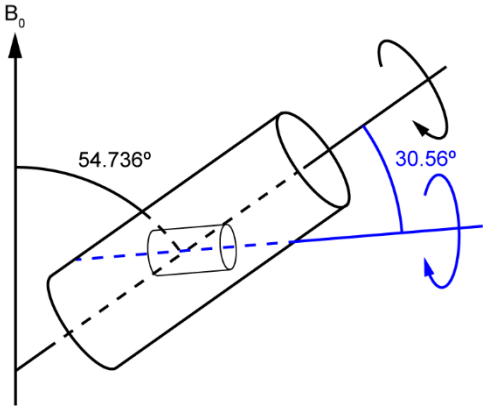

Figure 3.16. *Schematic representation of the experimental setup for DOR.*

As mentioned previously, even under the application of MAS, quadrupolar CT lineshapes are still affected by second-order quadrupolar broadening. However, several approaches have been developed to remove or mitigate the effect of this type of broadening.

3.2.3.1 Ultrahigh Magnetic Fields

As previously outlined, second-order quadrupolar broadening is inversely dependent on ω_0. Therefore, by increasing the B_0 field strength, it is possible to reduce this broadening. This is illustrated in Figure 3.15, which shows the effect of acquiring spectra at different B_0 on simulated ^{23}Na (spin I = 3/2) CT lineshapes. In 2002, Gan *et al.*[72] demonstrated that it is possible to effectively mitigate the effects of second-order quadrupolar broadening if a high enough B_0 field is used. By means of a hybrid superconducting-resistive magnet with B_0 = 40 T, they were able to acquire a ^{27}Al MAS NMR spectrum of $Al_{18}B_4O_{33}$. At this extremely high magnetic field strength, the resonances are predominantly broadened by B_0 field imperfections. The current B_0 field limit for superconducting NMR magnets is, however, lower than this example, at 24 T.[73]

3.2.3.2 Double Rotation

The double rotation (DOR) method[74] can be considered as an extension of MAS. In DOR, an inner rotor spins inside a larger outer rotor, with the outer one set at 54.736° relative to B_0 to remove second-rank anisotropic broadening, while the inner one is inclined at 30.56° with respect to the outer rotor, to remove fourth-rank anisotropic

broadening. This is schematically illustrated in Figure 3.16. This, in theory, should result in the complete removal of all quadrupolar broadening, but as the large outer rotor restricts rotation rates to ~2 kHz, the result is an NMR spectrum that contains a complex manifold of spinning sidebands that can make spectral analysis and interpretation more challenging. Additionally, DOR requires specialist and potentially expensive hardware.

3.2.3.3 Dynamic Angle Spinning

Like DOR, Dynamic Angle Spinning (DAS)[75] aims to remove quadrupolar broadening by rotating the sample around two angles, but this is done sequentially, as a 2D experiment, instead of simultaneously. Magnetisation evolves in t_1 while the rotor is aligned along one angle, then before t_2 the angle is adjusted so that the first- and second-order perturbations are refocused, leaving only the isotropic peaks. Long T_1 relaxation times are required, as between t_1 and t_2 the magnetisation has to be stored along the z-axis and so does not evolve. As with DOR, specialist hardware is required for DAS experiments.

3.2.3.4 Multiple-Quantum Magic Angle Spinning

Other methods also exist that do not require alteration of the rotation angle, instead using spin manipulation to acquire a spectrum free from quadrupolar broadening. A key example is the multiple-quantum magic angle spinning (MQMAS) experiment first introduced by Frydman and Harwood.[76] Unlike the DOR and DAS techniques described above, MQMAS can be carried out using standard MAS hardware, which makes it a more convenient and less expensive option for the routine acquisition of isotropic spectra of quadrupolar nuclei. It is a 2D experiment, applicable to nuclei with half integer spin quantum number, where the CT is correlated with a symmetric (*i.e.*, $m_I \leftrightarrow -m_I$) multiple quantum (MQ) transition. Direct excitation of MQ magnetisation is formally forbidden by NMR selection rules though, so the filtration stage of the experiment suffers from poor sensitivity. This is one of the principal disadvantages of the MQMAS experiment, although several approaches have been devised to increase experimental efficiency.[77-79] The resulting 2D spectrum obtained after Fourier transformation shows the CT MAS lineshape in the δ_2 dimension. In the δ_1 dimension

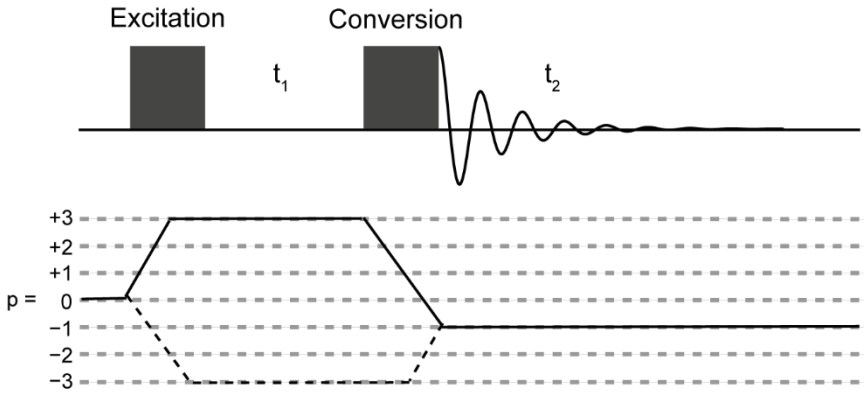

Figure 3.17. *Pulse sequence and coherence transfer pathway for a two pulse MQMAS experiment based on that introduced by Frydman and Harwood.[76] In the coherence transfer pathway diagram, the echo and anti-echo pathways are indicated by solid and dashed lines, respectively. The coherence transfer pathway that is followed depends on the MQMAS ratio of the spin quantum number. For spin I = 3/2, the ratio for 3QMAS is negative, so the p = −3 pathway is followed.*

there is a high-resolution isotropic spectrum that is free from quadrupolar broadening after appropriate processing.[6] Theoretically, the MQMAS experiment can be performed on any quadrupolar nucleus with half-integer spin quantum number, *via* any available symmetric odd-ordered coherences. The ratio of the fourth-rank coefficients for the MQ and SQ coherences, $A^4(I,m_I)/A^4(I,1/2)$, differs from the corresponding coefficients of the isotropic terms, $A^0(I,m_I)/A^0(I,1/2)$.[6,76,80] The ratio of the anisotropic fourth-rank coefficients differs depending on the spin system and coherence order, as shown in Table 3.2. In this work, triple-quantum (3Q) MQMAS experiments have been utilised exclusively.

The original MQMAS experiment used a two-pulse approach for the generation of 3Q coherences.[76] An adapted version of this pulse sequence is shown in Figure 3.17. The principal disadvantage of this method is that the resulting spectrum displays "phase-twist" lineshapes[6] and, as a result, modified sequences have subsequently been introduced in order to obtain pure absorption-mode lineshapes.

One example of a modified MQMAS sequence is the z-filtered experiment,[81] the pulse sequence for which is provided in Figure 3.18(a). For the case of a 3QMAS experiment, the sequence proceeds as follows: 3Q coherences are excited by the first

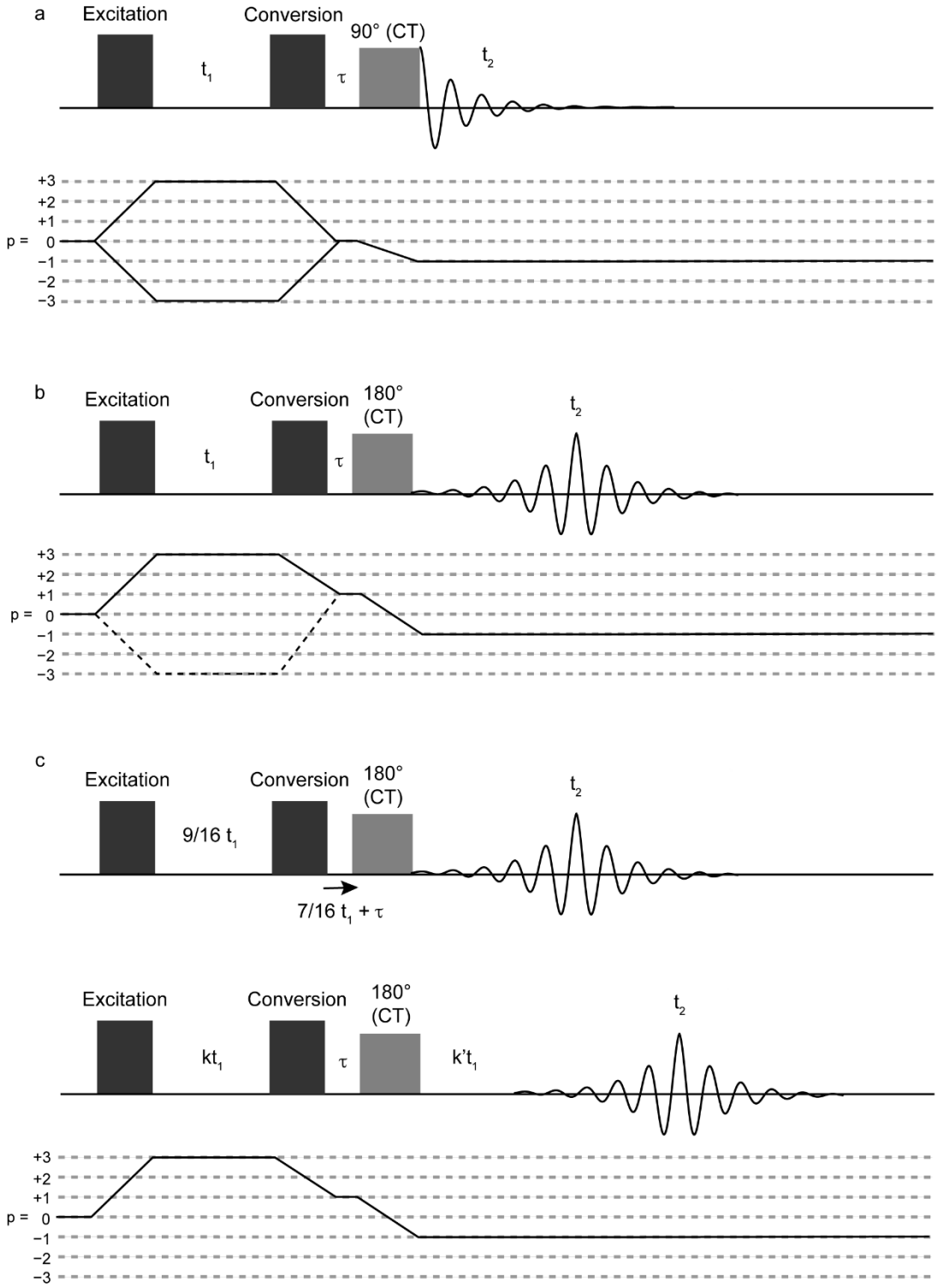

Figure 3.18. *Pulse sequences and coherence pathways for (a) the z-filtered MQMAS experiment (b) shifted echo MQMAS and (c) split-t_1 shifted echo MQMAS (spin I = 3/2) (upper) and split-t_1 shifted echo MQMAS (spin I ≥ 5/2) (lower) experiments. In the coherence pathway in (b), the dashed line denotes the pathway followed for spin I = 3/2 nuclei.*

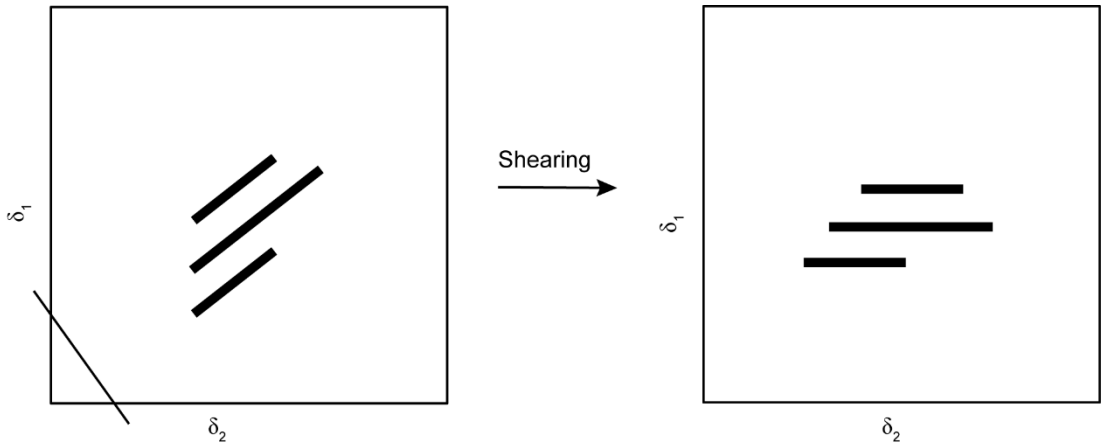

Figure 3.19. *An illustration of the effect of shearing transformation on a schematic MQMAS spectrum.*

Table 3.2. *MQMAS ratios R ($A^4(I,m_I)/A^4(I,1/2)$) for half-integer quadrupolar nuclei.*

Spin I	$m_I = \pm 3/2$	$m_I = \pm 5/2$	$m_I = \pm 7/2$	$m_I = \pm 9/2$
3/2	−7/9			
5/2	19/12	−25/12		
7/2	101/45	11/9	−161/45	
9/2	91/36	95/36	7/18	−31/6

pulse. This is followed by the evolution time, t_1, then a second pulse that converts the coherence order to zero. Next, there is a z-filter delay, τ, during which magnetisation is stored along the z-axis, parallel to B_0 (in the laboratory frame). The application of a third low power 90° CT "selective" pulse, excites observable p = −1 magnetisation, before acquisition of the FID.[6,81] The 2D spectrum obtained from a z-filtered MQMAS experiment contains a set of ridge-like lineshapes which lie along a gradient equal to the MQMAS ratio for the particular nucleus under study. A projection orthogonal to these ridges produces an isotropic spectrum. In order to obtain a spectrum where the ridges are parallel to δ_2, and the isotropic spectrum can be obtained directly from a projection onto δ_1, a shearing transformation is required.[6] This is schematically illustrated in Figure 3.19. In this work, all sheared z-filtered MQMAS spectra presented have been referenced in δ_1 according to the convention proposed by Pike *et*

al.,[82] unless otherwise indicated.

Alternatively, a three-pulse MQMAS experiment may be carried out *via* a shifted-echo approach.[83] The coherence pathway used for this sequence depends on both spin I and sign of the MQMAS ratio. In the case of 3QMAS, for spin I = 3/2, the ratio is negative, so the p = −3 pathway is used. For spin I = 5/2, 7/2 and 9/2, the 3QMAS ratio is positive and the p = +3 pathway is followed. After a delay, τ, a refocusing CT selective 180° pulse is applied. This shifts the subsequent whole echo, and allows it to be acquired. It is necessary for T_2 relaxation to be of sufficient duration to enable the acquisition of a whole echo. As with the z-filtered experiment, a shearing transformation is required to obtain ridges parallel to δ_2. The pulse sequence for the 3QMAS shifted-echo experiment is shown in Figure 3.18(b). In the split-t_1 version of this experiment developed by Brown and Wimperis[84] however, shearing of the spectrum is not necessary. This is because the second-order broadening is completely refocused after t_1. In this experiment, the t_1 evolution time is divided into two contributions according to the MQMAS ratio (values for these contributions are given in Appendix C). In the 3QMAS case, the pulse sequence consists of an excitation pulse followed by a part of t_1 (the MQ contribution). Next, a pulse is used to convert coherence order from p = +3 to p = +1, and this is followed by an echo delay, τ. A low power 180° CT selective pulse then precedes the remaining t_1 portion (the CT contribution). By splitting the t_1 period between MQ and CT evolution, the second-order quadrupolar broadening is refocused at the end of t_1. In the resulting spectrum, the second-order broadened ridges are parallel to the δ_2 axis, and a spectrum free from quadrupolar broadening is obtained by a projection on to the δ_1 axis. Pulse sequences for the 3QMAS split-t_1 shifted-echo experiment are shown in Figure 3.18(c).

3.2.3.5 Extracting NMR Parameters from MQMAS Spectra

One of the great strengths of the MQMAS experiment is that it enables values for several useful NMR parameters to be obtained.[6] By extracting cross sections of the lineshapes from along the ridges in the 2D spectrum, analytical fitting can be carried out and values for δ_{iso} (isotropic chemical shift), C_Q (quadrupolar coupling constant), and η_Q (quadrupolar asymmetry parameter), obtained. Alternatively, for disordered samples, the 2D spectrum can be modelled using the Czjzek distribution,[85] a procedure

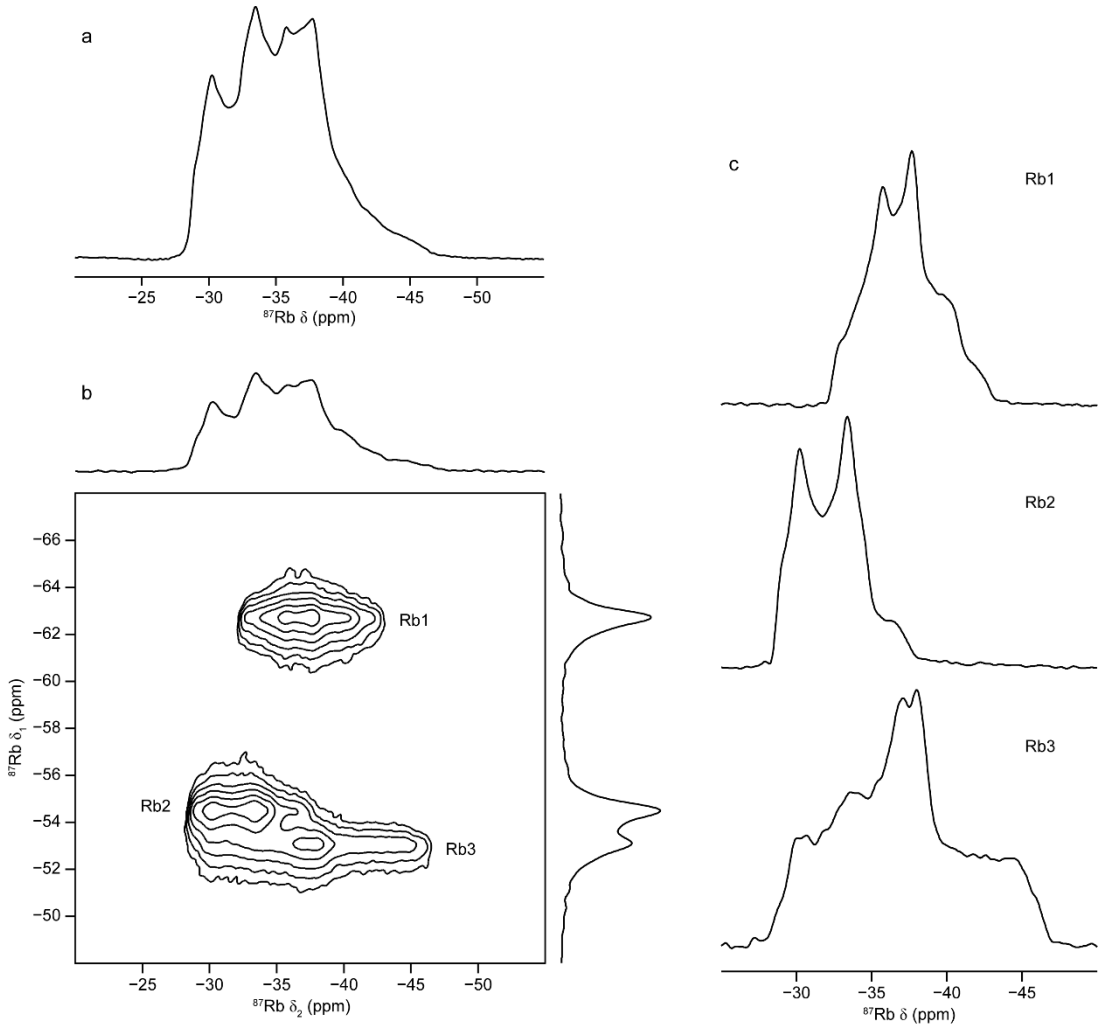

Figure 3.20. *(a) ^{87}Rb (9.4 T, 14 kHz MAS) NMR spectrum of $RbNO_3$. (b) ^{87}Rb (9.4 T, 14 kHz MAS) z-filtered 3QMAS NMR spectrum of $RbNO_3$. A shearing transformation has been applied. (c) Cross sections parallel to δ_2 extracted from the spectrum shown in (b).*

Table 3.3. *^{87}Rb NMR parameters (isotropic chemical shift, δ_{iso}, quadrupolar coupling constant, C_Q, quadrupolar asymmetry, η_Q and quadrupolar product, $P_Q = C_Q(1 + \eta_Q^2 / 3)^{1/2}$) for $RbNO_3$.*

Site	C_Q / MHz	δ_{iso} (ppm)	η_Q	P_Q / MHz
Rb1	1.60	−32.3	0.6	1.75
Rb2	1.63	−27.9	0.3	1.61
Rb3	2.00	−29.5	0.9	2.31

which can be carried out *via* fitting software such as DMFit.[86] If neither of these approaches are possible due to, for example, lineshape distortion or overlapping of ridges, then the position of the centre of gravity of the 2D lineshape (δ_1, δ_2), can be used to obtain the δ_{iso} and P_Q (quadrupolar product), where P_Q is a combination of C_Q and η_Q, as defined in Equation 2.40.

The following example, in Figure 3.20, demonstrates the utility of the MQMAS experiment. Figure 3.20(a) shows the ^{87}Rb (spin I = 3/2) MAS NMR spectrum of $RbNO_3$. It contains several overlapping CT lineshapes, making analysis and interpretation of each component difficult. By performing a 3QMAS experiment, the spectrum in Figure 3.20(b) was obtained. Here, it is possible to distinguish the three Rb sites, and in δ_1 their resonances are now unaffected by quadrupolar broadening. Furthermore, by extracting cross sections from along each of the ridges, as shown in Figure 3.20(c), NMR parameters can be obtained in the manner described above. The parameters for each Rb site (designated here as Rb1, Rb2 and Rb3) in $RbNO_3$ are given in Table 3.3. P_Q is equal to C_Q for the case where $\eta_Q = 0$, and because η_Q can have a value of between 0 and 1, P_Q can deviate from C_Q at maximum by 15.5% (for the case where $\eta_Q = 1$).[87]

3.2.3.6 Satellite-Transition Magic Angle Spinning

In addition to MQMAS, the satellite-transition magic angle spinning (STMAS) experiment, can also be used to obtain isotropic spectra. Introduced in 2000 by Gan,[88] it is similar in nature to MQMAS, but instead of utilising MQ transitions, the single-quantum satellite transitions (STs) are correlated to the CT, which increases the sensitivity significantly. STs are, however, also affected by first-order quadrupolar broadening, making the experiment more difficult to carry out. The magic angle must be set with high accuracy (± 0.002°), the rotation rate has to be very stable (<±1 Hz) and the pulses in the sequence must be timed very accurately.[89] The pulse sequence for the STMAS experiment is similar to MQMAS (with p = ±1 ST replacing p = ±3 MQ), as is the appearance of the resulting spectrum.

3.2.4 Experimental Aspects of DNP NMR Spectroscopy

In Chapter 2, the theory underlying the signal enhancement technique known as dynamic nuclear polarisation (DNP) was introduced. In this section, information is provided on the practical aspects of the technique, particularly sample preparation and instrumentation.

3.2.4.1 Sample Preparation for DNP Experiments

DNP is well-known for its ability to enhance the sensitivity of solid-state NMR experiments by transferring magnetisation from unpaired electrons to nearby nuclei.[90] In the DNP experiment, an exogenous radical is introduced as a polarisation source using standard wet impregnation techniques.[91] Continuous wave microwave irradiation then polarises the NMR-active nuclei in the sample, with the extent of polarisation being dependent on several factors *e.g.*, abundance, gyromagnetic ratio and relaxation properties of the nucleus. ^{1}H nuclei are usually the most rapidly polarised, with spin diffusion mechanisms efficiently distributing this enhanced nuclear polarisation across protons of the sample and solvent,[92-96] from where conventional CP can then be applied to transfer the polarised spin from ^{1}H to less receptive nuclei. The exogenous radical source and hyperpolarised protons reside at the surface of the sample to provide a convenient enhancement of surface NMR signals relative to those of the bulk. As a result, DNP experiments have been given the label DNP-SENS, where SENS stands for Surface Enhanced NMR Spectroscopy.[97] Thus, DNP enables the aforementioned challenges of surface insensitivity and poor S/N to be overcome, so that NMR spectroscopy can be used to efficiently characterise the surface structures of a diverse range of materials.

DNP experiments are typically performed at low temperature (~100 K) in order to facilitate glass formation and to more effectively saturate the EPR transitions, hence achieving greater polarisation *via* the cross effect. In addition to the DNP effect, a Boltzmann-based signal enhancement is also obtained by virtue of the low temperatures employed. The enhancement factor, ε, determined from the ratio of signal intensities with microwave irradiation on and off, is governed by several factors including, temperature, microwave power, concentration of the exogenous radical

source and the extent of surface wetting.[93,98-100] Proton density in particular has a profound effect on signal enhancement, as a direct consequence of the complex pathway of polarisation transfer from electron to target nucleus. Achieving efficient signal enhancement requires both an appreciable accumulation of ^{1}H polarised spin and facile spin diffusion, which is governed by the nature of the coupled proton network comprising the surface and surrounding solvent. If the ^{1}H T_1 time is too short, enhanced polarisation will dissipate before it can be sufficiently distributed through the sample. The efficacy of DNP will therefore diminish with short T_1 relaxation times. This can however, be overcome by exchanging fast relaxing protons with deuterons or functional groups with more slowly relaxing protons.[101] For example, high levels of deuteration are known to produce large ^{1}H enhancements in d_8-glycerol/D_2O/H_2O frozen solutions, where deuteration slows relaxation among remaining protons and allows polarisation to be distributed over a smaller reservoir of ^{1}H nuclei.[102] The combined effect is a more efficient channelling of polarisation to those protons that contribute directly to CP. Halogenated solvents are also found to provide a significantly higher ε than their non-halogenated analogues, an observation that is again assigned to a reduction of the ^{1}H density in the solvent.[103] A coupled proton network is essential for the transfer of spin polarisation to occur, but if proton density is too high, then relaxation rates are adversely affected and the polarisation transfer efficiency is diminished. Therefore, it can be seen that the relationship between ^{1}H and ε is non-monotonous,[102] highlighting the importance of sample preparation.

3.2.4.2 DNP NMR Instrumentation

The NMR spectrometer system used to perform DNP NMR experiments can be considered an extension of the conventional solid-state NMR one. DNP NMR instruments for solid-state applications were first successfully developed by the Griffin research group at the Massachusetts Institute of Technology in the 1990s.[104-106] It was these efforts that led to the development of present day commercial spectrometers by, among others, Bruker Biospin,[100,107] which have been installed in several research laboratories around the world. These systems are comprised of several individual components, and detailed description of each can be found in the works of Rosay *et al.*,[108] Matsuki *et al.*[109,110] and Griffin and co-workers.[111]

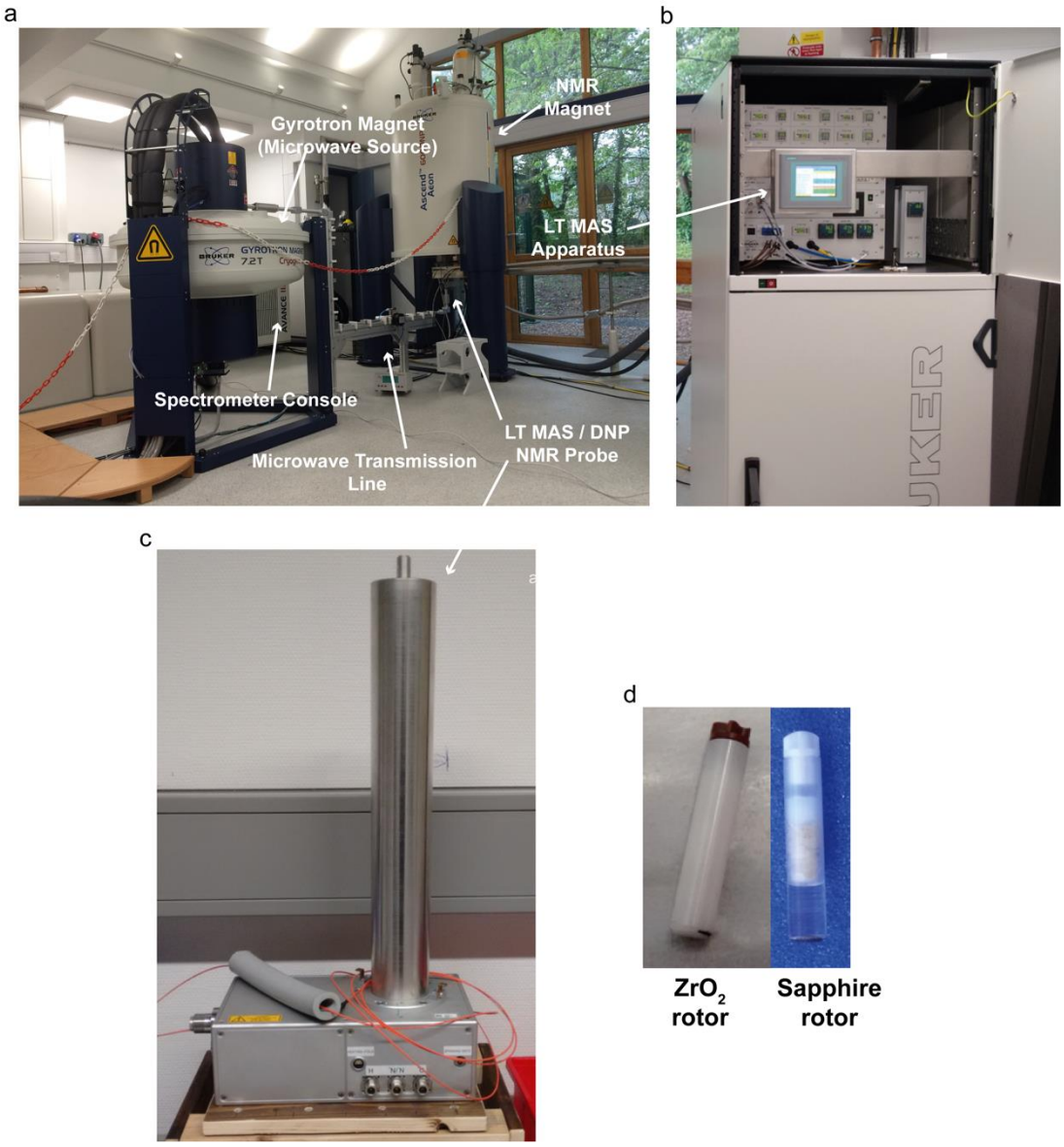

Figure 3.21. *Annotated photographs of (a) The 14.1/7.2 T DNP NMR system installed at the University of Nottingham, UK. (b) The LT MAS apparatus for the system shown in (a). (c) A DNP NMR probe in use at the Ecole Polytechnique Fédérale de Lausanne, Switzerland. (d) 3.2 mm ZrO_2 and sapphire (α-Al_2O_3) rotors used for DNP NMR experiments.*

A brief summary of the principal parts of instrumentation is given below *via* reference to the annotated photographs in Figure 3.21.

NMR magnet (Figure 3.21(a)): these are very similar to conventional wide bore solid-state NMR magnets. However, additionally they are equipped with sweep coils to enable the use of a range of polarising agents, for direct DNP experiments involving nuclei other than ^{1}H, and investigating polarisation transfer mechanisms.[109,110,112]

Commercial Bruker DNP NMR magnets are available in three B_0 field strengths of 9.4 T, 14.1 T and 18.8 T.[107]

Gyrotron (Figure 3.21(a)): this is the instrument that generates the high power microwaves required for polarisation transfer from unpaired electrons to nuclei, and consists of a gyrotron tube sealed inside a strong magnetic field. Gyrotrons operate by transferring energy from an electron beam to an electromagnetic wave.[108] Commercial gyrotrons are available in 4.8, 7.2 and 9.7 T magnetic field strengths, and current models do not require cryogenic liquid cooling.[107]

Microwave transmission line (Figure 3.21(a)): also called a waveguide, this consists of a series of interconnected aluminium tubes. Its purpose is to channel microwaves from the gyrotron to the sample under study inside the NMR probe. This is accomplished *via* a mirror optics box at the probe end of the transmission line.[113]

Low temperature magic angle spinning (LT MAS) unit (Figure 3.21(b)): as DNP NMR experiments typically take place at ~100 K, it is necessary to be able to perform stable MAS at this temperature. Commercial DNP LT MAS units are similar to that designed by Levitt and co-workers.[114] A stream of N_2 gas is passed through a heat exchange dewar filled with liquid nitrogen and sent to the NMR probe *via* an insulated transfer line and a variable temperature (VT) bore/probe insert. In order to reduce thermal losses, bearing and drive N_2 gas streams for MAS are cooled by bringing them into thermal contact with the cold VT gas.

LT MAS probe (Figure 3.21(c)): from an NMR perspective, the LT MAS probes operate in a similar manner to their room temperature (RT) equivalents. Unlike RT probes, they contain additional apparatus to accommodate the cooling of bearing and drive gas streams. Several designs exist,[114-117] but probes built by Bruker Biospin are based on that of Griffin and co-workers,[117] and allow for the insertion and ejection of rotors without warming up to RT beforehand. The majority of DNP probes are designed for 3.2 mm rotors, although the introduction of a commercial 1.9 mm LT MAS probe for DNP applications has recently been announced.[107]

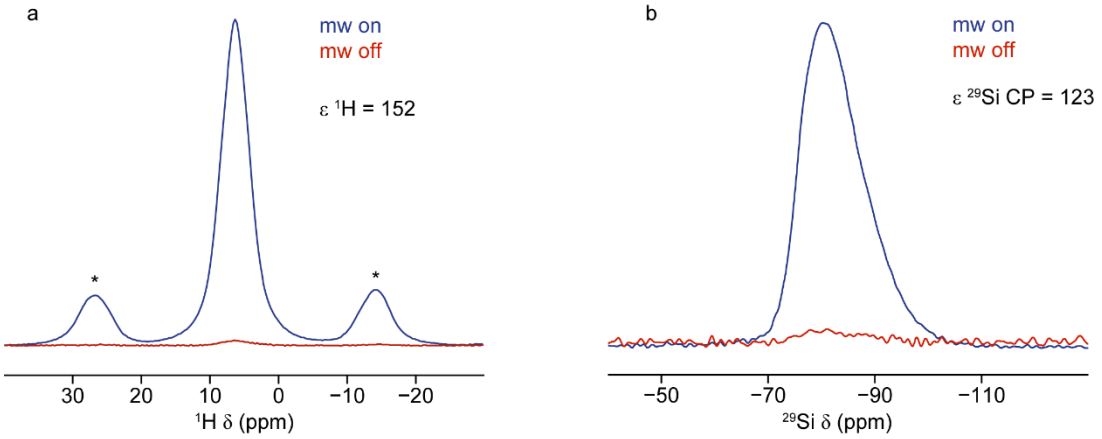

Figure 3.22. *(a) ^{1}H (9.4 T, 8 kHz MAS) DNP NMR spectrum of a 14 mM solution of TEKPol in 1,1,2,2-tetrachloroethane (TCE), impregnated onto ^{29}Si-γ-Al_2O_3 (1.5 wt% Si). * denotes a spinning sideband. (b) ^{1}H-^{29}Si (9.4 T, 8 kHz MAS, τ_{CP} = 3.5 ms) DNP CP NMR spectrum of ^{29}Si-γ-Al_2O_3. For both sets of spectra, enhancement factors, ε, are given in the top right corner. All spectra were acquired at ~100 K. mw = microwaves.*

DNP NMR rotors (Figure 3.21(d)): two types of 3.2 mm rotors can be utilised for solid-state DNP NMR experiments. Transparent rotors, machined from single crystals of synthetic sapphire (α-Al_2O_3), are generally preferred over ZrO_2 rotors, due to their higher thermal conductivity and their greater microwave transparency.[117] However, for ^{27}Al NMR experiments, ZrO_2 rotors should be used in order to avoid interference from the ^{27}Al background NMR signal from sapphire.[118] Rotor inserts are used to ensure that the radical/solvent matrix is contained in the rotor, and that the sample receives efficient rf and microwave irradiation.

3.2.4.3 Acquisition of DNP NMR Spectra

DNP has become well-known in the field of solid-state NMR spectroscopy for the signal enhancement it can provide *versus* conventional techniques.[90] As mentioned in Chapter 2, signal enhancement is usually denoted by ε. Where nuclei other than ^{1}H are being observed in an experiment, the enhancement factor is usually given in the form of, for example, "ε ^{27}Al CP = 20".[119] Variations in the magnitude of ε have been reported, ranging from 20 for ^{27}Al DNP NMR experiments on γ-Al_2O_3[119] to over 200 for ^{29}Si NMR analysis of mesoporous silica containing propyl azide species bound to

its surface.[120] It is important to note that ε does not reflect an enhancement over an equivalent conventional solid-state NMR experiment. Rather, it represents the gain in sensitivity obtained by the application of microwaves to the sample residing in the DNP NMR spectrometer. This is illustrated in Figure 3.22(a), which shows ^{1}H DNP NMR spectra of a 14 mM solution of TEKPol in1,1,2,2-tetrachloroethane (TCE),[120] impregnated onto ^{29}Si-γ-Al_2O_3. When microwaves are applied, a large signal enhancement of the TCE resonance (^{1}H δ = 6.2 ppm) is observed. A slightly reduced ε is obtained upon CP from ^{1}H to ^{29}Si in Si-γ-Al_2O_3, as shown in Figure 3.22(b). The overall enhancement remains significant though, allowing for the acquisition of 2D experiments, as detailed in Chapter 6 of this work. De Paëpe and co-workers[121] and Rossini *et al.*[122] argue that ε should be treated with a measure of caution, and that signal-to-noise ratio (S/N) per unit of time be used to quantify DNP enhancements instead. Both sets of researchers have introduced different methods in order to accomplish this goal. De Paëpe and co-workers propose the use of an "absolute sensitivity ratio" (ASR). This parameter is determined experimentally by comparing the S/N per unit square root of time between a DNP NMR experiment and a similar, conventional solid-state NMR experiment.[121] Rossini *et al.* advocate using the "overall sensitivity enhancement" (Σ) to assess DNP enhancements. The overall sensitivity enhancement is defined as

$$\Sigma = (\varepsilon)\,(\theta)\,\sqrt{\kappa}\,, \qquad (3.13)$$

where ε is the DNP enhancement factor, θ is the parameter which quantifies reduction of the NMR signal by paramagnetic effects (the "quenching factor"), and κ is the ratio of the nuclear T_1 relaxation times of nuclei in a dry sample and nuclei in a sample impregnated with radical solution.[122]

3.3 References

1. T. D. W. Claridge, *High-Resolution NMR Techniques in Organic Chemistry*, Elsevier, Amsterdam, 3rd Edn., 2016.

2. S. E. Ashbrook, D. M. Dawson and J. M. Griffin, in *Local Structural Characterisation*, Eds. D. W. Bruce, D. O'Hare and R. I. Walton, Wiley, Chichester, 2014.
3. E. R. Andrew, A. Bradbury and R. G. Eades, *Nature*, 1958, **182**, 1659.
4. I. J. Lowe, *Phys. Rev. Lett.*, 1959, **2**, 285.
5. Y. Q. Ye, M. Malon, C. Martineau, F. Taulelle and Y. Nishiyama, *J. Magn. Reson.*, 2014, **239**, 75.
6. D. C. Apperley, R. K. Harris and P. Hodgkinson, *Solid-State NMR: Basic Principles & Practice*, Momentum Press, New York, 2012.
7. R. N. Zare, *Angular Momentum: Understanding Spatial Aspects in Chemistry and Physics*, Wiley, Chichester, 1988.
8. J. D. Roberts, *ABCs of FT-NMR*, University Science Books, Sausalito, 2000.
9. E. L. Hahn, *Phys. Rev.*, 1950, **80**, 580.
10. S. R. Hartmann and E. L. Hahn, *Phys. Rev.*, 1962, **128**, 2042.
11. A. Pines, M. G. Gibby and J. S. Waugh, *J. Chem. Phys.*, 1972, **56**, 1776.
12. E. O. Stejskal, J. Schaefer and J. S. Waugh, *J. Magn. Reson.*, 1977, **28**, 105.
13. B. H. Meier, *Chem. Phys. Lett.*, 1992, **188**, 201.
14. A. Pines, M. G. Gibby and J. S. Waugh, *J. Chem. Phys.*, 1973, **59**, 569.
15. A. J. Vega, *Solid State Nucl. Magn. Reson.*, 1992, **1**, 17.
16. A. J. Vega, *J. Magn. Reson.*, 1992, **96**, 50.
17. V. I. Bakhmutov, *Chem. Rev.*, 2011, **111**, 530.
18. T. H. Walter, G. L. Turner and E. Oldfield, *J. Magn. Reson.*, 1988, **76**, 106.
19. T. H. Walter and E. Oldfield, *J. Phys. Chem.*, 1989, **93**, 6744.
20. D. H. Morris and P. D. Ellis, *J. Am. Chem. Soc.*, 1989, **111**, 6045.
21. J. Rocha, S. W. Carr and J. Klinowski, *Chem. Phys. Lett.*, 1991, **187**, 401.
22. D. M. de Wilmar, O. Clause and J.-B. d'Espinose de la Caillerie, *J. Phys. Chem. B*, 1998, **102**, 7023.
23. K. A. Denkenberger, R. A. Bowers, A. D. Jones and K. T. Mueller, *Langmuir*, 2007, **23**, 8855.
24. R. Wischert, P. Florian, C. Copéret, D. Massiot and P. Sautet, *J. Phys. Chem. C*, 2014, **118**, 15292.

25. R. R. Ernst, G. Bodenhausen and A. Wokaun, *Principles of Nuclear Magnetic Resonance in One and Two Dimensions*, Clarendon Press, Oxford, 1987.
26. M. Ernst, *J. Magn. Reson.*, 2003, **162**, 1.
27. A. E. Bennett, C. M. Rienstra, M. Auger, K. V. Lakshmi and R. G. Griffin, *J. Chem. Phys.*, 1995, **103**, 6951.
28. B. M. Fung, A. K. Khitrin and K. Ermolaev, *J. Magn. Reson.*, 2000, **142**, 97.
29. A. Detken, E. H. Hardy, M. Ernst and B. H. Meier, *Chem. Phys. Lett*., 2002, **56**, 298.
30. M. Weingarth, P. Tekely and G. Bodenhausen, *Chem. Phys. Lett.*, 2008, **466**, 247.
31. G. de Paëpe, P. Hodgkinson and L. Emsley, *Chem. Phys. Lett*., 2003, **376**, 259.
32. L. Delevoye, C. Fernandez, C. M. Morais, J.-P. Amoureux, V. Montouillout and J. Rocha, *Solid State Nucl. Magn. Reson.*, 2002, **22**, 501.
33. M. Lee and W. Goldburg, *Phys. Rev.*, 1965, **140**, 1261.
34. J. S. Waugh, L. Huber and U. Haeberlen, *Phys. Rev. Lett.*, 1968, **20**, 180.
35. U. Haeberlen and J. S. Waugh, *Phys. Rev.*, 1968, **175**, 453.
36. M. Mehring and J. S. Waugh, *Phys. Rev. B*, 1972, **5**, 3459.
37. B. C. Gerstein, R. G. Pembleton, R. C. Wilson and L. M. Ryan, *J. Chem. Phys.*, 1977, **66**, 361.
38. E. Vinogradov, P. K. Madhu and S. Vega, *Chem. Phys. Lett.*, 1999, **314**, 443.
39. A. Bielecki, A. Kolbert and M. H. Levitt, *Chem. Phys. Lett.*, 1989, **155**, 341.
40. D. Sakellariou, A. Lesage, P. Hodgkinson and L. Emsley, *Chem. Phys. Lett.*, 2000, **319**, 253.
41. B. Elena, G. De Paëpe and L. Emsley, *Chem. Phys. Lett.*, 2004, **398**, 532.
42. E. Salanger, R. S. Stein, S. Steuernagel, A. Lesage, B. Elena and L. Emsley, *Chem. Phys. Lett.*, 2009, **469**, 336.
43. E. Salanger, J.-N. Dumez, R. S. Stein, S. Steuernagel, A. Lesage, B. Elena-Herrmann and L. Emsley, *Chem. Phys. Lett.*, 2010, **498**, 214.
44. E. Vinogradov, P. K. Madhu and S. Vega, *Chem. Phys. Lett.*, 2002, **354**, 193.
45. M. Leskes, P. K. Madhu and S. Vega, *Chem. Phys. Lett.*, 2007, **447**, 370.
46. J. Brus and A. Jegorov, *J. Phys. Chem. A*, 2004, **108**, 3955.
47. G. A. Morris and R. Freeman, *J. Am. Chem. Soc.*, 1979, **101**, 760.

48. G. A. Morris, *J. Am. Chem. Soc.*, 1980, **102**, 428.
49. D. T. Pegg, D. M. Doddrell, W. M. Brooks and M. R. Bendall, *J. Magn. Reson.*, 1981, **44**, 32.
50. C. A. Fyfe, K. C. Wong-Moon, Y. Huang and H. Grondey, *J. Am. Chem. Soc.*, 1995, **117**, 10397.
51. C. Coelho, T. Azaïs, L. Bonhomme-Coury, G. Laurent and C. Bonhomme, *Inorg. Chem.*, 2007, **46**, 1379.
52. Y. Morizet, R. Vuilleumier and M. Paris, *Chem. Geol.*, 2015, **418**, 89.
53. E. De Vita and L. Frydman, *J. Magn. Reson.*, 2001, **148**, 327.
54. Z. Gan, *J. Magn. Reson.*, 2007, **184**, 39.
55. C. A. Fyfe, K. T. Mueller, H. Grondey and K. C. Wong-Moon, *Chem. Phys. Lett.*, 1992, **199**, 198.
56. M. Valla, A. J. Rossini, M. Caillot, C. Chizallet, P. Raybaud, M. Digne, A. Chaumonnot, A. Lesage, L. Emsley, J. A. van Bokhoven and C. Copéret, *J. Am. Chem. Soc.*, 2015, **137**, 10710.
57. L. A. O'Dell, P. Guerry, A. Wong, E. A. Abou Neel, T. N. Pham, J. C. Knowles, S. P. Brown and M. E. Smith, *Chem. Phys. Lett.*, 2008, **455**, 178.
58. A. Lesage, M. Bardet and L. Emsley, *J. Am. Chem. Soc.*, 1999, **121**, 10987.
59. S. Cadars, J. Sein, L. Duma, A. Lesage, T. N. Pham, J. H. Baltisberger, S. P. Brown and L. Emsley, *J. Magn. Reson.*, 2007, **188**, 24.
60. H. W. Spiess, *eMagRes*, 2012, **1**, 1.
61. W. Sommer, J. Gottwald, D. E. Demco and H. W. Spiess, *J. Magn. Reson. A*, 1995, **113**, 131.
62. M. Feike, D. E. Demco, R. Graf, J. Gottwald, S. Hafner and H. W. Spiess, *J. Magn. Reson. A*, 1996, **122**, 214.
63. C. Martineau, C. Legein, J.-Y. Buzaré and F. Fayon, *Phys. Chem. Chem. Phys.*, 2009, **11**, 950.
64. M. Hohwy, H. J. Jakobsen, M. Eden, M. H. Levitt and N. C. Nielsen, *J. Chem. Phys.*, 1998, **108**, 2686.
65. R. Tycko and G. Dabbagh, *Chem. Phys. Lett.*, 1990, **173**, 461.
66. R. Verel, M. Baldus, M. Ernst and B. H. Meier, *Chem. Phys. Lett.*, 1998, **287**, 421.

67. T. Guillion and J. Schaefer, *J. Magn. Reson.*, 1989, **81**, 196.
68. H. Y. Carr and E. M. Purcell, *Phys. Rev.*, 1954, **94**, 630.
69. S. Meiboom and D. Gill, *Rev. Sci. Instrum.*, 1958, **29**, 688.
70. K. K. Dey, J. T. Ash, N. M. Trease and P. J. Grandinetti, *J. Chem. Phys.*, 2010, **133**, 054501.
71. F. H. Larsen, H. J. Jakobsen, P. D. Ellis and N.C. Nielsen, *J. Magn. Reson.*, 1998, **131**, 144.
72. Z. Gan, P. Gor'kov, T. A. Cross, A. Samoson and D. Massiot, *J. Am. Chem. Soc.*, 2002, **124**, 5634.
73. K. Hashia, S. Ohkia, S. Matsumotoa, G. Nishijimaa, A. Gotoa, K. Deguchia, K. Yamadaa, T. Noguchia, S. Sakaia, M. Takahashib, Y. Yanagisawab, S. Iguchib, T. Yamazakib, H. Maedab, R. Tanakad, T. Nemotod, H. Suematsud, T. Mikie, K. Saitoe and T. Shimizua, *J. Magn. Reson.*, 2015, **256**, 30.
74. A. Samoson, E. Lippmaa and A. Pines, *Mol. Phys.*, 1988, **65**, 1013.
75. A. Llor and J. Virlet, *Chem. Phys. Lett.*, 1988, **152**, 248.
76. L. Frydman and J. S. Harwood, *J. Am. Chem. Soc.*, 1995, **117**, 5367.
77. D. Iuga, H. Schäfer, R. Verhagen and A. P. M. Kentgens, *J. Magn. Reson.*, 2000, **147**, 192.
78. K. H. Lim, T. Charpentier and A. Pines, *J. Magn. Reson.*, 2002, **154**, 196.
79. H. Colaux, D. M. Dawson and S. E. Ashbrook, *J. Phys. Chem. A*, 2014, **118**, 6018.
80. A. Medek, J. S. Harwood and L. Frydman, *J. Am. Chem. Soc.*, 1995, **117**, 12779.
81. J. P. Amoureux, C. Fernandez and S. Steuernagel, *J. Magn. Reson. A*, 1996, **123**, 116.
82. K. J. Pike, R. P. Malde, S. E. Ashbrook, J. McManus and S. Wimperis, *Solid State Nucl. Magn. Reson.*, 2000, **16**, 203.
83. D. Massiot, B. Touzo, D. Trumeau, J. P. Coutures, J. Virlet, P. Florian and P. J. Grandinetti, *Solid State Nucl. Magn. Reson.*, 1996, **6**, 73.
84. S. P. Brown and S. Wimperis, *J. Magn. Reson.*, 1997, **128**, 42.
85. G. Czjzek, J. Fink, F. Gotz, H. Schmidt, J. M. D. Coey, J. P. Rebouillat and A. Lienard, *Phys. Rev. B*, 1981, **23**, 2513.

86. (a) D. Massiot, F. Fayon, M. Capron, I. King, S. Le Calvé, B. Alonso, J.-O. Durand, B. Bujoli, Z. Gan and G. Hoatson, *Magn. Reson. Chem.* 2002, **40**, 70. (b) D. R. Neuville, L. Cormier and D. Massiot, *Geochim. Cosmochim. Acta*, 2004, **68**, 5071.
87. G. Engelhardt, A. P. M. Kentgens, H. Koller and A. Samoson, *Solid State Nucl. Magn. Reson.*, 1999, **15**, 171.
88. Z. Gan, *J. Am. Chem. Soc.*, 2000, **122**, 3242.
89. S. E. Ashbrook and S. Wimperis, *Prog. Nucl. Magn. Reson. Spectrosc.*, 2004, **45**, 53.
90. Q. Z. Ni, E. Daviso, T. V. Can, E. Markhasin, S. K. Jawla, T. M. Swager, R. J. Temkin, J. Herzfeld and R. G. Griffin, *Acc. Chem. Res.*, 2013, **46**, 1933.
91. A. C. Pinon, A. J. Rossini, C. M. Widdifield, D. Gajan and L. Emsley, *Mol. Pharmaceutics*, 2015, **12**, 4146.
92. M. Rosay, A-C. Zeri, N. S. Astrof, S. J. Opella, J. Herzfeld and R. G. Griffin, *J. Am. Chem. Soc.*, 2001, **123**, 1010.
93. P. C. A. van der Wel, K. N. Hu, J. Lewandowski and R. G. Griffin, *J. Am. Chem. Soc.*, 2006, **128**, 10840.
94. A. B. Barnes, B. Corzilius, M. L. Mak-Jurkauskas, L. B. Andreas, V. S. Bajaj, Y. Matsuki, M. L. Belenky, J. Lugtenburg, J. R. Sirigiri, R. J. Temkin, J. Herzfeld and R. G. Griffin, *Phys. Chem. Chem. Phys.*, 2010, **12**, 5861.
95. Y. Hovav, A. Feintuch and S. Vega, *J. Chem. Phys.*, 2011, **134**, 074509.
96. Y. Hovav, A. Feintuch and S. Vega, *J. Magn. Reson.*, 2012, **214**, 29.
97. A. Lesage, M. Lelli, D. Gajan, M. A. Caporini, V. Vitzthum, P. Mieville, J. Alazun, A. Roussey, C. Thieuleux, A. Mehdi, G. Bodenhausen, C. Copéret and L. Emsley, *J. Am. Chem. Soc.*, 2010, **132**, 15459.
98. T. Maly, G. T. Debelouchina, V. S. Bajaj, K-N. Hu, C-G. Joo, M. L. Mak-Jurkauskas, J. R. Sirigiri, P. C. A. van der Wel, J. Herzfeld, R. J. Temkin and R. G. Griffin, *J. Chem. Phys.*, 2008, **128**, 052211.
99. K. N. Hu, C. Song, H. H. Yu, T. M. Swager and R. G. Griffin, *J. Chem. Phys.*, 2008, **128**, 052302.

100. M. Rosay, L. Tometich, S. Pawsey, R. Bader, R. Schauwecker, M. Blank, P. M. Borchard, S. R. Cauffman, K. L. Felch, R. T. Weber, R. J. Temkin, R. G. Griffin and W. E. Maas, *Phys. Chem. Chem. Phys.*, 2010, **12**, 5850.
101. A. Zagdoun, A. J. Rossini, M. P. Conley, W. R. Grüning, M. Schwarzwälder M. Lelli, W. T. Franks, H. Oschkinat, C. Copéret, L. Emsley and A. Lesage, *Angew. Chem. Int. Ed.*, 2013, **52**, 1222.
102. U. Akbey, W. T. Franks, A. Linden, S. Lange, R. G. Griffin, B-J. van Rossum and H. Oschkinat, *Angew. Chem. Int. Ed.*, 2010, **49**, 7803.
103. A. Zagdoun, A. J. Rossini, D. Gajan, A. Bourdolle, O. Ouari, M. Rosay, W. E. Maas, P. Tordo, M. Lelli, L. Emsley, A. Lesage and C. Copéret, *Chem. Commun.*, 2012, **48**, 654.
104. L. R. Becerra, G. J. Gerfen, R. J. Temkin, D. J. Singel and R. G. Griffin, *Phys. Rev. Lett.*, 1993, **71**, 3561.
105. L. R. Becerra, G. J. Gerfen, B. F. Bellew, J. A. Bryant, D. A. Hall, S. J. Inati, R. T. Weber, S. Un, T. F. Prisner, A. E. Mcdermott, K. W. Fishbein, K. E. Kreischer, R. J. Temkin, D. J. Singel and R. G. Griffin, *J. Magn. Reson. A*, 1995, **117**, 28.
106. V. Weis, M. Bennati, M. Rosay, J. A. Bryant and R. G. Griffin, *J. Magn. Reson.*, 1999, **140**, 293.
107. DNP-NMR, https://www.bruker.com/products/mr/nmr/dnp-nmr, (accessed March 2017).
108. M. Rosay, M. Blank and F. Engelke, *J. Magn. Reson.*, 2016, **264**, 88.
109. Y. Matsuki, H. Takahashi, K. Ueda, T. Idehara, I. Ogawa, M. Toda, H. Akutsua and T. Fujiwara, *Phys, Chem. Chem. Phys.*, 2010, **12**, 5799.
110. Y. Matsukia, T. Ideharab, J. Fukazawaa and T. Fujiwara, *J. Magn. Reson.*, 2016, **264**, 107.
111. A. A. Smith, B. Corzilius, J. A. Bryant, R. DeRocher, P. P. Woskov, R. J. Temkin and R. G. Griffin, *J. Magn. Reson.*, 2012, **223**, 170.
112. T. Maly, J. Bryant, D. Ruben and R. G. Griffin, *J. Magn. Reson.*, 2006, **183**, 303.
113. P. P. Woskov, V. S. Bajaj, M. K. Hornstein, R. J. Temkin and R. G. Griffin, *IEEE Trans. Microw. Theory Tech.*, 2005, **53**, 1863.

114. M. Concistrè, O. G. Johannessen, E. Carignani, M. Geppi and M. H. Levitt, *Acc. Chem. Res.*, 2013, **46**, 1914.
115. A. Samoson, T. Tuherm, J. Past, A. Reinhold, T. Anupõld and I. Heinmaa, *Top. Curr. Chem.*, 2004, **246**, 15.
116. K. R. Thurber and R. Tycko, *J. Magn. Reson.*, 2008, **195**, 179.
117. A. B. Barnes, M. L. Mak-Jurkauskas, Y. Matsuki, V. S. Bajaj, P. C. A. van der Wel, R. DeRocher, J. Bryant, J. R. Sirigiri, R. J. Temkin, J. Lugtenburg, J. Herzfeld and R. G. Griffin, *J. Magn. Reson.*, 2009, **198**, 261.
118. F. Pourpoint, A. S. L. Thankamony, C. Volkringer, T. Loiseau, J. Trébosc, F. Aussenac, D. Carnevale, G. Bodenhausen, H. Vezin, O. Lafon and J-P. Amoureux, *Chem. Commun.*, 2014, **50**, 933.
119. V. Vitzthum, P. Miéville, D. Carnevale, M. A. Caporini, D. Gajan, C. Copéret, M. Lelli, A. Zagdoun, A. J. Rossini, A. Lesage, L. Emsley and G. Bodenhausen, *Chem. Commun.*, 2012, **48**, 1988.
120. A. Zagdoun, G. Casano, O. Ouari, M. Schwarzwalder, A. J. Rossini, F. Aussenac, M. Yulikov, G. Jeschke, C. Coperet, A. Lesage, P. Tordo and L. Emsley, *J. Am. Chem. Soc.*, 2013, **135**, 12790.
121. H. Takahashi, C. Fernández-de-Alba, D. Lee, V. Maurel, S. Gambarelli, M. Bardet, S. Hediger, A-L. Barra and G. De Paëpe, *J. Magn. Reson.*, 2014, **239**, 91.
122. A. J. Rossini, A. Zagdoun, M. Lelli, D. Gajan, F. Rascón, M. Rosay, W. E. Maas, C. Copéret, A. Lesage and L. Emsley, *Chem. Sci.*, 2012, **3**, 108.

Chapter 4. Sample Preparation and Experimental Details

In this chapter, details are provided for each of the solid-state NMR and DNP NMR experiments for all the projects that have been undertaken in this work. Information on the origin and/or preparation of samples that have been studied in this thesis are also provided. Details of ^{17}O enrichment procedures are also given.

4.1 General Solid-State NMR Experimental Details

Solid-state NMR spectra were acquired using Bruker Avance III spectrometers, equipped with 9.4 T, 14.1 T or 20.0 T widebore magnets operating at Larmor frequencies of 400.13 MHz, 600.13 or 850.13 MHz for ^{1}H, respectively. Powdered samples were packed into 1.3, 1.9, 3.2 or 4 mm ZrO_2 rotors and rotated at MAS rates of between 10 and 55 kHz, using conventional double or triple resonance probes. Additional experimental details are provided in the extended figure captions in Appendix A. Chemical shifts are shown (quoted in ppm) relative to primary reference standards,[1] measured using secondary references, as described in Appendix B. Calibration of ^{17}O 3QMAS experiments performed in Chapter 6 was carried out using either ^{17}O-enriched amorphous SiO_2 (provided by Miss Giulia Bignami, St Andrews), or 75% ^{17}O-enriched orthoenstatite ($MgSiO_3$) (courtesy of Dr Andrew Berry, Australian National University). The facility manager at St Andrews, Dr Daniel Dawson, is thanked for experimental assistance. Spectra acquired at 20.0 T were recorded at the UK 850 MHz solid-state NMR facility, which was funded by EPSRC and BBSRC (contract reference PR140003), as well as the University of Warwick including *via* part funding through Birmingham Science City Advanced Materials Projects 1 and 2 supported by Advantage West Midlands (AWM) and the European Regional Development Fund (ERDF). Collaborative assistance from the 850 MHz Facility Manager (Dr Dinu Iuga, University of Warwick) is acknowledged. The contribution of Mr Bonifác Légrády (St Andrews) to some of the experiments presented in Chapter 6 is also acknowledged.

DNP NMR experiments were performed using either a Bruker Avance I (Ecole Polytechnique Fédérale de Lausanne (EPFL), Switzerland) or a Bruker Avance III spectrometer (DNP MAS NMR Facility, University of Nottingham, UK). The spectrometer at EPFL was equipped with a 9.4 T widebore magnet operating at a Larmor frequency of 400.21 MHz for ^{1}H. A 9.7 T gyrotron magnet was utilised for the generation of microwaves, operating at a frequency of 263 GHz. Professor Lyndon Emsley is thanked for facilitating the use of the spectrometer in Lausanne, along with his postdoctoral researchers, Dr Brennan Walder and Dr Jasmine Viger-Gravel, who provided valuable insights and assistance. The spectrometer at the University of Nottingham was equipped with a 14.1 T widebore magnet operating at a Larmor frequency of 600.13 MHz for ^{1}H. A 7.2 T gyrotron magnet was utilised for the generation of microwaves, operating at a frequency of 395 GHz. The assistance of the facility manager, Dr Subhradip Paul (University of Nottingham), is acknowledged. Dr Jeremy Titman (University of Nottingham) is also thanked for helpful discussions. On both DNP NMR instruments, the field of the NMR magnet was set such that microwave irradiation occurred at the ^{1}H positive enhancement maximum of nitroxide biradicals. Incipient wetness impregnation of powdered samples (~25 mg) was performed with a solution (16-24 μl) of the nitroxide biradical polarizing agent TEKPol[2] in 1,1,2,2-tetrachloroethane (TCE)[3] (14-20 mM). Impregnated samples were packed into 3.2 mm sapphire or ZrO_2 rotors, and frozen at 100 K inside a 3.2 mm triple resonance LT MAS probe using dry N_2 as the bearing and drive gas. Samples were typically subjected to multiple thawing cycles by ejecting the sample into the catcher in the room temperature region of the probe, in order to minimise the amount of oxygen in the biradical solution (which would decrease DNP enhancements).[4,5] Samples were rotated at MAS rates between 8 and 13.2 kHz. Chemical shifts are shown (in ppm) relative to an internal reference of of TCE (^{1}H δ = 6.2 ppm)[6,7] for 9.4 T spectra, and relative to primary reference standards,[1] measured using secondary references (spectra were acquired at ~298 K), for 14.1 T spectra (see Appendix B for more details).

Offline processing of experimental NMR spectra was performed using Bruker TopSpin 3.5 or DMFit.[8] Fits of spectra were obtained with the Solid Lineshape Analysis (SOLA) module within Bruker TopSpin 3.5, or *via* DMFit,[8] which includes

implementation of the Czjzek distribution of the EFG and a Gaussian distribution of δ_{iso}[9] to model quadrupolar NMR spectra of disordered samples.[10]

4.2 Sample Details

4.2.1 Chapter 1

L-alanine was obtained from Sigma-Aldrich and used without further purification. Samples of the silicon phosphate material and Zeolite USY were provided by Sasol UK Ltd. TiO_2 (anatase) and MgO were acquired from Sigma-Aldrich and ^{17}O enriched according to the procedures outlined later in this chapter.

4.2.2 Chapter 2

L-alanine was obtained from Sigma-Aldrich and used without further purification.

4.2.3 Chapter 3

L-alanine, glycine, 1[^{13}C]-glycine and $RbNO_3$ were obtained from Sigma-Aldrich and used without further purification. SnO_2 was acquired from Fisher Chemical and used as-received. γ-Al_2O_3 was obtained from Sasol UK Ltd. A sample of this material was partially dehydrated by heating it *in vacuo* at 150 °C for ~24 h. Further samples of γ-Al_2O_3 were ^{17}O enriched according to the procedure outlined later in this chapter. U[^{13}C]-L-alanine was obtained from Isotec Ltd and used as-received. $K_7Na[Nb_6O_{19}]$ was provided by Professor Richard Walton (University of Warwick). ^{29}Si-γ-Al_2O_3 (1.5 wt% Si) was prepared according to the procedure outlined in subsection 4.2.6 below. Details of wet impregnation of this material with DNP radical/solvent solutions are also given in that subsection.

4.2.4 Chapter 5

γ-Al_2O_3 was obtained from Sasol UK Ltd. Co-γ-Al_2O_3 and Co-Si-γ-Al_2O_3 materials were prepared according to the procedures briefly described below.

COLL10: Co_3O_4 supported on γ-Al_2O_3 (10 wt% Co). This material was prepared by a colloidal route,[11] using $Co(NO_3)_2{\cdot}6H_2O$ combined with a surfactant. Pt (0.1 wt%) was also introduced (using $Pt(NH_3)_4(NO_3)_2$) as a promoter.[12] Calcination was carried out in NO (1% NO/He, 250 °C for 6 h, ramp rate of 1 °C min^{-1}). The average Co_3O_4 crystallite size was <5 nm.

IW5: Co_3O_4 supported on γ-Al_2O_3 (5.4 wt% Co). This material was prepared by incipient wetness methods,[13] using $Co(NO_3)_2{\cdot}6H_2O$. Pt (0.1 wt%) was also introduced (using $Pt(NH_3)_4(NO_3)_2$) as a promoter.[12] Calcination was carried out in NO (1% NO/He, 250 °C for 6 h, ramp rate of 1 °C min^{-1}). The average Co_3O_4 crystallite size was <5 nm.

IW17: Co_3O_4 supported on Si-γ-Al_2O_3 (1.5 wt% Si) (17 wt% Co). This material was prepared by incipient wetness methods,[13] using $Co(NO_3)_2{\cdot}6H_2O$. Pt (0.1 wt%) was also introduced (using $Pt(NH_3)_4(NO_3)_2$) as a promoter.[12] Calcination was carried out in NO (1% NO/He, 250 °C for 6 h, ramp rate of 1 °C min^{-1}). The average Co_3O_4 crystallite size was 15-16 nm.

IW21: Co_3O_4 supported on Si-γ-Al_2O_3 (1.5 wt% Si) (21 wt% Co). This material was prepared by incipient wetness methods,[13] using $Co(NO_3)_2{\cdot}6H_2O$. Pt (0.1 wt%) was also introduced (using $Pt(NH_3)_4(NO_3)_2$) as a promoter.[12] Calcination was carried out in NO (1% NO/He, 250 °C for 6 h, ramp rate of 1 °C min^{-1}). The average Co_3O_4 crystallite size was 15-16 nm.

Series Two:

IWN020: Co_3O_4 supported on γ-Al_2O_3 (20 wt% Co). This material was prepared by incipient wetness methods,[13] using $Co(NO_3)_2{\cdot}6H_2O$. 0.025 wt% Pt was also introduced (using $Pt(NH_3)_4(NO_3)_2$) as a promoter. Calcination was carried out in NO (1% NO/He, 250 °C for 6 h, ramp rate of 1 °C min^{-1}). The average Co_3O_4 crystallite size was <5 nm.

IWN010: Co_3O_4 supported on γ-Al_2O_3 (10 wt% Co). This material was prepared by incipient wetness methods,[13] using 1/2 the Co loading of IWN020 (using $Co(NO_3)_2{\cdot}6H_2O$). 0.0125 wt% Pt (using $Pt(NH_3)_4(NO_3)_2$) was also introduced as a promoter. Calcination was carried out in NO (1% NO/He, 250 °C for 6 h, ramp rate of 1 °C min^{-1}). The average Co_3O_4 crystallite size was <5 nm.

IWN05: Co_3O_4 supported on γ-Al_2O_3 (5 wt% Co). This material was prepared by incipient wetness methods,[13] using 1/4 the Co loading of IWN020 (using $Co(NO_3)_2{\cdot}6H_2O$). 0.00625 wt% Pt (using $Pt(NH_3)_4(NO_3)_2$) was also introduced as a promoter. Calcination was carried out in NO (1% NO/He, 250 °C for 6 h, ramp rate of 1 °C min^{-1}). The average Co_3O_4 crystallite size was <5 nm.

Mixtures of IWN020 and γ-Al_2O_3 were prepared by gently grinding together the two materials in different proportions, using a mortar and pestle (75:50 IWN020:γ-Al_2O_3, 50:50 IWN020:γ-Al_2O_3 and 25:75 IWN020:γ-Al_2O_3).

$CoAl_2O_4$-based materials were provided by Sasol UK Ltd. The preparation of these samples is briefly described below.

$CoAl_2O_4$: Co-γ-Al_2O_3 (6 wt% Co) was prepared by incipient wetness methods,[13] using $Co(NO_3)_2{\cdot}6H_2O$. Calcination was carried out in NO (1% NO/He, 250 °C for 6 h, ramp rate of 1 °C min^{-1}). This material was then heated at 1000 °C for 6 h in a muffle furnace to produce $CoAl_2O_4$.

Co-$CoAl_2O_4$: this material was prepared by incipient wetness impregnation[13] of the previous material ($CoAl_2O_4$), using $Co(NO_3)_2{\cdot}6H_2O$ (resulting in 20 wt% Co). Calcination was carried out in NO (1% NO/He, 250 °C for 6 h, ramp rate of 1 °C min^{-1}) to produce Co_3O_4 supported on $CoAl_2O_4$.

$MgAl_2O_4$ was obtained from Sigma-Aldrich and used without further purification. Phase identity was confirmed by powder X-ray diffraction (PXRD) (additional details are provided in Appendix E).

4.2.5 Chapter 6

γ-Al_2O_3 was obtained from Sasol UK Ltd. TiO_2 (anatase) was acquired from Sigma-Aldrich and used without further purification. Phase identity was confirmed by PXRD (additional details are provided in Appendix E). Titanium-modified alumina materials were provided by Sasol UK Ltd. The preparation of these samples is briefly described below.

Ti-γ-Al_2O_3: this material was prepared by a conventional wet impregnation procedure.[14] γ-Al_2O_3 (Sasol, 98%) was impregnated with $Ti(OCH(CH_3)_2)_4$ (Sigma-Aldrich, 97%) dissolved in ethanol. Samples were then dried at 60 °C *in vacuo* and subsequently calcined in air at 550 °C for 2 h (ramp rate of 10 °C min^{-1}).

Ti-Al M50: this material was prepared *via* the co-hydrolysis[15] of Al-hexanoate and Ti-hexanoate. Drying and calcination was performed in the same manner as for Ti-γ-Al_2O_3.

Aliquots of both of the above materials were ^{17}O-enriched according to the procedures outlined in section 4.3 below.

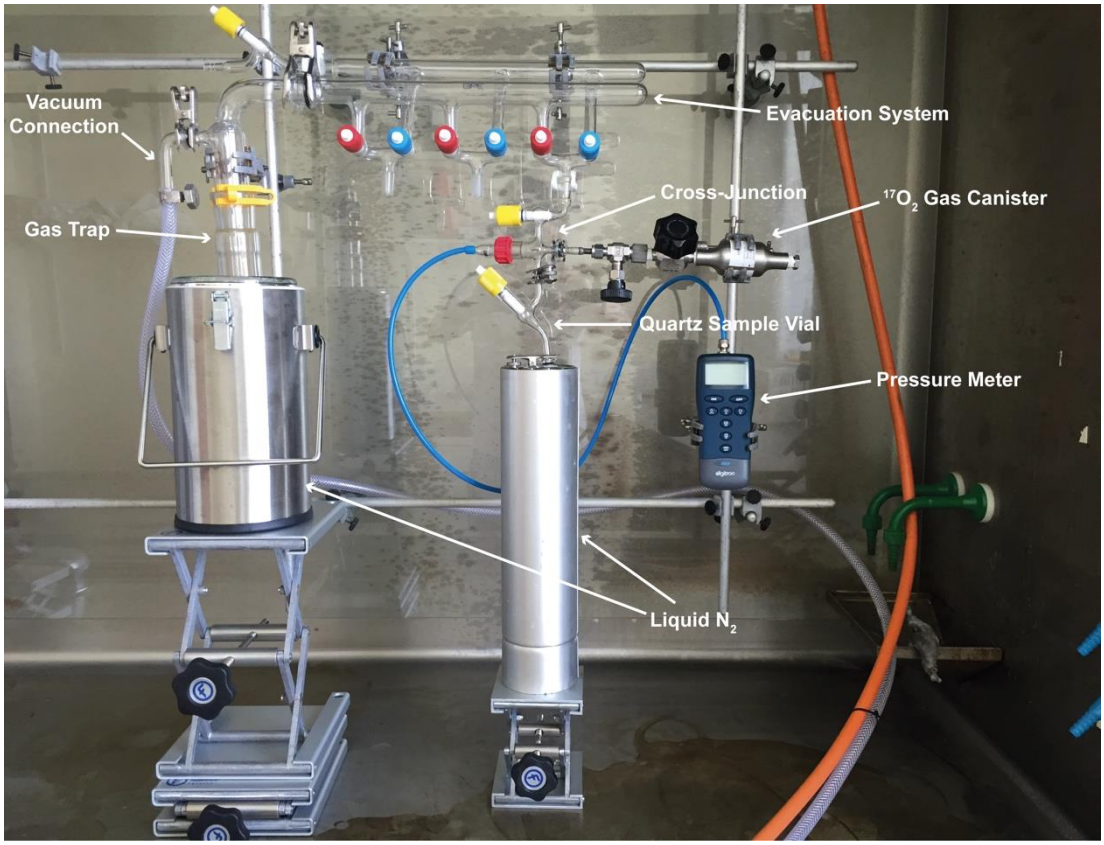

Figure 4.1. *Annotated photograph of the ^{17}O enrichment apparatus used to enrich the materials studied via ^{17}O solid-state NMR spectroscopy in this work.*

Preparation of the Si-γ-Al_2O_3 (1.5 wt% Si) material was carried out as follows: γ-Al_2O_3 (Sasol, 98%) was wet impregnated[16] with either conventional (Sigma-Aldrich, 98%) or 99% ^{29}Si-enriched (Cortecnet, >95%) tetraethyl orthosilicate (TEOS) dissolved in ethanol, in an inert (Ar) atmosphere. Samples were then dried at 60 °C *in vacuo* and subsequently calcined in air at 520 °C for 2 h (ramp rate of 10 °C min^{-1}). ^{29}Si-γ-Al_2O_3 with high silica loading (nominally 8 wt% Si) was prepared in the same way.

Si-γ-Al_2O_3 materials containing 2.8, 3.5 and 5.2 wt% Si were prepared by a multi-grafting approach,[16-19] in a manner similar to that described above, where the previous graft in the series was used as the starting material for the next graft. Samples were degassed at ~150 °C for a minimum of 12 h prior to wet impregnation. Final compositions of Si-γ-Al_2O_3 materials were confirmed by elemental analysis (ICP OES) and/or X-ray photoelectron spectroscopy (XPS). XPS experiments were carried out using a Kratos Axis Ultra-DLD photoelectron spectrometer (Sasol UK Ltd) with a

monochromatic Al K_α ($h\nu$ = 1486.6 eV) X-ray source, and the data were analysed using CasaXPS software. Dr Hervé Ménard (Sasol UK Ltd) is thanked for performing the XPS experiments and assisting with data processing and interpretation. Dr Paul Webb and Dr Hervé Ménard (Sasol UK Ltd) are thanked for their assistance with the preparation of the Si-γ-Al_2O_3 materials.

Dehydrated γ-Al_2O_3 and Si-γ-Al_2O_3 samples were dried *in vacuo* (150 or 300 °C, for durations of between ~6 and ~24 h) and subsequently packed into 4 mm ZrO_2 rotors in an inert (N_2) atmosphere.

Silica gel (grade 922, 200 mesh) was obtained from Sigma-Aldrich and was used as-received. Aliquots of γ-Al_2O_3, Si-γ-Al_2O_3 (1.5 wt% Si), Si-γ-Al_2O_3 (5.2 wt% Si) and ^{29}Si-enriched Si-γ-Al_2O_3 (1.5 wt% Si) were ^{17}O-enriched according to the procedures outlined in section 4.3 below. ^{17}O-enriched amorphous SiO_2 was provided by Miss Giulia Bignami (St Andrews).

4.3 ^{17}O Enrichment

As previously mentioned in Chapter 1, ^{17}O has a very low natural abundance (0.04%), which makes performing NMR experiments with this nucleus almost impossible on a reasonable timescale. Accordingly, in this work, materials studied by solid-state ^{17}O NMR spectroscopy have been ^{17}O-enriched *via* a post-synthetic gas exchange method similar to the one used by Grey and co-workers.[20] The assistance of Miss Arantxa Fernandes (St Andrews) with these procedures is gratefully acknowledged. Figure 4.1 shows the apparatus used for this type of enrichment. An O_2 gas canister, containing 70% $^{17}O_2$, is connected at one end of the cross junction, and a quartz vial containing ~100-200 mg of sample is attached at the other end. The system is then evacuated down to a pressure of <1 mbar. Once the apparatus has been checked for leakages, ^{17}O gas is allowed to flow into the sample vial under liquid N_2. This ensures that most of the gas condenses in the bottom part of the vial, where the sample resides. After an equilibration period, the quartz vial is then sealed, removed from the enrichment apparatus, and allowed to return to room temperature behind a safety shield. Finally,

it is heated in a furnace at the desired temperature and duration to allow $^{16}O/^{17}O$ exchange to occur. In this work, samples were heated at temperatures of between 300 and 700 °C for durations of between 6 and 48 h, using a ramp rate of 5 °C min^{-1}.

4.4 References

1. R. K. Harris, E. D. Becker, S. M. C. de Menezes, P. Granger, R. E. Hoffman and K. W. Zilm, *Pure Appl. Chem.*, 2008, **80**, 59.
2. A. Zagdoun, G. Casano, O. Ouari, M. Schwarzwälder, A. J. Rossini, F. Aussenac, M. Yulikov, G. Jeschke, C. Copéret, A. Lesage, P. Tordo and L. Emsley, *J. Am. Chem. Soc.*, 2013, **135**, 12790.
3. A. Zagdoun, A. J. Rossini, D. Gajan, A. Bourdolle, O. Ouari, M. Rosay, W. E. Maas, P. Tordo, M. Lelli, L. Emsley, A. Lesage and C. Copéret, *Chem. Commun.*, 2012, **48**, 654.
4. D. J. Kubicki, A. J. Rossini, A. Purea, A. Zagdoun, O. Ouari, P. Tordo, F. Engelke, A. Lesage and L. Emsley, *J. Am. Chem. Soc.*, 2014, **136**, 15711.
5. D. J. Kubicki, G. Casano, M. Schwarzwälder, S. Abel, C. Sauvée, K. Ganesan, M. Yulikov, A. J. Rossini, G. Jeschke, C. Copéret, A. Lesage, P. Tordo, O. Ouari and L. Emsley, *Chem. Sci.*, 2016, **7**, 550.
6. R. K. Harris, E. D. Becker, S. M. C. de Menezes, R. Goodfellow and P. Granger, *Pure Appl. Chem.*, 2001, **73**, 1795.
7. A. J. Rossini, C. M. Widdifield, A. Zagdoun, M. Lelli, M. Schwarzwälder, C. Copéret, A. Lesage and L. Emsley, *J. Am. Chem. Soc.*, 2014, **136**, 2324.
8. D. Massiot, F. Fayon, M. Capron, I. King, S. Le Calvé, B. Alonso, J.-O. Durand, B. Bujoli, Z. Gan and G. Hoatson, *Magn. Reson. Chem.* 2002, **40**, 70.
9. G. Czjzek, J. Fink, F. Gotz, H. Schmidt, J. M. D. Coey, J. P. Rebouillat and A. Lienard, *Phys. Rev. B*, 1981, **23**, 2513.
10. D. R. Neuville, L. Cormier and D. Massiot, *Geochim. Cosmochim. Acta*, 2004, **68**, 5071.
11. S. Sadasivan, R. M. Bellabarba and R. P. Tooze, *Nanoscale*, 2013, **5**, 11139.
12. G. Prieto, M. I. S. De Mello, P. Concepción, R. Murciano, S. B. C. Pergher and A. Martínez, *ACS Catal.*, 2015, **5**, 3323.

13. P. Munnik, P. E. de Jongh, and K. P. de Jong, *Chem. Rev.*, 2015, **115**, 6687.
14. J. B. Rosenholm, H. Rahiala, J. Puputti, V. Stathopoulos, P. Pomonis, I. Beurroies and K. Backfolk, *Colloids Surf. A*, 2004, **250**, 289.
15. C. Lahousse, F. Maugé, J. Bachelier and J-C. Lavalley, *J. Chem. Soc. Faraday Trans.*, 1995, **9**, 2907.
16. M. Caillot, A. Chaumonnot, M. Digne and J. A. van Bokhoven, *J. Catal.*, 2014, **316**, 47.
17. M. Caillot, A. Chaumonnot, M. Digne, C. Poleunis, D. P. Debecker and J. A. van Bokhoven, *Micropor. Mesopor. Mater.*, 2014, **185**, 179.
18. M. Valla, A. J. Rossini, M. Caillot, C. Chizallet, P. Raybaud, M. Digne, A. Chaumonnot, A. Lesage, L. Emsley, J. A. van Bokhoven and C. Copéret, *J. Am. Chem. Soc.*, 2015, **137**, 10710.
19. F. Hoffmann, M. Cornelius, J. Morell and M. Fröba, *Angew. Chem. Int. Ed.*, 2006, **45**, 3216.
20. J. E. Readman, N. Kim, M. Ziliox and C. P. Grey, *Chem. Commun.*, 2002, **23**, 2808.

Chapter 5. Investigation of Supported Metal Catalysts

This chapter describes an investigation of alumina-supported cobalt oxide-based catalysts by solid-state NMR spectroscopy. The application of ^{1}H and ^{27}Al NMR techniques to the study of the Co-γ-Al_2O_3 and Co-γ-$CoAl_2O_4$ systems have provided insights into the influence of metal oxide loading and crystallite size on the metal-support interaction in these heterogeneous catalysts. Additionally, detailed characterisation of γ-Al_2O_3 has been carried out, providing valuable information about the surface/bulk chemistry of this underlying support material.

5.1 Introduction to Supported Metal Catalysts

The F-T synthesis process, introduced in Chapter 1, is one of the key methods in the modern world for the large-scale production of liquid hydrocarbons.[1] F-T reactions are catalysed by transition metals such as Co, Ni, Fe, Rh or Ru supported on a variety of porous materials.[2] Out of these, Co, Fe and Ru are the most commonly studied transition metals due to their good selectivity for higher molecular weight hydrocarbons, a desirable trait for industrial applications.[3] Ru is considered to be the best catalyst for F-T synthesis, being highly active, capable of operating at low reaction temperatures and able to produce long chain hydrocarbons without the addition of promoter species.[4] Unfortunately, Ru is not suitable for use in commercial reactor systems due to its high cost and scarcity, meaning that Fe and Co are usually the transition metals of choice in industrial settings.[3,4] Fe has the advantages of being very abundant and inexpensive, but is susceptible to deactivation *via* carbon deposition or the breakup of constituent catalysts. Fe catalysts are, however, suitable for use with H_2-poor feedstocks, opening up the possibility for them to be used in the conversion of coal and biomass to hydrocarbons.[3,4,5] By comparison, Co, whilst more expensive than Fe, is resistant to deactivation and exhibits CO conversion rates that are less affected by the presence of H_2O in the reactant stream. As a result, Co catalysts represent the best compromise for the production of long chain hydrocarbons from H_2-rich syngas mixtures.[3,6]

It has been determined that the activity level of a Co F-T catalyst is related to the number of Co atoms that are present on its surface – *i.e.*, the more Co atoms, the higher the catalytic activity.[6] Therefore, in order to maximise the amount of Co species present on the surface of the catalyst, these materials are prepared by depositing Co oxide onto supports possessing high surface area. Commonly used examples of such supports include oxide materials such as TiO_2, SiO_2 and Al_2O_3, as they display favourable catalytic activity when compared to other materials,[7] and their porous nature serves to regulate the size of the Co oxide particles that are formed. A brief description of these principal support materials is given below.

TiO_2, or titania, is the simplest oxide of the transition metal titanium. The two most common forms of this material are the tetragonal structures rutile (the most stable form) and anatase (stable, but can be transformed into rutile at high temperatures).[9] Both of these forms are composed of TiO_6 units that are connected by sharing two and four edges for rutile and anatase, respectively.[10] The advantages of TiO_2 as a support stem from the fact that both forms are inexpensive and safe to handle.[11] From a catalytic perspective, it has also been shown to be resistant to coking (the formation of carbonaceous residues on the catalyst surface), particularly in comparison to SiO_2-based catalysts.[12]

SiO_2, or silica, is an oxide of the group 14 element silicon. It exists in several different forms and is found most commonly in nature as either the crystalline phase quartz, or as amorphous SiO_2.[13] When used as a support, it is often in the form of mesoporous silica,[14,15] where the SiO_2 structure contains pores of up to 300 Å in diameter.[16] Mesoporous silicas are attractive catalyst supports due to their very high surface areas and uniform pore size distributions. These features allow for efficient control of the dispersion and size of Co particles, two factors which have been shown to directly affect F-T reaction rate and product selectivity.[17]

Al_2O_3, or alumina, is a polymorphic oxide of aluminium. Its thermodynamically stable phase is α-Al_2O_3, occurring in nature as corundum, where all Al ions are equivalently

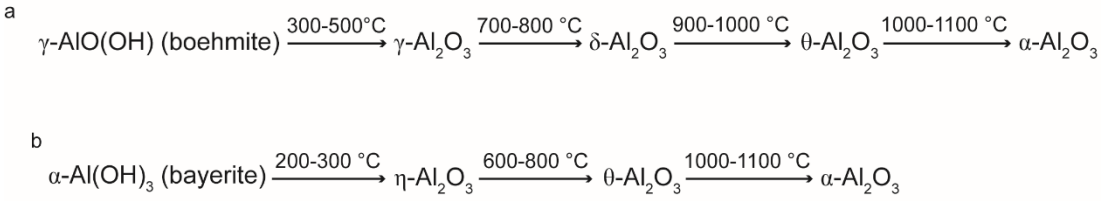

Scheme 5.1. *Phase transitions undergone by Al_2O_3 polymorphs upon heating at increasing temperatures, beginning from the aluminium oxyhydroxides (a) boehmite or (b) bayerite.*[22]

octahedrally-coordinated in a hexagonally close packed (hcp) array.[18] α-Al_2O_3 itself has found use in catalysis, thanks to its intrinsic strength and stability. It has been documented as a suitable support material for the preparation of Ag-based catalysts for reactions such as the selective oxidation of ethylene[19,20] and the reduction of NO_x.[21] Other polymorphs of Al_2O_3 are metastable and one form can typically be obtained by high-temperature calcination of the previous one in the series, as outlined in Scheme 5.1. By dehydrating the aluminium oxyhydroxide material boehmite at between 300 and 500 °C, γ-Al_2O_3 is produced.[22] It is also possible to obtain γ-Al_2O_3 by dehydrating pseudoboehmite, a poorly crystalline form of AlO(OH). In this case, the resulting alumina typically possesses a very high surface area, about 5 times greater than an analogous material synthesised from boehemite.[23] As with most of the other metastable polymorphs, γ-Al_2O_3 is comprised of a defect cubic spinel structure similar to that of the "ideal" spinel arrangement found in $MgAl_2O_4$, but possessing site vacancies in the positions otherwise filled by Mg.[24] Al occupies octahedral and tetrahedral sites in the bulk structure, with additional pentahedral Al sites also found at the surface.[24,25]

Out of all the polymorphs of alumina, γ-Al_2O_3 is most commonly used for catalytic applications,[24] and is often used as a support for F-T synthesis catalysts. Its attractiveness in this role stems from its high thermal stability at the temperatures employed for F-T reactions, and its resistance to attrition[26] (the breakdown/fragmentation of catalyst particles[27]). Metal sites deposited on γ-Al_2O_3 tend to be highly dispersed across the support, leading to a high level of active surface area available for catalysis, which in turn improves catalyst performance.[28,29] In this work, the catalyst samples studied were prepared using Co as the transition metal, and

either γ-Al_2O_3 or Si-modified γ-Al_2O_3 as the support material. It has been shown that creation of a silica overlayer protects against the formation of cobalt aluminate species, which can reduce the number of active sites available for catalysis.[30]

A particularly notable feature of Co-γ-Al_2O_3-based catalysts is the presence of a strong metal-support interaction (MSI). There are three types of MSI that have been identified. The first is a physical obstruction of the active particles (usually a metal) which causes a modification of activity and/or adsorption behaviour *e.g.*, by "decoration" of the metal particles by material diffusing from the support onto them. The second is an electronic effect in which the varying oxidation state of a reducible support (*e.g.*, TiO_2 or CeO_2) affects the electronic surface bands of the metal particle, causing modification of the chemisorption behaviour of gas species on the metal and therefore of the catalyst's activity and/or selectivity. The third is a relatively strong "bonding" (covalent, ionic or van der Waals) between the support and the surface metal which acts to fix them in position and so decrease their rates of surface diffusion and coalescence, decreasing loss of specific surface area by particle sintering. This can also apply to single atoms of the active phase.[3,4,23,26]

The "bonding" type of MSI phenomenon was first identified in 1978 by Tauster *et al.* for noble metals (*e.g.*, Pt and Pd) supported on TiO_2.[31] They observed that when these catalysts were subjected to high-temperature reduction (the process by which metal oxides are converted to metal particles, prior to the beginning of a catalytic reaction[32]), their ability to chemisorb H_2 and CO was greatly reduced.[31] By ruling out the possibility of metal agglomeration (the "clumping together" of metal particles that reduces the amount of active sites[33]), Tauster *et al.* deduced the presence of a chemical interaction, *i.e.*, covalent bond formation, between the TiO_2 bulk structure and the group 8 surface metal species.[31,34] This has been termed a "strong metal-support interaction" (SMSI) and continues to be a major subject of research in the field of heterogeneous catalysis.[35-37] The MSI that is present in Co-γ-Al_2O_3-based catalysts, whilst related to the one first observed by Tauster *et al.*, differs somewhat. It is characterised by a "pre-reduction" interaction between deposited Co_3O_4 particles and the γ-Al_2O_3 support. Upon initial deposition of Co, the precursor compound displays

only weak interaction with the support. Subsequent drying and calcination steps produce Co_3O_4 crystallites dispersed across the γ-Al_2O_3 surface.[3] The crystallite size is governed primarily by the initial Co loading, with higher loadings tending to favour the formation of larger crystallites, which are less well dispersed than smaller ones.[3,26] The reaction of small Co oxide particles with γ-Al_2O_3 is thought to cause the formation of Co aluminate-like spinel structures, which, as mentioned above, are not catalytically active. This "interaction phase" is also problematic because unlike Co_3O_4, it cannot be reduced to the active Co metal phase required for F-T synthesis.[38] The MSI also affects the overall ease with which the catalyst can be reduced, requiring high temperatures for longer durations, two factors which are known to reduce the active Co surface area.[39] In order to compensate for these issues, catalysts are often modified by the addition of so-called "reduction promoters".[3] These are typically noble metals such as Pt, Pd, Rh or Ru that are introduced during the synthesis process.[3] It has been observed that addition of even a small amount of promoter (*e.g.*, 0.5 wt%) lowers the temperature required to reduce Co_3O_4 species to the active metal phase.[40,41] It has been hypothesised that in the case of Pt, reduction occurs at these metal centres first, allowing "hydrogen spillover" to occur onto Co_3O_4, causing nucleation to Co metal sites.[42] This translates into profound effects upon catalytic activity. For example, Schanke *et al.*, observed that the addition of 0.4 wt% Pt to supported cobalt catalysts increased CO hydrogenation rates by 3-5 times over those recorded for non-promoted analogues.[43] This effect has also been documented for cases where other metal promoters have been employed, such as Ru,[44] Pd[45] and Re.[45,46]

5.2 Solid-State NMR Spectroscopy of Disordered Materials

It was mentioned above that in this work, the catalyst samples studied were prepared using cobalt as the transition metal supported on γ-Al_2O_3-based materials. Below is an outline of the considerations and approaches for characterising systems such as these that lack long range order, using solid-state NMR spectroscopy.

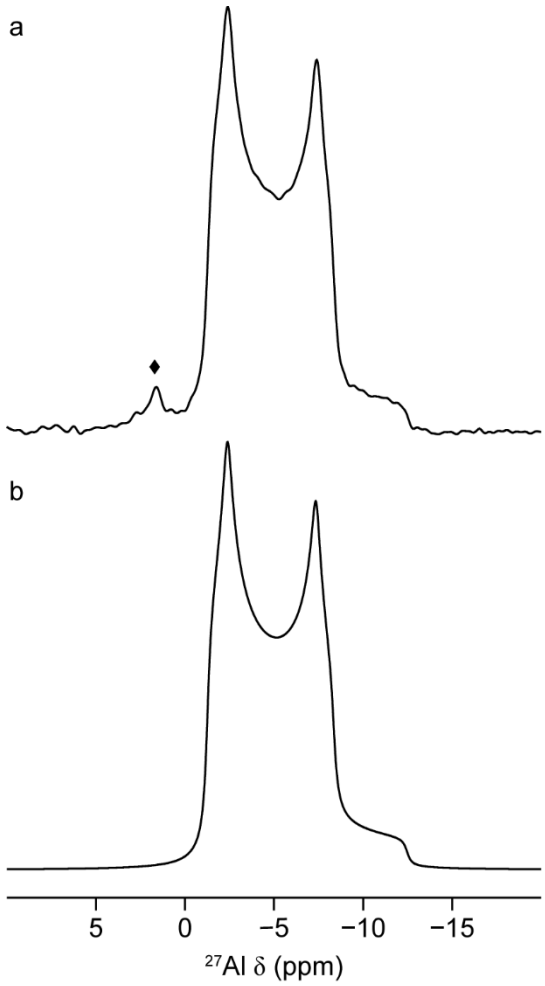

Figure 5.1. *(a) ^{27}Al (9.4 T, 14 kHz MAS) short flip angle DP NMR spectrum of the CT of aluminium acetylacetonate (Al(acac)$_3$). ♦ denotes the centreband of the inner (±1/2 ↔ ±3/2) satellite transition.[47] (b) Lineshape fit of the experimental spectrum shown in (a). The following NMR parameters were obtained: C_Q = 3.0 MHz; η_Q = 0.16 and δ_{iso} = 0.0 ppm.*

^{27}Al is one of the three NMR-active nuclei found in Al_2O_3-based materials. As mentioned in Chapter 1, it possesses moderate receptivity, 100% natural abundance, and ^{27}Al NMR spectroscopy is a very good probe of coordination number. In crystalline materials with well-defined crystallographic sites, the ^{27}Al CT spectra present as a second-order quadrupolar powder patterns resembling those in Chapters 2 and 3. An experimental example of this is given in Figure 5.1, which features the ^{27}Al MAS NMR spectrum of aluminium acetylacetonate (Al(acac)$_3$). A single site with octahedral coordination can be easily identified, and the well-defined power pattern allows for lineshape fitting to be carried out. By doing so, the following values can be

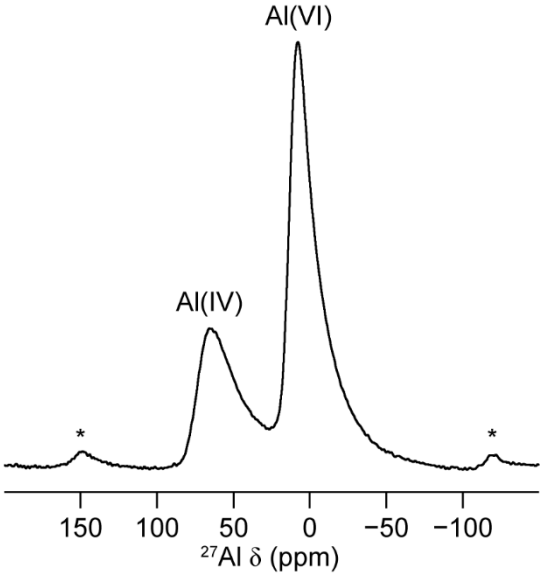

Figure 5.2. *^{27}Al (9.4 T, 14 kHz MAS) short flip angle DP NMR spectrum of γ-Al_2O_3. * denotes a spinning sideband.*

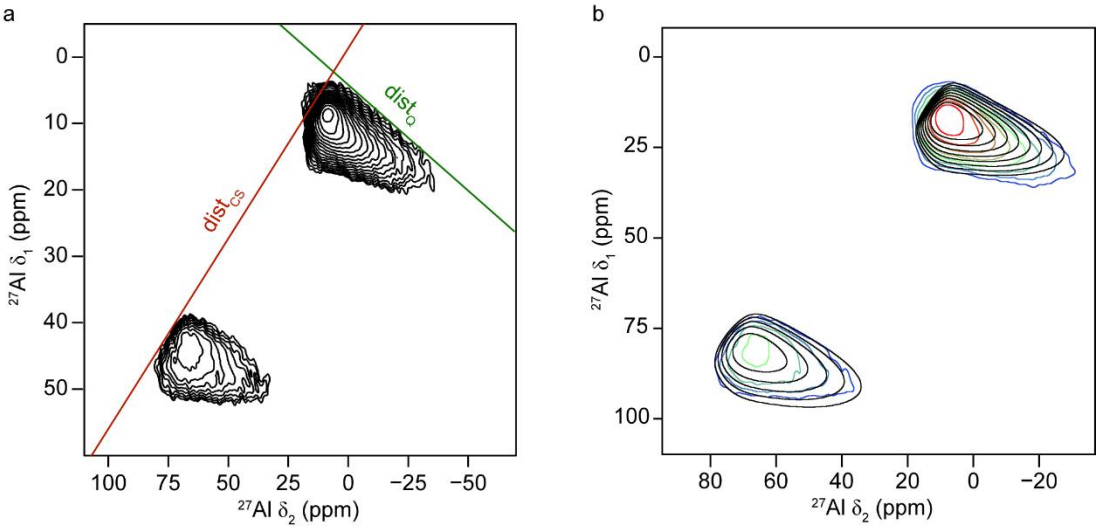

Figure 5.3. *(a) ^{27}Al (9.4 T, 14 kHz MAS) z-filtered 3QMAS spectrum of γ-Al_2O_3, with lines indicating distributions of chemical shifts ($dist_{CS}$) and quadrupolar parameters ($dist_Q$). A shearing transformation has been applied. (b) ^{27}Al (9.4 T, 14 kHz MAS) z-filtered 3QMAS spectrum of γ-Al_2O_3, with fits using the Czjzek model for the EFG and a Gaussian distribution of δ_{iso} (black lines) overlaid on each resonance (coloured lines). A shearing transformation has been applied. In (b) referencing in δ_1 was carried out according to the convention proposed by Amoureux and Fernandez,[58] in order for the Czjzek model to be implemented within DMFit.[54,57]*

Table 5.1. *NMR parameters (average quadrupolar coupling constant, $<C_Q>$, average isotropic chemical shift, $<\delta_{iso}>$ and full width at half maximum of the Gaussian distribution of the isotropic chemical shift, FWHM $dist_{CS}$) for γ-Al_2O_3, extracted using the Czjzek model for the EFG and a Gaussian distribution of the isotropic chemical shift.*

Site	$<C_Q>$ / MHz	$<\delta_{iso}>$ (ppm)	FWHM $dist_{CS}$ (ppm)
Al(IV)	5.5 (2)	75 (2)	9 (2)
Al(VI)	4.4 (2)	13 (2)	6 (2)

extracted - $C_Q = 3.0$ MHz, $\eta_Q = 0.16$ and $\delta_{iso} = 0.0$ ppm, which are in general agreement with published data.[47] The well-defined powder patterns described above are generally only observed for highly-ordered materials. Many of the systems of interest to materials chemists, such as glasses,[48] ceramics,[49] cements[50] and catalysts (as in this work) however, do not share this feature. Solid-state NMR spectra of such materials, particularly for quadrupolar nuclei like ^{27}Al, look distinctly different from the one shown in Figure 5.1. γ-Al_2O_3 provides a particularly good example of this, as can be seen from its ^{27}Al MAS NMR spectrum in Figure 5.2. Here, the lineshapes corresponding to Al(IV) and Al(VI) species lack the characteristic features observed in the previous figure. A notable observation though, is the presence of an upfield "tail", resulting from a distribution of quadrupolar parameters, with additional broadening caused by a distribution of δ_{iso}.[51] The shape of these resonances is determined by the magnitude and nature of these two distributions, and whether they exhibit any correlation.[51,52] For these reasons, it is quite challenging to extract detailed NMR parameters from the MAS NMR spectrum of γ-Al_2O_3. Approaches to overcome this hurdle do exist, however, and a particularly relevant example is the one pioneered by Massiot and co-workers.[53-55] By making use of the fact that both C_Q and η_Q are related to the principal components of the EFG tensor, a joint distribution of these parameters can be assumed. Spectral lineshapes can then be fitted using the Czjzek distribution of the EFG[56] and a Gaussian distribution of δ_{iso},[55] allowing NMR parameters to be extracted. The 3QMAS NMR experiment, introduced in Chapter 3, can also be a useful tool when studying quadrupolar nuclei in disordered samples. By observing the shape of the ridge lineshapes in the 2D spectrum, insight can be gained

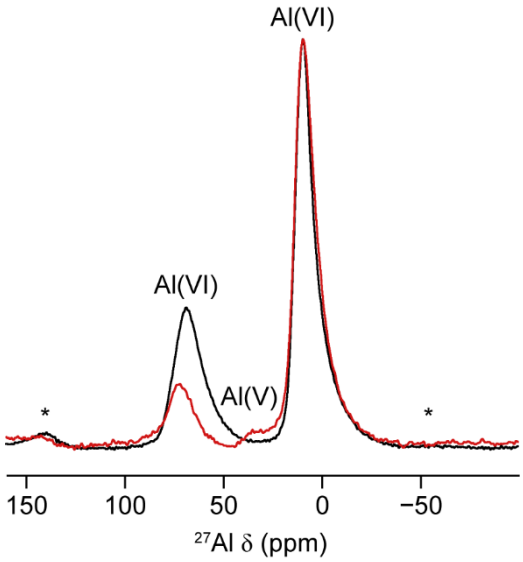

Figure 5.4. *^{27}Al (14.1 T, 20 kHz MAS) short flip angle DP NMR (black) and ^{1}H-^{27}Al (14.1 T, 20 kHz MAS, τ_{CP} = 0.8 ms) CP NMR (red) spectra of γ-Al_2O_3. * denotes a spinning sideband.*

into the distributions of NMR parameters that exist and their correlation. This is illustrated for γ-Al_2O_3 in Figure 5.3(a), which shows its ^{27}Al 3QMAS spectrum. The coloured axes on the spectrum displays the gradients along which broadening indicates a distribution of chemical shifts ($dist_{CS}$) or quadrupolar parameters ($dist_Q$) is present. The Czjzek model can also be applied to fit the resonances in 3QMAS spectra, and this can be implemented in freely available software such as DMFit,[57] allowing for the extraction of average values for C_Q and δ_{iso} for Al(IV) and Al(VI) sites.[54] The implementation of this approach is shown in Figure 5.3(b), which displays the Czjzek model fit of the ^{27}Al 3QMAS spectrum of γ-Al_2O_3, carried out using DMFit. The NMR parameters obtained *via* this method are provided in Table 5.1. It can be seen that the average C_Q for tetrahedrally-coordinated Al sites is ~1 MHz greater than that of the octahedral Al species. This is likely to be indicative of the fact that Al fills positions arising from defects in the 'ideal' spinel structure, reflecting the deviation of γ-Al_2O_3 away from an ordered structure. This is further reinforced by the large chemical shift distribution for both sites. As with C_Q, this value is greater for Al species occupying defect tetrahedral positions.

5.3 Characterising the Surface Structure of γ-Al_2O_3

It has been demonstrated that the use of both 1D and 2D ^{27}Al NMR techniques are able to reveal the presence of Al(IV) and Al(VI) sites in the structure of γ-Al_2O_3. It was mentioned above though, that this material also contains pentahedrally-coordinated Al sites, a feature which is not readily observed in the spectra presented in Figures 5.2 and 5.3. Indeed, early ^{1}H-^{27}Al CP NMR experiments by Morris and Ellis[59] showed no detectable resonances attributable to Al(V) species in samples of commercial γ-Al_2O_3. However, a subsequent ^{27}Al DP NMR study by Chen *et al.*[60] demonstrated that calcination of boehmite ground in a ball mill produced an alumina with an appreciable quantity of Al(V). Interestingly, it was also shown that calcination of boehmite without prior ball milling produced a material without a detectable Al(V) peak in its ^{27}Al DP NMR spectrum. The authors attributed this finding to the ball milled alumina being more thermally stable than the non-milled material. It was proposed that Al(V) sites in the non-milled structure were more likely to undergo rearrangement to form four- or six-coordinate species.[60] Since commercial γ-Al_2O_3 is normally produced from the calcination of boehmite (or pseudoboehmite[23]) that has not been subjected to prior milling, there is uncertainty as to whether five-coordinate species exist in the industrially-relevant material. Subsequent studies by Peden and co-workers have demonstrated that the use of ultrahigh magnetic fields, *i.e.*, 21.1 T, allows for the identification of a five-coordinate Al resonance in commercially obtained γ-Al_2O_3, as a result of a reduction in second-order quadrupolar broadening.[61-63] Furthermore, by doping with Ba or La oxides, these researchers showed that Al(V) is likely to be located at the surface of the oxide.[61,62]

As mentioned in Chapter 3, although CP from spin I = 1/2 to quadrupolar nuclei offers generally poor prospects for signal enhancement, it is well-suited to the task of "spectral editing". This makes it a good approach for the detection of the surface species in γ-Al_2O_3. Figure 5.4 shows the ^{27}Al DP and CP NMR spectra of this material, in black and red respectively. It can be seen that the application of CP enables the observation of an Al(V) resonance that is not seen in the DP spectrum. Additionally, the overlay of the two spectra in Figure 5.4, shows that there is a noticeable difference

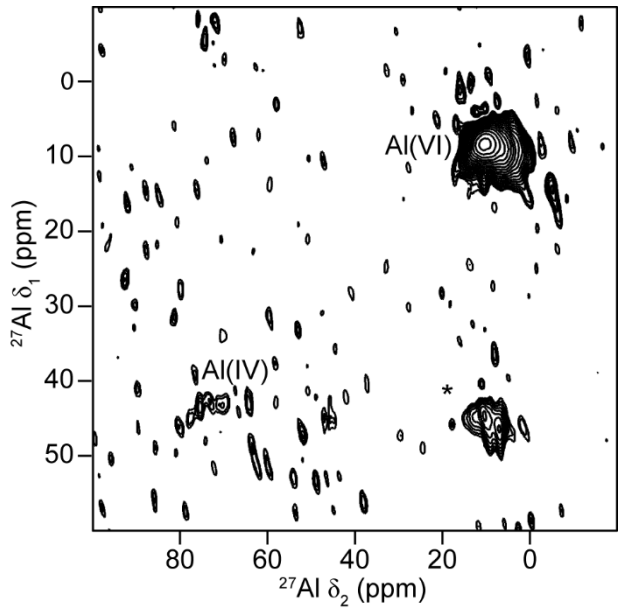

Figure 5.5. *^{1}H-^{27}Al (14.1 T, 14 kHz MAS, τ_{CP} = 0.8 ms) z-filtered CP 3QMAS NMR spectrum of γ-Al_2O_3. A shearing transformation has been applied. Resonances corresponding to Al(IV) and Al(VI) species are labelled. * denotes a spinning sideband.*

Table 5.2. *NMR parameters (average quadrupolar product, $<P_Q>$ and average isotropic chemical shift, $<\delta_{iso}>$) for the Al(VI) sites in γ-Al_2O_3, obtained from the z-filtered CP 3QMAS spectrum (Al(VI)[a]) in Figure 5.5, and a conventional z-filtered 3QMAS spectrum (Al(VI)[b]) (shown in Figure 5.13(a)). Both spectra were acquired at 14.1 T and 14 kHz MAS.*

Site	$<P_Q>$ / MHz	$<\delta_{iso}>$ (ppm)
Al(VI)[a]	3.6 (2)	13 (2)
Al(VI)[b]	3.4 (2)	13 (2)

in the intensity of the Al(IV) resonance between them. It may be inferred from this that, relative to octahedral Al, less tetrahedral Al resides at the surface of γ-Al_2O_3. Additionally, it can be argued that pentahedral Al species are primarily resident on the oxide surface, due to the lack of an observable corresponding resonance in the ^{27}Al DP NMR spectrum. This finding is in agreement with the work of Lee *et al.*,[25] who studied γ-Al_2O_3 using DNP enhanced solid-state NMR techniques. By means of surface selective and so-called "bulk filtered" ^{27}Al 3QMAS experiments, these researchers demonstrated that Al(V) is only located in the first surface layer of the oxide.

In order to explore further the predominant species that are found in the surface structure of γ-Al_2O_3, the use of additional NMR techniques is required. As mentioned above (and in Chapter 3), the 3QMAS experiment is well suited to providing high-resolution spectra containing additional information about local environments experienced by given species. Thus, in principle, it ought to be possible to combine CP and 3QMAS together in an approach that allows a 2D spectrum of, for example, Al surface sites to be acquired. Indeed, an example of a spectrum obtained from this kind of experiment is shown in Figure 5.5. Here, a ^{1}H-^{27}Al CP 3QMAS experiment was used to acquire a spectrum of γ-Al_2O_3. The sequence employed here is based on the z-filtered experiment introduced by Ashbrook and Wimperis,[64] where p = ±3 coherences are excited from the p = ±1 coherences created by CP from ^{1}H. The combination of 3Q filtration and CP means that this type of experiment is quite insensitive. Nonetheless, with careful setup and an extended period of signal averaging, a spectrum can be obtained for moderately receptive nuclei such as ^{27}Al. The spectrum shown above features a relatively well resolved resonance corresponding to Al(VI) species, along with an additional one tentatively assigned to Al(IV). No identifiable resonance for Al(V) species is observed though, which is initially surprising given the surface selective nature of the CP 3QMAS experiment. However, in the work of Lee *et al.*[25] previously mentioned, only a small, relatively low intensity peak was seen in their DNP-enhanced CP 3QMAS spectrum. This suggests that the insensitivity of the experiment under conventional solid-state NMR conditions is responsible for the lack of an observable Al(V) resonance. The same line of reasoning may also be applied to the low intensity of the Al(IV) resonance. It is also possible though, that there are fewer tetrahedral Al sites at the surface of γ-Al_2O_3. Certainly, it appears to be the case that octahedrally-coordinated Al sites are the predominant Al surface species in this material. Using the position of the centre of gravity of the Al(VI) lineshape, average P_Q and δ_{iso} values were obtained, and are given in Table 5.2. Also given are the values obtained from a conventional (non-CP) z-filtered 3QMAS spectrum acquired at the same field (14.1 T). The P_Q values are in close agreement, suggesting that, on average, the two types of Al(VI) experience similar local environments. This could be the case if a proportion of these species occupy the second surface layer of the oxide,[25] and are not directly exposed.

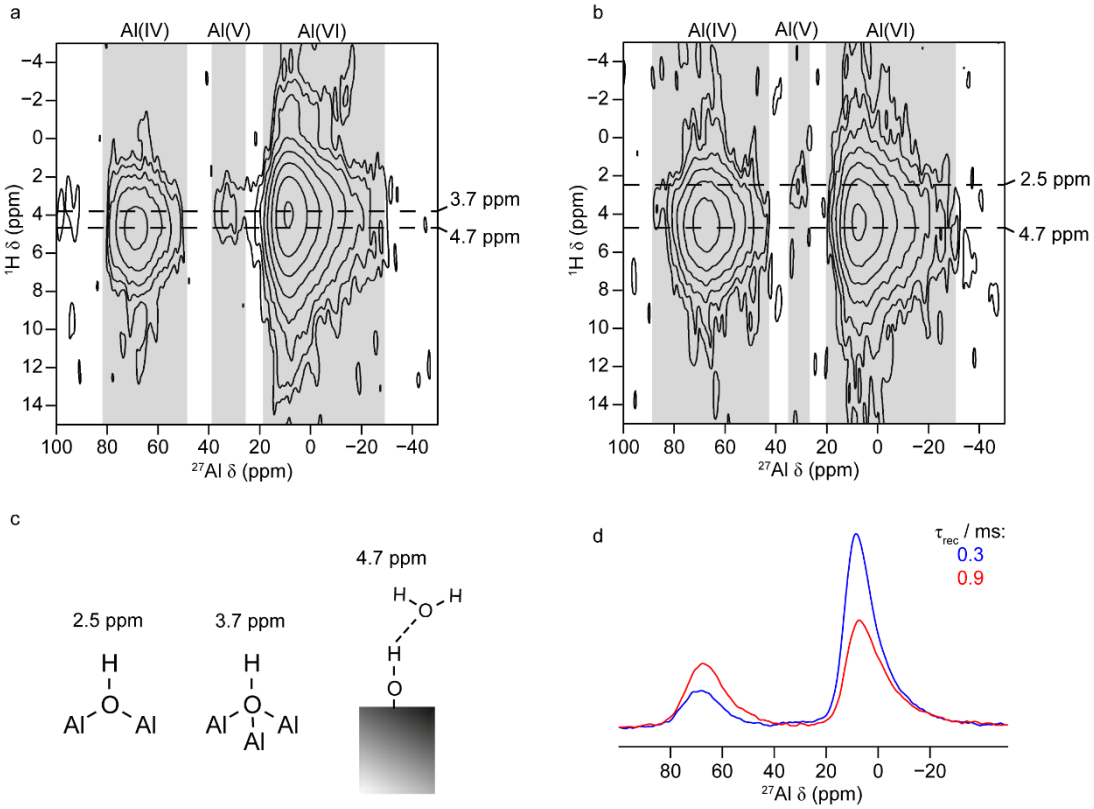

Figure 5.6. *^{1}H-^{27}Al (14.1 T, 40 kHz MAS) D-HMQC spectra of γ-Al_2O_3, acquired with (a) τ_{rec} = 0.3 ms and (b) τ_{rec} = 0.9 ms. In both spectra, annotations have been provided for resonance assignments/chemical shift values. (c) Schematic representations of the functional groups observed in the spectra shown in (a) and (b), along with corresponding ^{1}H δ_{iso} values. (d) Overlaid projections of the ^{27}Al dimension of the 2D spectra in (a) (blue) and (b) (red).*

It is also desirable to probe further the interactions between H and Al species on the surface of γ-Al_2O_3. By means of 2D correlation experiments, this is indeed possible. One experiment that has found good applicability in solid-state NMR spectroscopy is the D-HMQC (dipolar heteronuclear multiple-quantum correlation) experiment. This is a through-space correlation experiment initially adapted by Gan and co-workers[65,66] from the original solution-state through-bond technique introduced in 1979.[67] It was further developed and brought to greater prominence by Delevoye and co-workers,[68] who have demonstrated its potential as a useful tool for structural investigations of oxide-type materials.[68-70] Controlled reintroduction of the dipolar coupling between two nuclei allows for the acquisition of a spectrum that can be edited based on spatial proximities, similar to the CP HETCOR experiment. The advantage of the D-HMQC technique though, is that it is highly robust with respect to rf offset and is relatively

straightforward to optimise, compared a CP-based experiment for a quadrupolar nucleus.[68] In this work, D-HMQC experiments have been performed using the $SR4^2_1$ recoupling scheme developed by Brinkmann and Kentgens.[71] This method is capable of being used under fast MAS (up to ~60 kHz)[71] and has been shown to be very robust against rf field inhomogeneity.[68,72] Figure 5.6 presents ^{1}H-^{27}Al D-HMQC spectra of γ-Al_2O_3 recorded using different dipolar recoupling durations (τ_{rec}). In Figure 5.6(a), a short τ_{rec} value (0.3 ms) has been used. The presence of resonances corresponding to Al(IV), Al(V) and Al(VI) in the ^{27}Al dimension are observed here, and all correlate with a region of the ^{1}H dimension corresponding to ^{1}H $\delta_{iso} \approx 3.7$ ppm. Based on the results reported by Taoufik *et al.*,[70] this resonance has been assigned to Al_3-OH species on the surface of the oxide. Al(IV) and Al(VI) species are also seen to correlate with ^{1}H $\delta_{iso} \approx 4.7$ ppm, which can be attributed to adsorbed H_2O.[73-75] Very little correlation is observed between this region of the ^{1}H spectrum and the Al(V) resonance, suggesting that pentacoordinated species are less likely to interact with H_2O molecules, possibly due to their reduced presence in the first surface layer of γ-Al_2O_3.[25] When τ_{rec} is extended to 0.9 ms, as in Figure 5.6(b), Al(V) is seen to correlate exclusively with a component at ^{1}H $\delta_{iso} \approx 2.5$ ppm, assigned to Al_2-OH species.[70] This suggests that at least two types of Al(V) environments exist on the γ-Al_2O_3, one of which more readily interacts with external species such as adsorbed H_2O, due to its closer proximity to such molecules at the "top" of the surface region. Figure 5.6(c) provides a schematic illustration of the observed functional groups and their corresponding ^{1}H δ values. In Figure 5.6(d), the projections of the ^{27}Al dimension of the spectra in parts (a) and (b) are shown overlaid. They reveal that as τ_{rec} is increased, the intensity of the Al(VI) resonance decreases, accompanied by a corresponding increase in the intensity of the Al(IV) resonance. This, in combination with the ^{27}Al CP 3QMAS data, supports the assertion that Al(VI) species are dominant at the immediate surface of γ-Al_2O_3. As a greater distance between H and Al is probed, "buried" Al(IV) species are more readily detected than their top-level Al(VI) counterparts. A shift in the position of the Al(V) resonance, by $\delta \approx 3$ ppm, is further suggestive of the presence of two distinct types of pentacoordinated species.

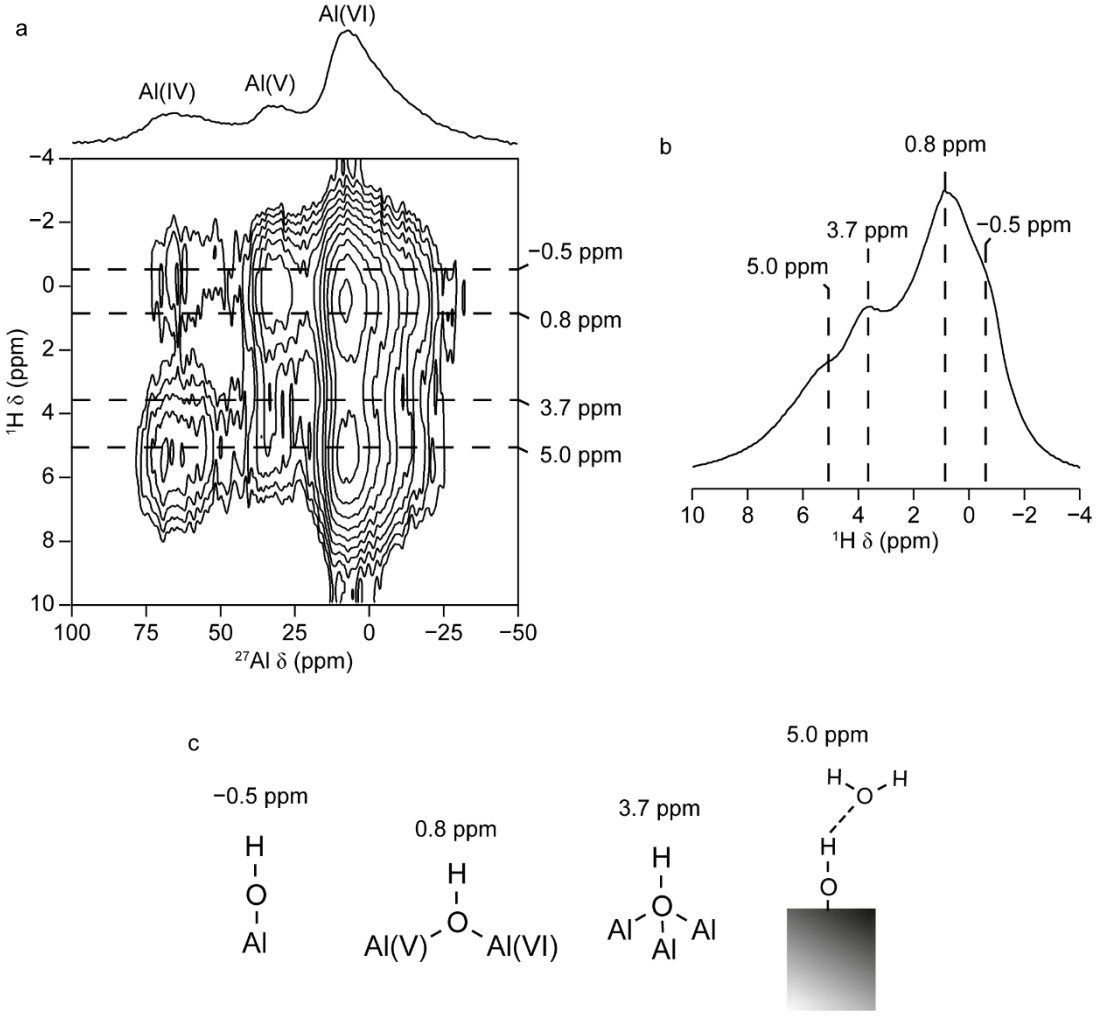

Figure 5.7. *(a) ^{1}H-^{27}Al (9.4 T, 14 kHz MAS, τ_{rec} = 0.43 ms) D-HMQC spectrum of γ-Al_2O_3 dehydrated in vacuo at 300 °C for ~6 h. A projection is shown for the ^{27}Al dimension. Annotations have been provided for resonance assignments/chemical shift values. (b) ^{1}H (9.4 T, 14 kHz MAS) NMR spectrum of the γ-Al_2O_3 sample studied in (a). Chemical shift values for resonances are indicated. (c) Schematic representations of the functional groups observed in the spectra shown in (a) and (b), along with corresponding ^{1}H δ_{iso} values.*

γ-Al_2O_3 is a hygroscopic material,[76,77] a property which makes it and other aluminas suitable for use as a desiccant for air drying in the chemicals[78] and water treatment industries.[79] Accordingly, γ-Al_2O_3 that has not been subjected to drying procedures is present in a hydrated state,[25,80,81] and discussion up until this point has focused on material where this is indeed the case. Further insight into the arrangement of aluminol functional groups can be gained by removal of adsorbed water, as demonstrated here.

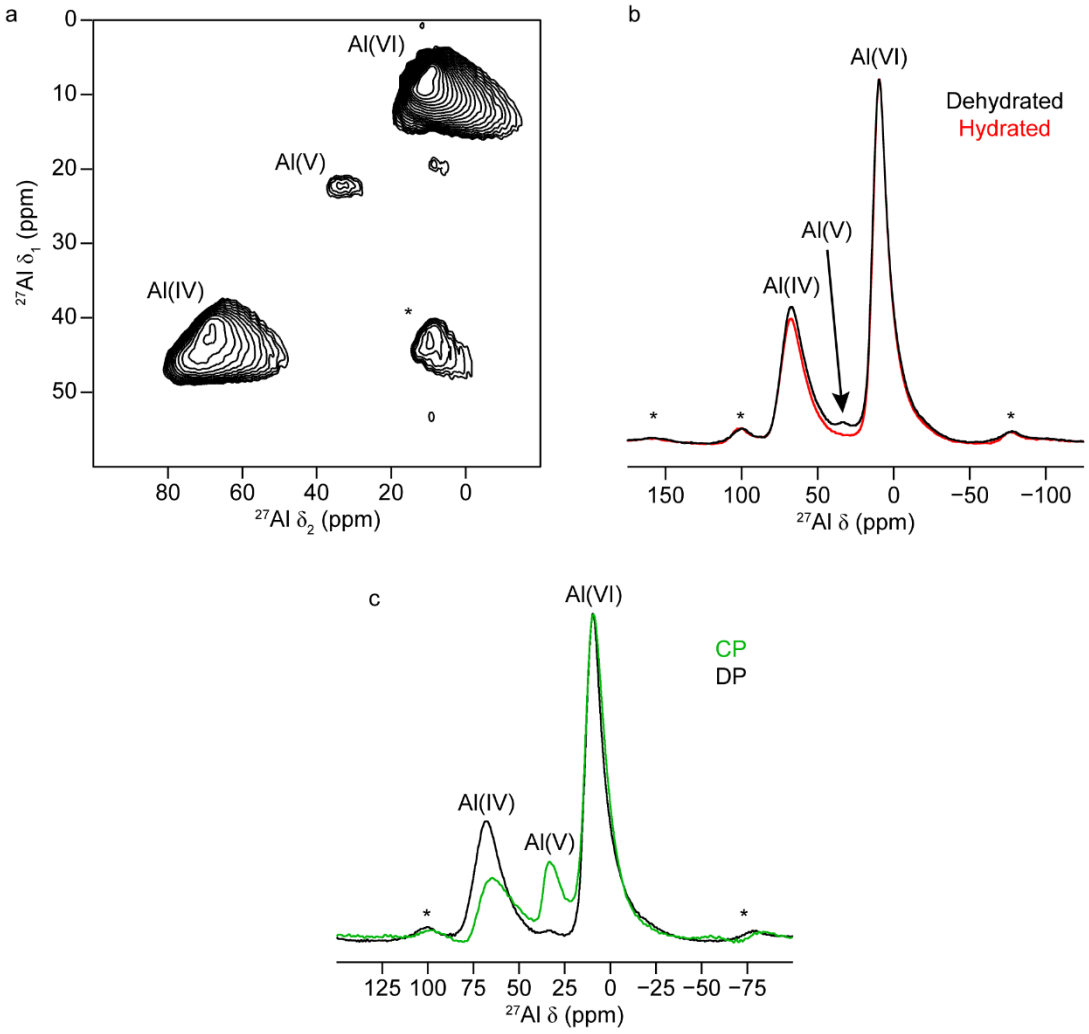

Figure 5.8. *(a) ^{27}Al (14.1 T, 14 kHz MAS) z-filtered 3QMAS spectrum of γ-Al_2O_3 dehydrated in vacuo at 300 °C for 6 h. A shearing transformation has been applied. (b) Overlay of ^{27}Al (14.1 T, 14 kHz MAS) short flip angle DP NMR spectra of hydrated (red) and dehydrated γ-Al_2O_3 (300 °C, 6 h) (black). (c) Overlay of ^{27}Al (14.1 T, 14 kHz MAS, black) short flip angle DP and ^{1}H-^{27}Al (14.1 T, 14 kHz MAS, τ_{CP} = 0.8 ms, green) CP NMR spectra of spectrum of dehydrated γ-Al_2O_3 (300 °C, 6 h), where spectra have been scaled with respect to the Al(VI) resonance. In all spectra, * denotes a spinning sideband.*

Table 5.3. *NMR parameters (average quadrupolar product, $<P_Q>$ and average isotropic chemical shift, $<\delta_{iso}>$) for the Al sites in dehydrated γ-Al_2O_3 (300 °C, 6 h), obtained from the z-filtered 3QMAS spectrum in Figure 5.8(a).*

Site	$<P_Q>$ / MHz	$<\delta_{iso}>$ (ppm)
Al(IV)	5.3 (2)	77 (2)
Al(V)	4.4 (1)	38 (1)
Al(VI)	3.3 (2)	14 (2)

A sample of γ-Al_2O_3 was dried under vacuum for ~6 h and subsequently packed into a 4 mm rotor under an inert (N_2) atmosphere, in order to prevent rehydration from exposure to atmospheric H_2O. Figure 5.7(a) shows the ^1H-^{27}Al D-HMQC spectrum of this sample acquired using a relatively short τ_{rec} value (0.43 ms). A notable feature of the spectrum is the presence of a relatively intense resonance attributable to Al(V) species. Removal of adsorbed H_2O may thus facilitate a rearrangement or "scrambling" effect on the surface of γ-Al_2O_3 that results in the generation of additional pentacoordinated sites. Correlation between Al sites and four distinct H environments is also observed. By means of comparison with the ^1H MAS NMR spectrum shown in Figure 5.7(b), these resonances can be assigned following the work of Taoufik *et al.*,[70] and the findings discussed above for hydrated γ-Al_2O_3. Notably, it can be observed that dehydration facilitates the observation of isolated (non-bridging) AlOH species, principally (but not exclusively) connected to tetrahedral Al sites. The resonance at ^1H $\delta_{iso} \approx 0.8$ ppm is assigned to Al_2OH species anchored by Al(IV) and Al(V) species. The shift in this resonance to lower ppm values with respect to hydrated γ-Al_2O_3, can be attributed to a reduction in hydrogen bonding as a result of the removal of substantial adsorbed H_2O. It may also be the case that this site is bonded to different types of Al sites.[70] Al_3-OH species (^1H $\delta_{iso} \approx 3.7$ ppm) continue to be observed on the oxide surface, suggesting that they remain largely unaffected by any surface "scrambling" or effects associated with thermal treatment of the oxide. A fourth resonance is also observed at ^1H $\delta_{iso} \approx 5.0$ ppm, which is assigned to residual adsorbed H_2O molecules on the surface of the oxide. [73-75] Adsorbed water is known to be particularly difficult to remove from aluminas, requiring temperatures in excess of 350

°C or the use of high vacuum.[73,82] The assignments outlined above are summarised schematically in Figure 5.7(c).

The ^{27}Al 3QMAS spectrum of dehydrated γ-Al_2O_3, shown in Figure 5.8(a), reveals the extent of the structural rearrangement that has taken place on the surface of this material. Of note is the presence of a resonance assigned to Al(V), that is not observed in the corresponding spectrum of hydrated γ-Al_2O_3, suggesting that there has been an increase in the quantity of this species present. This is further highlighted by comparing the ^{27}Al DP MAS NMR spectra of the hydrated and dehydrated γ-Al_2O_3 samples, as shown in Figure 5.8(b). Comparison of the DP and CP MAS spectra of dehydrated γ-Al_2O_3, displayed in Figure 5.8(c), confirms that the vast majority of pentahedral Al still reside at the surface of the material. Previously, researchers have reported C_Q values for Al(V) in excess of 7 MHz,[25,70] in contrast to the lower average P_Q value extracted from the spectrum in Figure 5.8(a), of 4.4 MHz. However, it has been observed by Wischert *et al*.[83] that the local symmetry of Al sites is increased when bonded to OH groups, which in turn decreases the C_Q for those particular sites. Moreover, they obtained a very similar Al(V) C_Q value (4.5 MHz) for a sample of γ-Al_2O_3 dehydrated at 300 °C, and C_Q was seen to increase by 0.8 MHz when a second sample of γ-Al_2O_3 was treated at 500 °C. This suggests that in the material studied in this work, the Al(V) in dehydrated γ-Al_2O_3 are connected to surface OH groups, an assertion borne out by the evidence obtained from ^{1}H-^{27}Al D-HMQC experiments. Wischert *et al*. also report that hydroxylated Al(V) should display a resonance at ^{27}Al $\delta \approx 40$ ppm,[83] an observation which is consistent with the figure given in Table 5.3 above. The P_Q values obtained for Al(IV) and Al(VI) sites are very similar to those obtained for hydrated γ-Al_2O_3. As these are likely to correspond to bulk Al species, this is to be expected, given that the "scrambling" or rearrangement phenomena described above are surface level effects, governed by the extent to which γ-Al_2O_3 is hydrated.[84]

5.4 Supported Metal Catalysts: Co-γ-Al_2O_3 and Co-Si-γ-Al_2O_3 Materials

To ascertain the effect of cobalt oxide modification on the structure of γ-Al_2O_3 and its analogues, two collections of model catalysts were studied using solid-state NMR spectroscopy. They have been designated as series one and series two.

5.4.1 Series One

The model catalysts in series one consist of materials prepared by both colloidal[85] and incipient wetness[86] methods with different cobalt loadings and differing crystallite sizes. Full details of their preparation have been provided in Chapter 4, and for ease of reference, they are briefly summarised below.

COLL10: Co_3O_4 supported on γ-Al_2O_3 (10 wt% Co). This material was prepared by a colloidal route.[85] The average Co_3O_4 crystallite size was <5 nm.

IW5: Co_3O_4 supported on γ-Al_2O_3 (5.4 wt% Co). This material was prepared by incipient wetness techniques.[33] The average Co_3O_4 crystallite size was <5 nm.

IW17: Co_3O_4 supported on Si-γ-Al_2O_3 (1.5 wt% Si) (17 wt% Co). This material was prepared by incipient wetness methods.[33] The average Co_3O_4 crystallite size was 15-16 nm.

IW21: Co_3O_4 supported on Si-γ-Al_2O_3 (1.5 wt% Si) (21 wt% Co). This material was also prepared by an incipient wetness route.[33] The average Co_3O_4 crystallite size was 15-16 nm.

Incipient wetness impregnation is generally recognised as a catalyst preparation method that is both relatively straightforward to carry out and produces little waste. As a result, it has proven to be quite a popular avenue for the synthesis of supported metal catalysts.[33] Alternatively, colloidal approaches can be utilised for catalyst preparation. Several procedures have been documented,[85-88] but the one used to prepare the material studied in this work involves combining $Co(NO_3)_2 \cdot 6H_2O$ with a

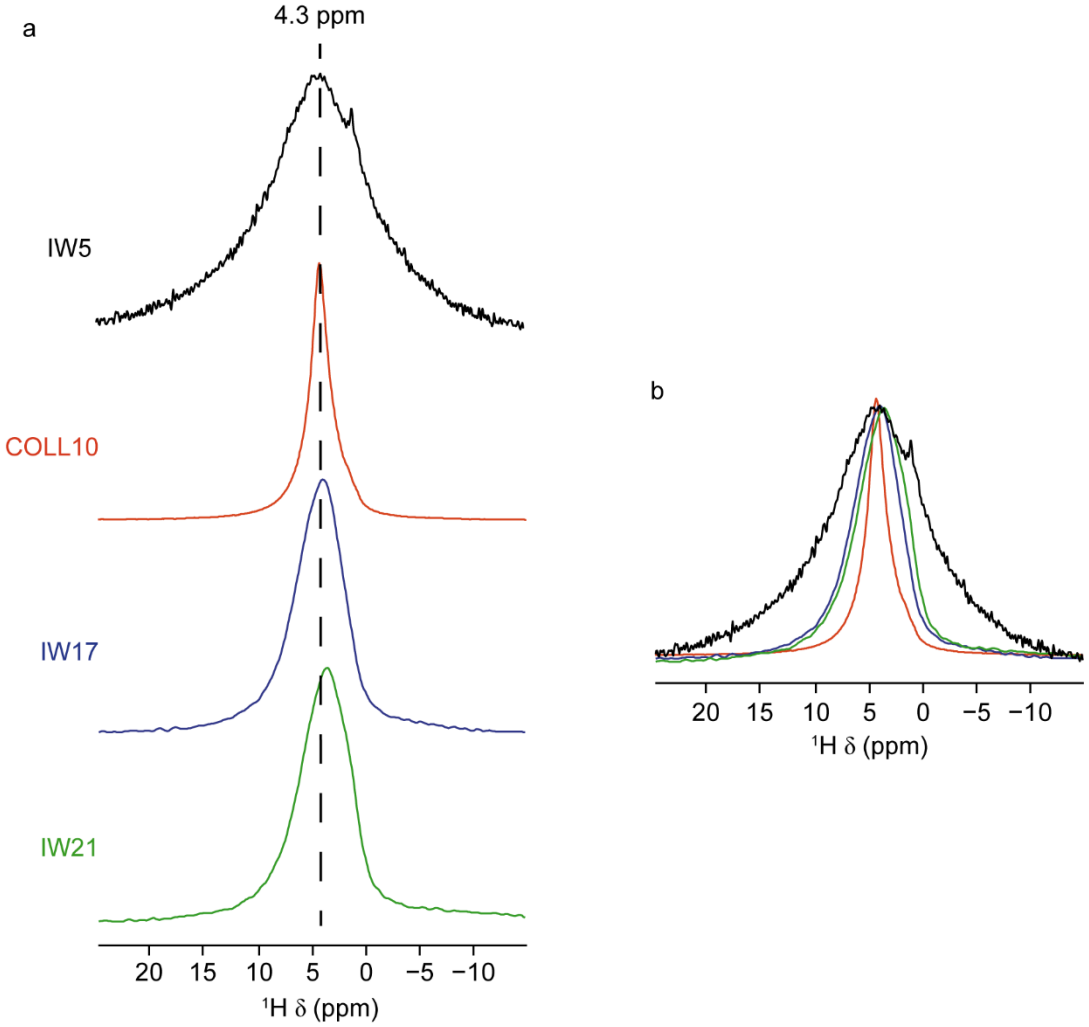

Figure 5.9. *^{1}H (9.4 T, 40 kHz MAS) NMR spectra of series one catalysts (a) stacked and (b) overlaid and normalised.*

Table 5.4. *^{1}H T_2' values determined for the series one catalysts IW21, IW5 and COLL10. RSS = residual sum of squares, which represents the amount of error remaining between the regression function and the dataset.*

IW21		IW5		COLL10	
T_2' (1) / μs	T_2' (2) / μs	T_2' (1) / μs	T_2' (2) / μs	T_2' (1) / μs	T_2' (2) / μs
109	817	49	420	216	1700
RSS = 4.6×10^{-3}		RSS = 5.0×10^{-3}		RSS = 1.5×10^{-3}	

surfactant to create Co oxide nanoparticles. These particles are then dispersed in an organic solvent and combined with the desired support, in this case, γ-Al_2O_3.[85] Synthesising Co oxide nanoparticles in this manner allows for their size and shape to be well controlled.[89] Figure 5.9 shows the ^{1}H MAS NMR spectra of the series one samples. They all exhibit a single resonance at ^{1}H $\delta_{iso} \approx 4.3$ ppm, which is likely to be due to adsorbed H_2O.[73-75] While the positions of the resonances show little change, as seen in Figure 5.9(a), considerable variation is observed in their linewidth, with the narrowest line (~4 kHz) for COLL10. IW17 and IW21 both give broader resonances (~8 kHz), consistent with adding (*via* incipient wetness impregnation) more metal oxide onto the surface of the support, but the spectrum of IW5 contains the broadest line (~16 kHz). This large variation in linewidths is well illustrated in Figure 5.9(b), where the spectra are overlaid. The introduction of small metal oxide particles by incipient wetness impregnation appears to create a high metal oxide surface area that forms a more intimate interface with the support. This may be considered analogous to the "bonding" type of MSI previously introduced in section 5.2, which subsequently exerts a greater effect upon the surface protons, manifesting as broadening of the spectral line. It is this effect, termed here as a "proton-metal oxide interaction", that is observable *via* solid state NMR spectroscopy and is able to inform on the extent and nature of the MSI in the materials studied in this work. Coupling between the electronic and nuclear spins can enhance both the spin-lattice (T_1) and spin-spin (T_2) relaxation of the nucleus, often by several orders of magnitude. Under MAS, spin-spin relaxation is usually the principal cause of line broadening for a spin I = 1/2 nucleus.[90] In solids, in addition to the mechanism that yields "true" T_2 relaxation, other interactions may contribute to the linewidth, including higher-order terms of the heteronuclear dipolar interaction which result in homogeneous broadening of spectral lines (in paramagnetic systems, there is also a contribution from interactions with electrons). As a result, a modified parameter, the time constant T_2', can be measured *via* a spin echo experiment featuring an incremented τ duration. In solids, it therefore follows that $T_2' < T_2$.[91] Accordingly, ^{1}H T_2' relaxation was measured for samples IW21, IW5 and COLL10 in series one. The values of T_2' are provided in Table 5.4. The ^{1}H NMR spectrum of each sample has two components, one with a significantly faster T_2' than the other. It is believed that one type of H species is in close proximity

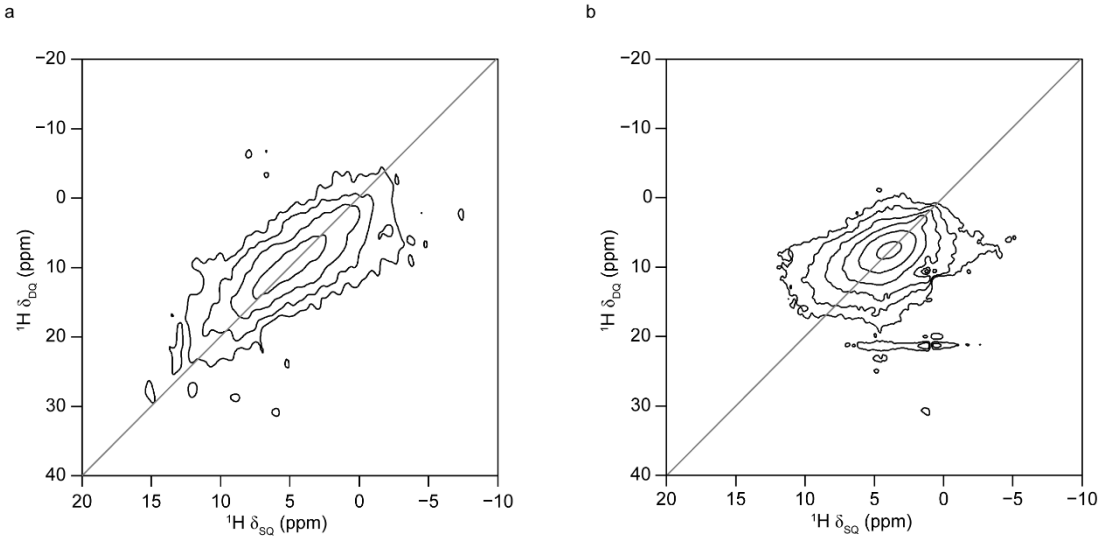

Figure 5.10. *^{1}H-^{1}H (9.4 T, 40 kHz MAS) SQ-DQ spectra of (a) IW5 and (b) COLL10. Both spectra were acquired using one block of BABA excitation/conversion. The solid grey line denotes the $\delta_{DQ} = 2\delta_{SQ}$ autocorrelation diagonal.*

to Co oxide crystallites and is therefore more influenced by these paramagnetic centres. The other type of H environment is located further from these centres but, provided that an MSI exists in the material, they are still influenced by paramagnetism. Notably, in the material that appears to exhibit the greatest paramagnetic interaction (IW5), ^{1}H T_2' values for both sites are noticeably shorter than for the other two samples. Additionally, in COLL10, ^{1}H T_2' values are highest. Indeed, the site believed to be located further from the Co oxide particles in this material has a T_2' value over four times longer than for the same site on IW5, suggesting the absence of a proton-metal oxide interaction. The colloidal route used to prepare COLL10 is known to generate crystalline Co_3O_4 particles with a nanocube morphology.[85,89] These well-defined quantum dots,[89] when combined with γ-Al_2O_3, likely form a co-mixture featuring self-contained Co_3O_4 units dispersed across the oxide surface. Such an arrangement lacks extensive "intimate contact" with the support material and therefore does not exhibit a MSI like that found in the catalysts prepared by incipient wetness impregnation.

It was postulated above that at least one of the H-containing species present at the surface of the series one catalysts is likely to be adsorbed H_2O. In order to verify this hypothesis, ^{1}H homonuclear 2D correlation experiments were performed using the

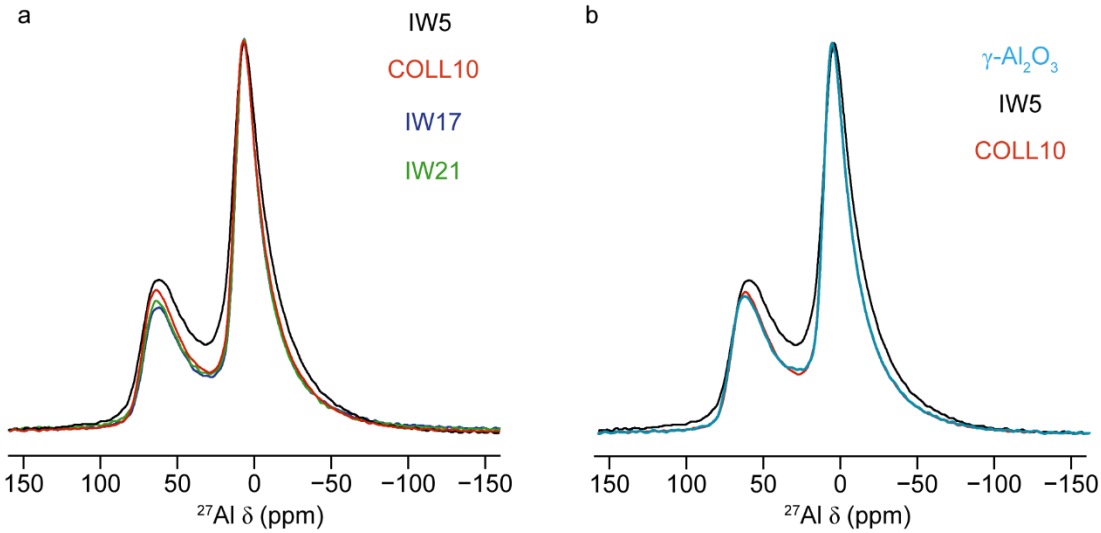

Figure 5.11. *^{27}Al (9.4 T, 40 kHz MAS) DP NMR spectra overlaid of (a) series one catalysts and (b) γ-Al_2O_3, IW5 and COLL10. Spectra have been normalised with respect to the Al(VI) resonance.*

BABA dipolar recoupling scheme[92,93] described in Chapter 3. In Figure 5.10, spectra acquired using this sequence are shown for the model catalysts IW5 and COLL10, the samples showing the greatest and smallest extent of a proton-metal oxide interaction, respectively. In both cases, the spectra show a component, centered at ^{1}H $\delta_{SQ} \approx 5$ ppm, on the autocorrelation diagonal. This indicates that the principal H species at the surface may indeed be bound H_2O. It follows that this could be the case if the formation of hydroxyl groups is impeded by the deposition of Co oxide, either during synthesis or by the extensive surface of these metal oxide particles blocking available anchoring points. A similar observation was made by Mastikhin *et al.*,[94] who studied samples of γ-Al_2O_3 impregnated with vanadium and molybdenum species. They found that the modification of γ-Al_2O_3 in this way greatly reduced the quantity of OH groups present in the materials. The ^{1}H resonances observed in that study were attributed to OH species buried in cavity spaces or bound in a V-O-H or Mo-O-H arrangement. An analogous situation is not readily identifiable in the present work, likely due to the difference in morphology between Co_3O_4 and V/Mo species, *i.e.*, Co_3O_4 exists in particle form rather than as an overlayer. The paramagnetic nature of Co_3O_4 may also preclude the detection of OH groups, as the signals from these species could be unobservable due to their proximity to the metal oxide particles. Such an observation

may be thought of as roughly analogous to the "bleaching" effect induced by paramagnetic polarising agents used in DNP NMR spectroscopy.[95-97]

To ascertain the effect of Co oxide modification on the γ-Al_2O_3-based support structure, ^{27}Al DP MAS NMR spectra of series one samples were acquired. Figure 5.11(a) shows the results for all four model catalysts overlaid together, and normalised with respect to the Al(VI) resonance. It is observed that as the Co loading increases, the contribution from Al(IV) decreases slightly relative to that of Al(VI). This may be suggestive of a greater concentration of Co oxide particles facilitating binding with tetrahedral sites, which have been established earlier in this chapter to be less abundant on the surface of γ-Al_2O_3. This assertion is made with a degree of caution though, as both the size of Co oxide particles and the type of support do vary between these model catalysts. This hypothesis is explored more systematically for samples in series two, in the next subsection of this chapter. A degree of broadening of the spectral lineshape is observed for the ^{27}Al NMR spectrum of IW5. This effect is relatively small however, indicating that only a small proportion of Al species are affected by the presence of paramagnetic Co_3O_4 species. As most of the alumina structure is found in the bulk, this supports the assertion that the MSI is chiefly a surface-level phenomenon, as indicated by the differing proton-metal oxide interactions observed from ^{1}H NMR data. In Figure 5.11(b), the ^{27}Al NMR spectra of colloidal and incipient wetness-based samples are compared with that of their support material, γ-Al_2O_3. Despite the addition of 10 wt% Co, no additional broadening of the spectral lineshape of COLL10 is evident. This seems to support the observation that "intimate contact" of Co oxide particles with the support is necessary to establish a MSI. As was indicated from ^{1}H NMR above, this co-mixture of self-contained nanocubes appears to lack this feature. Interestingly, for the sample IW5, the Al(IV) resonance shows an increase (relative to that of Al(VI)) with respect to both COLL10 and the support material. It may be tentatively suggested that this can be viewed as a reduction in Al(VI) intensity, possibly indicating that at low loadings, small Co oxide crystallites are primarily located next to surface octahedral Al sites.

5.4.2 Series Two

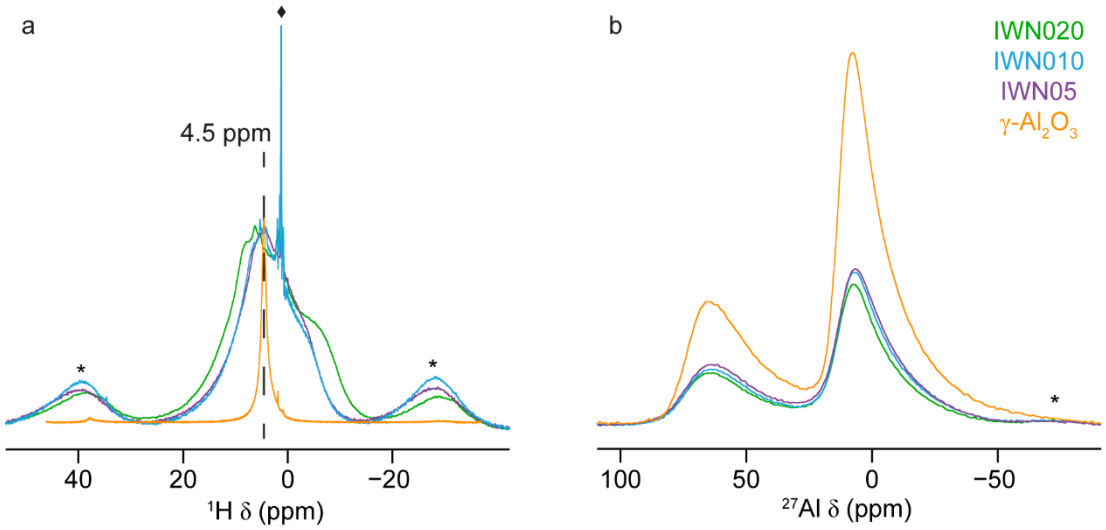

Figure 5.12. *(a) ^{1}H (14.1 T, 20 kHz MAS) NMR spectra of γ-Al_2O_3 and series two catalysts overlaid. Intensities have been normalised with respect to the maximum point of the γ-Al_2O_3 lineshape. ♦ denotes background signal. (b) ^{27}Al (9.4 T, 14 kHz MAS) short flip angle DP NMR spectra of the samples studied in (a). Spectra have been scaled with respect to the number of transients and the mass of sample contained within each 4 mm rotor. In both (a) and (b), * denotes a spinning sideband.*

The model catalysts in series two consist of materials prepared by incipient wetness methods[86] with different cobalt loadings but the same crystallite size. This series was selected to attempt to ascertain the effect of varying the Co loading on materials comprised of small metal oxide crystallites. Full details of their preparation have been provided in Chapter 4. As for series one, the samples in series two are briefly summarised below as a reference aid.

IWN020: Co_3O_4 supported on γ-Al_2O_3 (20 wt% Co). This material was prepared by incipient wetness methods.[86]

IWN010: Co_3O_4 supported on γ-Al_2O_3 (10 wt% Co). This material was prepared by incipient wetness methods. [86]

IWN05: Co_3O_4 supported on γ-Al_2O_3 (5 wt% Co). This material was prepared by incipient wetness methods. [86]

In all cases, the average Co_3O_4 crystallite size was <5 nm.

Figure 5.12(a) shows ^{1}H MAS NMR spectra of the second series of catalysts and γ-Al_2O_3. The spectrum of starting material is characterised by a relatively sharp resonance at ^{1}H $\delta_{iso} \approx 4.5$ ppm. The first addition of Co_3O_4 appears to establish the aforementioned "intimate contact" with the surface of γ-Al_2O_3. Preparation of a material with double the metal loading (10 wt%) results in the same level of proton-metal oxide interaction as for a loading of 5 wt%, perhaps due to a degree of agglomeration[33] occurring between metal oxide crystallites. It is only when a larger amount of Co oxide is impregnated that this interaction can be further extended. Addition of 20 wt% is sufficient to dramatically reduce the amount of protons present on the surface, in a manner analogous to the "titration" effect observed by Mastikhin *et al.*,[94] which was described above for series one catalysts. The low concentration of surface H species is further evidenced by the appearance of features at ^{1}H $\delta_{iso} \approx 1$ and 7 ppm, which are likely to result from background from the probe, cap or rotor. Despite the application of the DEPTH sequence, designed to suppress background signals,[98] it has been reported that residual peaks of this nature can be observed if the sample contains a sufficiently small quantity of protons.[99] The identity of the spurious signals observed in series two catalysts was determined by acquiring an equivalent experiment using an empty 4 mm rotor. The spectrum that was obtained bore strong resemblance to that which was observed by Feng and Reimer.[99] A broad manifold underlying the background spectrum is observed that stretches across to ^{1}H $\delta \approx -15$ ppm, and it is thought that this results from adsorbed H_2O. A ^{1}H MAS NMR spectrum of IWN020 was acquired after vacuum drying (150 ºC for 5 h) and packing in inert (N_2) atmosphere. It revealed the loss of this broad underlying feature, displaying only residual background signal. This confirms that at high Co loadings, adsorbed H_2O is the predominant proton-containing species present in the material. In Figure 5.12(b), the ^{27}Al DP NMR spectra of series two catalysts and γ-Al_2O_3 are presented. Spectra have been scaled with respect to the number of transients and the mass of sample contained within each rotor. A reduction in signal intensity in the ^{27}Al spectra of the catalyst materials can be seen, and a similar trend in the broadening of the ^{1}H spectral lineshapes can be observed. A similar phenomenon was previously reported by Caldarelli *et al.* for ^{27}Al NMR of cobalt-loaded aluminosilicates.[100] These researchers

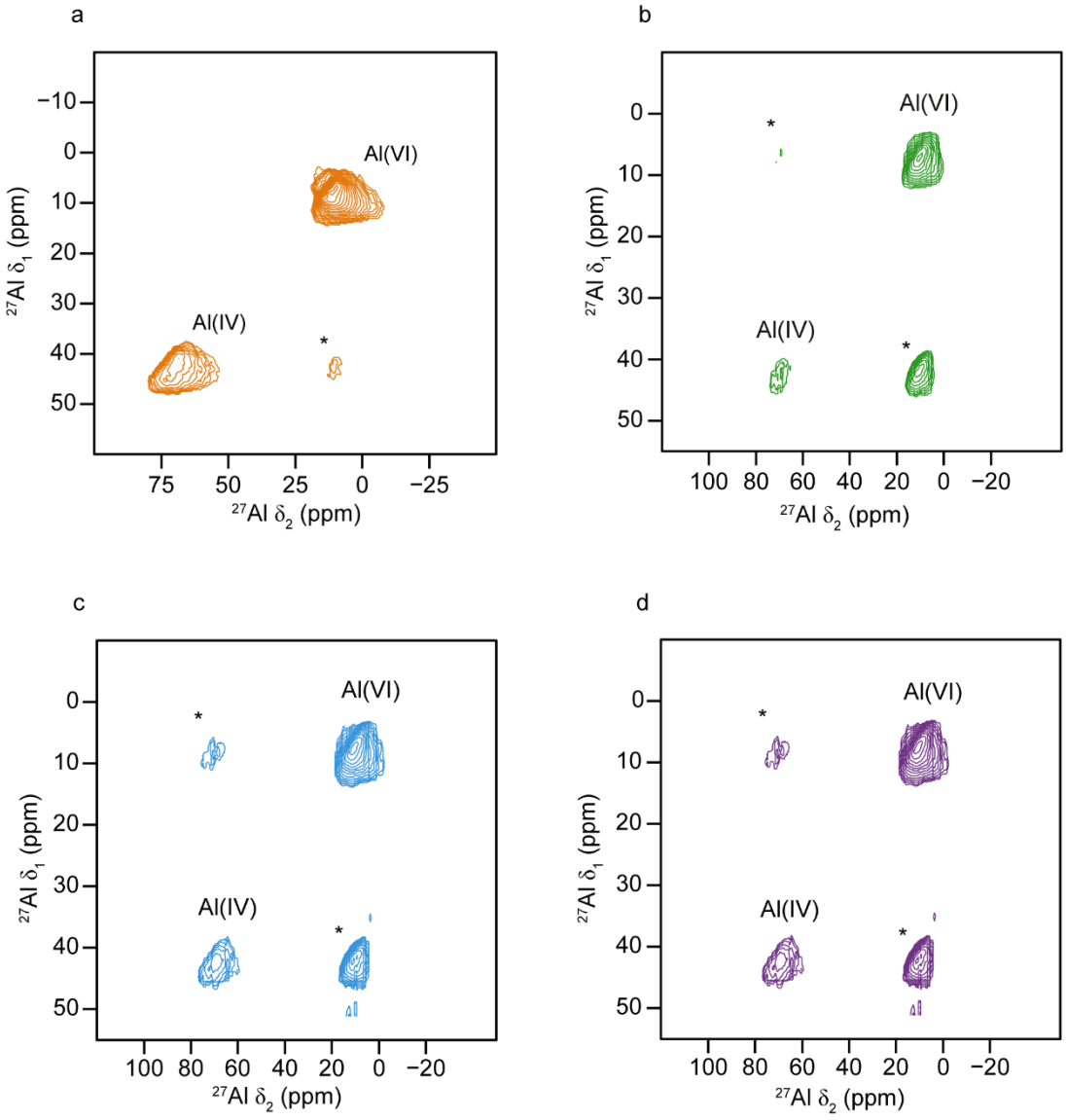

Figure 5.13. *^{27}Al (14.1 T, 14 kHz MAS) z-filtered 3QMAS spectra of (a) γ-Al_2O_3, (b) IWN020, (c) IWN010 and (d) IWN05. A shearing transformation has been applied to all spectra. Resonances corresponding to Al(IV) and Al(VI) species are labelled. * denotes a spinning sideband.*

attributed the reduction in signal intensity in the zeolite mordenite to the resonance from octahedral Al being shifted by interactions with nearby paramagnetic Co oxide. Specifically, they surmised that the resonance became shifted by the hyperfine contact interaction, as well as being broadened by paramagnetic relaxation enhancement effects.[100] In the present work, the ^{27}Al data serves to reinforce the hypothesis that the presence of a MSI is related to the extent of Co oxide surface coverage. At 20 wt%

Table 5.5. *NMR parameters (and average quadrupolar product, $<P_Q>$ and average isotropic chemical shift, $<\delta_{iso}>$) for the Al sites in γ-Al_2O_3, IWN020, 010 and 05, obtained from the z-filtered 3QMAS spectra in Figure 5.13.*

Sample	Al(IV)		Al(VI)	
	$<P_Q>$ / MHz	$<\delta_{iso}>$ (ppm)	$<P_Q>$ / MHz	$<\delta_{iso}>$ (ppm)
γ-Al_2O_3	5.6 (2)	77 (2)	3.4 (2)	13 (2)
IWN020	3.6 (2)	75 (2)	4.0 (2)	14 (2)
IWN010	3.4 (2)	76 (2)	3.8 (2)	13 (2)
IWN05	3.5 (2)	77 (2)	4.1 (2)	13 (2)

loading, the vast majority of the γ-Al_2O_3 is intimately contacted with Co oxide crystallites. Indeed, Caldarelli *et al.* suggest that the formation of Co-O bonds is highly likely for a sample prepared *via* wet impregnation.[100]

To gain further insight into the interaction of Co with Al in the support material of series two catalysts, ^{27}Al 3QMAS experiments were performed, and the corresponding spectra are shown in Figure 5.13. A reduction in intensity in of the Al(IV) resonance is observed as Co oxide is added to the alumina surface, generally proportional to the amount of Co oxide that has been loaded. A decrease in the average P_Q of the Al(IV) site is also observed when Co oxide is added to the γ-Al_2O_3 support, although increasing the loading does not exert any further change in this value. The combination of these two observations serve to indicate that Al(IV) is the preferred binding site for small cobalt oxide crystallites, regardless of the quantity of Co_3O_4 that is impregnated. This is further supported by the fact that no significant change in the average P_Q or δ_{iso} values of the Al(VI) site is observed. This second, somewhat counterintuitive observation, can be explained by the aforementioned "bleaching" effect, considering that at high loadings, more Al(VI) species are likely to be rendered unobservable by the increased likelihood of being in close proximity to paramagnetic Co_3O_4.[100] It therefore follows that as the Co loading increases, the average δ_{iso} value is more likely to correspond to those Al(VI) species that are still observable. It is probable that such sites can be found in the bulk of the support structure.

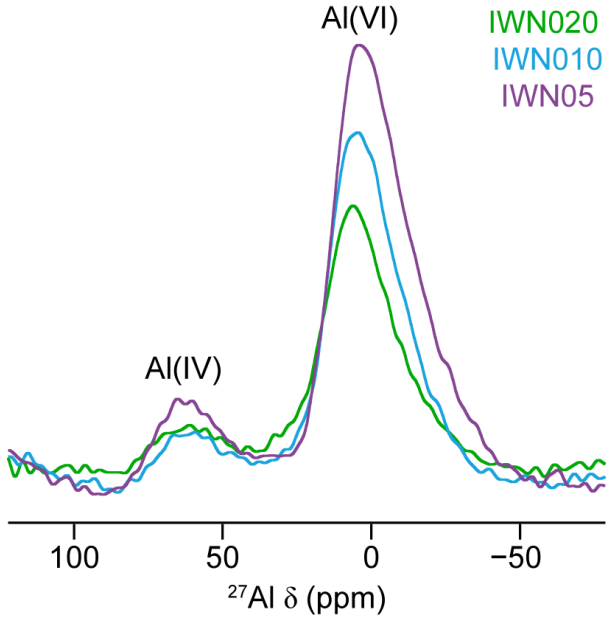

Figure 5.14. *^{1}H-^{27}Al (9.4 T, 14 kHz MAS, τ_{CP} = 0.8 ms) CP NMR spectra of series two catalyst materials. The mass of sample in each rotor and the number of transients in each experiment were the same for all samples.*

To explore further the effect of Co_3O_4 deposition on the surface environments of γ-Al_2O_3, ^{1}H-^{27}Al CP NMR experiments were performed on the series two catalysts, and Figure 5.14 shows the spectra that were obtained. It can be seen that as the Co loading is increased, the overall signal intensity decreases, consistent with a reduction in the amount of H species present on the alumina surface. Doubling of the Co loading also results in a shift of the Al(VI) δ_{obs} value by ~1 ppm towards higher frequency. This can be explained by a change in the local environment experienced by this type of Al, possibly *via* a change in δ_{iso}. As the Co loading is increased, surface Al(VI) species are more likely to be found in close proximity to Co oxide crystallites than, for example, OH groups, and therefore in a different local environment. The low intensity of the Al(IV) resonances for each material can be attributed to both the paramagnetic nature of the Co oxide particles, and the insensitivity of the experiment as a result of the reduction in the quantity of H species. Indeed, extensive signal averaging was required (each experiment was ~16 h in duration) to achieve the levels of sensitivity displayed in Figure 5.14.

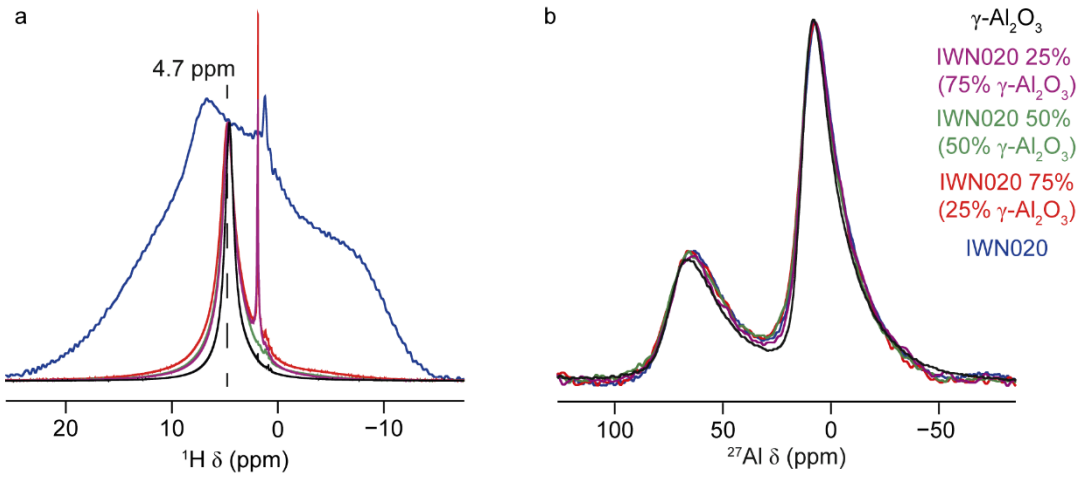

Figure 5.15. *(a) ^{1}H (14.1 T, 20 kHz MAS) NMR spectra of IWN020, γ-Al_2O_3 and IWN020:γ-Al_2O_3 ground mixtures overlaid. Spectra have been normalised to give equal intensities at 4.7 ppm. The sharp peaks at ^{1}H $\delta_{iso} \approx 2$ ppm are attributed to residual solvent.[101] The sharp feature at ^{1}H $\delta_{iso} \approx 0$ ppm in the spectra of IWN020 results from background signal.[99] (b) ^{27}Al (9.4 T, 14 kHz MAS) short flip angle DP NMR spectra of the same samples studied in (a). Spectra have been normalised with respect to the Al(VI) resonance.*

Table 5.6. *^{1}H T_1 values determined for IWN020, γ-Al_2O_3 and IWN020:γ-Al_2O_3 ground mixtures. RSS = residual sum of squares, which represents the amount of error remaining between the regression function and the dataset.*

Sample	^{1}H T_1 / ms	RSS
IWN020	6	2.1×10^{-4}
IWN020 75% (25% γ-Al_2O_3)	23	5.2×10^{-2}
IWN020 50% (50% γ-Al_2O_3)	22	7.1×10^{-2}
IWN020 25% (75% γ-Al_2O_3)	33	1.6×10^{-2}
γ-Al_2O_3	90	1.8×10^{-3}

It has been proposed that "intimate contact" between metal oxide crystallites and the support surface is key to the formation of a MSI. To more extensively verify this theory, aliquots of IWN020 (20 wt% Co) and γ-Al_2O_3 were ground together using a mortar and pestle, to create mixtures of the following proportions - 75:25 IWN020:γ-Al_2O_3, 50:50 IWN020:γ-Al_2O_3 and 25:75 IWN020:γ-Al_2O_3. In Figure 5.15(a), the ^{1}H

MAS NMR spectra of these samples are shown overlaid. Upon mixing with as little as 25% γ-Al_2O_3, the resonance attributed to adsorbed H_2O narrows substantially from ~23 kHz to ~5.6 kHz in width. Preparation of mixtures with increased amounts of γ-Al_2O_3 does not seem to decrease the linewidth any further. This suggests that the action of grinding the catalyst together with a small amount of alumina is sufficient to disrupt the "intimate contact" that exists between Co oxide crystallites and surface proton species. In the absence of this feature, there is no longer a significant MSI present. This assertion is supported by the ^1H T_1 values obtained for these materials, *via* a saturation recovery sequence.[102] The data reveal that the introduction of γ-Al_2O_3 results in a significant lengthening of the spin-lattice relaxation time, suggesting that the proton-metal oxide interaction has been weakened. The fact that the mixed materials still display shorter T_1 durations than γ-Al_2O_3 does indicate that some residual interaction does still take place. ^{27}Al MAS NMR spectra in Figure 5.15(b) show no discernable change in linewidth between all samples, indicating that the MSI is chiefly a surface level phenomenon facilitated by "intimate contact" between metal oxide and support.

5.5 Supported Metal Catalysts: $CoAl_2O_4$ Materials

It was mentioned at the beginning of this chapter that the formation of Co aluminate-like spinel structures can occur when small Co_3O_4 particles interact with the surface γ-Al_2O_3. This "interaction phase" is problematic in F-T synthesis, as it is not catalytically active and so reduces catalyst performance in this reaction.[38] However, $CoAl_2O_4$ have been shown to display properties such as high thermal stability[103] and resistance to deactivation *via* compounds such as SO_2.[104] These attributes make $CoAl_2O_4$ suitable for use as catalysts for automotive emissions control,[105] oxidation of CO,[104] CO_2 reforming of CH_4[103] and non-oxidative dehydrogenation of propane.[106]

To ascertain the effect of incorporating Co onto the surface and into bulk support structures, $CoAl_2O_4$-based catalyst materials were investigated using ^1H and ^{27}Al solid-state NMR spectroscopy. $MgAl_2O_4$ was also studied in order to provide a comparison with an analogous diamagnetic spinel structure. The preparation of these

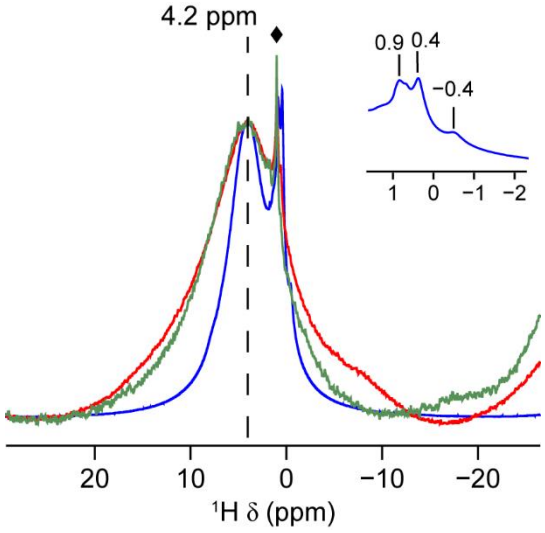

Figure 5.16. *^{1}H (9.4 T, 14 kHz MAS) NMR spectra of $MgAl_2O_4$ (blue), $CoAl_2O_4$ (red) and Co-$CoAl_2O_4$ (green). Spectra have been scaled with respect to the centre of the $MgAl_2O_4$ resonance at ^{1}H $\delta_{iso} \approx 4.2$ ppm. Expansions of the upfield resonances in the spectrum of $MgAl_2O_4$ are also shown inset. ♦ denotes background signal.*

samples is briefly described below.

$CoAl_2O_4$: Co-γ-Al_2O_3 (6 wt% Co) was heated at 1000 °C for 6 h in a muffle furnace to produce $CoAl_2O_4$.

Co-$CoAl_2O_4$: this material was prepared by incipient wetness impregnation[86] of $CoAl_2O_4$, followed by calcination, to produce Co-$CoAl_2O_4$ (20 wt% Co).

$MgAl_2O_4$ was obtained commercially. Phase identity was confirmed *via* PXRD (see Appendix E for additional details).

Figure 5.16 shows the ^{1}H MAS NMR spectra of the three spinel materials described above. The lineshape of $MgAl_2O_4$ features several resonances, the broadest of which, at ^{1}H $\delta_{iso} \approx 4.2$ ppm, is assigned to adsorbed H_2O on the surface of the material.[73-75] The remaining contributions to the lineshape are in the upfield region of the spectrum. The signal at ^{1}H $\delta_{iso} \approx -0.4$ ppm is attributed to isolated Al(IV)OH surface species,[70]

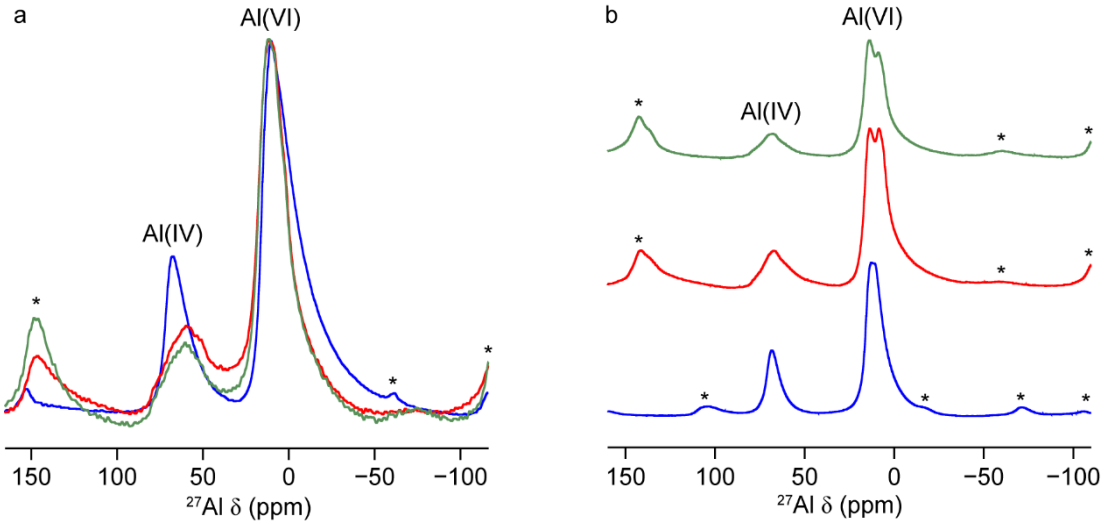

Figure 5.17. *(a) ^{27}Al (9.4 T, 14 kHz MAS) short flip angle DP NMR spectra of $MgAl_2O_4$ (blue), $CoAl_2O_4$ (red) and Co-$CoAl_2O_4$ (green). Spectra have been scaled with respect to the Al(VI) resonance. (b) ^{27}Al (14.1 T, 14 kHz MAS (blue) and 20 kHz MAS (red and green)) DP NMR spectra of $MgAl_2O_4$ (blue), $CoAl_2O_4$ (red) and Co-$CoAl_2O_4$ (green). In both (a) and (b), * denotes a spinning sideband.*

as discussed in section 5.3 above. The resonances at ^{1}H $\delta_{iso} \approx 0.4$ and 0.9 ppm are assigned to isolated MgOH[107] and Al(VI)OH[108] functional groups, respectively. The spectra of $CoAl_2O_4$ and Co-$CoAl_2O_4$ are both characterised by a broad resonance centred at ^{1}H $\delta_{iso} \approx 4.2$ ppm. The $CoAl_2O_4$ lineshape also features a broad component located between ^{1}H $\delta \approx 0$ and −15 ppm. This may correspond to surface OH protons in close proximity to Co oxide species, as it has been documented that the ^{1}H/^{2}H resonances in solid cobalt acetylacetonate become shifted to negative ppm values and extensively broadened as a result of H species being located close to paramagnetic Co oxide units.[109]

The overlaid ^{27}Al DP NMR spectra of the three spinel materials, acquired at 9.4 T, are presented in Figure 5.17(a). From this data, the presence of both Al(IV) and Al(VI) species in all three aluminates can be confirmed. Initially, such a finding would seem to be surprising, as the "ideal" spinel structure should only feature octahedral Al sites.[24] However, it is quite common, in the case of $MgAl_2O_4$, for tetrahedral site vacancies to be present due to "cation mixing" and Al can substitute into these, giving

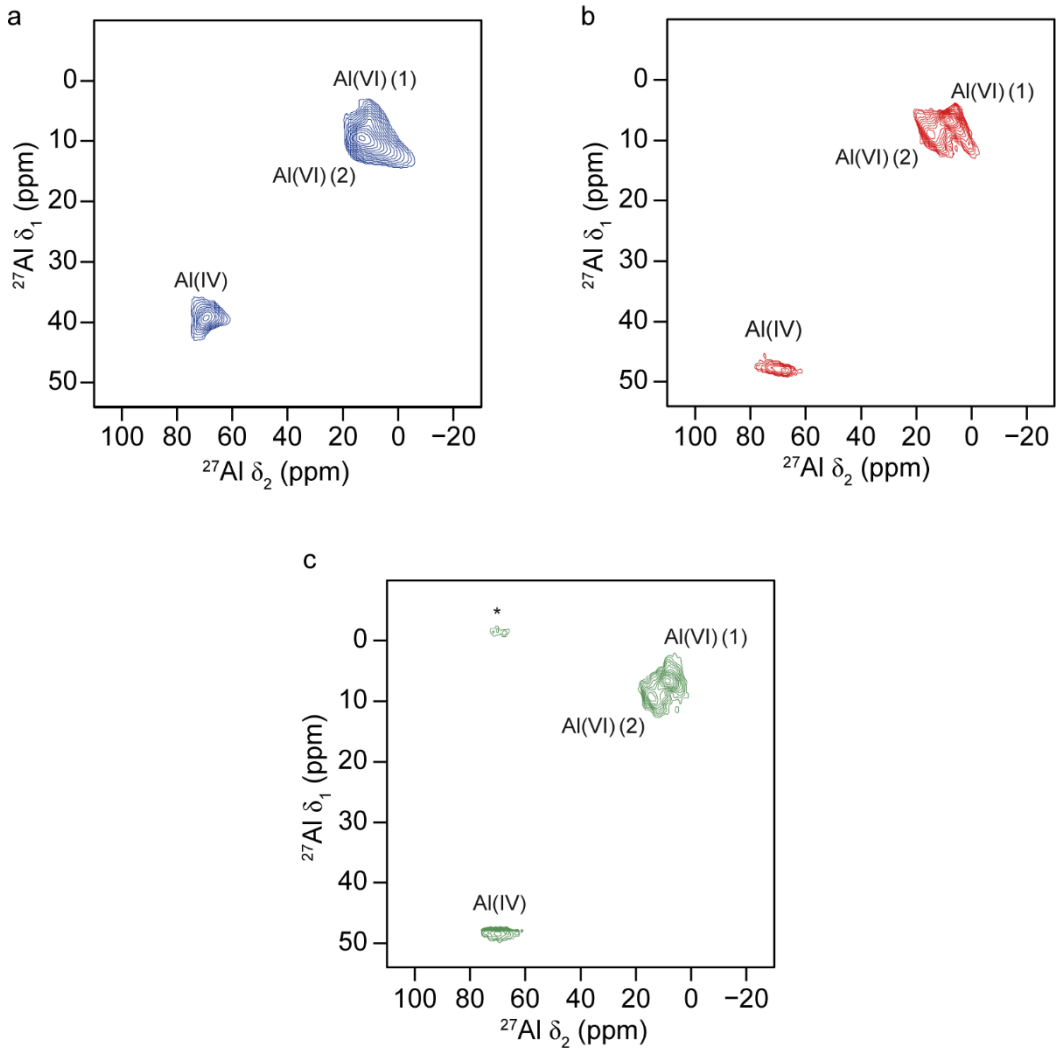

Figure 5.18. *^{27}Al (14. 1 T, 14 kHz MAS (a) and 20 kHz MAS (b and c)) z-filtered 3QMAS spectra of (a) $MgAl_2O_4$, (b) $CoAl_2O_4$ and (c) Co-$CoAl_2O_4$. A shearing transformation has been applied to all spectra. Resonances corresponding to Al(IV) and Al(VI) species are labelled. * denotes a spinning sideband.*

rise to Al(IV) species.[110] This also seems to be the case for both $CoAl_2O_4$ and Co-$CoAl_2O_4$, although their tetrahedral resonances show reduced intensity compared to those of $MgAl_2O_4$. It has been reported though, that the occupation of tetrahedral sites by Al in $CoAl_2O_4$ is disfavoured at low temperature and pressure, instead Al prefers to adopt predominantly Al(VI) arrangements.[111] This finding is consistent with the results observed above, as well as prior work by Angeletti *et al.* that indicated that the

Table 5.7. *NMR parameters (average quadrupolar product, $\langle P_Q \rangle$ and average isotropic chemical shift, $\langle \delta_{iso} \rangle$) for the Al sites in $MgAl_2O_4$, $CoAl_2O_4$ and Co-$CoAl_2O_4$, obtained from the z-filtered 3QMAS spectra in Figure 5.18.*

Sample	Al(IV)		Al(VI)			
	$\langle P_Q \rangle$ / MHz	$\langle \delta_{iso} \rangle$	$\langle P_Q \rangle$ / MHz		$\langle \delta_{iso} \rangle$ (ppm)	
			(Site 1)	(Site 2)	(Site 1)	(Site 2)
$MgAl_2O_4$	2.5 (2)	71 (2)	3.4 (3)	2.7 (3)	12 (3)	16 (3)
$CoAl_2O_4$	6.6 (2)	81 (2)	3.2 (3)	2.3 (3)	11 (3)	16 (3)
Co-$CoAl_2O_4$	6.9 (2)	82 (2)	3.1 (3)	2.7 (3)	11 (3)	16 (3)

majority of tetrahedral sites in $CoAl_2O_4$-type structures are occupied by Co^{2+} ions.[112] A reduction in the intensity of the Al(IV) peak going from $CoAl_2O_4$ to Co-$CoAl_2O_4$, suggests that this may be the surface binding site for Co oxide crystallites, in line with the trend observed for series two catalysts in section 5.4.2 above. Figure 5.17(b) shows ^{27}Al DP NMR spectra of the aluminate materials acquired at a higher magnetic field strength of 14.1 T. Owing to the increased chemical shift dispersion and the reduction in second-order quadrupolar broadening, a splitting of the Al(VI) resonance can be observed, suggesting the presence of two types of octahedral Al species in both $CoAl_2O_4$ and Co-$CoAl_2O_4$, although it is not evident that this is the case for $MgAl_2O_4$. Additionally, the $CoAl_2O_4$ materials display markedly broader Al(IV) resonances when compared to $MgAl_2O_4$, indicative of distinctly different local environments, or because of paramagnetic broadening, in these two types of spinel structure. To further investigate these findings, ^{27}Al 3QMAS experiments were performed at 14.1 T, and the spectra that were obtained are shown in Figure 5.18. They confirm that there are indeed two types of Al(VI) site present in $CoAl_2O_4$ and Co-$CoAl_2O_4$ as hypothesised, as well as in $MgAl_2O_4$ which although reported by other researchers previously,[110] was not readily apparent from the 1D NMR spectra obtained in this work. Table 5.7 gives the NMR parameters that were extracted from each of the 3QMAS spectra in Figure 5.18 above. A relatively low average P_Q value is observed for the Al(IV) site in $MgAl_2O_4$. This is consistent with the fact that tetrahedral vacancies become readily available in this material through cation rearrangement,[110] and Al appears to readily

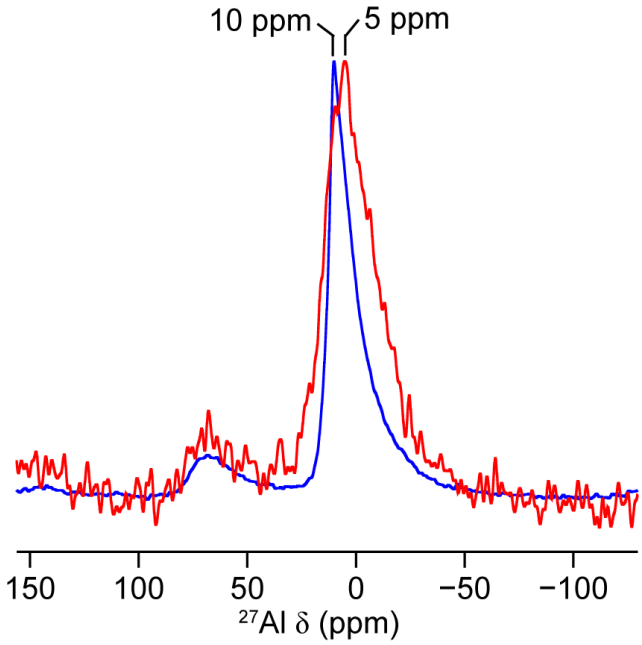

Figure 5.19. *^{1}H-^{27}Al (9.4 T, 14 kHz MAS, τ_{CP} = 0.8 ms) CP NMR spectra of $MgAl_2O_4$ (blue) and $CoAl_2O_4$ (red).*

substitute into them, and experiences a relatively ordered local environment. By contrast, notably large average P_Q values are seen for the Al(IV) sites in both $CoAl_2O_4$ and Co-$CoAl_2O_4$. $CoAl_2O_4$ seems less prone to exhibiting tetrahedral site vacancies, and where they do exist, the Al that substitutes into these experiences a stronger quadrupolar interaction. ^{59}Co, (spin I = 7/2) is the sole (100%) naturally-abundant stable isotope of cobalt and possesses a large quadrupole moment (42 Q/fm^2). By contrast, ^{25}Mg (spin I = 5/2) has a natural abundance of 10%. All other Mg isotopes are NMR inactive. The quadrupole moment of ^{25}Mg (19.94 Q/fm^2) is less than half that of ^{59}Co.[113] A tetrahedrally-coordinated Al with neighbouring Co units will therefore experience a substantially different local environment than one with neighbouring Mg units. This is further evidenced by the increase in the average δ_{iso} value by ~10 ppm going from a Mg-containing to Co-containing spinels. As seen from the spectra in Figure 5.18, there are two types of Al(VI) sites present in each of the three spinel materials. One of these sites exhibits a slightly larger average P_Q value than the other across all three materials studied. This tentatively suggests that one Al(VI) site may be located closer to the surface of the spinel, but in a similar overall local environment to its smaller P_Q counterpart. This is in reasonable agreement with

a previous study of $MgAl_2O_4$ by Kashii *et al.*,[110] who attributed the increased average P_Q value of one of the octahedral Al sites to those species residing in a more distorted coordination environment. However, additional investigations are required in order to confirm this hypothesis. The average P_Q values of both Al(VI) sites exhibit no increase going from a Mg-containing spinel to Co-containing ones though, indicating that this type of Al species is not likely to be located close to or be bonded with, Co sites in either of the two samples studied.

To explore further the surface environments of the aluminate materials, ^{1}H-^{27}Al CP NMR experiments on $MgAl_2O_4$ and $CoAl_2O_4$ were performed. The experiment was also attempted on an aliquot of Co-$CoAl_2O_4$ and although successful, displayed a significantly reduced level of sensitivity when compared to the other two samples. This may be due in part to the low level of protons residing at the surface of this material. Figure 5.19 shows the NMR spectra that were obtained from these experiments on $MgAl_2O_4$ and $CoAl_2O_4$. They reveal that both Al(IV) and Al(VI) species are present near the surface of both spinel materials, with Al(VI) being the most predominant. A variation of ^{27}Al $\delta_{obs} \approx 5$ ppm reflects two characteristically-different surface Al(VI) species. One receives magnetisation from protons associated with adsorbed H_2O, MgOH and AlOH environments. Magnetisation transfer to the other type of surface Al(VI) originates predominantly only from adsorbed H_2O, although there may also be a contribution from AlOH species. A reduction in intensity of the Al(IV) resonance for both materials, compared to their ^{27}Al DP NMR spectra, suggests that only some of these Al sites are located close to the surface. This is particularly evident for $MgAl_2O_4$, and indicates that the majority of Al(IV) species are found in the bulk of this particular material, a theory consistent with previously documented "cation mixing" behaviour.[110]

5.6 Conclusions

The work presented in this chapter has demonstrated that ^{1}H and ^{27}Al solid-state NMR spectroscopy is an effective and versatile tool for the characterisation of γ-Al_2O_3-based supported metal catalysts. CP and D-HMQC experiments applied on the γ-Al_2O_3

support have conclusively demonstrated the existence of Al(V) sites on the surface of this material. It has been shown that removal of adsorbed H_2O may facilitate a rearrangement effect on the surface of γ-Al_2O_3 that promotes the generation of this type of Al species. Data obtained for Co-γ-Al_2O_3 model catalysts indicates that the MSI does exist in many of these systems, and is most prominent for materials containing small, well dispersed Co oxide crystallites. Incipient wetness impregnation-based methods appear to promote the formation of a MSI to a far greater extent than colloidal approaches, which tend to favour the formation of co-mixtures that are composed of self-contained Co oxide "nanocubes". Although the deposition of Co_3O_4 onto the surface of γ-Al_2O_3 effectively removes OH functionality, the hygroscopic nature of the alumina allows the extent of the MSI to be visualised by observing the extent of the proton-metal oxide interaction, by ^{1}H MAS NMR *via* the presence of adsorbed H_2O. Therefore, in these materials, water can be said to be both adventitious and advantageous. Results obtained from ^{1}H-^{27}Al CP and ^{27}Al z-filtered 3QMAS experiments indicate Al(IV) environments to be the preferential interfacial site for Co oxide crystallites on the surface of γ-Al_2O_3. It has also been shown that this may be the case for Co spinel aluminate materials. In addition, the surface chemistry of the diamagnetic analogue $MgAl_2O_4$ has also been investigated, with MgOH and AlOH environments identified. It has also been demonstrated that two types of Al(VI) species are present in $MgAl_2O_4$, $CoAl_2O_4$ and Co-$CoAl_2O_4$, one of which may be located closer to the surface of the spinels. These findings, whilst providing valuable insights into the surface/bulk chemistry of supported metal catalysts, also demonstrate the necessity for further investigation of these industrially-relevant materials.

5.7 References

1. A. de Klerk, *Green Chem*., 2008, **10**, 1249.
2. G. Prieto, M. I. S. De Mello, P. Concepción, R. Murciano, S. B. C. Pergher and A. Martínez, *ACS Catal.*, 2015, **5**, 3323.
3. A. Y. Khodakov, W. Chu and P. Fongarland, *Chem. Rev.*, 2007, **107**, 1692.
4. H. Jahangiri, J. Bennett, P. Mahjoubi, K. Wilson and S. Gu, *Catal. Sci. Technol.*, 2014, **4**, 2210.

5. J. Hu, F. Yu and Y. Lu, *Catalysts*, 2012, **2**, 303.
6. E. Inglesia, *Appl. Catal. A*, 1997, **161**, 59.
7. C. R. Reuel and C. H. Bartholomew, *J. Catal.* 1984, **85**, 78.
8. Q. Zhang, J. Kang and Y. Wang, *ChemCatChem*, 2010, **2**, 1030.
9. D. A. H. Hanaor and C. C. Sorrell, *J. Mater. Sci.*, 2011, **46**, 855.
10. X. Sun, M. Dyballa, J. Yan, L. Li, N. Guan and M. Hunger, *Chem. Phys. Lett.*, 2014, **594**, 34.
11. K. Shimura, T. Miyazawa, T. Hanaoka and S. Hirata, *Appl. Catal. A*, 2013, **460-461**, 8.
12. M. C. J. Bradford and M. A. Vannice, *Appl. Catal. A*, 1996, **142**, 73.
13. W. A. Deer, R. A. Howie and J. Zussman, *An Introduction to the Rock-Forming Minerals*, Pearson Education, Harlow, 1992.
14. Y. Ohtsuka, T. Arai, S. Takasaki, and N. Tsubouchi, *Energy Fuels*, 2003, **17**, 804.
15. A. Martínez, C. López, F. Márquez, and I. Díaz, *J. Catal.*, 2003, **220**, 486.
16. D. Zhao, J. Feng, Q. Huo, N. Melosh, G. H. Fredrickson, B. F. Chmelka and G. D. Stucky, *Science*, 1998, **279**, 548.
17. A. Griboval-Constant, A. Y. Khodakov, R. Bechara and V. L. Zholobenko, *Stud. Surf. Sci. Catal.*, 2002, **144**, 609.
18. A. R. West, *Solid State Chemistry and its Applications*, Wiley, Chichester, 2nd Edn., 2014.
19. P. C. Borman and K. R. Westerterp, *Ind. Eng. Chem. Res.*, 1995, **34**, 49.
20. D. M. Minahan and G. B. Hoflund, *J. Catal.*, 1996, **158**, 109.
21. X. She and M. Flytzani-Stephanopoulos, *J. Catal.*, 2006, **237**, 79.
22. I. Levin and D. Brandon, *J. Am. Ceram. Soc.*, 1998, **81**, 1995.
23. G. Busca, *Chem. Rev.*, 2007, **107**, 5366.
24. M. Trueba and S. P. Trasatti, *Eur. J. Inorg. Chem.*, 2005, 3393.
25. D. Lee, N. T. Duong, O. Lafon and G. De Paëpe, *J. Phys. Chem. C*, 2014, **118**, 25065.
26. G. Jacobs, T. K. Das, Y. Zhang, J. Li, G. Racoillet and B. H. Davis, *Appl. Catal. A*, 2002, **233**, 263.
27. T. Lin, X. Meng and L. Shi, *Ind. Eng. Chem. Res.*, 2012, **51**, 13123.

28. A. Zhao, W. Ying, H. Zhang, H. Ma and D. Fang, *Catal. Commun.*, 2012, **17**, 34.
29. S. Jang, S. W. Kang, D. H. Chun, H-T. Lee, J-I. Yang, H. Jung, H-D. Jeong, K. M. Nam and J. C. Park, *New J. Chem.*, 2017, **41**, 2756.
30. A. Jean-Marie, A. Griboval-Constant, A. Y. Khodakov and F. Diehl, *C. R. Chimie*, 2009, **12**, 660.
31. S. J. Tauster, S. C. Fung and R. L. Garten, *J. Am. Chem. Soc.*, 1978, **100**, 170.
32. R. Bechara, D. Balloy and D. Vanhove, *Appl. Catal. A*, 2001, **207**, 343.
33. P. Munnik, P. E. de Jongh and K. P. de Jong, *Chem. Rev.*, 2015, **115**, 6687.
34. S. J. Tauster, *Acc. Chem. Res.*, 1987, **20**, 389.
35. B. K. Min, A. K. Santra and D. W. Goodman, *Catal. Today*, 2003, **85**, 113.
36. M. Bowker, P. Stone, P. Morrall, R. Smith, R. Bennett, N. Perkins, R. Kvon, C. Pang, E. Fourre and M. Hall, *J. Catal.*, 2005, **234**, 172.
37. D. W. Goodman, *Catal. Lett.*, 2005, **99**, 1.
38. K. S. Chung and F. E. Massoth, *J. Catal.*, 1980, **64**, 320.
39. *US Pat.* US20100048742A1, 2010.
40. G. E. Batley, A. Ekstrom and D. A. Johnson, *J. Catal.*, 1975, **34**, 368.
41. H. F. van't Blik, J. D. C. Koningsberger and R. Prins, *J. Catal.* 1986, **97**, 210.
42. G. Jacobs, J. A. Chaney, P. M. Patterson, T. K. Das, J. C. Maillot and B. H. Davis, *J. Synchrotron Radiat.*, 2004, **11**, 414.
43. D. Schanke, S. Vada, E. A. Blekkan, A. M. Hilmen, A. Hoff and A. Holmen, *J. Catal.*, 1995, **156**, 85.
44. A. Kogelbauer, J. G. Goodwin Jr and R. Oukaci, *J. Catal.*, 1996, **160**, 125.
45. W. Ma, G. Jacobs, R. A. Keogh, D. B. Bukur and B. H. Davis, *Appl. Catal. A*, 2012, **437-438**, 1.
46. T. K Das, G. Jacobs, P. M. Patterson, W. A. Conner, J. Li and B. H Davis, *Fuel*, 2003, **82**, 805.
47. A. Wong, M. E. Smith, V. Terskikh and G. Wu, *Can. J. Chem.*, 2011, **89**, 1087.
48. S. K. Lee and J. F. Stebbins, *J. Phys. Chem. B*, 2000, **104**, 4091.
49. J. Livage, F. Babonneau, M. Chatry and L. Coury, *Ceram. Int.*, 1997, **23**, 13.
50. A. Rawal, B. J. Smith, G. L. Athens, C. L. Edwards, L. Roberts, V. Gupta and B. F. Chmelka, *J. Am. Chem. Soc.*, 2010, **132**, 7321.

51. A. P. M. Kentgens, *Geoderma*, 1997, **80**, 271.
52. R. F. Moran, D. M. Dawson and S. E. Ashbrook, *Int. Rev. Phys. Chem.*, 2017, **36**, 39.
53. B. Bureau, G. Silly, J. Y. Buzare, C. Legein and D. Massiot, *Solid State Nucl. Magn. Reson.*, 1999, **14**, 181.
54. D. R. Neuville, L. Cormier and D. Massiot, *Geochim. Cosmochim. Acta*, 2004, **68**, 5071.
55. J.-B. d'Espinose de Lacaillerie, C. Fretigny and D. Massiot, *J. Magn. Reson.*, 2008, **192**, 244.
56. G. Czjzek, J. Fink, F. Gotz, H. Schmidt, J. M. D. Coey, J. P. Rebouillat and A. Lienard, *Phys. Rev. B*, 1981, **23**, 2513.
57. D. Massiot, F. Fayon, M. Capron, I. King, S. Le Calvé, B. Alonso, J.-O. Durand, B. Bujoli, Z. Gan and G. Hoatson, *Magn. Reson. Chem.*, 2002, **40**, 70.
58. J.-P. Amoureux and C. Fernandez, *Solid State Nucl. Magn. Reson.*, 1998, **10**, 211.
59. D. H. Morris and P. D. Ellis, *J. Am. Chem. Soc.*, 1989, **111**, 6045.
60. F. R. Chen, J. G. Davis and J. J. Fripiat, *J. Catal.*, 1992, **133**, 263.
61. J. H. Kwak, J. Z. Hu, D. H. Kim, J. Szanyi and C. H. F. Peden, *J. Catal.*, 2007, **251**, 189.
62. J. H. Kwak, J. Hu, A. Lukaski, D. H. Kim, J. Szanyi and C. H. F. Peden, *J. Phys. Chem. C*, 2008, **112**, 9486.
63. J. Z. Hu, S. Xu, J. H. Kwak, M. Y. Hu, C. Wan, Z. Zhao, J. Szanyi, X. Bao, X. Han, Y. Wang and C. H. F. Peden, *J. Catal.*, 2016, **336**, 85.
64. S. E. Ashbrook and S. Wimperis, *Chem. Phys. Lett.*, 2001, **340**, 500.
65. Z. Gan, *J. Magn. Reson.*, 2007, **184**, 39.
66. J. Trébosc, B. Hu, J.-P. Amoureux and Z. Gan, *J. Magn. Reson.*, 2007, **186**, 220.
67. L. Müller, *J. Am. Chem. Soc.*, 1979, **101**, 4481.
68. G. Tricot, J. Trébosc, F. Pourpoint, R. Gauvin and L. Delevoye, *Annu. Rep. NMR Spectrosc.*, 2014, **81**, 145.

69. N. Merle, J. Trébosc, A. Baudouin, I. Del Rosal, L. Maron, K. Szeto, M. Genelot, A. Mortreux, M. Taoufik, L. Delevoye and R. M. Gauvin, *J. Am. Chem. Soc.*, 2012, **134**, 9263.
70. M. Taoufik, K. C. Szeto, N. Merle, I. D. Rosal, L. Maron, J. Trébosc, G. Tricot, R. M. Gauvin and L. Delevoye, *Chem. Eur. J.*, 2014, **20**, 4038.
71. A. Brinkmann and A. P. M. Kentgens, *J. Am. Chem. Soc.*, 2006, **128**, 14758.
72. X. Lu, O. Lafon, J. Trébosc, G. Tricot, L. Delevoye, F. Méar, L. Montagne and J.-P. Amoureux, *J. Chem. Phys.*, 2012, **137**, 144201.
73. J. J. Fitzgerald, G. Piedra, S. F. Dec, M. Seger and G. E. Maciel, *J. Am. Chem. Soc.*, 1997, **119**, 7832.
74. J. Z. Hu, J. H. Kwak, J. E. Herrera, Y. Wang and C. H. F. Peden, *Solid State Nucl. Magn. Reson.*, 2005, **27**, 200.
75. M. B. Osman, S. Diallo-Garcia, V. Herledan, D. Brouri, T. Yoshioka, J. Kubo, Y. Millot and G. Costentin, *J. Phys. Chem. C*, 2015, **119**, 23008.
76. S. Novak, S. M. H. Olhero, J. M. F. Ferreira and A. Zupančič, *Rheol. Acta*, 2004, **43**, 559.
77. *US Pat.* US2431370A, 1947.
78. *US Pat.* US3623993A, 1971.
79. W. D. Bellamy, F. Damez, B. Langlais, A. Montiel, K. L. Rakness, D. A. Reckhow and C. M. Robson, in *Ozone in Water Treatment: Application and Engineering*, Eds. B. Langlais, D. A. Reckhow and D. R. Brink, CRC Press, Boca Raton, 1991.
80. J. Joubert, P. Fleurat-Lessard, F. Delbecq and P. Sautet, *J. Phys. Chem. B*, 2006, **110**, 7392.
81. D. S. Maciver, H. H. Tobin and R. T. Barth, *J. Catal.*, 1963, **2**, 485.
82. T. M. H. Costa, M. R. Gallas, E. V. Benvenutti and J. A. H. da Jornada, *J. Phys. Chem. B*, 1999, **103**, 4278.
83. R. Wischert, P. Florian, C. Copéret, D. Massiot and P. Sautet, *J. Phys. Chem. C*, 2014, **118**, 15292.
84. D. Coster, A. L. Biumenfeld, and J. J. Fripiat, *J. Phys. Chem.*, 1994, **98**, 6201.
85. S. Sadasivan, R. M. Bellabarba and R. P. Tooze, *Nanoscale*, 2013, **5**, 11139.

86. V. Iablokov, S. K. Beaumont, S. Alayoglu, V. V. Pushkarev, C. Specht, J. Gao, A. P. Alivisatos, N. Kruse and G. A. Somorjai, *Nano Lett.*, 2012, **12**, 3091.
87. V. F. Puntes, K. Krishnan and A. P. Alivisatos, *Top. Catal.*, 2002, **19**, 145.
88. A. Roucoux, J. Schulz and H. Patin, *Chem. Rev.*, 2002, **102**, 3757.
89. R. Xu and C. H. Zeng, *Langmuir*, 2004, **20**, 9780.
90. V. I. Bakhmutov, *Solid-State NMR in Materials Science Principles and Applications*, CRC Press, Boca Raton, 2012.
91. A. Lesage, M. Bardet and L. Emsley, *J. Am. Chem. Soc.*, 1999, **121**, 10987.
92. W. Sommer, J. Gottwald, D. E. Demco and H. W. Spiess, *J. Magn. Reson. A*, 1995, **113**, 131.
93. M. Feike, D. E. Demco, R. Graf, J. Gottwald, S. Hafner and H. W. Spiess, *J. Magn. Reson. A*, 1996, **122**, 214.
94. V. M. Mastikhin, A. V. Nosov, V. V. Terskikh and K. I. Zamaraev, *J. Phys. Chem.*, 1994, **98**, 13621.
95. V. Vitzthum, F. Borcard, S. Jannin, M. Morin, P. Miéville, M. A. Caporini, A. Sienkiewicz, S. Gerber-Lemaire and G. Bodenhausen, *ChemPhysChem*, 2011, **12**, 2929.
96. S. Lange, A. H. Linden, U. Akbey, W. T. Franks, N. M. Loening, B. J. van Rossum and H. Oschkinat, *J. Magn. Reson.*, 2012, **216**, 209.
97. K. R. Thurber and R. Tycko, *J. Chem. Phys*., 2014, **140**, 184201.
98. D. G. Cory and W. M. Ritchey, *J. Magn. Reson.*, 1988, **80**, 128.
99. J. Feng and J. A. Reimer, *J. Magn. Reson.*, 2011, **209**, 300.
100. S. Caldarelli, H. Pizzala, L. Arrighi, F. Ziarelli and G. Busca, *J. Phys. Chem. C.*, 2011, **115**, 10569.
101. H. E. Gottlieb, V. Kotlyar and A. Nudelman, *J. Org. Chem.*, 1997, **62**, 7512.
102. M. H. Levitt, *Spin Dynamics: Basics of Nuclear Magnetic Resonance*, Wiley, Chichester, 2nd Edn., 2008.
103. L. Xu, J. Zhang, F. Wang, K. Yuan, L. Wang, K. Wu, G. Xu and W. Chen, *RSC Adv.*, 2015, **5**, 48256.
104. V. Zarkov and D. Mehandjiev, *Appl. Catal. A*, 1993, **94**, 161.
105. P. Thormählen, E. Fridell, N. Cruise, M. Skoglundh and A. Palmqvist, *Appl. Catal. B*, 2001, **31**, 1.

106. B. Hu, W.-G. Kim, T. P. Sulmonetti, M. L. Sarazen, S. Tan, J. So, Y. Liu, R. Dixit, S. Nair and C. W. Jones, *ChemCatChem*, 2017, **9**, 3330.
107. Y. Jiang, J. Huang, W. Dai and M. Hunger, *Solid State Nucl. Magn. Reson.*, 2011, **39**, 116.
108. Z. Wang, Y. Jiang, O. Lafon, J. Trébosc, K. D. Kim, C. Stampfl, A. Baiker, J.-P. Amoureux and J. Huang, *Nat. Commun.*, 2016, **7**, 13820.
109. K. Liu, D. Ryan, K. Nakanishi and A. McDermott, *J. Am. Chem. Soc.*, 1995, **117**, 6897.
110. N. Kashii, N. Maekawa and Y. Hinatsu, *J. Am. Ceram. Soc.*, 1999, **82**, 1844.
111. R. Franco, F. Tielens, M. Calatayud and J. M. Recio, *High Press. Res.*, 2008, **28**, 521.
112. C. Angeletti, F. Pepe and P. Porta, *J. Chem. Soc., Faraday Trans. 1*, 1977, **73**, 1972.
113. R. K. Harris, E. D. Becker, S. M. C. de Menezes, R. Goodfellow and P. Granger, *Pure Appl. Chem.*, 2001, **73**, 1795.

Chapter 6. Exploring the Structures of Si- and Ti-Alumina Catalysts

This chapter describes efforts to understand the structure of silicated alumina catalysts. It outlines the insight into the surface chemistry and interatomic interactions that has been gained using multinuclear (^{1}H, ^{29}Si, ^{27}Al and ^{17}O) solid-state NMR techniques. This includes the combined application of isotopic enrichment and DNP NMR spectroscopy to the study of model silicated alumina catalysts, which has facilitated the acquisition of conventional MAS and advanced 2D experiments. Two different approaches for silica grafting onto γ-Al_2O_3, "sequential grafting" and "single shot", are compared by combining information obtained from solid-state NMR and X-ray photoelectron spectroscopies. By doing so, a window is provided into the growth morphology of silica on catalytically-relevant oxide materials. The application of multinuclear solid-state NMR spectroscopic approaches (^{1}H, ^{27}Al and ^{17}O) for elucidating the structure of two types of titanium-modified catalysts are also described. Insights have been provided into the relationship between preparation route and catalyst structure, both in terms of the location of Ti species and the interfacial role of Al(V).

6.1 Introduction to Silicated Alumina Catalysts

Silicated aluminas are an important analogue of the catalytically-active aluminium oxide family. The modification of γ-Al_2O_3 with silica results in materials with high surface areas that possess Brønsted acidity, unlocking their potential for use in catalytic applications.[1] These materials are commonly employed as solid acid catalysts and are an integral part of many key industrial processes, including fluid catalytic cracking, the conversion of syngas to dimethyl ether, ethanol dehydration and skeletal isomerisation.[1-6]

The presence of both Si and Al at the surface generates the mild acidity that is essential to catalytic behaviour,[1] but a full consensus on the detailed structure of these acidic environments has yet to be reached.[2-4] Understanding the catalytic behaviour of these

functionalised materials requires a molecular level description of the reactive surface, which is far from trivial. The difficulty lies partly in the diverse range of possible surface structures and in their typically amorphous character. For example, the catalytic surface does not exhibit sufficient long-range order to allow for structure determination *via* diffraction-based methods.[7] Vibrational spectroscopy can provide information on the presence of various structural motifs, using molecular probes, but the spectra obtained are often highly complex, leading to difficult and subjective/uncertain data interpretation.[8] As a result, the connectivity between Si and Al species is not easily assessed using this approach.

6.2 DNP NMR and Isotopic Enrichment: A Combined Spectroscopic Approach

Solid-state NMR spectroscopy is ideally suited to investigating the local environment of Si and Al in silicated aluminas, having no requirement for long-range order and being sensitive to small changes in local chemical environments.[9-11] However, this technique suffers from inherently low sensitivity (particularly for ^{29}Si, which has a natural abundance of 4.7%). The resulting long acquisition times, for low levels of Si incorporation present additional challenges, particularly for the implementation of more complex multinuclear and multidimensional experiments.[12] Furthermore, it can be difficult to distinguish signals of the bulk from those of the surface, where reaction chemistry occurs. For example, the suitability of conventional ^{27}Al solid-state NMR spectroscopy is debatable for the characterisation of transition aluminas since most of the detectable signal reflects coordination geometries of the bulk rather than the nature of the surface that is responsible for catalytic reaction chemistry.[13]

Recent years have seen an improvement in the sensitivity of NMR experiments facilitated by the use of DNP. As outlined in Chapters 2 and 3, DNP can, owing to the high signal enhancements available, aid in overcoming the inherently poor sensitivity of many NMR experiments and is being applied increasingly to probe the detailed surface structure of a diverse range of materials.[14-16] It has previously been mentioned that DNP enhancements are described by the DNP enhancement factor, ε. This is determined from the ratio of signal intensities in spectra acquired with and without

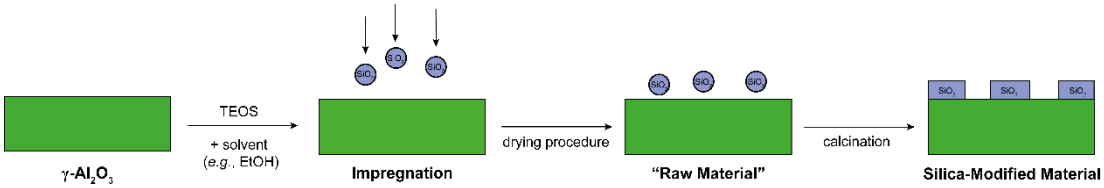

Figure 6.1. *Schematic illustration of the procedure used to prepare the silicated alumina materials studied in this work.*

microwave irradiation and is dependent on temperature, microwave power, concentration of the exogenous radical source and the extent of surface wetting.[14,15] However, the intensity of the signals observed in a DNP experiment also depends on the efficiency of the CP transfer, which is dependent on the local ^{1}H density. For example, resonances resulting from lower-order Q^n Si centres (where Q^n denotes a species of structure $Si(OR)_n(OH)_{4-n}$, where R = Si or Al), which possess a high local proton density, may appear with higher signal intensity than species where n is higher order. Such effects have been previously demonstrated by Lelli *et al.* who investigated phenol-functionalised silica surfaces.[17] These researchers showed that at very short τ_{CP} values only ^{29}Si resonances from species in close proximity to ^{1}H were enhanced, whereas signal intensity associated with Q^n sites that were more remote from ^{1}H increased only at longer τ_{CP} values. Although this variation may restrict CP, and therefore DNP, to providing a more qualitative, rather than quantitative, description of surface structure, it also provides important information on the atomic-scale environment around each species. Ideally, the spectra edited based on spatial proximity should be compared to more quantitative spectra (*i.e.*, from conventional experiments that do not rely on any polarisation transfer and have sufficiently long recycle intervals to account for any differences in relative relaxation). The low Si content of silicated alumina surfaces makes this somewhat of a challenge, negating some or all of the time saving originally achieved by using DNP. One solution is to use isotopic enrichment, to improve the sensitivity of the conventional NMR experiment to such an extent that spectra can be acquired on a reasonable timescale, and spectral lineshapes can be compared to those acquired using CP/DNP. Enrichment also has a positive outcome for the sensitivity of both heteronuclear, and homonuclear, 2D correlation NMR experiments, made possible using DNP, but ultimately limited by the low natural abundance of NMR-active Si species.

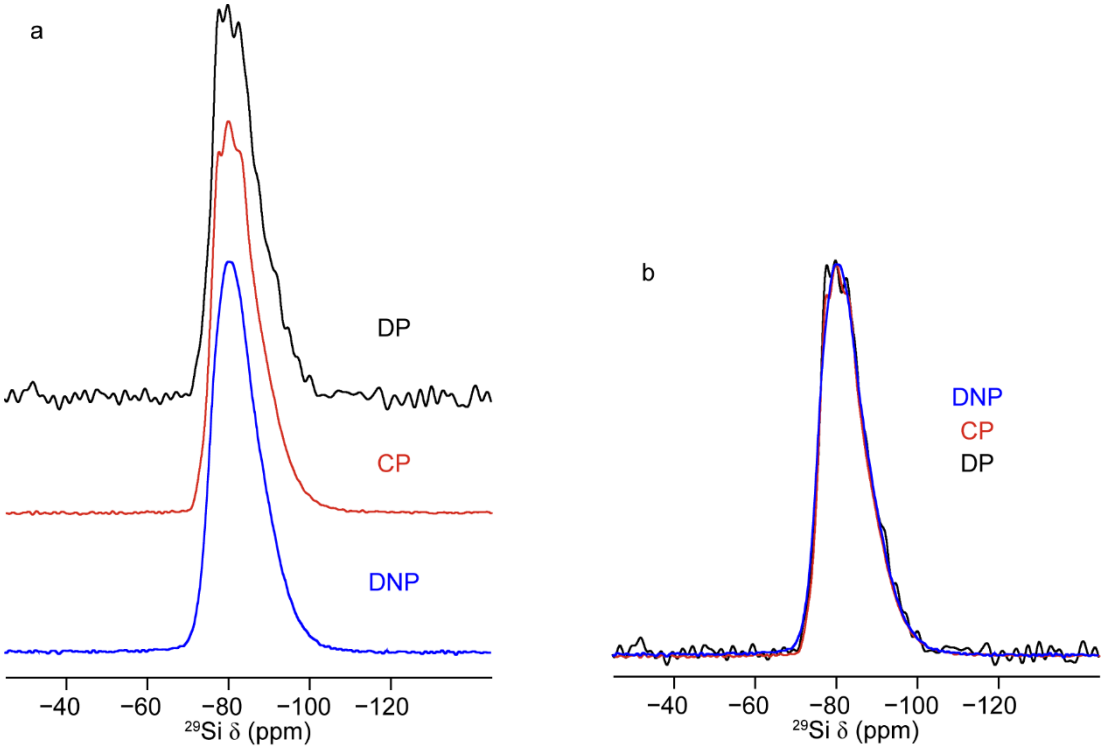

Figure 6.2. *^{29}Si and ^{1}H-^{29}Si (9.4 T, 10-14 kHz MAS) NMR spectra of 99% ^{29}Si-enriched Si-γ-Al_2O_3 (1.5 wt% Si), acquired using DP (black), CP (red) and DNP (blue). Spectra are shown (a) stacked and (b) overlaid. DP and CP spectra were acquired at room temperature on samples that had no radical added. The DNP spectrum was performed at 100 K. For CP and DNP spectra, τ_{CP} = 3 ms. In (b), spectral intensities have been normalised with respect to the centre of the lineshape in the DP NMR spectrum. For the DNP NMR spectrum, ε ^{29}Si CP = ~92.*

6.3 Silicated Alumina Model Catalysts: Si-γ-Al_2O_3 (1.5 wt% Si)

For this study, silicated alumina model catalysts containing 1.5 wt% Si were prepared by modification of γ-Al_2O_3 in the manner described in Chapter 4. ^{29}Si-enriched and non-enriched (natural abundance) versions of the material were prepared using either 99% ^{29}Si-enriched or conventional TEOS precursor, respectively. The preparation procedure is schematically illustrated in Figure 6.1.

Figure 6.2 shows ^{29}Si MAS NMR spectra of 99% ^{29}Si enriched Si-γ-Al_2O_3 (1.5 wt% Si), acquired *via* DP, CP and DNP. DP and CP experiments were all carried out at room temperature (298 K) on samples that did not have any radical added, while DNP experiments were carried out at low temperature (100 K). Given the inherently non-

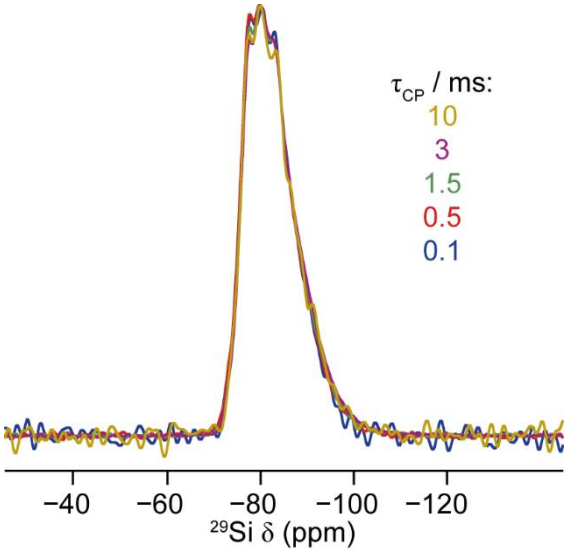

Figure 6.3. *^{1}H-^{29}Si (9.4 T, 10 kHz MAS) CP NMR spectra of 99% ^{29}Si-enriched Si- γ-Al_2O_3 (1.5 wt% Si) overlaid, acquired using τ_{CP} values between 0.1 and 10 ms. Spectral intensities have been normalised with respect to the centre of the lineshape.*

quantitative nature of CP and the additional surface sensitivity of DNP, the spectral lineshapes are remarkably similar, as shown in Figure 6.2(b), where the lineshapes are overlaid. The DP and CP spectra exhibit better resolution than the DNP spectrum, as a result either of increased relaxation arising from the presence of the radical or, more likely, owing to the lower temperature at which the experiments were performed. Despite the much greater sensitivity of the DNP spectrum, it is not possible to decompose the lineshape unambiguously into individual components. In contrast, four distinct environments can be discerned in the DP and CP NMR spectra. These consist of three sharp components at high frequency and a lower intensity, broader resonance at lower frequency.

Figure 6.3 shows the variation in the CP MAS NMR spectrum as a function of τ_{CP}. In contrast to the materials studied by Lelli *et al.*,[17] there are only very small differences observed in the spectral lineshape as τ_{CP} increases. It is not clear if this result suggests that no Q^4 species are present (*i.e.*, all Si are connected to at least one OH group), but is certainly possible at the low Si doping level (1.5 wt% Si) in the material studied here.[18,19] In general, a systematic shift in resonance position (of approximately −10 ppm) is expected as the number of coordinated bridging O species increases, typically resulting in the observation of Q^4 Si species at $\delta \approx -110$ ppm in silicates.[20] However,

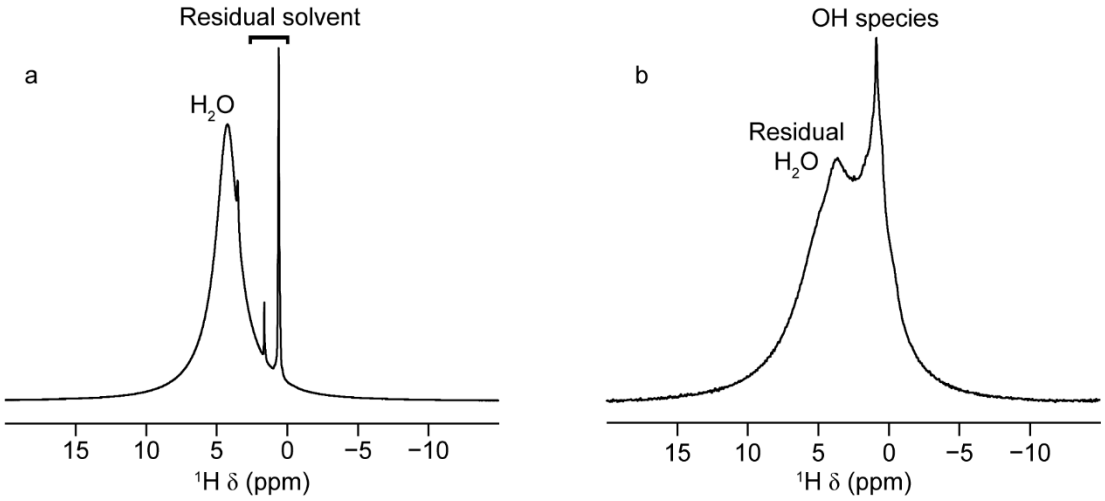

Figure 6.4. *^{1}H (9.4 T, 14 kHz MAS) NMR spectra of (a) hydrated and (b) dehydrated ^{29}Si-enriched Si-γ-Al_2O_3 (1.5 wt% Si). Relatively mild conditions were used for treatment to avoid surface dehydroxylation.*

this picture becomes more complex when considering the substitution of Si for Al (as in aluminosilicates), with an additional shift to higher frequency of 5 to 8 ppm per next nearest neighbor Al being observed.[21] As a result, it is difficult to unambiguously confirm whether Q^4 species are present in the spectra of Si-γ-Al_2O_3 simply of the basis of δ, although the observed signal extends over the region where these species are expected, even when considering the maximum possible substitution of Si for Al.

The features observed in the DP and CP spectral lineshapes in Figure 6.2 suggest the presence of differing Q^n species, making it even more noteworthy that very little variation in the spectral lineshape is observed between the two experiments and/or as a function of τ_{CP}. If Q^4 species are present, then it is clear from Figure 6.3 that the CP polarisation transfer remains equally efficient for all species, irrespective of the number of hydroxyl groups attached. However, it is possible that the presence of adventitious surface H_2O, previously encountered in Chapter 5, known to form extensive and strong H-bonding with silanols,[22-24] could affect the spectral intensities observed. To determine if adventitious H_2O plays a role in the CP dynamics, the ^{29}Si enriched Si-γ-Al_2O_3 material was dehydrated *in vacuo* at 150 °C and packed into a ZrO_2 rotor in a glovebox. Relatively mild conditions were used for dehydration to avoid any surface dehydroxylation. Verification of dehydration was obtained using ^{1}H

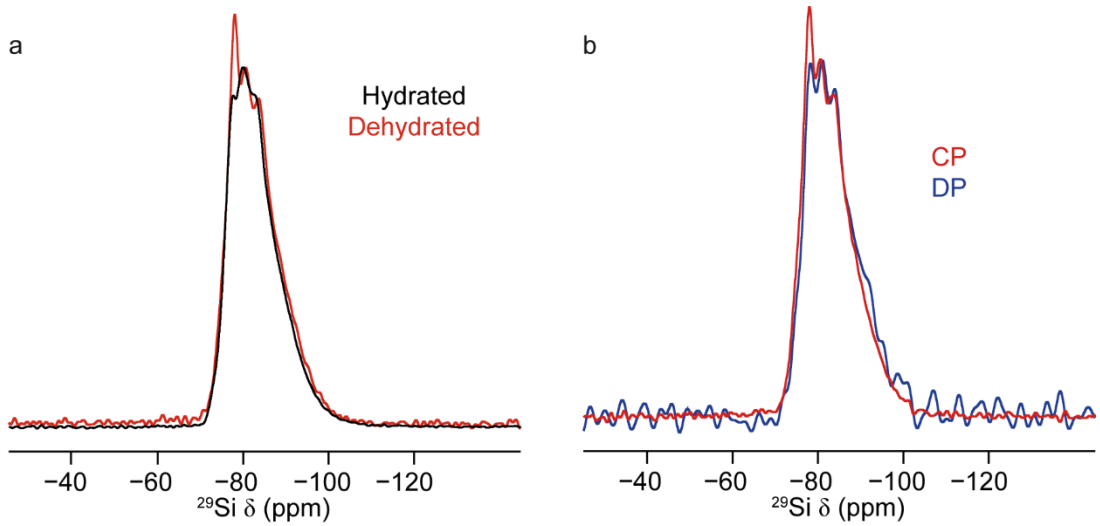

Figure 6.5. *(a) Comparison of ^{1}H-^{29}Si (9.4 T, 10 kHz MAS, τ_{CP} = 3 ms) CP NMR spectra of hydrated (black) and dehydrated (red) 99% ^{29}Si-enriched Si-γ-Al_2O_3 (1.5 wt% Si). Spectral intensities have been normalised with respect to the centre of the lineshape in the spectrum of the hydrated material. (b) ^{29}Si (9.4 T, 10-14 kHz MAS) NMR spectra of dehydrated ^{29}Si-enriched Si-γ-Al_2O_3 (1.5 wt% Si), acquired directly (blue) and using CP (red). Spectral intensities have been normalised with respect to the centre of the lineshape in the DP NMR spectrum.*

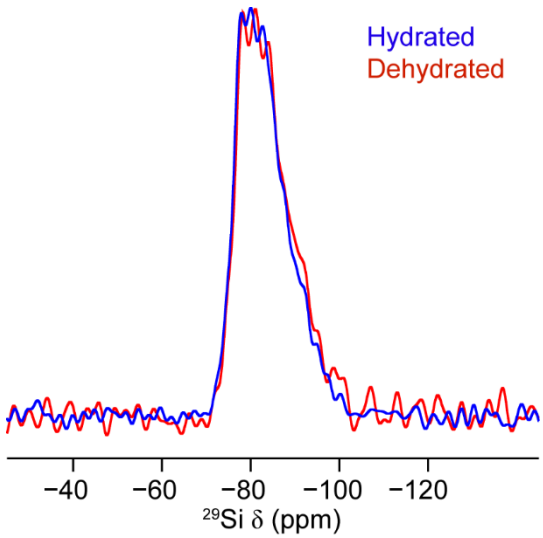

Figure 6.6. *^{29}Si (9.4 T, 14 kHz MAS) DP NMR spectra of hydrated (blue) and dehydrated (red) ^{29}Si-enriched Si-γ-Al_2O_3 (1.5 wt% Si). Spectral intensities have been normalised with respect to the centre of the lineshape in the spectrum of the hydrated material.*

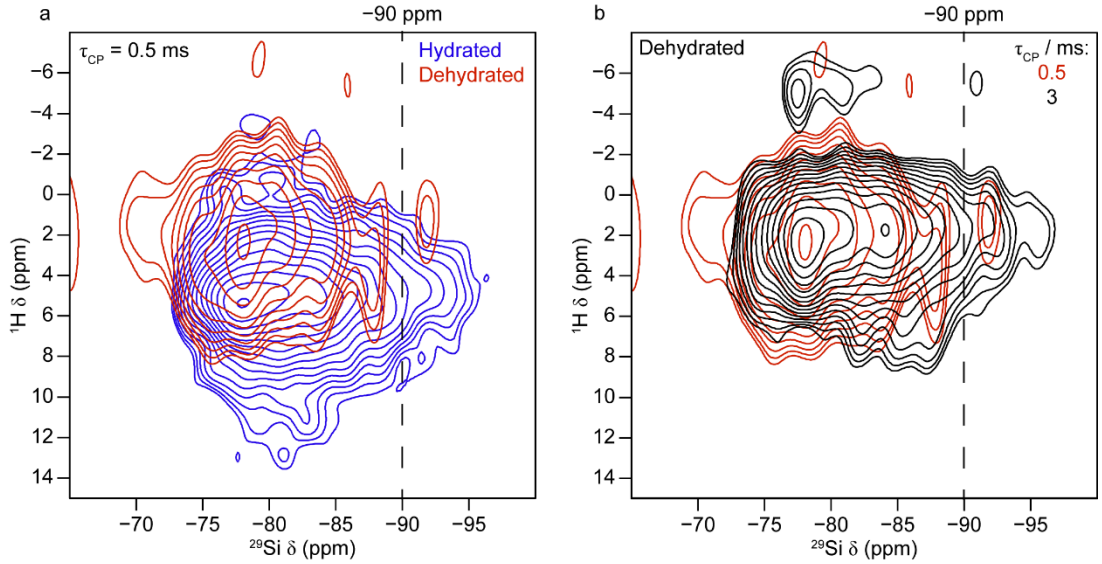

Figure 6.7. *^{1}H-^{29}Si (9.4 T, 10 kHz MAS, τ_{CP} = 0.5 or 3 ms) CP HETCOR NMR spectra of ^{29}Si-enriched Si-γ-Al_2O_3 (1.5 wt% Si), demonstrating the effect of (a) the hydration level of the sample and (b) τ_{CP} on the dehydrated material.*

MAS NMR, as seen in Figure 6.4, where spectra of as-made (*i.e.*, hydrated) and dehydrated Si-γ-Al_2O_3 are compared. They reveal a significant decrease in the intensity of the resonance attributed to H_2O (although not a complete removal of this signal), but retention of surface OH groups. Figure 6.5(a) compares the ^{29}Si CP MAS spectra of hydrated and dehydrated Si-γ-Al_2O_3 and reveals a change in the relative intensities of the spectral components, with an increase in signal intensity of the peak at $\delta = -78$ ppm, confirming the higher density of OH groups. This change is noticeable, but small, perhaps reflecting the retention of some water. The DP and CP spectra of dehydrated Si-γ-Al_2O_3 are similar, as shown in Figure 6.5(b), with a relative increase in the intensity of the signal at higher δ in the CP spectrum. Importantly, the DP NMR spectrum, displayed in Figure 6.6, remains largely unaffected by dehydration, an indication that surface structure has remained intact following treatment at an elevated temperature. It is evident that the H-bonded H_2O forms a sufficiently dense ^{1}H network at the silica surface, mediating efficient polarisation transfer to all Si species regardless of their chemical nature and OH functionality.

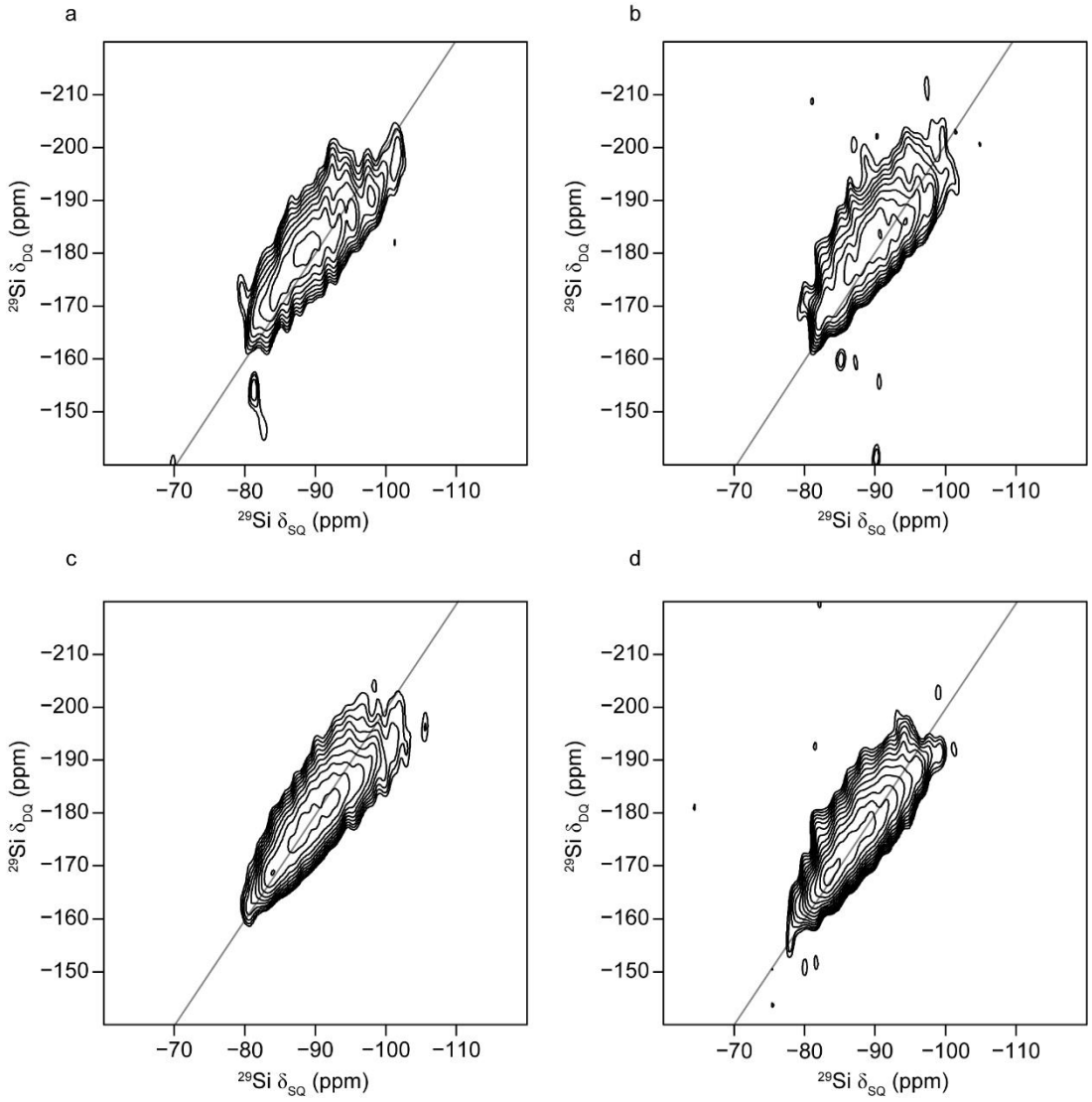

Figure 6.8. *^{29}Si (9.4 T, 12.5 kHz MAS) refocused CP INADEQUATE DNP NMR spectra of ^{29}Si-enriched Si-γ-Al_2O_3 (1.5 wt% Si), acquired using τ_J values of (a) 3.2 ms, (b) 6.4 ms, (c) 9.6 ms and (d) 16 ms. The solid grey line in each spectrum denotes the $\delta_{DQ} = 2\delta_{SQ}$ autocorrelation diagonal.*

Figure 6.7(a) compares ^{1}H-^{29}Si CP HETCOR NMR spectra of hydrated and dehydrated Si-γ-Al_2O_3 materials, and reveals distinct differences in the extent of correlation between ^{29}Si and ^{1}H upon the removal of H_2O. When dehydrated, higher-order Q^n species no longer correlate with surface protons because, in the absence of surface water, the ^{29}Si spectrum is influenced more significantly by local proton (OH) density. It is clear from Figure 6.7(b) that dehydration also results in a more significant variation in the spectral lineshape with τ_{CP}. At sufficiently long τ_{CP} values, correlations

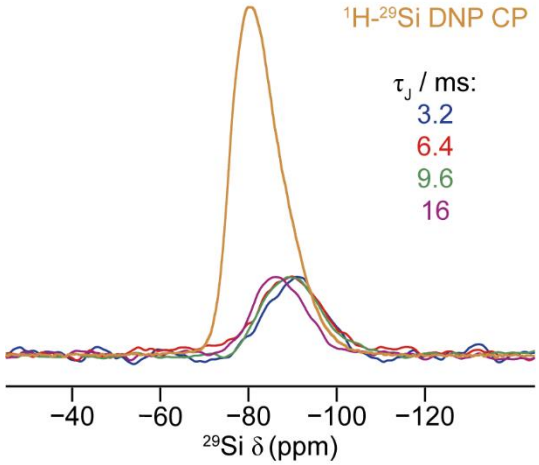

Figure 6.9. *Overlay of δ_2 projections of two-dimensional refocused INADEQUATE DNP NMR spectra, shown in Figure 6.8, as a function of τ_J. The ^{1}H-^{29}Si CP DNP NMR spectrum is also shown for comparison (τ_{CP} = 3 ms) (orange).*

to all Si species are observed, but intensity is lost from the region between −85 and −100 ppm as τ_{CP} is reduced. Therefore, it can be concluded that Q^4 species are indeed present at the silicated surface and, importantly, that the extent of signal amplification remains constant, irrespective of local hydroxyl density, by adventitious adsorbed H_2O when the sample is hydrated (or left under ambient conditions). Thus, perhaps unexpectedly, if sufficiently hydrated, DNP NMR spectra of such materials may be interpreted quantitatively and an accurate description of structure-function relationships can be obtained.

The combination of ^{29}Si isotopic enrichment and DNP NMR spectroscopy results in a significant signal enhancement that provides access to 2D experiments that may otherwise require prohibitively long acquisition times. Correlations exploiting through-bond J couplings can be valuable sources of structural information. As outlined in Chapter 3, the refocused INADEQUATE experiment[25] can be employed to investigate through-bond connectivity in materials. Variation of the J evolution time, τ_J, within the experiment enables the observation of signals exhibiting a range of scalar coupling strengths, with those possessing weaker couplings requiring longer τ_J to be observable. Figure 6.8(a) shows ^{29}Si CP MAS INADEQUATE DNP NMR spectra of

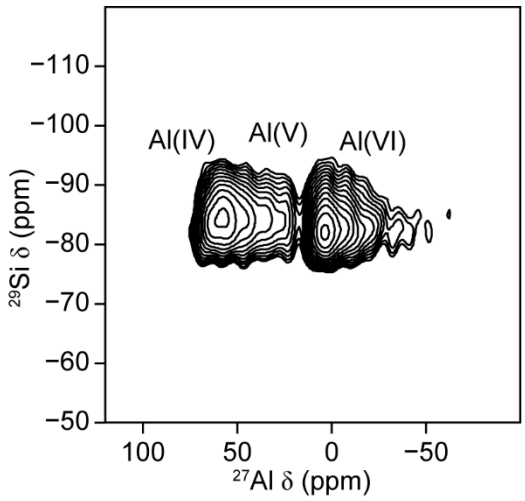

Figure 6.10. *^{29}Si-^{27}Al (9.4 T, 10 kHz MAS) dipolar CP INEPT DNP NMR spectrum of hydrated ^{29}Si-enriched Si-γ-Al_2O_3 (1.5 wt% Si).*

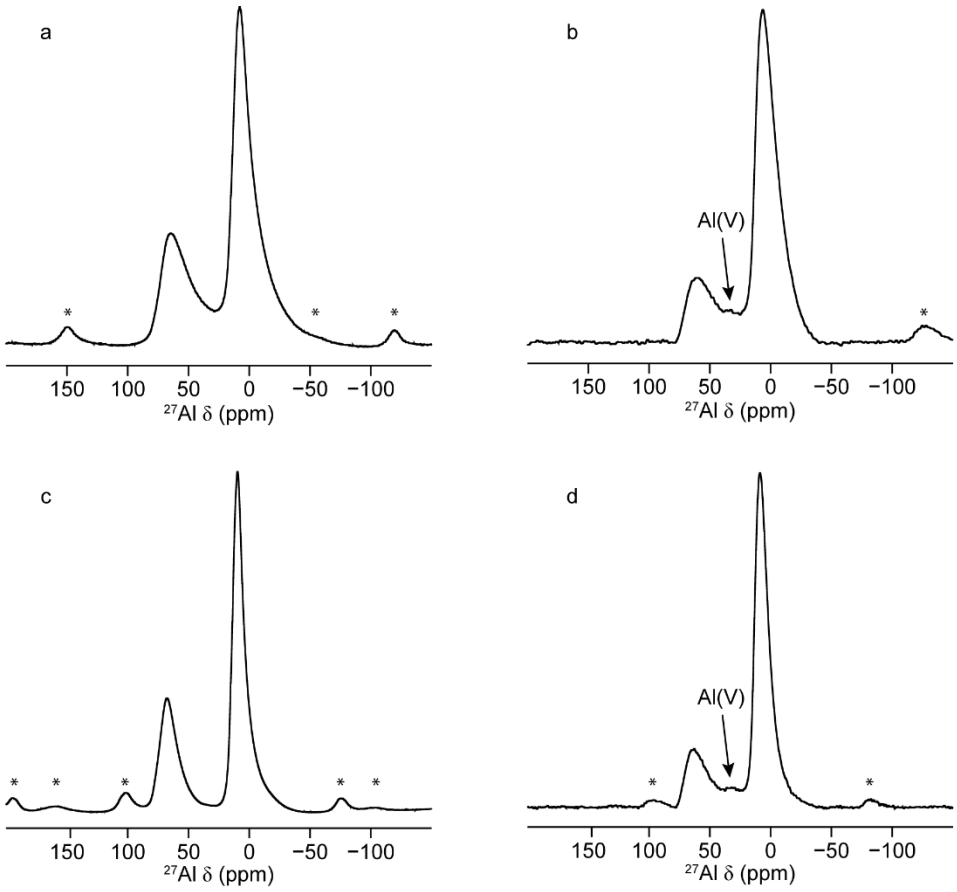

Figure 6.11. *^{27}Al (14 kHz MAS) spectra of 99% ^{29}Si-enriched Si-γ-Al_2O_3 (1.5 wt% Si), acquired at (a, b) 9.4 T and (c, d) 14.1 T, with (a, c) DP and (b, d) CP (τ_{CP} = 0.8 ms). * denotes a spinning sideband.*

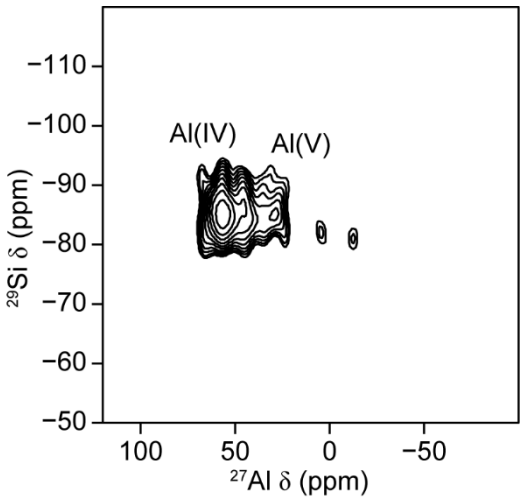

Figure 6.12. *^{29}Si-^{27}Al (9.4 T, 10 kHz MAS) scalar CP INEPT DNP NMR spectrum of hydrated ^{29}Si-enriched Si-γ-Al_2O_3 (1.5 wt% Si).*

hydrated Si-γ-Al_2O_3 (1.5 wt% Si). Despite the low Si content, the use of ^{29}Si isotopic enrichment combined with DNP facilitated spectral acquisition on a reasonable timescale (~4 h for one experiment). Signal is observed between –80 and –100 ppm, suggesting that only higher-order Q^n species are connected to Si, *i.e.*, the three sharper peaks at more positive shift result from isolated Q^n(nAl) species. Signal is observed over a range of ~20 ppm in δ_1, possibly indicating that this results from more than one chemical species, *e.g.*, Q^3 and Q^4 species. However, the correlation peak lies primarily along the $\delta_1 = 2\delta_2$ diagonal in the two-dimensional spectrum, confirming that Si species are only covalently connected to those with very similar shift and, hence, very similar environments. This would suggest the signal probably arises from only Q^4/Q^4 or Q^3/Q^3 correlations (rather than, for example, Q^4/Q^3), and the loss of this signal at longer τ_{CP} in the ^{1}H-^{29}Si HETCOR spectrum in Figure 6.7(b) supports a more likely assignment of Q^4/Q^4 species for this peak. Spectra acquired with additional, longer τ_J values, shown in Figure 6.8(b)-(d), also show only autocorrelation signal. Figure 6.9 shows projections of the spectra onto the δ_2 axis, demonstrating that signal shifts to higher δ as τ_J increases, indicating a positive correlation between ^{29}Si nuclear shielding and the homonuclear J coupling, an observation that has been found for other aluminosilicate materials, and is interpreted in terms of changes in the Si-O-Si bond angle.[26,27]

To provide a better understanding of the interfacial chemistry between the Si surface overlayer and the γ-Al_2O_3 structure upon which it resides, ^{29}Si-^{27}Al refocused INEPT experiments[28,29] were performed, with DNP being used to provide an improvement in sensitivity. As explained in Chapter 3, this experiment can probe scalar (through-bond) connectivity, or can be adapted in the solid state to actively recouple the dipolar interaction and provide information on through-space proximities. Both forms of this experiment have been used previously for the study of aluminosilicate materials.[30]

Figure 6.10 shows the ^{29}Si-^{27}Al dipolar INEPT DNP NMR spectrum of hydrated Si-γ-Al_2O_3, acquired using REDOR to recouple the dipolar interaction.[31] This reveals that Si is close in space to four-, five and six-coordinate Al (*i.e.*, Al(IV), Al(V) and Al(VI)). As Si is present only as a surface overlayer, the spectrum contains only Al species that are close to the surface. As described in Chapter 5, the ^{27}Al spectrum of bulk γ-Al_2O_3 contains signals that can be attributed to Al(IV) and Al(VI) species only.[32-33] However, the surface of γ-Al_2O_3 has been shown to contain Al(V) species. These can be seen using CP, where magnetisation is transferred from surface-based ^{1}H species, resulting in additional signal at ^{27}Al $\delta \approx 35$ ppm. DNP NMR experiments have also demonstrated the presence of Al(V) at the surface of γ-Al_2O_3. As discussed in Chapter 5, Lee *et al.* demonstrated that Al(V) resides only in the first surface layer, using a filtration experiment, where signals close to the surface dephase owing to their stronger dipolar couplings to ^{1}H.[34] The ^{27}Al DP NMR spectra of Si-γ-Al_2O_3, shown in Figure 6.11, reveal a similar picture, with resonances corresponding to Al(IV) and Al(VI) in the bulk material, while the CP spectrum also shows the presence of Al(V) at the surface, in agreement with recent work probing the nature of Brønsted acid sites.[36] Although Al(V) species are found at the surface of unmodified γ-Al_2O_3, it has been suggested that additional Al(V) is formed at the interface between Si and alumina, with the proportion of this species varying with the Si content.

Through-bond connectivity can be probed using the scalar ^{29}Si-^{27}Al INEPT DNP NMR experiment. The spectrum is shown in Figure 6.12. In contrast to the spectrum in Figure 6.10, this reveals that Si is covalently connected *via* Al(IV) and Al(V) anchor

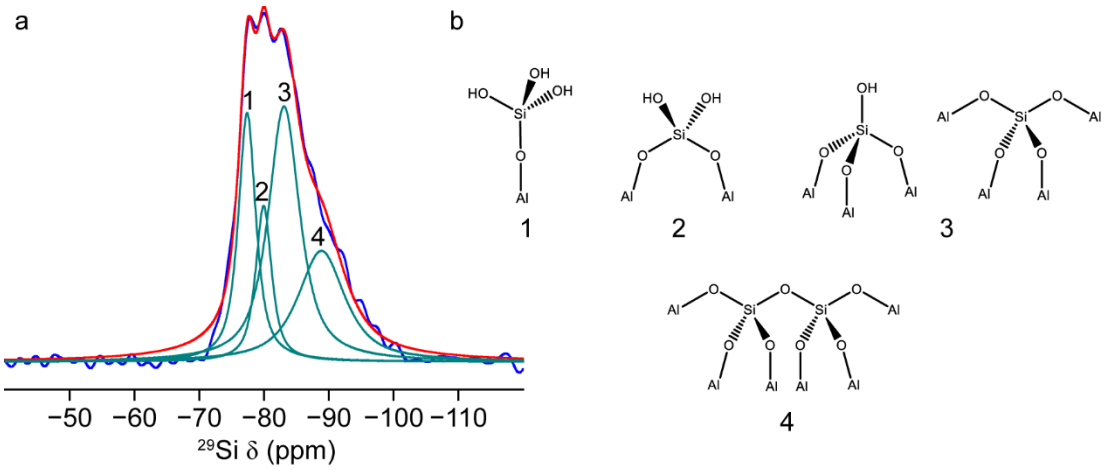

Figure 6.13. *(a) ^{29}Si (9.4 T, 14 kHz MAS) experimental (blue) and simulated (red) NMR spectra of hydrated ^{29}Si-enriched Si-γ-Al_2O_3 (1.5 wt% Si). Also shown are the individual components of the fit (green). (b) Simplified structural representations of the species assigned to each of the components shown in (a).*

Table 6.1. *^{29}Si chemical shifts (δ_{iso}), relative intensities and assignments for the contributions to the ^{29}Si MAS NMR spectrum of 99% ^{29}Si-enriched Si-γ-Al_2O_3 (1.5 wt% Si) shown in Figure 6.13(a).*

Component	δ_{iso} (ppm)	Relative Intensity (%)	Assignment
1	–77 (1)	22 (2)	Q^1(1Al)
2	–80 (1)	14 (3)	Q^2(2Al)
3	–83 (1)	34 (2)	Q^3(3Al) / Q^4(4Al)
4	–89 (2)	30 (2)	Q^4(3Al)

points. Therefore, only a spatial proximity to Al(VI) exists. It is also interesting to note from Figure 6.10 that Al(IV)/Al(V) species show the strongest through-space correlation with Si signal near –84 ppm, while Al(VI) species are more strongly correlated with signal at higher δ (*i.e.*, lower-order Q^n species), suggesting these are more frequently found near the surface.

Extracting quantitative information from the broadened ^{29}Si resonance observed using DNP NMR is not a trivial undertaking. The conventional ^{29}Si DP NMR spectrum of the ^{29}Si-enriched material exhibits better resolution and, when combined with the

information obtained from CP spectra, and particularly from the projection of the single-quantum dimension of the INADEQUATE spectra, a more robust deconvolution is possible, as shown in Figure 6.13, with parameters given in Table 6.1. Sharp components can be identified at –77, –80 and –83 ppm (where constraints on the positions and lineshapes were determined using variable contact time CP experiments), with a broader component at *ca*. –89 ppm. The position and lineshape of the latter is determined from the INADEQUATE spectra. By reference to the assignments of Lippmaa *et al*.[21] the three sharp signals can be assigned as Q^1(1Al) (resonance 1), Q^2(2Al) (resonance 2) and Q^3(3Al)/Q^4(4Al) (resonance 3) species. The opposing shifts that are induced by increased condensation of Si-O tetrahedra and substitution of Si with Al lead to an inevitable overlap of resonance frequencies for some species. Accordingly, it is difficult to discriminate between Q^3(3Al) and Q^4(4Al) based on chemical shift alone, and it is possible that both species contribute to the signal at −83 ppm. However, the presence of signal at –83 ppm in the ^{1}H-^{29}Si HETCOR spectrum in Figure 6.7(b) at short τ_{CP} values suggests a significant contribution to the intensity at this point must arise from Q^3(3Al) Si units. The projection of the ^{29}Si INADEQUATE spectrum in Figure 6.9 confirms that the component at –89 ppm contains primarily Si species within Si-O-Si linkages. As discussed above, the observation along the autocorrelation diagonal, and the loss of this signal in the ^{1}H- ^{29}Si HETCOR spectrum, suggests it results principally from interconnected Q^4(3Al) species, *i.e.*, $(OAl)_3Si\text{-}O\text{-}Si(OAl)_3$ linkages at this level of silica loading.

At first sight, it may seem unusual that the NMR experiments suggest that most Q^4 Si species are linked to a second Si centre. The low loading of Si in these samples ensures that most Si species are bonded only to Al (*i.e.*, Q^1(1Al), Q^2(2Al) and Q^3(3Al)). As Si forms a surface layer on the alumina it is less likely that it embeds to make four bonds to the surface Al, and that Q^4 Si species form (primarily, but not exclusively) when they are able to bond to a second Si unit on the surface.[36,37] As shown in Table 6.1 (and illustrated schematically in Figure 6.13(b)), from the spectrum in Figure 6.13(a) it has been determined Q^1(1Al) ≈ 22%; Q^2(2Al) ≈ 14%; Q^3(3Al)/Q^4(4Al) ≈ 34% and Q^4(3Al) ≈ 30%, suggesting that almost a third of the Si at the surface is connected to

another Si species, even at the low level of coverage used. It should be noted that although the recycle interval used for the ^{29}Si DP MAS spectrum was 120 s, the T_1 value was estimated to be on the order of ~1.5 h, making acquisition of a truly quantitative spectrum practically unfeasible. Although this may result in some uncertainty in the exact proportion of each species present, little difference was observed in the relative relaxation of the different Si species at shorter recycle intervals. Deconvolution of the ^{29}Si spectrum and assignment of the contributions of the component resonances would have been almost impossible using conventional NMR spectroscopy, and difficult by either DNP (owing to the lower resolution) or isotopic enrichment (owing to the lower sensitivity) alone.

6.4 Silica Growth on γ-Al_2O_3: "Sequential Grafting" and "Single Shot" Approaches

It was mentioned at the beginning of this Chapter that silicated aluminas play an important role in many industrial processes. The diverse range of reactions that this class of material catalyses requires that the structure be readily tunable, in order to obtain the composition required for a given application. For example, it has been found that in skeletal isomerisation reactions, materials with low silica loadings, such as the material studied above, are most the efficient.[38] In other processes however, such as the synthesis of dimethyl ether from methanol[39] and hydrocracking of F-T waxes,[40] higher silica loadings result in better catalytic performance.

To create structures with increasing silica loading levels in a consistent and reliable manner, it is desirable to be able to utilise a preparation method that offers controlled building up of the surface overlayer. One such approach is the sequential grafting method employed by van Bokhoven and co-workers.[30,41,42] Here, structures are built up in a sequential manner by depositing a known volume of Si precursor (*e.g.*, TEOS) onto the preceding silicated alumina, followed by drying/calcination steps. In this way, stepwise growth may be achieved whilst control of the loading level is maintained.

To gain more insight into the local structure of such catalysts, it is desirable to be able

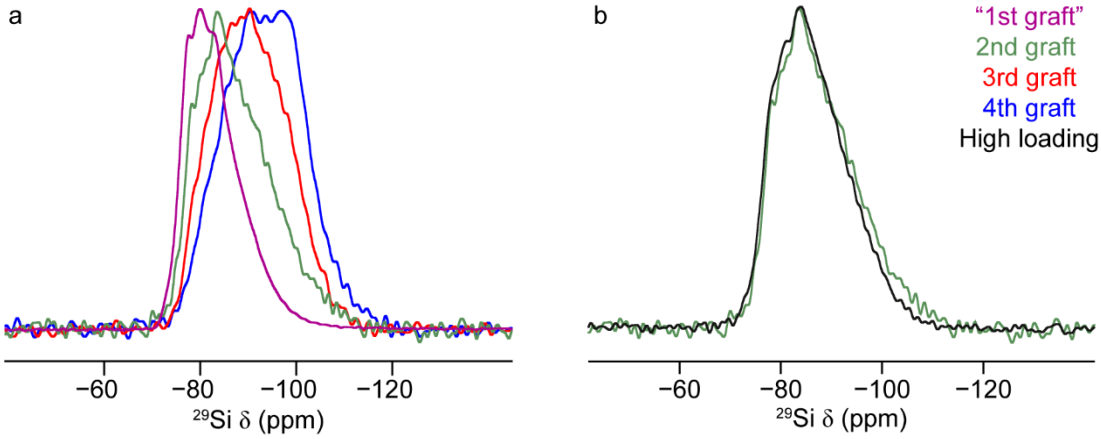

Figure 6.14. *(a) ^{1}H-^{29}Si (9.4 T, 10 kHz MAS) CP NMR spectra of ^{29}Si-enriched Si-γ-Al_2O_3 (1.5 wt% Si) and Si-γ-Al_2O_3 materials prepared by a sequential grafting approach (2.8, 3.5 and 5.2 wt% Si, respectively). (b) ^{1}H-^{29}Si (9.4 T, 10 kHz MAS) CP NMR spectra of Si-γ-Al_2O_3 2nd graft (2.8 wt% Si) and ^{29}Si-enriched Si-γ-Al_2O_3 (~8 wt% Si) prepared by a "single shot" approach. For all spectra, τ_{CP} = 3 ms. Spectral intensities have been normalised.*

to track the growth morphology of Si on the alumina surface as additional Si is loaded onto the material. Accordingly, in this work, Si-γ-Al_2O_3 materials containing 2.8, 3.5 and 5.2 wt% Si were prepared by sequential grafting, in a manner similar to that described above. Si-γ-Al_2O_3 containing 1.5 wt% Si was also included in this study as the first silica graft material. The ^{29}Si-enriched version of this material (hereafter referred to as "1st graft", including quotation marks) previously studied in Section 6.3, was prepared on a laboratory scale, whereas the natural abundance version, studied in the present section, was obtained commercially. The latter material was used as the base from which subsequent grafts were created. The differences between these samples are discussed in more detail later in this section. To ascertain how the growth morphology is influenced by the preparation route, a Si-γ-Al_2O_3 with high silica loading (nominally 8 wt% Si) was prepared by a "single shot" approach using 99% ^{29}Si-enriched TEOS deposited on γ-Al_2O_3 in a single grafting step. The aim of producing this sample was to attempt to determine whether the same structural environments could be created on the surface of γ-Al_2O_3, in one step *versus* four steps.

Figure 6.14(a) shows ^{1}H-^{29}Si CP NMR spectra of the Si-γ-Al_2O_3 materials prepared by a sequential grafting approach, along with a similar CP spectrum of ^{29}Si-enriched

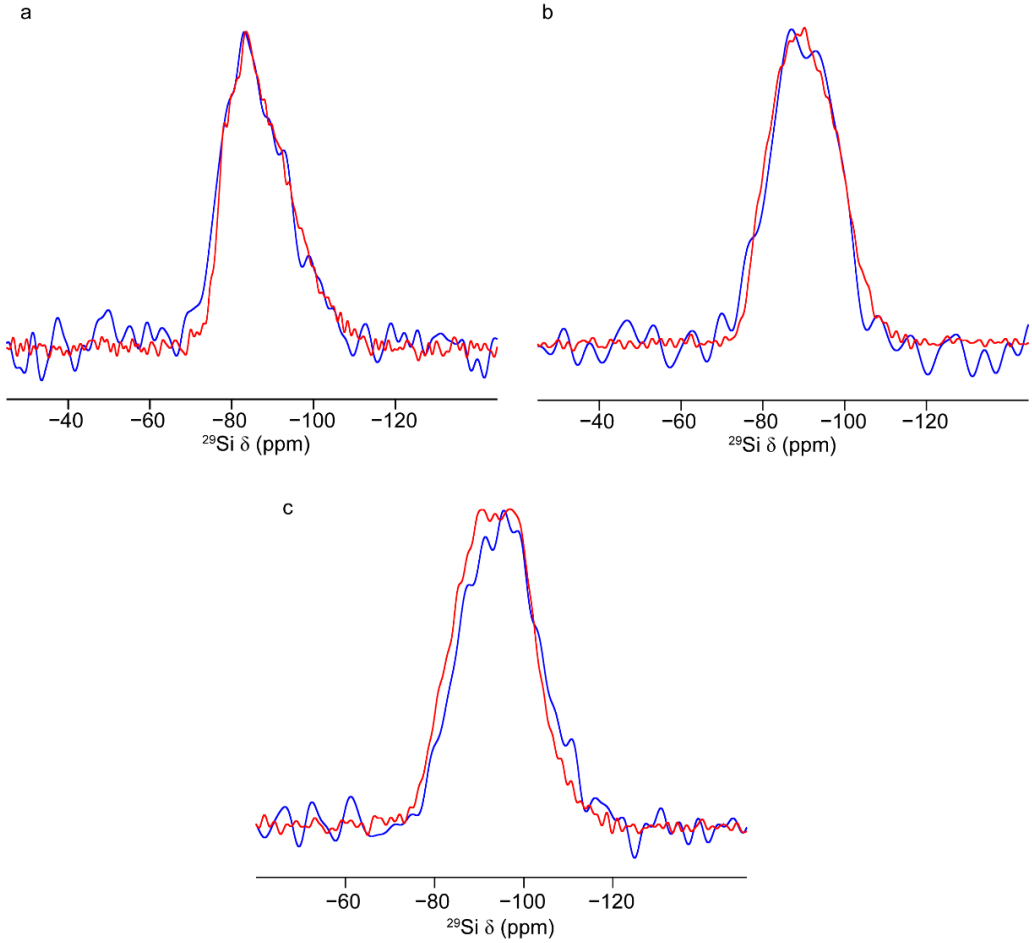

Figure 6.15. *^{29}Si (9.4 T, 14 kHz MAS) DP NMR (blue) and ^{1}H-^{29}Si (9.4 T, 10 kHz MAS, τ_{CP} = 3 ms) CP NMR (red) spectra of (a) 2nd, (b) 3rd and (c) 4th graft Si-γ-Al_2O_3 materials. Spectral intensities have been normalised.*

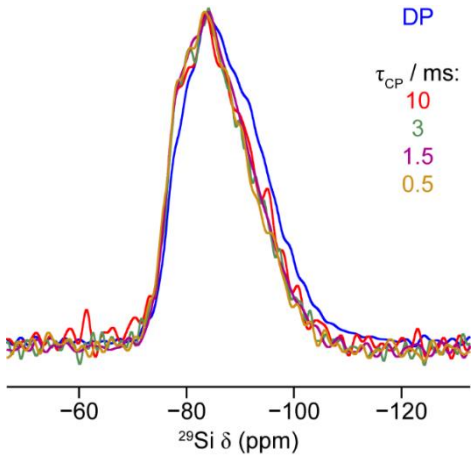

Figure 6.16. *^{29}Si (9.4 T, 14 kHz MAS) DP NMR and ^{1}H-^{29}Si (9.4 T, 10 kHz MAS, τ_{CP} = 0.5-10 ms) CP NMR spectra of "single shot" ^{29}Si-enriched Si-γ-Al_2O_3 (~8 wt% Si). Spectral intensities have been normalised.*

Si-γ-Al_2O_3 (1.5 wt% Si). The spectra clearly demonstrate a systematic evolution in the Si environments with each additional grafting step. A shift in each lineshape towards more negative δ indicates the formation of increasing amounts of higher-order Q^n species as the amount of silica is increased. This suggests that the reaction of TEOS with the oxide surface takes place primarily at hydroxyl group sites. In the spectrum of the 4th graft material, a significant reduction in the intensity of the region of the spectrum associated with Q^1(1Al) and Q^2(2Al) species is observed. It leads to the conclusion that by this stage, the majority of aluminol species have been consumed, leaving only silanols as suitable reaction points for additional deposited TEOS molecules. Given that the "single shot" preparation of Si-γ-Al_2O_3 was designed to deposit a high loading of silica precursor onto the γ-Al_2O_3 (~8 wt% Si), it may be expected that the ^{1}H-^{29}Si CP NMR spectrum would continue the trend observed for the sequential grafting samples. However, the data obtained reveals that this is in fact not the case. Figure 6.14(b) shows an overlay of the spectra of the 2nd graft material (2.8 wt% Si) and the high loading sample. It reveals that the two CP NMR spectra of these samples are remarkably similar, a surprising observation given their different preparation routes. It would appear that, based upon this initial evidence, that the "single shot" approach is able to generate well dispersed surface silica units. Significant lineshape intensity in the –90 ppm region of the spectrum indicates that extensive bridging Si-O-Si formation has also occurred, potentially of the type observed to be present in Si-γ-Al_2O_3 (1.5 wt% Si).

Considering the findings in Section 6.3, it was necessary to verify the extent to which the ^{1}H-^{29}Si CP NMR experiment could provide a complete description of the Si environments present in the multi grafted and high loading samples. Accordingly, ^{29}Si DP NMR experiments were performed on these materials. Despite the inherently low natural abundance of ^{29}Si present in these samples, extended signal averaging yielded spectra with a reasonable level of sensitivity. Figure 6.15 shows these spectra overlaid with CP NMR spectra for the 2nd, 3rd and 4th graft samples. The comparison demonstrates that the CP spectra (at least for τ_{CP} = 3 ms) show all Si environments present in the materials prepared by a multi-grafting approach. This suggests that all Si species are reasonably close to H species, either in the form of OH groups or

adventitious water, and precludes the formation of amorphous silica structures even after four grafting cycles. The same comparison between DP and CP NMR spectra may also be made for the "single shot" silicated alumina. This material was prepared with 99% ^{29}Si-enriched TEOS, allowing for the acquisition of multiple contact time CP spectra in approximately the same timeframe as one CP experiment at natural abundance. The ^{29}Si DP NMR experiment was also able to be performed in a reasonable time and exhibits good sensitivity. The resulting spectra are shown in Figure 6.16. The CP spectra show little variation in the lineshape, much like the spectra of Si-γ-Al_2O_3 (1.5 wt% Si) presented in Figure 6.3, suggesting that as before, adventitious surface water mediates efficient polarisation transfer for all CP contact times. However, unlike for Si-γ-Al_2O_3 (1.5 wt% Si), there is a discernible difference observed when comparing the ^{29}Si CP and DP spectra of the "single shot" silicated alumina. The CP spectra consistently "under represent" the full lineshape observable in the DP NMR experiment, in the region located at ^{29}Si $\delta \approx -100$ ppm. The chemical shift value,[9,24] in combination with the fact that the CP experiment does not detect this signal, indicates that this region corresponds to an amorphous silica-like "ball" structure that is proton deficient. The increased signal intensity in the CP spectra between −75 and −80 ppm suggests that proton rich lower-order Q^n species are present on the surface of this material, as indicated from the overlay with the 2nd graft sample in Figure 6.14(b). These findings point towards only a portion of the "single shot" silicated alumina being comprised of an amorphous "ball-like" component. The remainder of the surface structure is likely to be composed of previously observed aluminosilicate Q^n species.

Combining the findings obtained from solid-state NMR spectroscopy with additional analytical techniques has been shown to be a valuable approach to materials characterisation.[37,43-49] In this work, the silicated alumina materials presented above were also analysed by X-ray photoelectron spectroscopy (XPS). XPS experiments are carried out by exposing a solid sample to an X-ray beam, and measuring the kinetic energy and number of electrons that escape from atoms on the material's surface (typically down to a depth of 10 nm). A spectrum is obtained of intensity against binding energy, calculated from the measured kinetic energy. Peaks in the spectrum

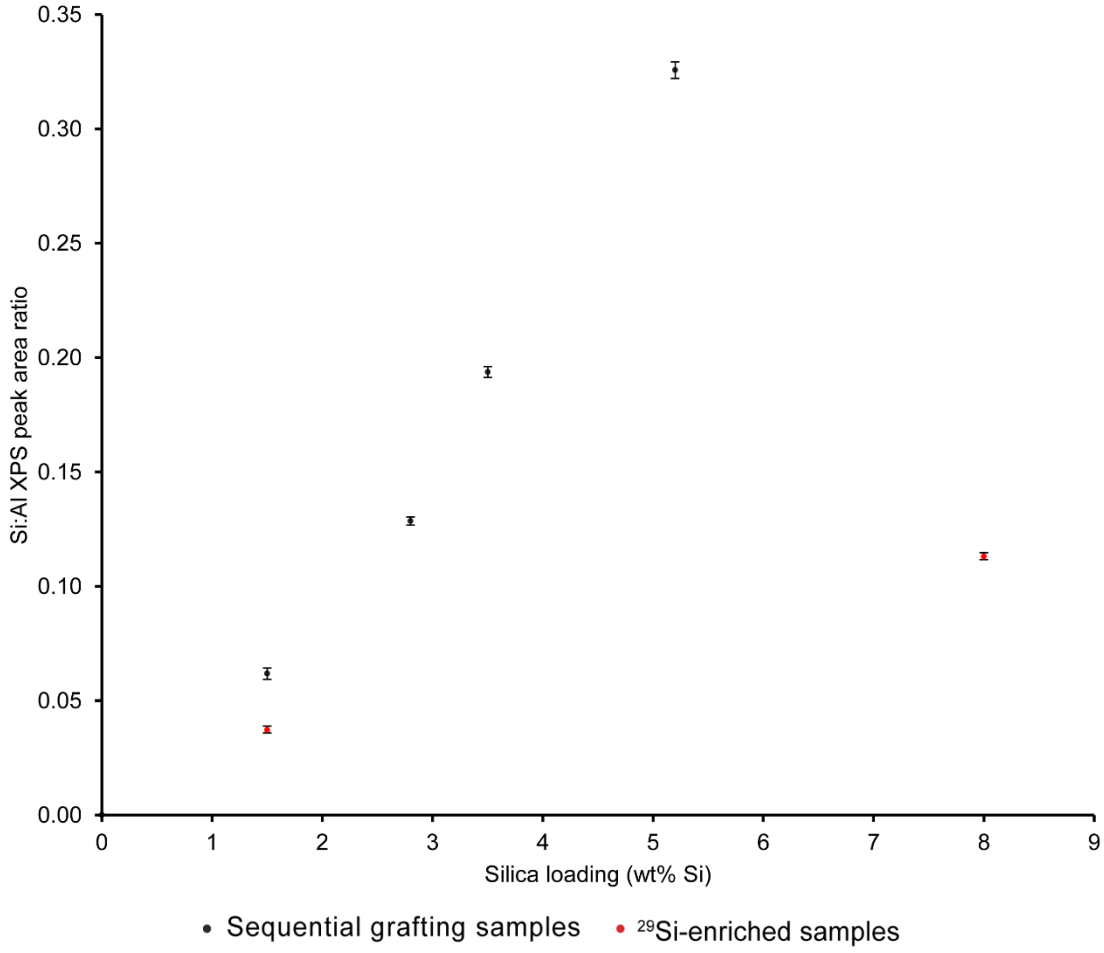

Figure 6.17. *Plot of silica loading (wt% Si) versus Si:Al peak area ratios in sequentially-grafted and* ^{29}*Si-enriched materials as determined by XPS.*

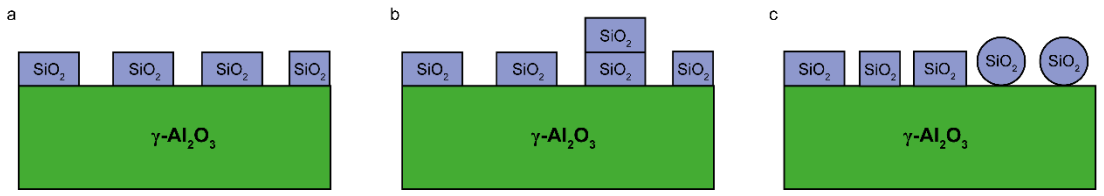

Figure 6.18. *Schematic diagrams showing the different silica growth modes taking place on* γ*-*Al_2O_3*. (a) 2D island growth that occurs at low loading levels, (b) 3D island "stacking" that forms after several grafting cycles, and (c) a mixed growth morphology consisting of 2D islands accompanied by the formation of amorphous* SiO_2 *"ball" structures.*

result from atoms emitting electrons of characteristic energies, which depend on the element and surface environment.[50,51] XPS has been extensively used to characterise

the surface environments in aluminosilicate materials,[51-63] owing to its ability to provide information on elemental composition, oxidation state and phase dispersion.[50,51] Of particular use for aluminosilicates, is that the surface Si:Al ratio of a sample can be determined by fitting the relevant peaks in the XPS spectrum with Gaussian-Lorentzian components, after appropriate background correction.[61,62]

Figure 6.17 shows Si:Al peak ratios, determined *via* XPS, plotted against the nominal silica loading level of sequentially-grafted and "single shot" silicated alumina materials. Initially, it may be expected that a linear relationship between silica loading and Si:Al ratio will be followed. This reflects a situation where the implementation of additional grafting cycles results in the creation of a 2D monolayer-like structure on the γ-Al_2O_3 surface, *i.e.*, as additional Si species are formed, they fill in the spaces between the Si units already present. However, by the 3rd silica graft, a deviation away from this behaviour is seen, which becomes more pronounced as one further graft is applied. By this point, a significantly higher Si:Al ratio is observed than would be expected for a monolayer-type overlayer, and it may be surmised that 3D "stacking" of Si islands occurs with additional of grafting cycles. ^{29}Si solid-state NMR spectroscopy has already shown in this work that amorphous SiO_2-like structures are unlikely to be formed in the multi-grafted materials, lending further support for this theory. XPS analysis was also performed on the "single shot" (8 wt% Si) silicated alumina sample. It shows that despite its high silica loading, the Si:Al ratio is remarkably low, lying outside both the monolayer and island growth trends already discussed. This result supports the proposal from ^{29}Si solid-state NMR spectroscopy, where the formation of SiO_2-like "balls" was suggested. The underestimation of the "true" Si:Al ratio is possible if such dense silica structures are present on the surface of γ-Al_2O_3, preventing the excitation of photoelectrons by the X-ray beam, from the inner core of these species. Two different silica growth morphologies have therefore been revealed, which are strongly dependent on the way in which silica is deposited onto the γ-Al_2O_3 surface. The two models are schematically illustrated in Figure 6.18, one of which depicts 3D island "stacking" that forms after several grafting cycles (Figure 6.18(b)), and the other a mixed growth morphology consisting of 2D islands accompanied by the formation of amorphous SiO_2 "ball" structures (Figure 6.18(c)).

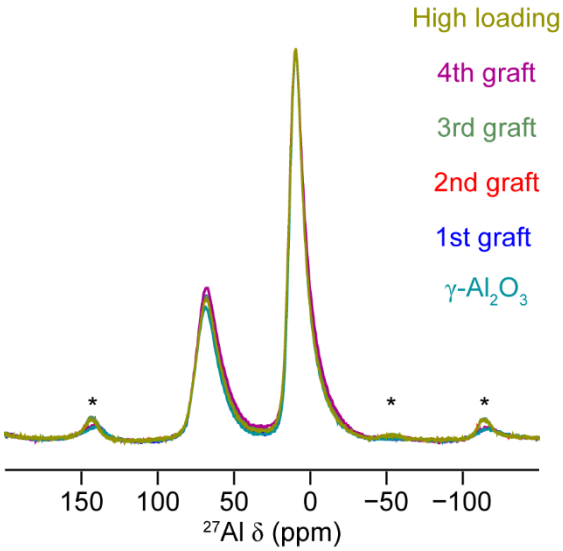

Figure 6.19. *^{27}Al (14.1 T, 20 kHz MAS) DP NMR spectra of γ-Al_2O_3, Si-γ-Al_2O_3 materials prepared by a sequential grafting approach and Si-γ-Al_2O_3 (8 wt% Si, "high loading") prepared via a "single shot" method. Spectra have been normalised with respect to the Al(VI) resonance. * denotes a spinning sideband.*

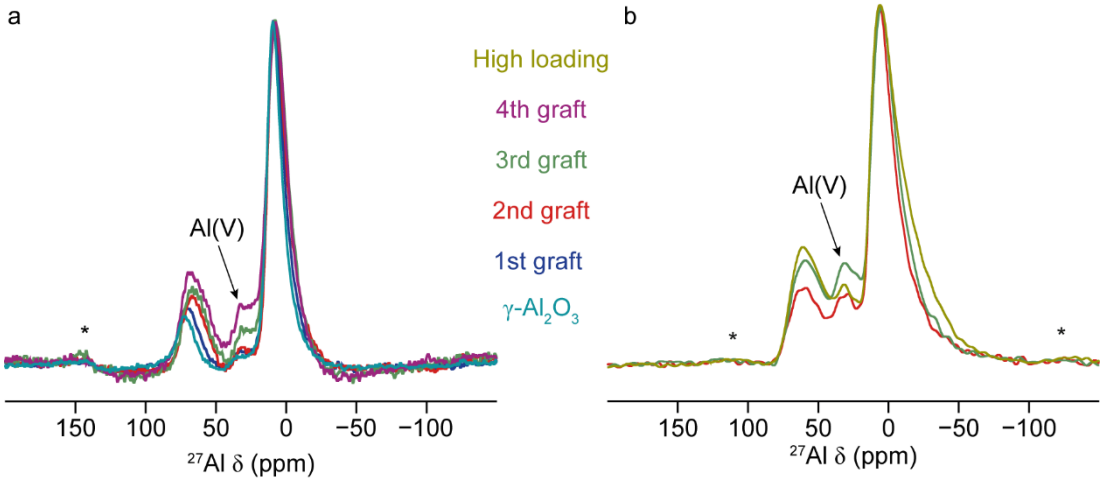

Figure 6.20. *(a) ^{1}H-^{27}Al (14.1 T, 20 kHz MAS, τ_{CP} = 0.8 ms) CP NMR spectra of γ-Al_2O_3 and Si-γ-Al_2O_3 materials prepared by a sequential grafting approach. (b) ^{1}H-^{27}Al (9.4 T, 10 kHz MAS, τ_{CP} = 0.8 ms) DNP CP NMR spectra of Si-γ-Al_2O_3 2nd graft, 3rd graft and high loading materials. In both (a) and (b), spectra have been normalised with respect to the Al(VI) resonance. * denotes a spinning sideband.*

One further observation can also be noted from the XPS data in Figure 6.17. The ^{29}Si-enriched 1.5 wt% Si sample is seen to exhibit a lower Si:Al ratio than its natural abundance ^{29}Si counterpart. This may result from the way in which these two materials were obtained. The ^{29}Si-enriched sample was prepared on a laboratory scale, with wet

impregnation carried out under inert atmosphere. By contrast, the natural abundance ^{29}Si sample was obtained commercially, as part of a standard large volume batch produced on an industrial scale. Although the precise preparation details of this particular silicated alumina are not readily available (as it is a commercial product), production routes for similar catalysts indicate that the industrial process differs from the one employed on a laboratory scale.[64,65] Certainly, the material obtained for this study is envisaged to be similar the one prepared with ^{29}Si-enriched precursor, but its precise composition is unlikely to be identical. A difference in the Si:Al ratios for these samples is perhaps to be expected, and warrants further investigation in future studies. Some additional insights will also be provided, from a ^{17}O NMR perspective, later in this chapter.

To determine the effect of silica deposition by sequential grafting and "single shot" approaches on the underlying γ-Al_2O_3 structure, ^{27}Al NMR experiments were performed. Figure 6.19 shows ^{27}Al DP NMR spectra acquired for samples of γ-Al_2O_3, Si-γ-Al_2O_3 materials prepared by a sequential grafting approach and Si-γ-Al_2O_3 (8 wt% Si) prepared *via* a "single shot" method. Very little differences can be discerned between the overlaid spectra, suggesting that the bulk γ-Al_2O_3 remains largely unperturbed by the grafting processes that have been applied. ^{1}H-^{27}Al CP NMR spectra of unmodified γ-Al_2O_3 and the sequential Si grafting materials are presented in Figure 6.20(a). It can be seen that the intensity of the resonances corresponding to four- and five-coordinate Al sites increases as a function of additional grafting cycles. In the Si-γ-Al_2O_3 (1.5 wt% Si) material, these Al sites were identified as the anchoring points for silica growth on the surface of γ-Al_2O_3. It therefore follows that their corresponding resonances should display increased intensity as the interface between Si and Al becomes more pronounced. A consistent upfield shift in the position of the Al(IV) and Al(V) resonances is also evident, consistent with an increase in the shielding of these nuclei, as a result of increasing silica coverage. These findings differ from recent observations by Valla *et al.*, who studied similar materials by DNP NMR spectroscopy. These researchers found no significant increase in Al(V) intensity with additional grafting steps.[30] However, this may be rationalised by the data presented in Figure 6.20(b), which shows ^{1}H-^{27}Al DNP NMR spectra of 2nd graft, 3rd graft and

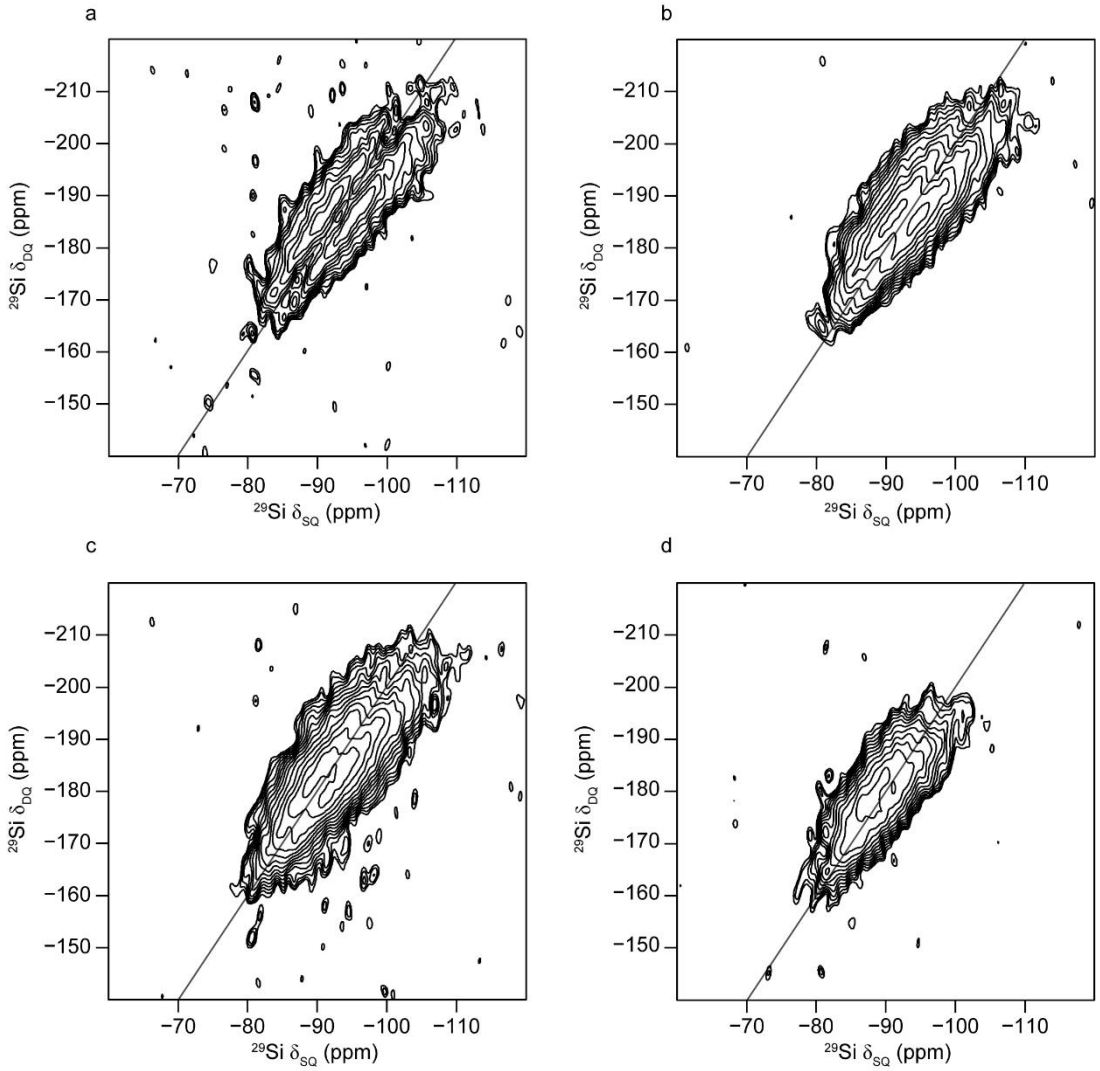

Figure 6.21. *^{29}Si (9.4 T, 12.5 kHz MAS) refocused CP INADEQUATE DNP NMR spectra of ^{29}Si-enriched Si-γ-Al_2O_3 (8 wt% Si), acquired using τ_J values of (a) 3.2 ms, (b) 6.4 ms, (c) 9.6 ms and (d) 16 ms. The solid grey line in each spectrum denotes the $\delta_{DQ} = 2\delta_{SQ}$ autocorrelation diagonal.*

high loading Si-γ-Al_2O_3 materials. Given the increased amount of Si present in the high loading sample (8 wt%), it might be expected that the spectrum of this sample will continue to follow the pattern observed in Figure 6.20(a), but this is not the case. Whilst the Al(IV) resonance does behave as expected, the Al(V) resonance lies outside the trend, displaying an intensity approximately equal to that of the 2nd graft (2.8 wt% Si) sample. It appears that, whilst the silica species are indeed anchored to the alumina surface (*via* Al(V) sites), the level of overlayer formation is reduced with respected to

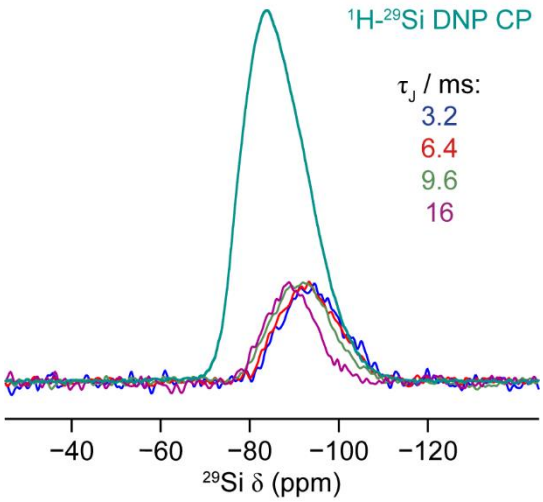

Figure 6.22. *Overlay of δ_2 projections of two-dimensional refocused INADEQUATE DNP NMR spectra, shown in Figure 6.21, as a function of τ_J. The ^{1}H-^{29}Si CP DNP NMR spectrum is also shown for comparison (τ_{CP} = 3 ms) (cyan).*

the sequentially grafted materials. The amorphous SiO_2-like "balls" are likely to be responsible for this difference, as whilst they are connected to the surface, they do not promote the formation of a well-defined Si-Al interface, characterised by increased connectivity to Al(V) sites. It is possible therefore, that Valla *et al.*[30] employed a grafting approach that resulted in the generation of an initial silicated alumina that more closely resembles the "single shot" material in the present work, as suggested by their ^{29}Si DNP NMR data. As a result, subsequent grafting cycles may have generated materials without a distinct Si-Al interface, a growth morphology which seems to disfavour the generation of Al(V) surface sites.

6.5 Further Investigations of "Single Shot" Silicated Alumina: Insights from 2D DNP NMR Spectroscopy

In Section 6.3, it was demonstrated that the combination of isotopic enrichment and DNP NMR spectroscopy can facilitate a better understanding of the interfacial chemistry between the silica surface overlayer and the γ-Al_2O_3 bulk. Preparing the "single shot" silicated alumina with 99% ^{29}Si TEOS therefore, allows this approach to be extended to study this material further using 2D correlation experiments. Figure 6.21 shows ^{29}Si CP MAS INADEQUATE DNP NMR spectra of the high silica

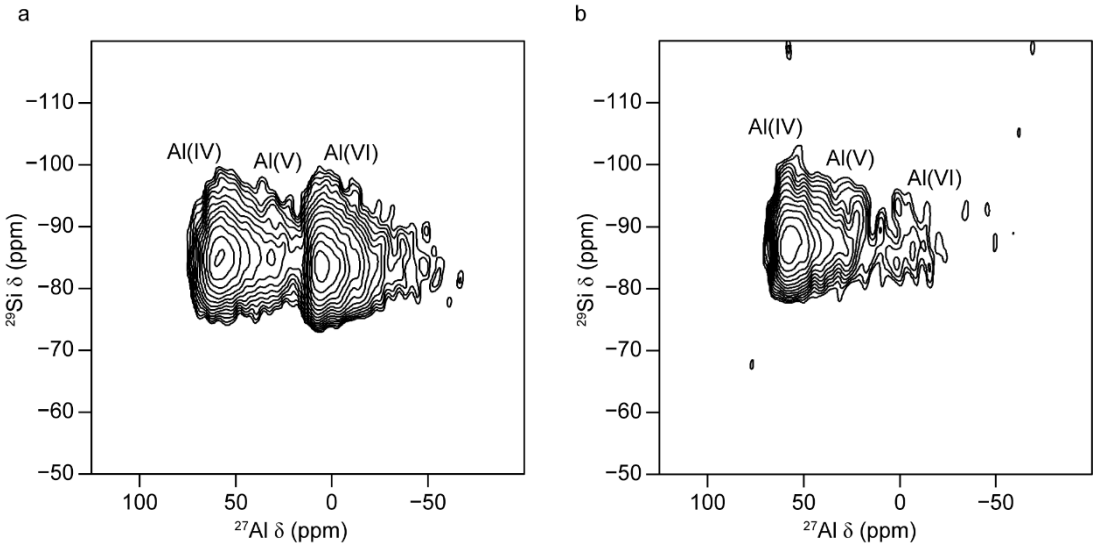

Figure 6.23. *^{29}Si-^{27}Al (9.4 T, 10 kHz MAS) CP INEPT DNP NMR spectrum of ^{29}Si-enriched high silica loading Si-γ-Al_2O_3 (8 wt% Si), with transfer via the (a) dipolar and (b) scalar coupling.*

loading material. Signal is observed between –80 and –110 ppm, suggesting that, as for Si-γ-Al_2O_3, only higher-order Q^n species are connected to Si. At J evolution times of up to 9.6 ms, two cross peaks are present on either side of the $\delta_1 = 2\delta_2$ diagonal, at $\delta_2 \approx$ –90 and –95 ppm. This is an indication that silica species are covalently connected to those with similar, but distinct chemical shifts and therefore somewhat different environments. Based on the assignments of Lippmaa *et al.*,[21] these signals may arise from Q^4/Q^4 species in a Q^4(3Al)-Q^4(2Al) arrangement. At the longest J evolution time, 16 ms, only autocorrelation signal at $\delta_2 \approx$ –90 ppm is observed. This finding is demonstrated more clearly in Figure 6.22, where projections of the spectra onto the δ_2 axis are shown. Loss of signal from the ≈ –95 ppm region of the spectrum is evident. It indicates that some Q^4(3Al) pairs do exist in this material, consistent with a structural model where little if any 3D "island stacking" has occurred. Si species are instead primarily connected to each other and/or to the γ-Al_2O_3 surface. Signal corresponding to amorphous silica-type structures is less readily observable in the INADEQUATE spectra, which may be at first be surprising given that this experiment has previously been applied on zeolites[66-68] and functionalised silica nanoparticles.[69] However, this is perhaps explained when it is considered that the INADEQUATE experiment, being enhanced by DNP, is preceded by a CP (from ^{1}H) step. As Figure 6.16 demonstrates,

the ^{1}H-^{29}Si CP experiment underrepresents a portion of the total lineshape observable by direct polarisation. It therefore follows that this resonance, attributed to amorphous silica-like "balls", will also not as readily observable in the 2D experiment.

It was also demonstrated in Section 6.3 that the interfacial chemistry between Si and Al can be probed effectively *via* ^{29}Si-^{27}Al refocused INEPT experiments.[28,29] Figure 6.23(a) shows the ^{29}Si-^{27}Al dipolar INEPT DNP NMR spectrum of high silica loading silicated alumina, where REDOR was used to recouple the dipolar interaction.[31] It reveals that Si is close in space to Al(IV), Al(V) and Al(VI) species, as previously observed for Si-γ-Al_2O_3 (1.5 wt% Si). In the high silica loading material though, all Al species, including Al(VI), show the strongest through-space correlation with Si signal near –84 ppm. This finding suggests that Al(VI) species are no longer directly exposed at the surface, as in the 1.5 wt% Si material, consistent with a growth model that, whilst generating some dense amorphous Si species, is still able to achieve a reasonably high degree of Si dispersion. The scalar ^{29}Si-^{27}Al INEPT DNP NMR spectrum of high silica loading silicated alumina is shown in Figure 6.23(b). In contrast to the equivalent spectrum of Si-γ-Al_2O_3 (1.5 wt% Si), presented in Figure 6.12, reveals that Si is covalently connected *via* all three types of Al environment (Al(IV), (V) and (VI)). The strongest correlation for all Al species is with Si signal near –87 ppm, which may be attributable to Q^4(3Al) units. This shift to more negative ppm values (in the ^{29}Si dimension) in the scalar correlation spectrum *versus* the dipolar one, suggests that whilst Si units are anchored to all types of Al coordination environment, overall, they are in spatial proximity to Al units which are not covalently bonded to Si. This indicates that there is little, if any, Si penetration into the bulk γ-Al_2O_3 structure, even at a high silica loading of 8 wt%. Notably, no resonances corresponding to amorphous silica-type units are observable in either spectrum in Figure 6.23. This can also be accounted for by considering that these experiments also feature a CP component in the same way as the refocused INADEQUATE sequence. Additionally, a certain proportion of a given silica "ball" may not be expected to connect with the γ-Al_2O_3 surface, either spatially, due to the dense nature of such a structure, or covalently, as a result of a lack of Q^n environments with next nearest neighbour Al units.

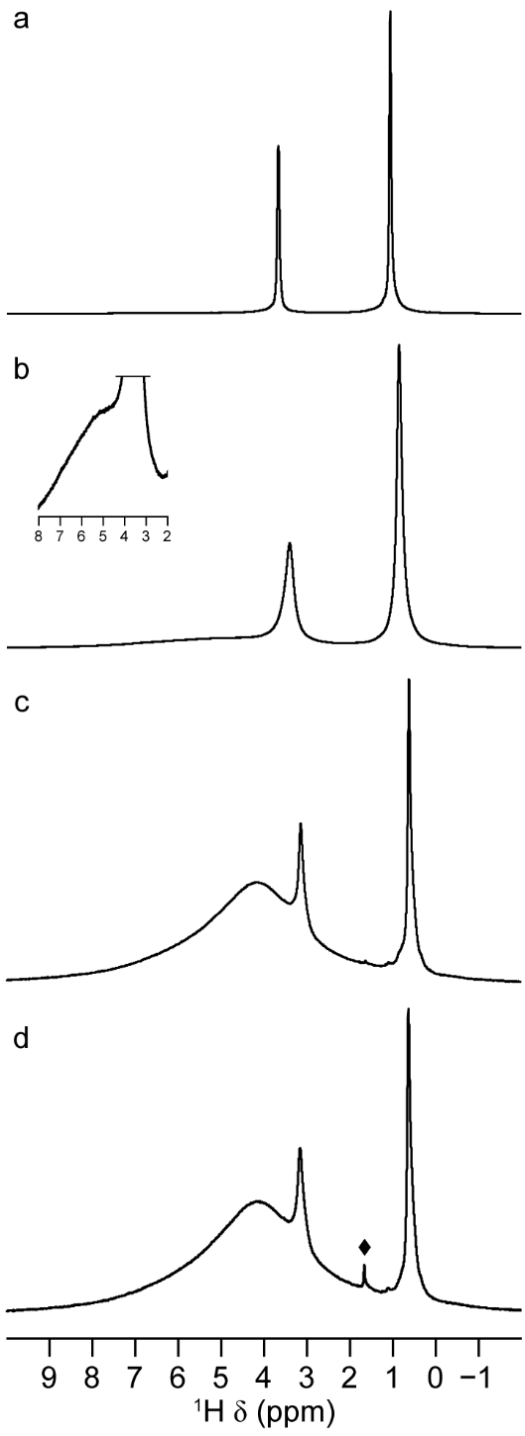

Figure 6.24. *^{1}H (9.4 T, 10 kHz MAS) NMR spectra of as-made high silica loading Si-γ-Al_2O_3 (8 wt% Si) acquired (a) directly after synthesis and after ageing for (b) ~2 weeks, (c) ~1 year and (d) ~1 year and 1 month. ♦ denotes a peak from the rotor cap.[78] In (b), an expansion of the spectrum is also shown inset.*

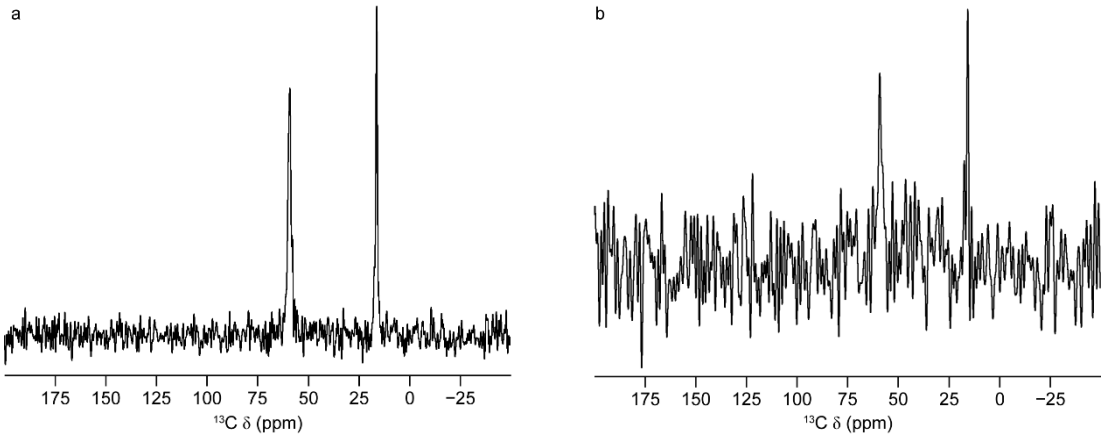

Figure 6.25. *^{1}H-^{13}C (9.4 T, 10 kHz MAS, τ_{CP} = 3 ms) CP NMR spectra of as-made high silica loading Si-γ-Al_2O_3 (8 wt% Si) acquired after ageing for (a) ~2 weeks and (b) ~1 year. The same experimental parameters were used to acquire both spectra.*

6.6 As-made "Single Shot" Silicated Alumina: Following the Effect of Long-Term Ageing

One of the principal steps in the preparation of aluminosilicate materials is high temperature calcination, which typically takes place after the principal synthesis steps have been performed.[30,41-44,70] A material that has not undergone calcination is generally described as being "as-made" and typically still contains residual templating, modifying or structure-directing agents.[71-73] The study of such materials can offer insights into the formation of local structural environments, which is an important consideration for functional materials.[73]

NMR spectroscopy is ideally suited to the task of monitoring the structural evolution of silicate-based materials over time, due to its sensitivity to small changes in local chemical environments.[9,45,74-77] Accordingly, an aliquot of as-made "single shot" silicated alumina was acquired for study in this way. The material was obtained after the vacuum drying phase of the synthetic procedure was completed, prior to high temperature calcination of the main product.

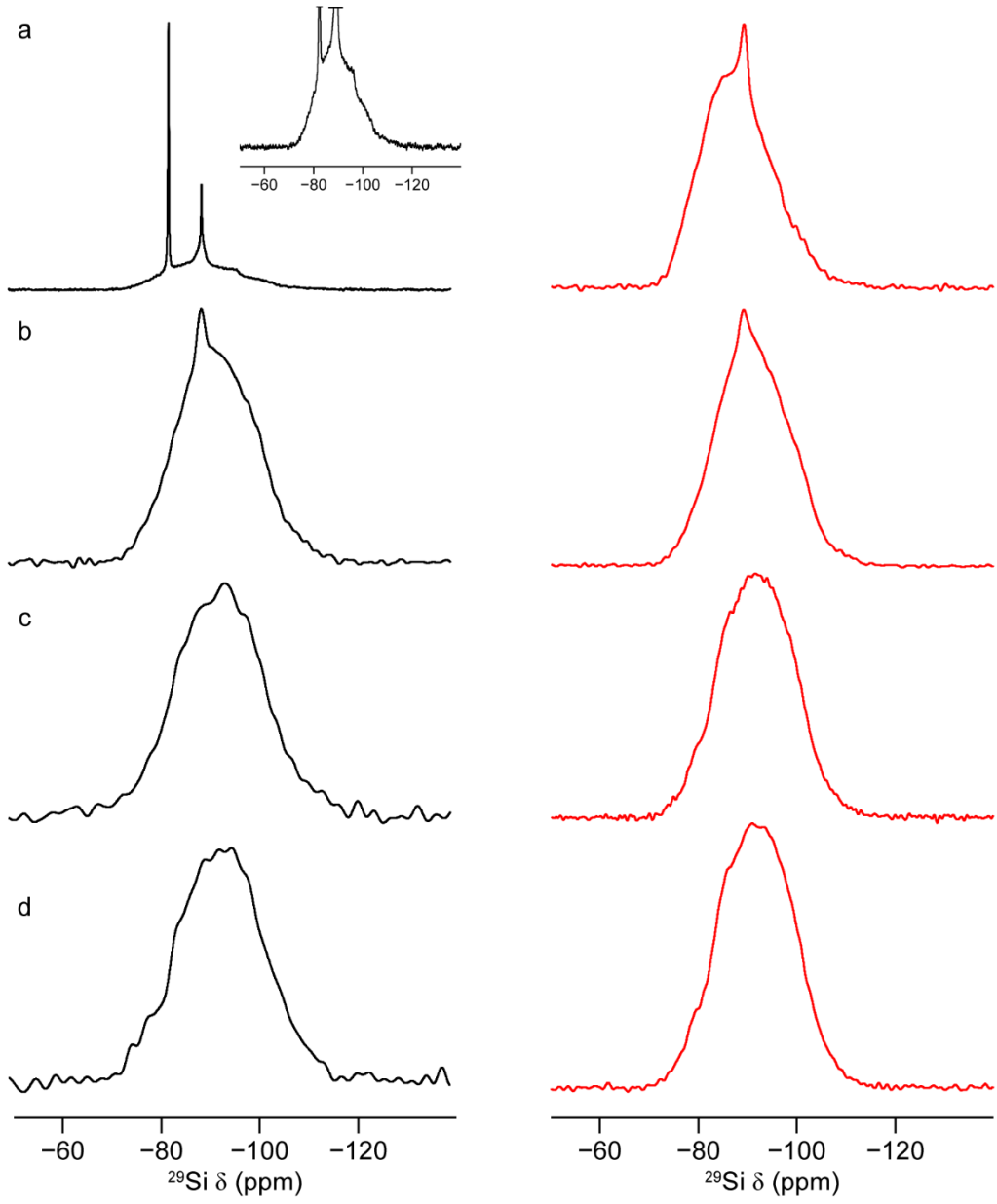

Figure 6.26. *^{29}Si (9.4 T, 14 kHz MAS) DP NMR (black) and ^{1}H-^{29}Si (9.4 T, 10 kHz MAS, τ_{CP} = 3 ms) CP NMR spectra (red) of as-made ^{29}Si-enriched high silica loading Si-γ-Al_2O_3 (8 wt% Si). Spectra were acquired (a) directly after synthesis and after ageing for (b) ~2 weeks, (c) ~1 year and (d) ~1 year and 1 month. In (a), an expansion of part of the spectrum is shown inset.*

^{1}H MAS NMR spectra of as-made Si-γ-Al_2O_3 high silica loading were acquired after different ageing times. The material was kept in a closed vial, with samples taken for analysis at intervals of ~2 weeks, ~1 year and ~1 year and 1 month. Figure 6.24(a) shows the spectrum obtained directly after the material was synthesised. Two sharp resonances are identifiable at ^{1}H $\delta_{iso} \approx 1.0$ and ≈ 3.7 ppm and are assigned to CH_3 and

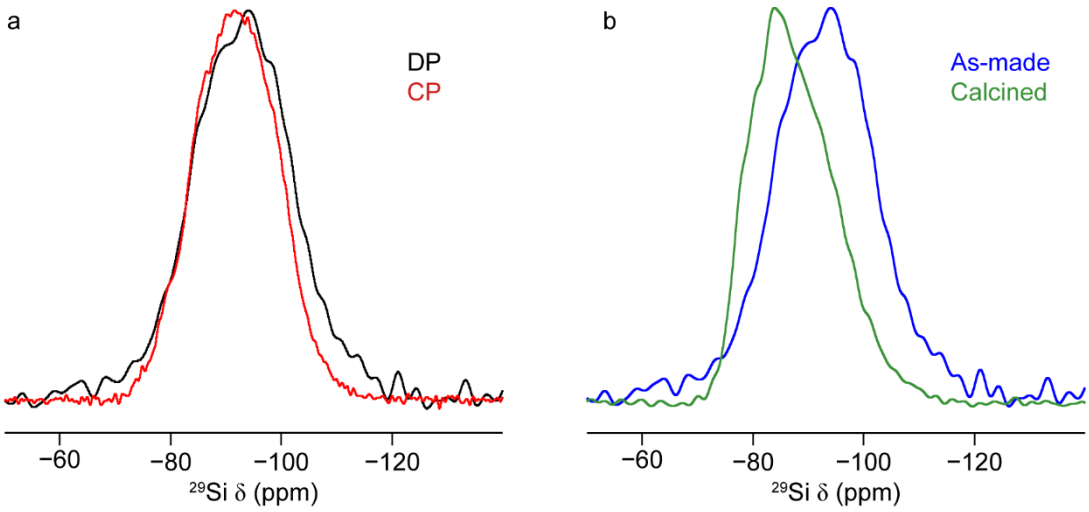

Figure 6.27. *(a) ^{29}Si (9.4 T, 14 kHz MAS) DP (black) and CP (red) NMR spectra of as-made high silica loading Si-γ-Al_2O_3 (8 wt% Si) aged for ~1 year. (b) ^{29}Si (9.4 T, 14 kHz MAS) DP NMR spectra of as-made high silica loading Si-γ-Al_2O_3 (8 wt% Si) aged for ~1 year (blue) and calcined high silica loading Si-γ-Al_2O_3 (8 wt% Si) (green). Spectral intensities have been normalised.*

CH_2 groups of TEOS, respectively.[79,80] While it is possible that these peaks may also correspond to ethanol (the solvent used during synthesis), it is unlikely, as the vacuum drying procedure is designed to remove volatile solvents from the material after wet impregnation. It appears that after drying is complete, a significant amount of molecular TEOS remains on the surface of γ-Al_2O_3, although its exact structural arrangement cannot be determined from ^{1}H NMR experiments alone. Subsequent ageing results in the evolution of a resonance at ^{1}H $\delta \approx 4$-5 ppm, consistent with the adsorption of H_2O onto the surface of Si-γ-Al_2O_3.[22-24] A substantial decrease in the sensitivity of TEOS resonances was also observed, indicating a loss of molecular TEOS, either by evaporation, or formation of new Si surface environments. This was also observed *via* ^{1}H-^{13}C CP NMR experiments, the spectra from which are shown in Figure 6.25. The spectrum obtained after the material was aged for *ca.* 2 weeks (Figure 6.25(a)) displays signals at ^{13}C $\delta_{iso} \approx 16$ and ≈ 59 ppm, which are assigned to CH_3 and CH_2 groups of TEOS, respectively.[80] After a total ageing time of *ca.* 1 year, the same peaks can still be identified in the ^{1}H-^{13}C CP NMR spectrum in Figure 6.25(b), albeit accompanied by a significant sensitivity decrease, despite the use of the same experimental parameters as for the first experiment.

To discern the effect of long-term ageing on the Si environments present on the surface of as-made "single shot" Si-γ-Al_2O_3, ^{29}Si DP and ^{1}H-^{29}Si CP NMR experiments were performed. In the DP NMR spectra of the newly synthesised material, two sharp resonances can be identified. The first, at ^{29}Si $\delta_{iso} \approx -82.5$ ppm, is assigned to liquid-state TEOS and the second, at ^{29}Si $\delta_{iso} \approx -89.3$ ppm, is attributed to TEOS groups anchored to the surface of γ-Al_2O_3.[80] An expansion of the ^{29}Si DP NMR spectrum in Figure 6.26(a) reveals a broad lineshape underlying the sharp TEOS peaks, indicating that the formation of Q^n species begins very rapidly after the completion of the drying process. As the ageing process progresses, the sharp peaks are lost from the DP NMR spectra and the broad feature becomes shifted upfield. Over time, the condensation of TEOS on the surface of γ-Al_2O_3 results in the formation higher-order Q^n species, accompanied by the exudation of organic components. ^{1}H-^{29}Si CP NMR reveals that the anchored organic species remain connected to the surface, with a relatively sharp peak at ^{29}Si $\delta_{iso} \approx -89.3$ ppm evident in the spectrum of the two-week-old sample. Although subsequent ^{1}H-^{29}Si CP NMR spectra do not display this feature, the presence of TEOS resonances in the ^{1}H-^{13}C CP NMR spectrum in Figure 6.25(b) suggests that a small quantity of this functional group still remains. It appears the reaction may have reached completion after a period of ~1 year, as no significant change in the ^{29}Si DP or CP lineshapes in Figures 6.26(c) or (d) can be detected. It is not known though at what stage the reaction reached completion from the data available. By overlaying the ^{29}Si DP and CP spectra of "single shot" Si-γ-Al_2O_3 aged for ~1 year, as in Figure 6.27(a), it can be seen that a portion of the DP lineshape (≈ −100 to −120 ppm) is not present in the CP NMR spectrum. This confirms that some of the Q^n species formed during the ageing process are not bonded to Al. Based on previous studies of amorphous SiO_2[24] and silica gel,[76] and by comparison with ^{29}Si NMR spectra obtained for equivalent materials, they are assigned to Q^3(3Si) and Q^4(4Si) sites. It is clear that the long-term ageing of as-made "single shot" Si-γ-Al_2O_3 promotes the formation of a structure similar to the one obtained by high-temperature calcination. Comparison of the ^{29}Si DP NMR spectra of the 1 year aged as-made material with the calcined "single

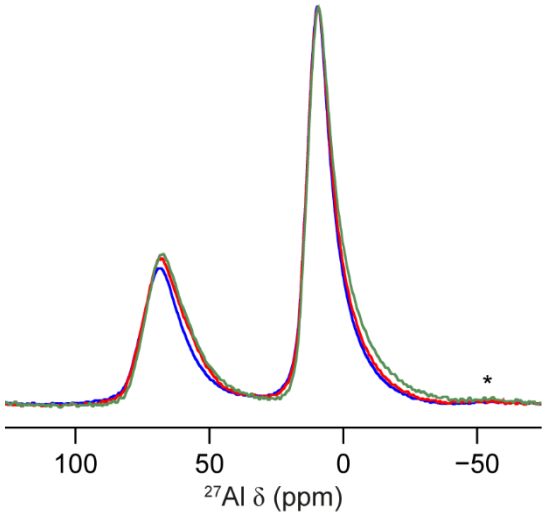

Figure 6.28. *^{27}Al (14.1 T, 20 kHz MAS) short flip angle DP NMR spectra of γ-Al_2O_3 (blue), calcined high silica loading Si-γ-Al_2O_3 (8 wt% Si) (green), and as-made high silica loading Si-γ-Al_2O_3 (8 wt% Si) aged for ~1 year and 4 months (red). * denotes a spinning sideband. Spectral intensities have been normalised.*

shot" Si-γ-Al_2O_3, as shown in Figure 6.27(b), reveals that the two structures are somewhat different. Long-term ageing promotes the formation of a structure with a greater proportion of silicate Q^n species than its calcined counterpart. Whilst calcination has previously been shown to result in a structure with some amorphous silica-like units, this route results in Si species which are more likely to be connected to Al centres on the γ-Al_2O_3 surface. ^{27}Al DP NMR experiments were performed for the calcined and as-made samples (after ageing for ~1 year and 4 months in the second case), and the corresponding spectra are shown in Figure 6.28, along with a spectrum of unmodified γ-Al_2O_3. The spectra are remarkably similar, showing only small variations in linewidth and peak intensity, consistent with what was previously observed for sequential grafting materials. This finding demonstrates that both calcination and gradual ageing routes generate only surface Si environments, leaving the bulk γ-Al_2O_3 largely unchanged.

6.7 ^{17}O Solid-State NMR Studies of γ-Al_2O_3 and Si-γ-Al_2O_3 Materials

In the study of oxide-based materials, ^{17}O solid-state NMR spectroscopy is well placed to offer useful insights into structure, thanks to its sensitivity to changes in local

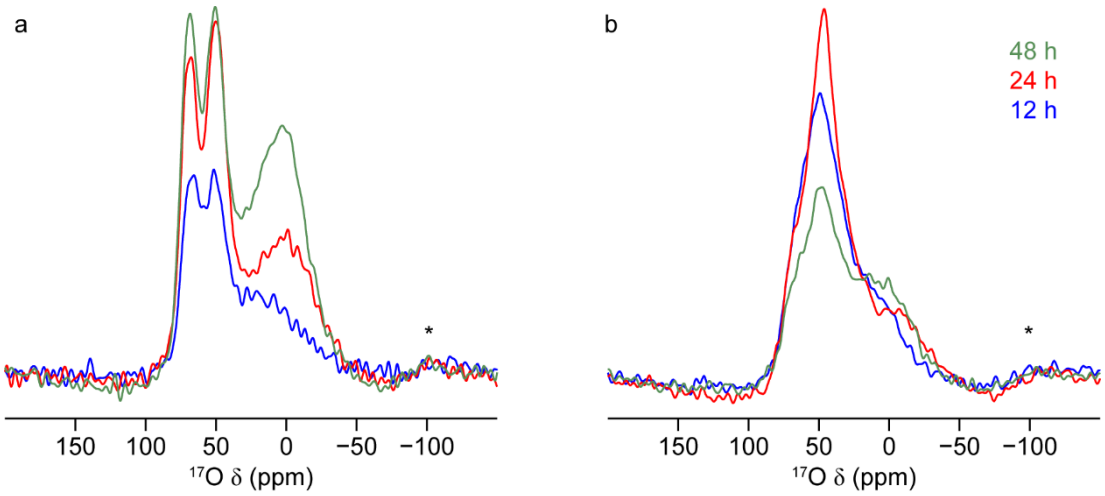

Figure 6.29. *^{17}O (14.1 T, 14 kHz MAS) short flip angle DP NMR spectra of (a) γ-Al_2O_3 and (b) Si-γ-Al_2O_3 (1.5 wt% Si), ^{17}O enriched for heating times of 12 (blue), 24 (red) and 48 h (green). Spectra have been scaled with respect to the number of transients and the mass of sample contained within each 4 mm rotor. * denotes a spinning sideband.*

chemical environments.[9,82,83] As outlined in previous chapters, the primary disadvantage of studying ^{17}O is its very low natural abundance. Although in certain cases it is possible to acquire NMR spectra under these conditions,[84] isotopic enrichment is usually necessary for advanced experiments.[9,82,83] Oldfield and co-workers were amongst the first to exploit ^{17}O solid-state NMR spectroscopy for the study of a variety of oxide materials, by using ^{17}O-enriched reagents during the synthetic process.[85-90] Whilst this approach has become relatively popular,[91-94] it means that the desired compounds must be specifically designed and prepared with ^{17}O NMR studies in mind. The post-synthesis gas exchange procedure, introduced in Chapters 1 and 4, offers an enrichment route that allows, in principle, for the study of conventionally synthesised and commercially obtained samples. Grey and co-workers have demonstrated its effectiveness in the characterisation of several materials, including zeolites[95-98] and oxide nanoparticles,[99,100] and it has been used in the present work to facilitate ^{17}O solid-state NMR studies of γ-Al_2O_3 and Si-γ-Al_2O_3 materials.

In order to identify optimum enrichment conditions for the aforementioned catalyst materials, ^{17}O gas exchange was carried out at different temperatures and heating durations on γ-Al_2O_3. From reference to the works of Peng *et al.*[97,98] and Klug *et al.*[101]

samples were enriched at temperatures of 300, 400 and 500 °C for a duration of 12 h. No signals were observed for a sample enriched at 300 °C and for that enriched at 400 °C signal was seen only after an extended period of signal averaging (~16 h). Enrichment at 500 °C resulted in a good level of sensitivity in a relatively short period of time (~0.5 h), so this temperature was selected for further experiments. Aliquots of γ-Al_2O_3 and Si-γ-Al_2O_3 (1.5 wt% Si) were heated, as before, in a 70% $^{17}O_2$ atmosphere, for intervals of 12, 24 and 48 h. The ^{17}O NMR spectra of the resulting materials, recorded using a short flip angle pulse, are shown in Figure 6.29. By reference to the data reported by Walter and Oldfield[90] and Klug *et al.*,[101] the following preliminary assignments can be made – the region between ^{17}O $\delta \approx -50$ and 10 ppm to surface O sites, and between ^{17}O $\delta \approx 10$ and 80 ppm to subsurface and bulk species. In Figure 6.29(a), signal intensity increases along with the enrichment duration, suggesting that for γ-Al_2O_3, longer heating times promote a greater degree of $^{16}O/^{17}O$ exchange throughout the structure. The same trend however, does not seem to be replicated for Si-γ-Al_2O_3 (1.5 wt% Si). An increase in signal intensity in the subsurface/bulk region of the spectrum is initially seen when the heating duration is doubled. A further increase, to 48 h, in contrast to γ-Al_2O_3, results in a notable decrease in intensity of this part of the spectral lineshape. It may be that extended heating time results in a "back exchange" reaction between ^{17}O and ^{16}O that was initially displaced from the material.

It has been previously observed that the presence of a surface overlayer affects enrichment behaviour.[101] Klug *et al.* reported a decrease in the amount of signal obtained compared to the unmodified γ-Al_2O_3 support, surmising that V_2O_5 species supported on γ-Al_2O_3 inhibited $^{16}O/^{17}O$ exchange with the bulk structure.[101] The reduced intensity of the broad component centred at ^{17}O $\delta \approx 0$ ppm in the spectrum of Si-γ-Al_2O_3 (1.5 wt% Si), compared to that of γ-Al_2O_3 is also clear. Whilst it is not possible to unambiguously assign this peak, one contribution may be from adsorbed H_2O.[99-103] Since isotopic exchange takes place in a sealed vial, any water bound to the surface of the oxide will not be able to escape, and could therefore become enriched along with the solid material. The addition of a Si surface overlayer could reduce the hygroscopic nature of the γ-Al_2O_3 support, resulting in less water adsorption onto the

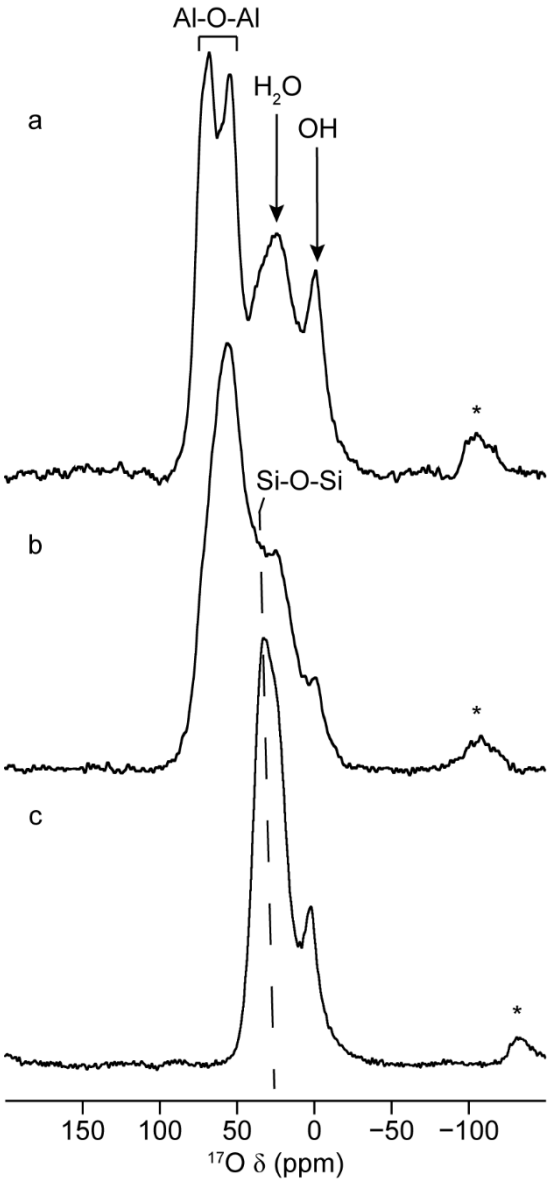

Figure 6.30. *^{17}O (20.0 T, 20 kHz MAS) DP NMR spectra of ^{17}O-enriched (a) γ-Al_2O_3, (500 °C for 24 h) (b) Si-γ-Al_2O_3 (500 °C for 24 h) and (c) amorphous SiO_2 (enriched during synthesis). * denotes a spinning sideband.*

surface.

Figure 6.30 shows ^{17}O NMR spectra of γ-Al_2O_3 and Si-γ-Al_2O_3 (1.5 wt% Si) ^{17}O-enriched at 500 °C for 24 h, along with the spectrum of ^{17}O-enriched amorphous SiO_2, all acquired at 20.0 T. The use of such a very high field strength allows for increased spectral resolution, thanks to a reduction in second-order quadrupolar broadening. As

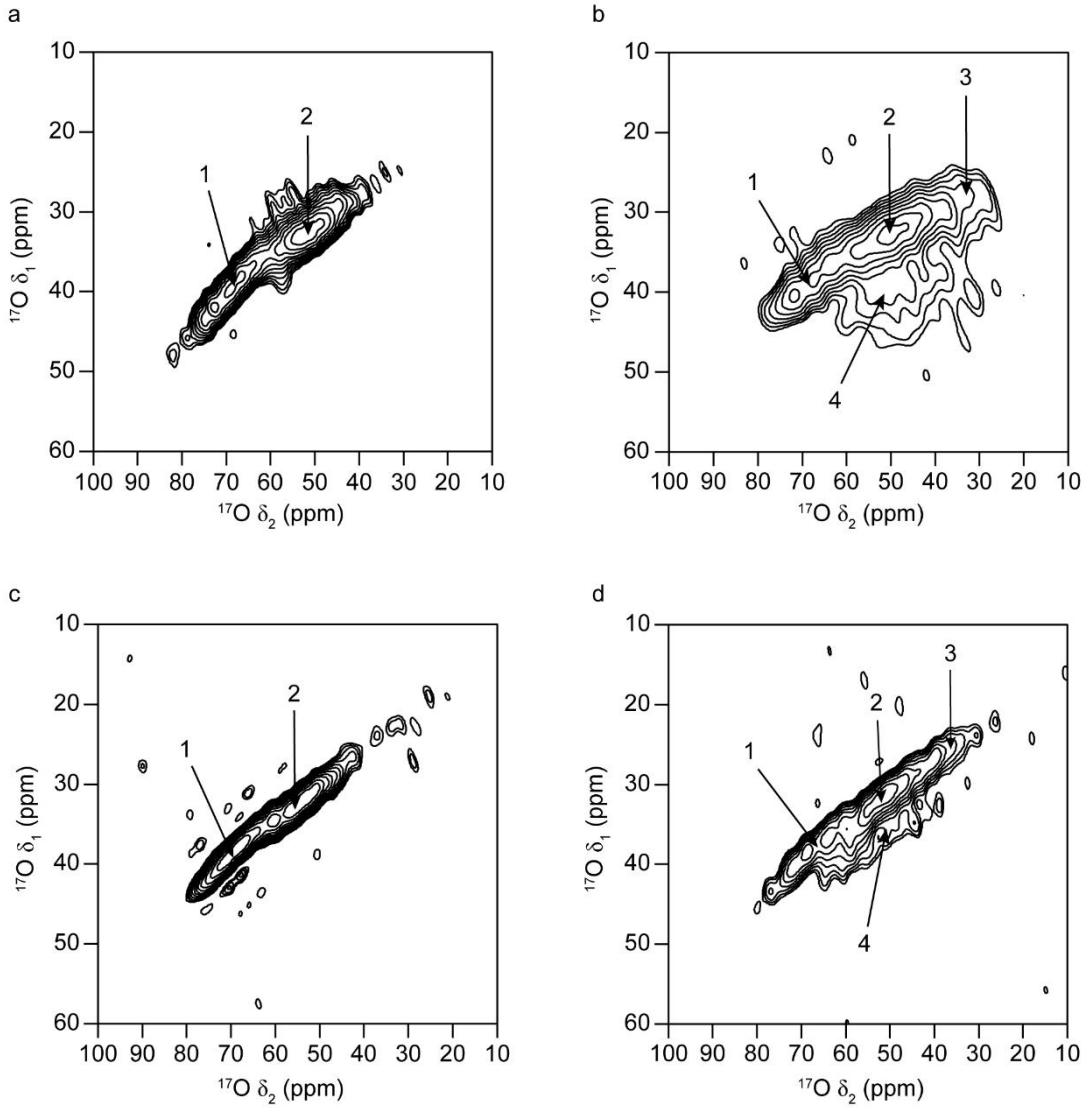

Figure 6.31. *^{17}O z-filtered 3QMAS NMR spectra of (a) and (c) γ-Al_2O_3, and (b) and (d) Si-γ-Al_2O_3 (1.5 wt% Si) ^{17}O-enriched at 500 °C for 24 h. Spectra were acquired at (a) and (b) 14.1 T and 14 kHz MAS, and (c) and (d) 20.0 T and 20 kHz MAS. In all spectra, shearing transformations have been applied. Peak assignments are as follows: 1 = Al-O-Al (OAl_4); 2 = Al-O-Al (OAl_3); 3 = Si-O-Al; 4 = Si-O-Si.*

a result, distinct O sites in these materials can now be more readily identified. Relatively sharp peaks can be seen in all spectra around 0 ppm, likely to correspond to OH groups on the surface of the materials.[88,104,105] In the spectra of γ-Al_2O_3 and Si-γ-Al_2O_3 (1.5 wt% Si), the peak is located at ^{17}O $\delta \approx -1$ ppm, whereas in the spectrum of amorphous SiO_2, it is observed at ^{17}O $\delta \approx 1.5$ ppm. This suggests that, despite the presence of a Si layer, the predominant observable isolated OH group in Si-γ-Al_2O_3 is AlOH, not SiOH, as is present in amorphous SiO_2. Given the linewidth of these peaks

Table 6.2. *NMR parameters (average quadrupolar product, $<P_Q>$ and average isotropic chemical shift, $<\delta_{iso}>$) for the O sites in ^{17}O-enriched (500 °C for 24 h) γ-Al_2O_3 and Si-γ-Al_2O_3 (1.5 wt% Si), obtained from the z-filtered 3QMAS spectra in Figure 6.31(a) and (b) (14.1 T).*

Site	γ-Al_2O_3		Si-γ-Al_2O_3 (1.5 wt% Si)	
	$<P_Q>$ / MHz	$<\delta_{iso}>$ (ppm)	$<P_Q>$ / MHz	$<\delta_{iso}>$ (ppm)
Al-O-Al (OAl_4)	1.5 (3)	73 (3)	1.7 (3)	67 (3)
Al-O-Al (OAl_3)	2.3 (3)	57 (3)	2.5 (3)	55 (3)
Si-O-Al	-	-	3.3 (3)	43 (3)
Si-O-Si	-	-	4.4 (3)	62 (3)

Table 6.3. *NMR parameters (average quadrupolar product, $<P_Q>$ and average isotropic chemical shift, $<\delta_{iso}>$) for the O sites in ^{17}O-enriched (500 °C for 24 h) γ-Al_2O_3 and Si-γ-Al_2O_3 (1.5 wt% Si), obtained from the z-filtered 3QMAS spectra in Figure 6.31(c) and (d) (20.0 T).*

Site	γ-Al_2O_3		Si-γ-Al_2O_3 (1.5 wt% Si)	
	$<P_Q>$ / MHz	$<\delta_{iso}>$ (ppm)	$<P_Q>$ / MHz	$<\delta_{iso}>$ (ppm)
Al-O-Al (OAl_4)	1.3 (3)	72 (3)	1.6 (3)	70 (3)
Al-O-Al (OAl_3)	2.5 (3)	60 (3)	2.5 (3)	59 (3)
Si-O-Al	-	-	3.5 (3)	45 (3)
Si-O-Si	-	-	4.4 (3)	63 (3)

(~20 ppm at 20.0 T) however, it is possible that SiOH species are present in Si-γ-Al_2O_3 (1.5 wt% Si), that are not resolved in the MAS spectrum. At the higher field, it is now possible to confirm the presence of a broad resonance attributed to adsorbed water, [99-103] and as in Figure 6.29, it is most intense in the spectrum of γ-Al_2O_3. This region overlaps with the expected position of the Si-O-Si species,[105] which is evident in the spectrum of amorphous SiO_2. It is therefore not possible from the ^{17}O MAS spectrum alone to unambiguously confirm the presence Si-O-Si in Si-γ-Al_2O_3 (1.5 wt% Si). The presence of at least one, possibly two types of Al-O-Al linkages can however be identified in both γ-Al_2O_3 and Si-γ-Al_2O_3 (1.5 wt% Si).[90,101,106]

In order to undertake more detailed characterisation of the oxygen sites present in γ-Al_2O_3 and Si-γ-Al_2O_3 (1.5 wt% Si), high-resolution experiments are required. One

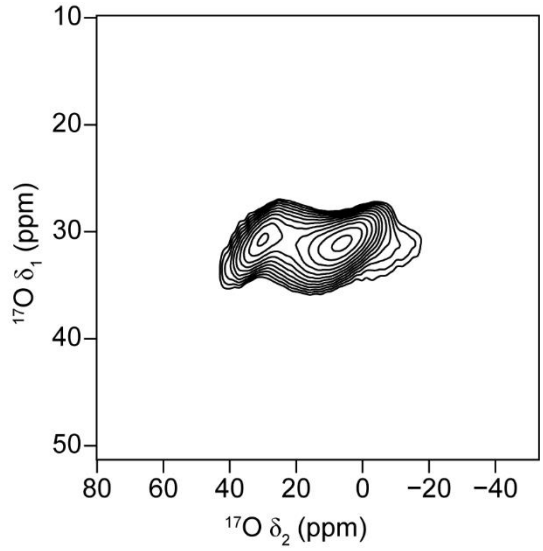

Figure 6.32. *^{17}O (14.1 T, 14 kHz MAS) z-filtered 3QMAS NMR spectrum of ^{17}O-enriched amorphous SiO_2 (enriched during synthesis). A shearing transformation has been applied.*

Table 6.4. *NMR parameters (average quadrupolar product, $\langle P_Q \rangle$ and average isotropic chemical shift, $\langle \delta_{iso} \rangle$) for the Si-O-Si site in ^{17}O-enriched amorphous SiO_2 (enriched during synthesis), obtained from the z-filtered 3QMAS spectrum in Figure 6.32.*

$\langle P_Q \rangle$ / MHz	$\langle \delta_{iso} \rangle$ (ppm)
5.0 (2)	43 (2)

such example that has previously been introduced in this work is the 3QMAS experiment. Figure 6.31 shows 3QMAS spectra of γ-Al_2O_3 and Si-γ-Al_2O_3 (1.5 wt% Si) ^{17}O-enriched at 500 °C for 24 h, acquired at external magnetic field strengths of 14.1 and 20.0 T. Two sites are identifiable in the spectra of γ-Al_2O_3 and four in the spectra of Si-γ-Al_2O_3 (1.5 wt% Si). The corresponding NMR parameters, given in Tables 6.2 and 6.3, were extracted and by comparison with a comprehensive collection of published data, can be assigned as follows: 1 = Al-O-Al (OAl_4); 2 = Al-O-Al (OAl_3); 3 = Si-O-Al and 4 = Si-O-Si.[86,90,98,101-111] The identification of two Al-O-Al sites in these materials is consistent with previous computational modelling studies of γ-Al_2O_3, where it was reported that tricoordinated oxygen sites are found at the surface of the material.[112,113] Work by Chen and Huang[102] identified the presence of unreacted alumina in an aluminophosphate prepared using dry gel conversion, and using ^{17}O

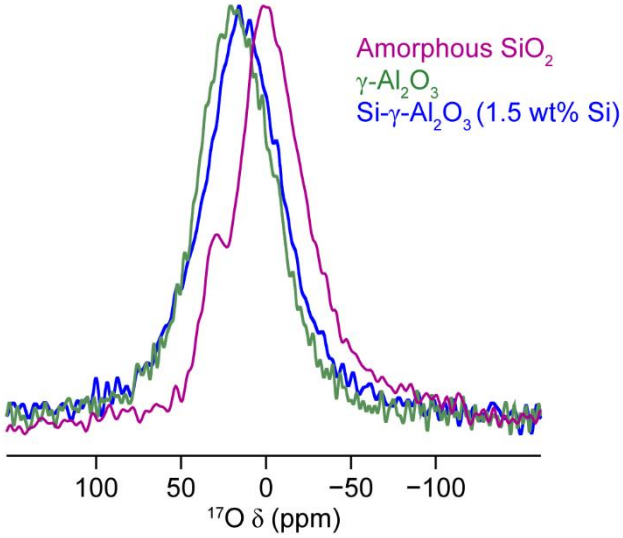

Figure 6.33. *^{1}H-^{17}O (14.1 T, 14 kHz MAS) CP NMR spectra of ^{17}O-enriched amorphous SiO_2, (pink), γ-Al_2O_3 (500 °C for 12 h) (green) and Si-γ-Al_2O_3 (1.5 wt% Si) (500 °C for 12 h) (blue). τ_{CP} = 0.4 (blue) or 0.5 ms (pink and green).*

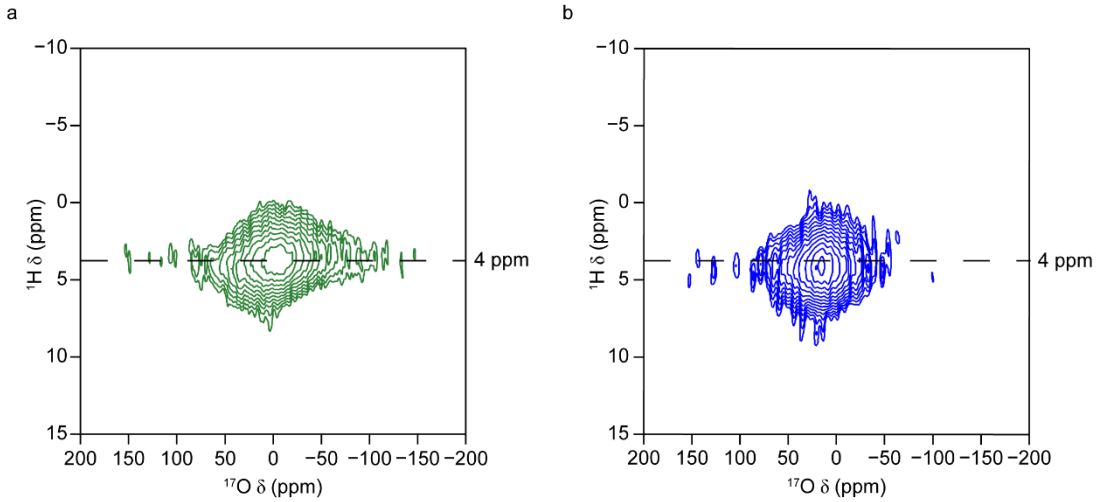

Figure 6.34. *^{1}H-^{17}O (14.1 T, 20 and 14 kHz MAS) CP HETCOR NMR spectra of (a) ^{17}O-enriched γ-Al_2O_3 (500 °C for 12 h) (green, τ_{CP} = 0.5 ms) and (b) ^{17}O-enriched Si-γ-Al_2O_3 (1.5 wt% Si) (500 °C for 12 h) (blue, τ_{CP} = 0.4 ms).*

NMR spectroscopy, they obtained C_Q and δ_{iso} values (4.2 MHz and 79 ppm, respectively) for the OAl_3 site. These values are larger than those reported in the present work for an equivalent site in γ-Al_2O_3 Si-γ-Al_2O_3 (1.5 wt% Si), but some factors should be considered regarding this observation. The data presented by Chen and Huang[102] is consistent with earlier figures obtained by Walter and Oldfield[90] for a

sample of ^{17}O-enriched θ-Al_2O_3. The θ form of alumina is known to differ structurally from γ-Al_2O_3, possessing, for example, very few, or no, Al(V) species[114,115] and such a change points towards two different surface morphologies between the two alumina polymorphs. Whilst Walter and Oldfield were not able to obtain NMR parameters for γ-Al_2O_3, they did report that β-Ga_2O_3, an isomorph of γ-Al_2O_3, possesses a ^{17}O C_Q of 2.5 MHz.[90] Stebbins *et al.* have also reported this to be the case for OAl_3 in aluminosilicate glasses.[110] The present assignment of OAl_3 in γ-Al_2O_3 therefore represents the most plausible one based upon currently available data.

The ^{17}O z-filtered 3QMAS NMR spectrum of amorphous SiO_2, acquired at 14.1 T, is presented in Figure 6.32. The average NMR parameters for the Si-O-Si species, given in Table 6.4, show generally good agreement with the corresponding species in Si-γ-Al_2O_3 (1.5 wt% Si). The variation in δ_{iso} values between the two materials can be accounted for by the differing structural arrangements of each type of Si-O-Si linkage. In amorphous SiO_2, Si-O-Si is present throughout the bulk structure as the only type of connection between Si atoms. By contrast, in Si-γ-Al_2O_3 (1.5 wt% Si), the Si-O-Si species form part of a surface overlayer on alumina, with nearby functional groups being Si-O-Al and Al-O-Al. The C_Q values of the two types of Si-O-Si species are quite similar, particularly given the respective errors on the values. Notably, resonances corresponding to hydroxyl oxygen species were not observed in 3QMAS spectra of γ-Al_2O_3 or Si-γ-Al_2O_3 (1.5 wt% Si). However, as van Eck *et al.*[116] have noted, from studies of sol-gel produced silica, the characterisation of OH groups can be challenging. These authors reported a range of different SiOH species, some of which had very low C_Q values (~200 kHz), which due to the inefficiency of exciting 3Q coherences when C_Q is small, means their signals are difficult to observe in a 3QMAS experiment. Additionally, it was found that SiOH oxygens possessed very rapid T_1 relaxation times (~0.1 ms), resulting from high hydroxyl hydrogen mobility creating rapidly fluctuating dipolar fields.[116] Although van Eck *et al.* were able to observe SiOH signal in a 3QMAS experiment, this was likely only a subset of the total OH population, where C_Q values were determined to be in the range of 2.8–3.2 MHz, and spin-lattice relaxation was likely to be slower.[116] Lee *et al.* have reported, from studies of layered aluminosilicate materials, that AlOH groups are also difficult to

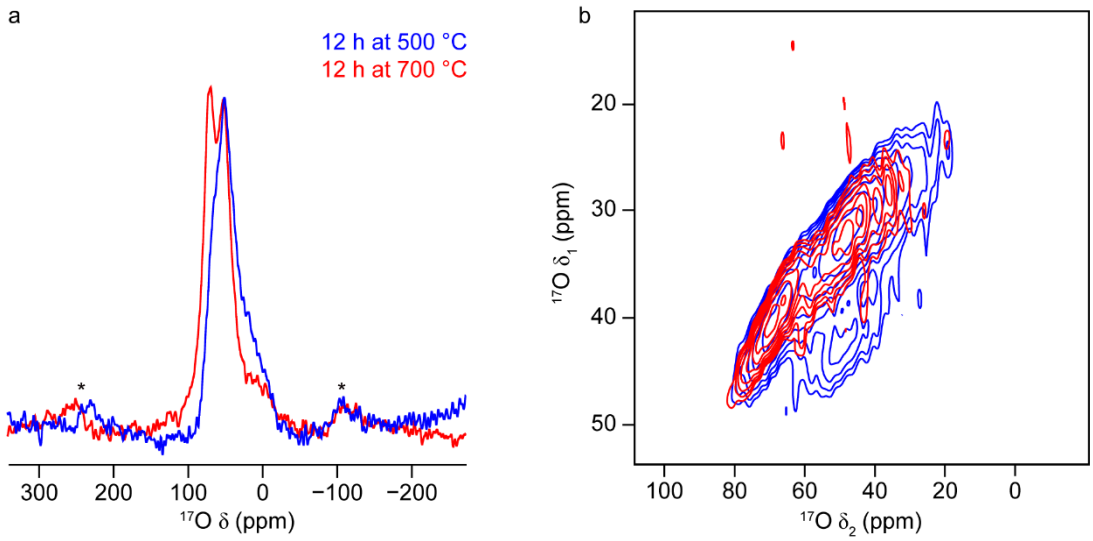

Figure 6.35. *^{17}O (14.1 T, 14 kHz MAS) (a) DP NMR and (b) z-filtered 3QMAS NMR spectra of Si-γ-Al_2O_3 (1.5 wt% Si), ^{17}O-enriched for 12 h at temperatures of 500 (blue) and 700 °C (red). In (b), a shearing transformation has been applied to both spectra. In (a), spectra have been normalised to the OAl_3 resonance, and * denotes a spinning sideband.*

observe by 3QMAS due to rapid T_1 relaxation, requiring a high concentration of these species to be present (and successfully ^{17}O enriched) in order to be detected.[104] These findings also have implications for the interpretation of ^{1}H-^{17}O CP NMR experiments. Figure 6.33 shows ^{1}H-^{17}O CP NMR spectra of ^{17}O-enriched γ-Al_2O_3, Si-γ-Al_2O_3 (1.5 wt% Si) (500 °C for 12 h) and ^{17}O-enriched amorphous SiO_2. A resonance, attributable to silanol oxygen species,[88,94,116] is evident at ^{17}O $\delta \approx 1.8$ ppm in the spectrum of ^{17}O-enriched amorphous SiO_2. The second resonance, at ^{17}O $\delta \approx 30$ ppm, is assigned to Si-O-Si sites,[94] likely close to the silica surface. By contrast, the ^{17}O resonances in the spectra of γ-Al_2O_3 and Si-γ-Al_2O_3 (1.5 wt% Si) are centred at ^{17}O $\delta \approx 15$ ppm. ^{1}H-^{17}O CP HETCOR spectra of γ-Al_2O_3 and Si-γ-Al_2O_3 (1.5 wt% Si) (^{17}O enriched at 500 °C for 12 h), displayed in Figure 6.34, shows that these resonances correlate with signals centred at ^{1}H $\delta_{iso} \approx 4$ ppm. This evidence indicates that adventitious water is predominant at the surface of these materials (at least when they are in the hydrated state). These findings do not preclude the presence of AlOH or SiOH sites in the alumina-based materials, but do suggest that they are not readily observable *via* CP from ^{1}H. This may be due to their unfavourable relaxation, or possibly as a result of a lower level of enrichment.

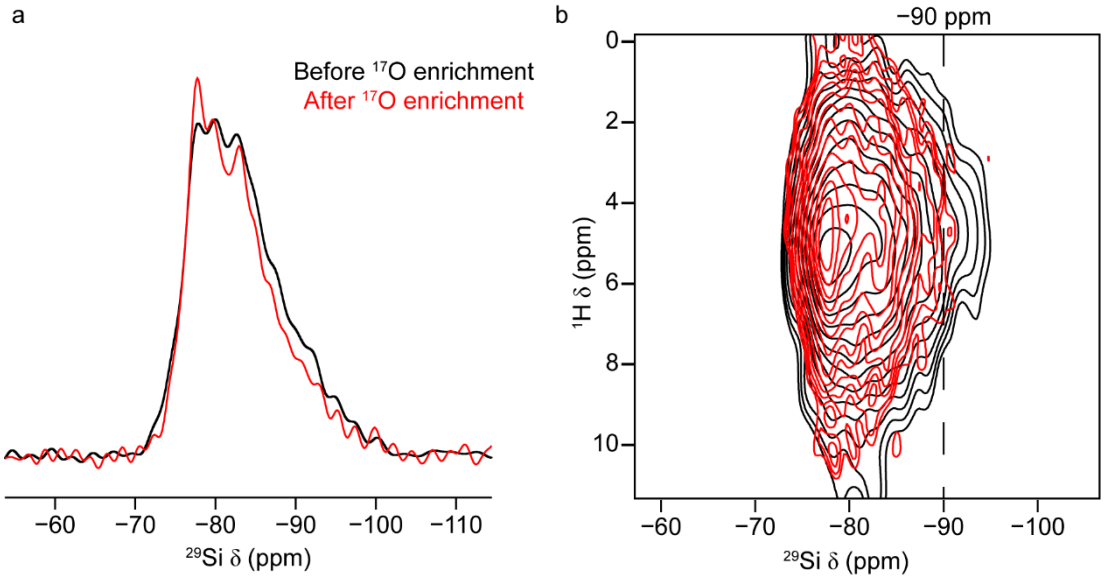

Figure 6.36. *(a) ^{29}Si (9.4 T, 14 kHz MAS) DP NMR and (b) ^{1}H-^{29}Si (9.4 T, 10 kHz MAS, τ_{CP} = 0.5 ms) CP HETCOR NMR spectra of ^{29}Si-enriched Si-γ-Al_2O_3 (1.5 wt% Si) before (black) and after (red) ^{17}O gas exchange enrichment at 500 °C for 24 h. In (a) spectra have been normalised.*

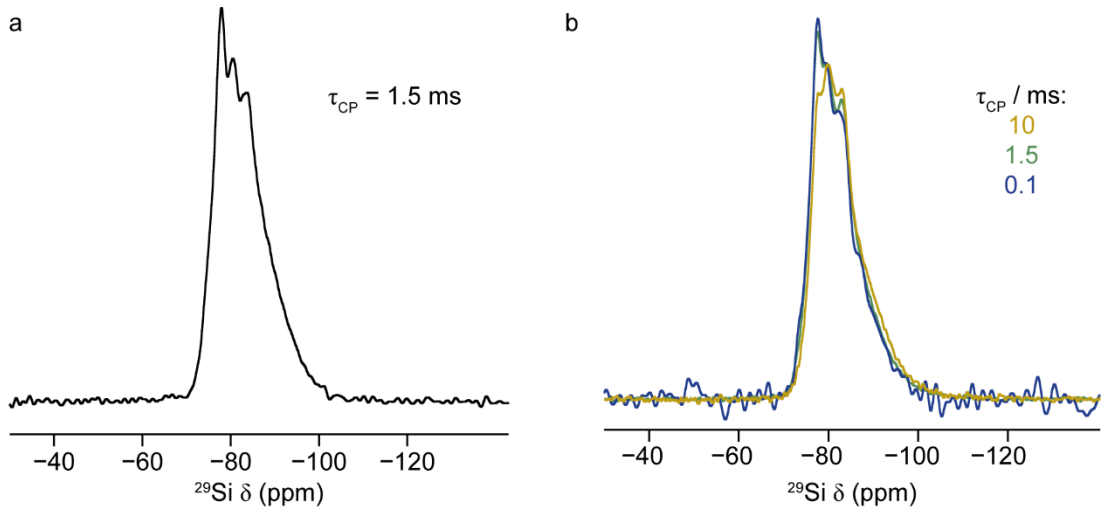

Figure 6.37. *^{1}H-^{29}Si (9.4 T, 10 kHz MAS) CP NMR spectra of (a) dehydrated ^{29}Si-enriched Si-γ-Al_2O_3 (1.5 wt% Si) (τ_{CP} = 1.5 ms) and (b) hydrated ^{29}Si- and ^{17}O-enriched Si-γ-Al_2O_3 (1.5 wt% Si) (^{17}O-enriched at 500 °C for 24 h) (τ_{CP} = 0.1, 1.5, or 10 ms). In (b) spectra have been normalised.*

In order to further explore the ^{17}O enrichment process in γ-Al_2O_3-based materials, ^{17}O gas exchange of Si-γ-Al_2O_3 (1.5 wt% Si) was carried out at a higher temperature of 700 °C for a heating duration 12 h. This temperature was chosen because it is the highest at which the material could be heated for an extended period, without effecting a phase transition in the supporting γ-Al_2O_3 structure.[114,115,117] The ^{17}O MAS NMR

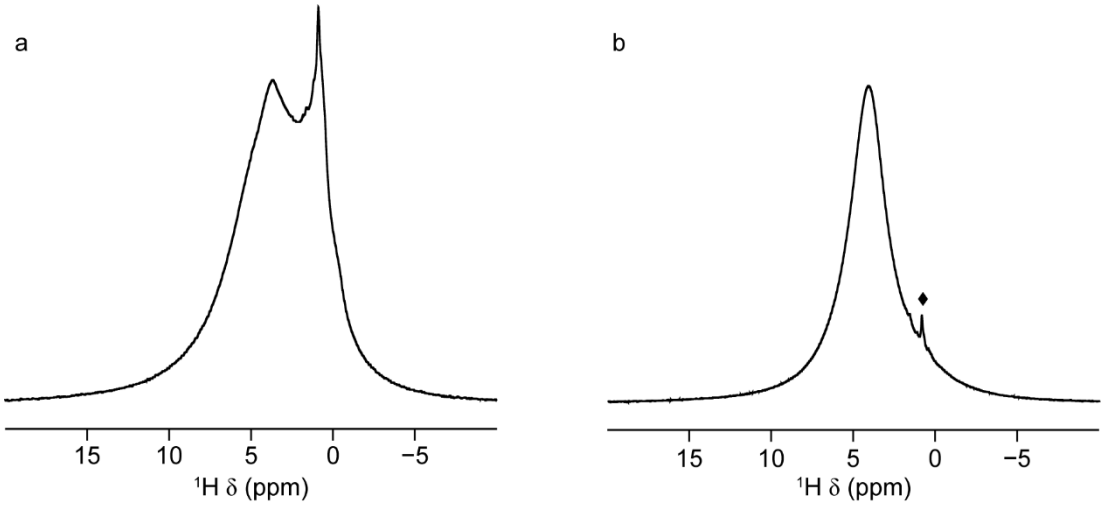

Figure 6.38. *^{1}H (9.4 T, 10 kHz MAS) NMR spectra of (a) partially dehydrated ^{29}Si-enriched Si-γ-Al_2O_3 (1.5 wt% Si) and (b) hydrated ^{29}Si- and ^{17}O-enriched Si-γ-Al_2O_3 (1.5 wt% Si) (^{17}O-enriched at 500 °C for 24 h). In (b), ♦ denotes a peak from the rotor cap.*[78]

spectrum of this sample is shown in Figure 6.35(a), where it is compared with an equivalent spectrum of Si-γ-Al_2O_3 (1.5 wt% Si) enriched at 500 °C for 12 h. The lineshape of the sample enriched at 700 °C appears distinctly different to that enriched at 500 °C, bearing more resemblance to the lineshapes of ^{17}O-enriched γ-Al_2O_3 in Figure 6.29. This observation suggests that ^{17}O enrichment at the higher temperature favours ^{16}O/^{17}O exchange with the underlying Al-O-Al sites. Comparison of the ^{17}O z-filtered 3QMAS spectra of the two Si-γ-Al_2O_3 (1.5 wt% Si) materials confirms this to be the case, with only the two γ-Al_2O_3-type oxygen sites (OAl_3 and OAl_4) being detectable in the spectrum of the sample enriched at 700 °C.

6.8 Characterisation of Doubly-Enriched (^{29}Si and ^{17}O) Si-γ-Al_2O_3 (1.5 wt% Si)

In preceding sections of this chapter, the characterisation of Si-γ-Al_2O_3 materials has been carried by isotopic enrichment of one particular nuclide. However, if double enrichment of ^{29}Si and ^{17}O could be accomplished, then it would open up the ability to attempt heteronuclear correlation experiments. This approach has been demonstrated to be a powerful way of obtaining detailed information regarding the local structure of zeolites.[94] Accordingly, a sample of ^{29}Si-enriched Si-γ-Al_2O_3 (1.5 wt% Si), previously investigated in Section 6.3, was ^{17}O-enriched using gas exchange

at 500 °C for 24 h. These conditions were chosen based on the findings in Section 6.6, where it was shown that they resulted in the highest level of enrichment for Si-γ-Al_2O_3 (1.5 wt% Si) of all the heating times studied. In order to ascertain what, if any, changes were effected on the structure of the material as a result of the ^{17}O enrichment process, ^{1}H and ^{29}Si NMR experiments were also performed. Figure 6.36(a) shows ^{29}Si DP NMR spectra of ^{29}Si-enriched Si-γ-Al_2O_3 (1.5 wt% Si) before and after being ^{17}O enriched. A notable lineshape change is observed in the post enrichment spectrum, particularly in the region at more negative ppm values, where intensity is lost. This is accompanied by a relative increase in lineshape intensity of the peak at ^{29}Si $\delta_{iso} \approx -77$ ppm. These changes are further highlighted in the CP HETCOR NMR spectra in Figure 6.36(b), where the intensity loss in the region around −90 ppm, corresponding to Si-O-Si linkages, is clearly evident. These findings suggest that hydrolysis of Si-O-Si bonds has occurred during the ^{17}O enrichment procedure, leading to a reduction in the amount of bridging Q^4(3Al) Si species, and an increase in non-bridging Si units. This reaction is likely to be driven by the enrichment conditions of high temperature, the presence of ^{17}O gas in a sealed vial, and the presence of adventitious water, which is released from the silicated alumina surface by extended heating at 500 °C. The fit model shown in Figure 6.13 was applied to the spectrum in Figure 6.36(a), and matched this lineshape well, requiring only the intensities of each component to be re-optimised. This indicates that the same species remain in the doubly-enriched Si-γ-Al_2O_3 (1.5 wt% Si), although the relative amounts of each Si unit have changed.

^{1}H-^{29}Si CP NMR spectra of dehydrated (150 °C, ~12 h) ^{29}Si-γ-Al_2O_3 (1.5 wt% Si), and hydrated doubly-enriched Si-γ-Al_2O_3 (1.5 wt% Si) are shown in Figure 6.37. The two spectra appear very similar at a CP contact time of 1.5 ms, indicating that the two different treatment methods (dehydration and ^{17}O-mediated hydrolysis) result in the ^{29}Si spectra being more significantly influenced by local OH density. This is confirmed by spectra obtained at additional contact times, where the longest value (10 ms) bears a strong resemblance to the spectrum of the material only enriched in ^{29}Si (Figure 6.3) Comparison of ^{1}H MAS NMR spectra of the two materials, shown in Figure 6.38, reveals that the doubly-enriched Si-γ-Al_2O_3 (1.5 wt% Si) is in a hydrated state, displaying an intense broad peak at ^{1}H $\delta_{iso} \approx 4.2$ ppm, characteristic of adsorbed H_2O.

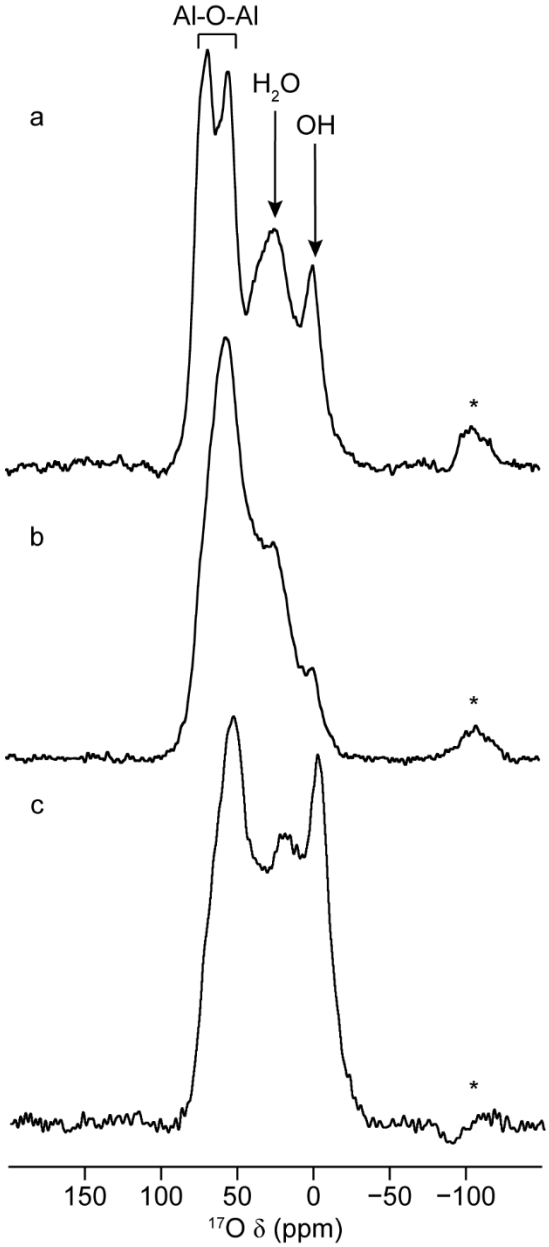

Figure 6.39. *^{17}O (20.0 T, 20 kHz MAS) DP NMR spectra of ^{17}O-enriched (a) γ-Al_2O_3, (500 °C for 24 h) (b) Si-γ-Al_2O_3 (500 °C for 24 h) and (c) doubly-enriched (^{29}Si and ^{17}O) Si-γ-Al_2O_3 (500 °C for 24 h). * denotes a spinning sideband.*

This finding demonstrates that ^{17}O-mediated hydrolysis appears to produce a Si overlayer containing a reduced amount of Si-O-Si bridging units and an increased volume of non-bridging surface Si species.

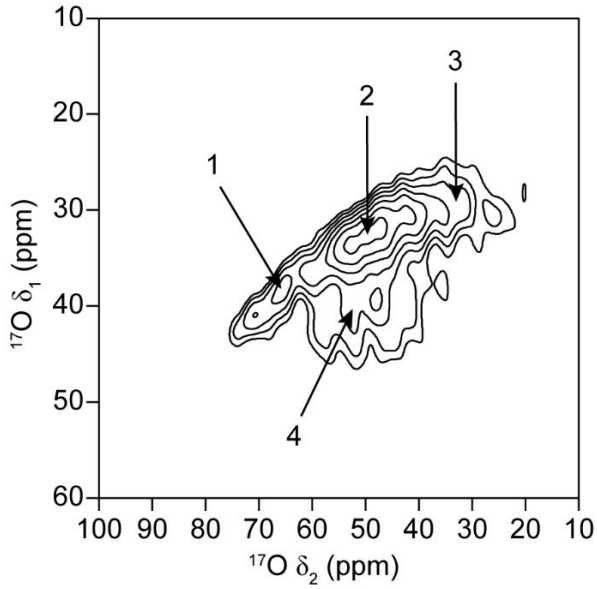

Figure 6.40. *^{17}O (14.1 T, 14 kHz MAS) z-filtered 3QMAS NMR spectrum of doubly-enriched (^{29}Si and ^{17}O) Si-γ-Al_2O_3 (1.5 wt% Si) (500 °C for 24 h). A shearing transformation has been applied. Peak assignments are as follows: 1 = Al-O-Al (OAl_4); 2 = Al-O-Al (OAl_3); 3 = Si-O-Al; 4 = Si-O-Si.*

Table 6.5. *NMR parameters (average quadrupolar product, $\langle P_Q \rangle$ and average isotropic chemical shift, $\langle \delta_{iso} \rangle$) for O sites in ^{29}Si- and ^{17}O-enriched (500 °C for 24 h) Si-γ-Al_2O_3 (1.5 wt% Si), obtained from the z-filtered 3QMAS spectrum in Figure 6.40 (14.1 T).*

Site	^{29}Si-γ-$Al_2{}^{17}O_3$ (1.5 wt% Si)	
	$\langle P_Q \rangle$ / MHz	$\langle \delta_{iso} \rangle$ (ppm)
Al-O-Al (OAl_4)	1.6 (3)	67 (3)
Al-O-Al (OAl_3)	2.5 (3)	60 (3)
Si-O-Al	3.8 (3)	45 (3)
Si-O-Si	4.1 (3)	66 (3)

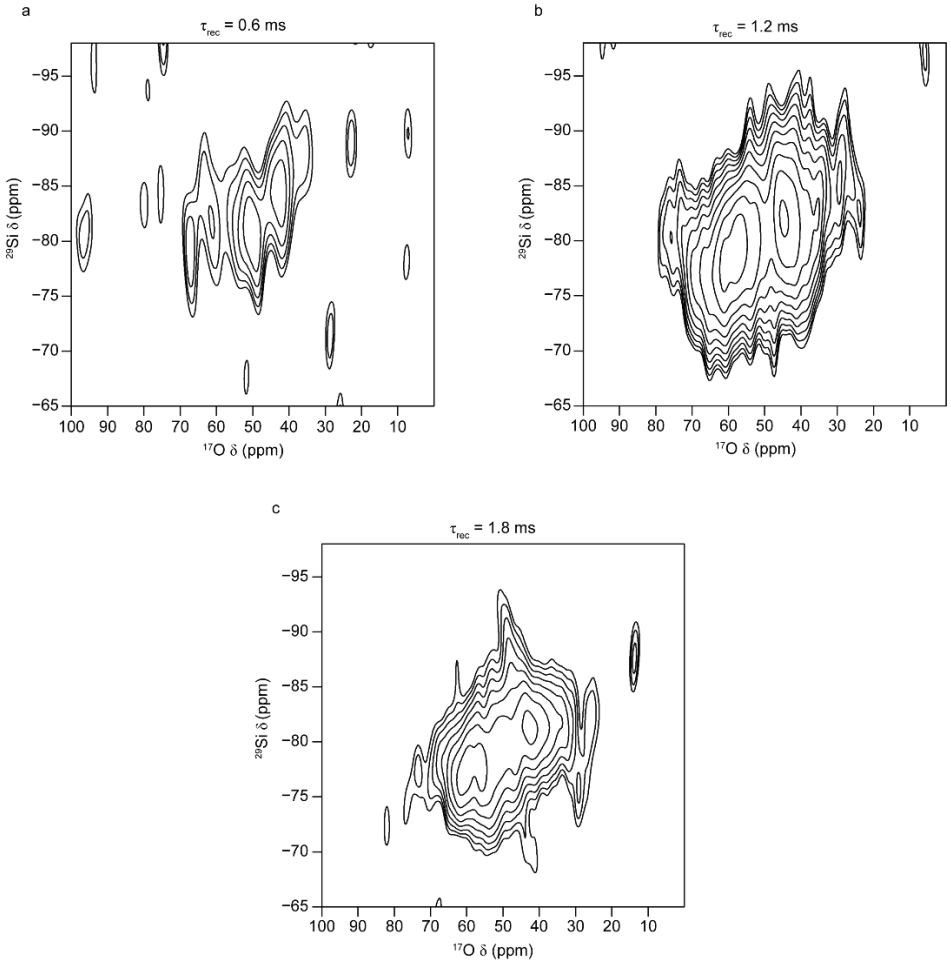

Figure 6.41. *^{29}Si-^{17}O (20.0 T, 20 kHz MAS) D-HMQC spectra of doubly-enriched (^{29}Si and ^{17}O) Si-γ-Al_2O_3 (^{17}O-enriched at 500 °C for 24 h), acquired with (a) τ_{rec} = 0.6 ms, (b) τ_{rec} = 1.2 ms and (c) τ_{rec} = 1.8 ms.*

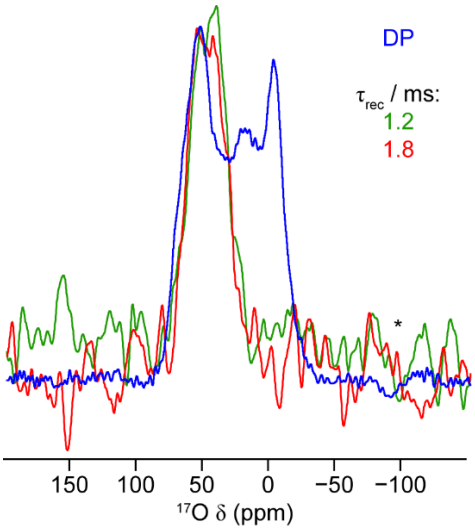

Figure 6.42. *Overlay of ^{17}O (δ_2) projections of D-HMQC spectra of doubly-enriched (^{29}Si and ^{17}O) Si-γ-Al_2O_3 (^{17}O-enriched at 500 °C for 24 h), shown in Figure 6.41, as a function of τ_{rec}. The ^{17}O DP NMR spectrum (blue) is also shown for comparison. * denotes a spinning sideband.*

Figure 6.39 shows ^{17}O NMR spectra of γ-Al_2O_3, Si-γ-Al_2O_3 (1.5 wt% Si) ^{17}O enriched at 500 °C for 24 h and doubly-enriched (^{29}Si and ^{17}O) Si-γ-Al_2O_3 (1.5 wt% Si), acquired at 20.0 T. It can be seen that the lineshape of the doubly-enriched Si-γ-Al_2O_3 (1.5 wt% Si) material in Figure 6.39(c), is distinctly different to its singly-enriched (^{17}O) counterpart. Specifically, a notable increase in the intensity of the hydroxyl oxygen resonance is evident, suggesting that, despite the presence of adsorbed H_2O, OH species have been successfully enriched by the gas exchange process, consistent with the prior findings from ^{29}Si and ^{1}H NMR spectroscopy. It is interesting to note that this result is not mirrored in the ^{17}O spectrum of singly-enriched (^{17}O) Si-γ-Al_2O_3 (1.5 wt% Si). As mentioned in Section 6.4, this material was obtained commercially, and as a result, the production process differs from the one employed on a laboratory scale, as was used for the doubly enriched silicated alumina sample. It would appear that the industrial synthesis route generates a material with a more extensively dehydroxylated surface than its laboratory-prepared counterpart, although the latter sample was shown above to have its OH functionality enhanced by the ^{17}O gas exchange process. However, the two materials are otherwise structurally very similar, as demonstrated by the ^{17}O z-filtered 3QMAS spectrum (acquired at 14.1 T) of doubly-enriched Si-γ-Al_2O_3 (1.5 wt% Si) in Figure 6.40, which bears a strong resemblance to the equivalent spectrum obtained for singly- (^{17}O) enriched Si-γ-Al_2O_3 (1.5 wt% Si), shown in Figure 6.31(b). The two sets of average NMR parameters (Tables 6.2 and 6.5) extracted from these spectra are also in very good agreement.

Since it was demonstrated that isotopic enrichment of both ^{29}Si and ^{17}O could be accomplished for a sample of Si-γ-Al_2O_3 (1.5 wt% Si), heteronuclear correlation experiments were attempted on this material. The D-HMQC experiment,[118] previously utilised successfully in Chapter 5 for NMR studies of γ-Al_2O_3, was employed in combination with the $SR4^2_1$ scheme for active recoupling of the ^{29}Si-^{17}O dipolar interaction.[119] These experiments were performed on a 20.0 T instrument, in order to take advantage of the increased resolution and reduction in second-order quadrupolar broadening (for ^{17}O) offered by this high field strength.[10,120] ^{29}Si-^{17}O D-HMQC spectra of doubly-enriched Si-γ-Al_2O_3 (1.5 wt% Si), acquired using three different dipolar

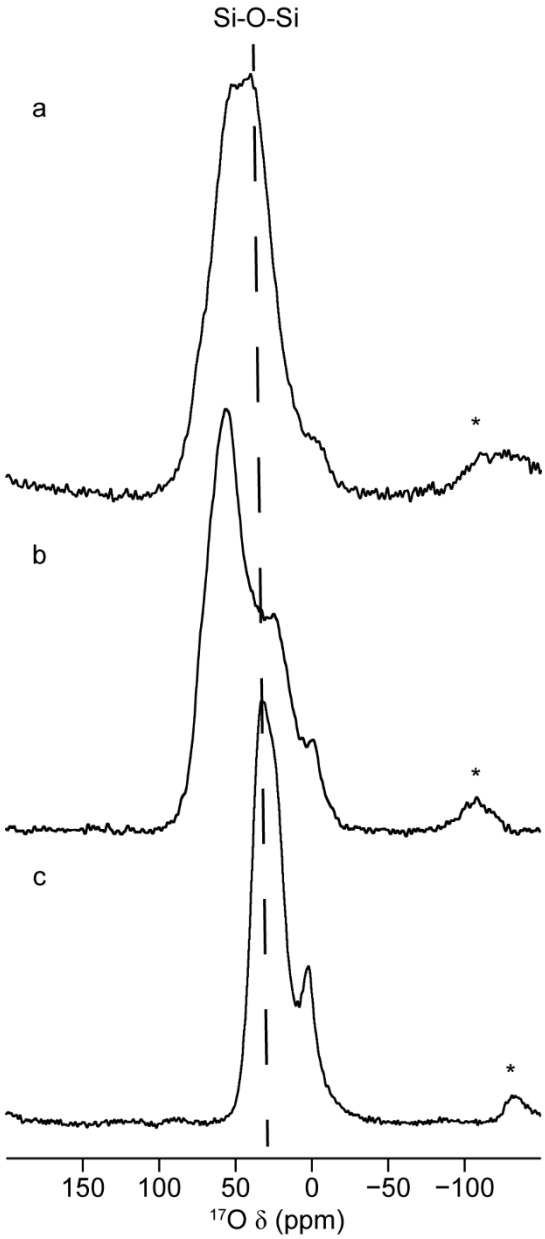

Figure 6.43. *^{17}O (20.0 T, 20 kHz MAS) DP NMR spectra of ^{17}O-enriched (a) Si-γ-Al_2O_3 4th graft (5.2 wt% Si) (700 °C for 12 h) (b) Si-γ-Al_2O_3 (500 °C for 24 h) and (c) amorphous SiO_2 (^{17}O-enriched during synthesis). * denotes a spinning sideband.*

recoupling times, are shown in Figure 6.41. Whilst the overlap of individual resonances in the ^{17}O dimension precludes unambiguous peak assignments, some general trends can be identified. At the shortest recoupling time (τ_{rec} = 0.6 ms), only weak correlations are seen, principally between higher-order Si (Q^3 and Q^4) and Al-O-Al species (OAl_3 and OAl_4). The fact that Q^4(3Al) bridging Si units primarily correlate with OAl_3 and OAl_4 oxygen species, rather than with Si-O-Si oxygens, is unexpected.

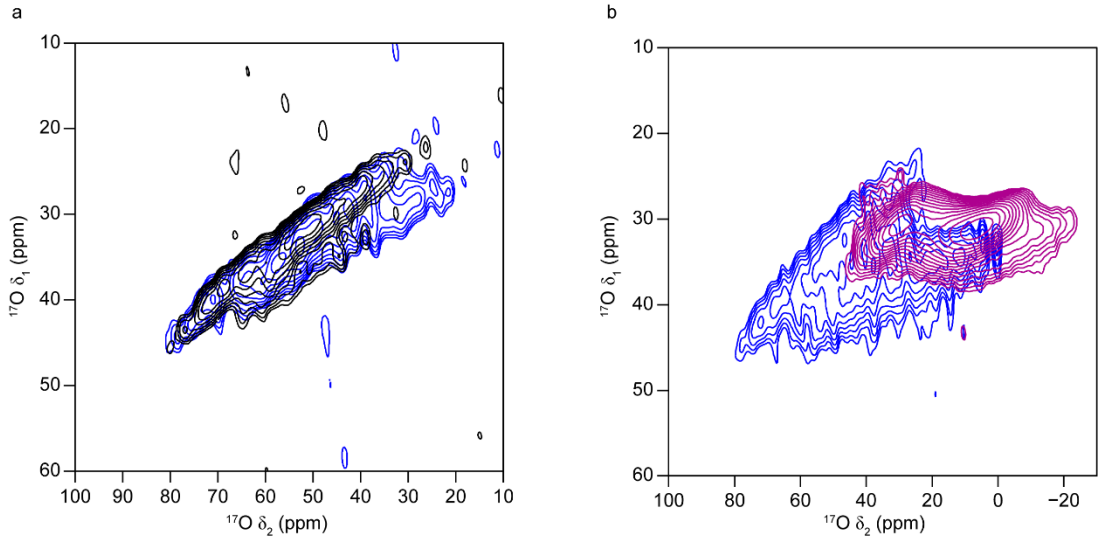

Figure 6.44. *^{17}O z-filtered 3QMAS NMR spectra of Si-γ-Al_2O_3 (1.5 wt% Si) (500 °C for 24 h) (black), Si-γ-Al_2O_3 4th graft (5.2 wt% Si) (700 °C for 12 h) (blue) and ^{17}O-enriched amorphous SiO_2, (pink). Spectra were acquired at (a) 20.0 T and 20 kHz MAS and (b) 14.1 T and 14 kHz MAS. A shearing transformation has been applied to all spectra.*

This finding is tentatively interpreted in terms of strong dipolar connectivity between these Si and O species, which is observable due to the through-space nature of the ^{29}Si-^{17}O D-HMQC experiment. It is also possible that Si-O-Si oxygen species are present, but identification of corresponding signals is obscured by limited resolution in the ^{17}O dimension. As the recoupling duration is increased, a much greater degree of correlation between oxygens at lower δ (potentially Si-O-Al linkages) and lower-order Q^n silicons (*i.e.*, Q^1 and Q^2 units) is observed. Figure 6.42 overlays projections of the ^{17}O dimension for τ_{rec} = 1.2 and 1.8 ms (the sensitivity level of the 0.6 ms spectrum was too low to be included), with the ^{17}O MAS NMR spectrum of doubly-enriched Si-γ-Al_2O_3 (1.5 wt% Si). It demonstrates that the ^{17}O signals that are observed are those attributed to oxygens in bridging arrangements (*i.e.*, Al-O-Al, Si-O-Al and Si-O-Si). Unfortunately, no signals corresponding to OH species can be seen at any of the recoupling durations employed. This is likely to be due to the rapid relaxation of the hydroxyl oxygens discussed previously, which means that any signal from these species substantially decays during recoupling. Nonetheless, the results obtained demonstrate that, by employing isotopic enrichment, ^{29}Si-^{17}O correlation experiments are possible, even at low silicon loading. Further investigation is certainly warranted, potentially by employing additional sequences such as J-HMQC[121] and MQ-

INEPT,[122,123] in order to probe through-bond connectivities and provide increased resolution, respectively.

6.9 ^{17}O Enrichment of Si-γ-Al_2O_3 4th Graft (5.2 wt% Si)

Considering the success of gas exchange for ^{17}O enrichment detailed in the previous section, it was desirable to test its use in the characterisation of multi-grafted materials. Accordingly, a sample of Si-γ-Al_2O_3 4th Graft (5.2 wt% Si) was ^{17}O enriched at 700 °C for 12 h. These conditions were chosen based on previous findings for Si-γ-Al_2O_3 (1.5 wt% Si), where it was revealed that the higher enrichment temperature favoured ^{16}O/^{17}O exchange with the bulk γ-Al_2O_3 support. Since the Si surface is known to be thicker in the 4th graft material, the aforementioned conditions were employed in order to improve the probability that oxygen species in the entire overlayer would be enriched. Figure 6.43 shows the ^{17}O MAS NMR spectra of ^{17}O-enriched Si-γ-Al_2O_3 4th graft (5.2 wt% Si) (enriched at 700 °C for 12 h), Si-γ-Al_2O_3 (enriched at 500 °C for 24 h) and ^{17}O-enriched amorphous SiO_2, acquired at an external field of 20.0 T. The spectrum of the 4th graft material exhibits a resonance in the region attributable to Si-O-Si species, that is distinctly more intense than that in the spectrum of Si-γ-Al_2O_3 (1.5 wt% Si). However, this evidence alone is insufficient to provide more insight about the type of Si bridging units that are present. In Figure 6.44(a), ^{17}O 3QMAS spectra of ^{17}O-enriched Si-γ-Al_2O_3 materials (1.5 and 5.2 wt%) acquired at 20.0 T are overlaid. In addition to the Si-O-Si oxygen species previously identified in Si-γ-Al_2O_3 (1.5 wt% Si), another resonance is also visible. Comparison of the 3QMAS spectrum of Si-γ-Al_2O_3 4th graft (5.2 wt% Si) acquired at an external field of 14.1 T with an equivalent spectrum of ^{17}O-enriched amorphous SiO_2 was also undertaken, and is shown in Figure 6.44(b). It reveals that the new resonance present in the spectrum of Si-γ-Al_2O_3 4th graft (5.2 wt% Si), is located at a similar position to the Si-O-Si resonance of amorphous SiO_2. This finding suggests that two types of bridging Si species are present in the 4th silica graft material – one which is similar to that found in Si-γ-Al_2O_3 (1.5 wt% Si), and another which closely resembles an amorphous silica-type of environment further away from the alumina support. Based on the findings from Section 6.4, this is more likely to correspond to Si-O-Si connections in "stacked"

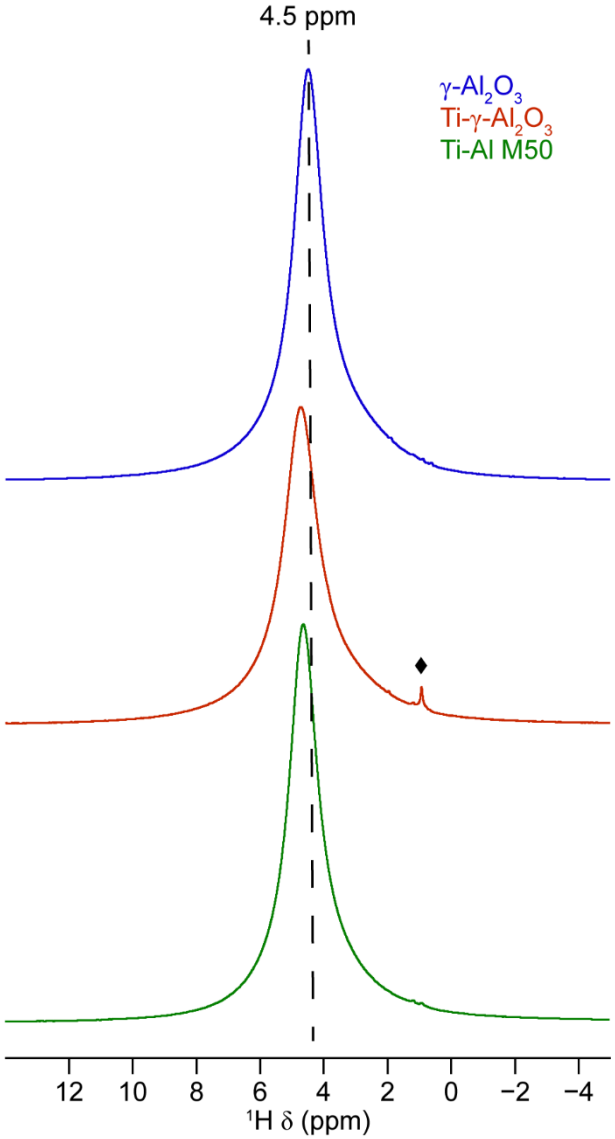

Figure 6.45. *^{1}H (14.1 T, 20 kHz MAS) NMR spectra of γ-Al_2O_3 (blue), Ti-γ-Al_2O_3 (red) and Ti-Al M50 (green). ♦ denotes a peak from the rotor cap.*[78]

3D silica islands, although the presence of some amorphous silica-like "ball" species cannot be ruled out.

6.10 Solid-State NMR Studies of Ti-Alumina Model Catalysts

Titanium-based oxides are widely used in industrial settings, having applications as components of solar cells,[124,125] sorbents for the safe disposal of nerve agents,[126] and heterogeneous catalysts.[127-129] In particular, it was found that surface modification of SiO_2 with Ti species improved the catalytic activity when used as a Co support for F-

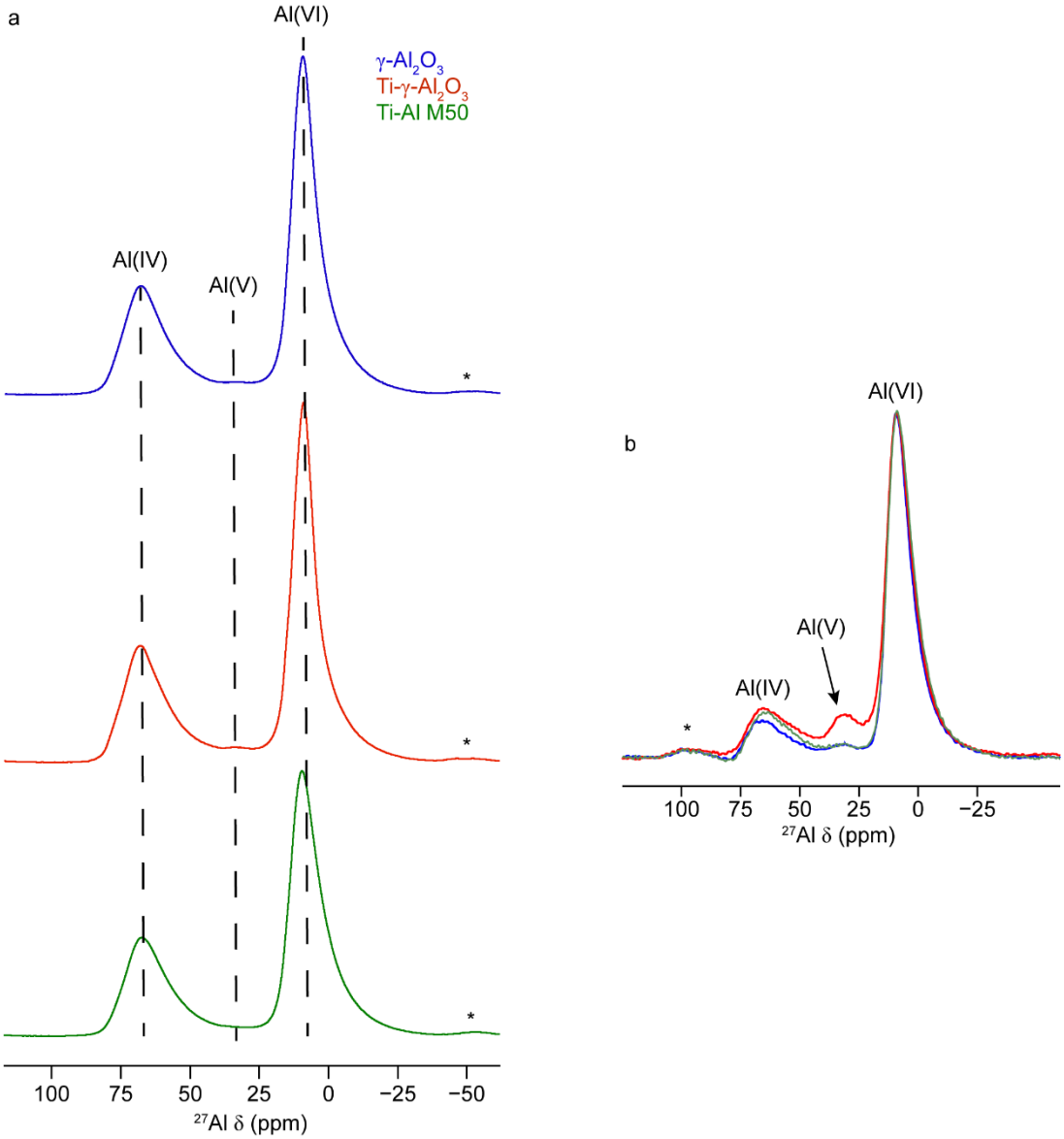

Figure 6.46. *(a) ^{27}Al (14.1 T, 20 kHz MAS) DP NMR spectra and (b) ^{1}H-^{27}Al (14.1 T, 14 kHz MAS, τ_{CP} = 0.8 ms) CP NMR spectra of of γ-Al_2O_3 (blue), Ti-γ-Al_2O_3 (red) and Ti-Al M50 (green). In (b), spectra have been normalised with respect to the Al(VI) resonance. * denotes a spinning sideband.*

T synthesis.[130] Mixed TiO_2-Al_2O_3 materials have also been determined to be highly effective hydrodesulfurisation (HDS) catalysts.[131] In the present work, solid-state NMR studies were undertaken on two Ti-alumina model catalysts, Ti-γ-Al_2O_3 (prepared by a conventional wet impregnation procedure[132]) and Ti-Al M50 (prepared by co-hydrolysis[133]). Preparation details are available in Chapter 4. The single-phase materials γ-Al_2O_3 and TiO_2 (anatase) were also studied for comparison. Figure 6.45

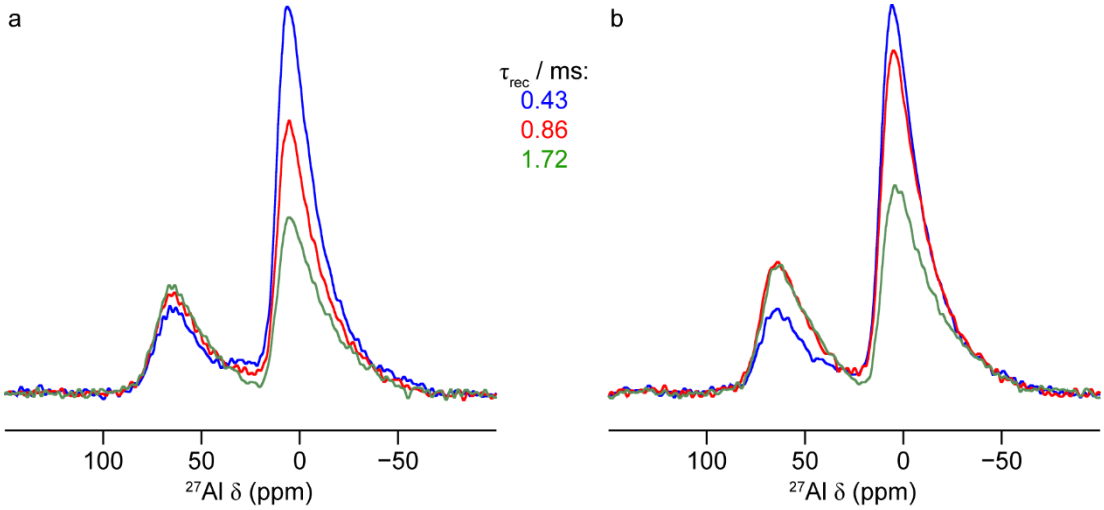

Figure 6.47. *^{1}H-^{27}Al (9.4 T, 14 kHz MAS) D-HMQC 1D NMR spectra of (a) Ti-γ-Al_2O_3 and (b) Ti-Al M50, acquired using τ_{rec} = 0.43 (blue), 0.86 (red) or 1.72 ms (green). In both (a) and (b), spectra have been scaled with respect to the number of transients averaged in each experiment.*

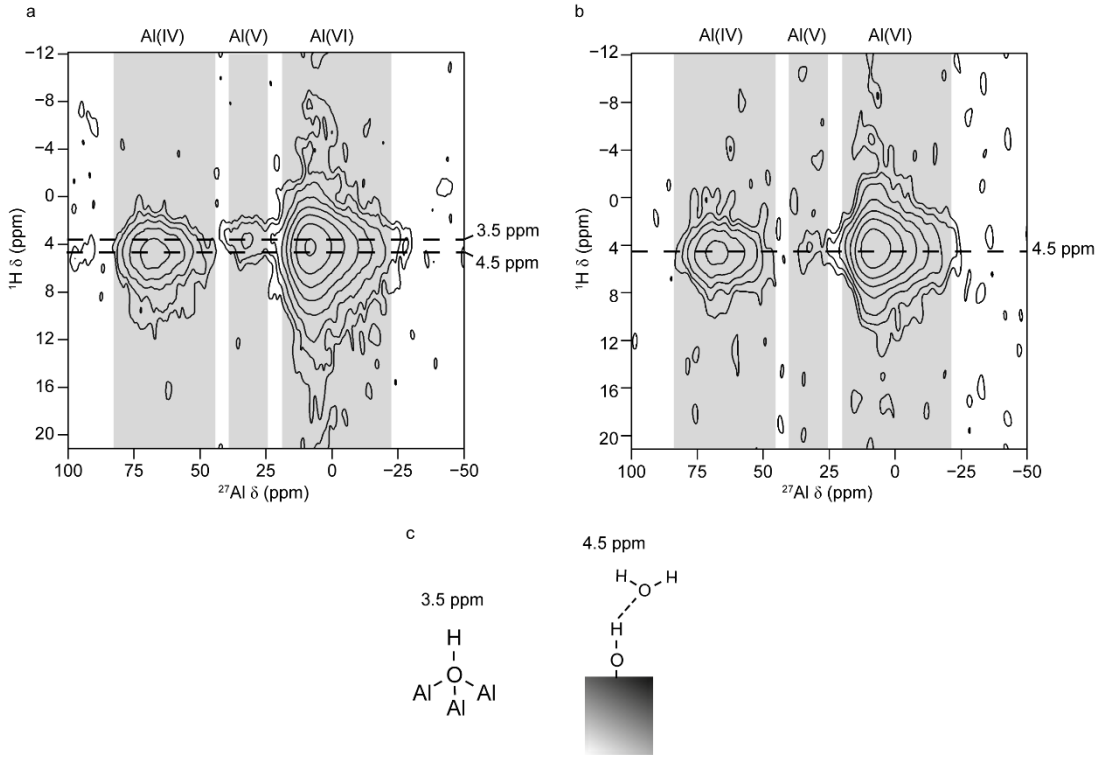

Figure 6.48. *^{1}H-^{27}Al (14.1 T, 40 kHz MAS) D-HMQC spectra of (a) Ti-γ-Al_2O_3, and (b) Ti-Al M50, acquired with τ_{rec} = 0.3 ms. (c) Schematic representations of the functional groups observed in the spectra shown in (a) and (b), along with corresponding ^{1}H δ_{iso} values.*

shows ^{1}H MAS NMR spectra obtained for γ-Al_2O_3, Ti-γ-Al_2O_3 and Ti-Al M50. All display a single resonance at, or close to, ^{1}H $\delta_{iso} \approx 4.5$ ppm, assigned to adsorbed surface H_2O.[22-24] A small downfield shift (~0.1 ppm) in the position of this peak is observed between γ-Al_2O_3 and Ti-Al M50. Such a finding is indicative that H_2O species experience different surface environments, although it is difficult to discern in detail what these might be. To obtain more insight into the chemistry of the underlying support, ^{27}Al NMR experiments were performed. Figure 6.46(a) shows ^{27}Al DP NMR spectra acquired for γ-Al_2O_3, Ti-γ-Al_2O_3 and Ti-Al M50. All three display signals characteristic of Al(IV) and Al(VI) coordination environments, and, in the spectra of γ-Al_2O_3 and Ti-γ-Al_2O_3, low intensity corresponding Al(V) species are also observed. ^{1}H-^{27}Al CP NMR experiments confirm that Al(V) sites are present on the surface of all three materials, as seen in Figure 6.46(b). The Al(V) resonance is notably more intense in the spectrum of Ti-γ-Al_2O_3, suggesting the possible formation of an Al/Ti interface, based on the prior findings in this chapter for Si-γ-Al_2O_3 materials. An increase in the intensity, relative to γ-Al_2O_3, of the Al(IV) signal in the spectra of Ti-γ-Al_2O_3 and Ti-Al M50 is also evident, indicating that the surface of both materials has been altered by the addition of Ti to the structures.

To explore the surface environments of the Ti-modified materials in more detail, ^{1}H-^{27}Al D-HMQC experiments were performed using the $SR4^2_1$ scheme for dipolar recoupling.[119] It has been shown that a 1D version of this sequence can be applied to obtain spectra edited based on spatial proximities of nuclei, in a similar way to the CP NMR experiment, but without being dependent on, for example, the $T_{1\rho}$ properties of those nuclei or the spin lock efficiency for each species.[118] ^{1}H-^{27}Al D-HMQC spectra acquired for Ti-γ-Al_2O_3 and Ti-Al M50 are displayed in Figure 6.47. In (a), the spectra of Ti-γ-Al_2O_3 feature a discernible Al(V) resonance which reduces in intensity as the recoupling duration is increased. In fact, at $\tau_{rec} = 1.72$ ms, it is not observable at all, suggesting that pentacoordinated Al is in close proximity to protons and therefore is primarily at the surface of Ti-γ-Al_2O_3. Identifiable signal from Al(V) can be seen only in the spectrum of Ti-Al M50 at $\tau_{rec} = 0.43$ ms, and has low intensity, implying the lack of an Al/Ti interface characteristic of surface overlayer formation. In the spectra of Ti-γ-Al_2O_3, the intensity of the Al(VI) peak decreases noticeably as a function of

increasing τ_{rec}, accompanied by a small increase in the intensity of the Al(IV) resonance. This observation suggests that octahedrally-coordinated Al species are more abundant near surface of the material, but that the amount of Al(IV) sites remains similar between surface and subsurface/bulk. By contrast, the equivalent peaks in the spectra of Ti-Al M50 exhibit different behaviour. As τ_{rec} increases, a more gradual decrease in the intensity of the Al(VI) resonance is observed, decreasing markedly only at the longest recoupling duration. This is accompanied by a more substantial increase in the intensity of the Al(IV) peak, although no change is seen between τ_{rec} = 0.86 and 1.72 ms. This points towards there being two different morphologies in the underlying structures of Ti-γ-Al_2O_3 and Ti-Al M50. It would appear that the latter material is characterised by the presence of an increased amount of Al(VI) in the subsurface, relative to Ti-γ-Al_2O_3. Al(IV) also seem to be more abundant at lower layers of the Ti-Al M50 structure, whereas in Ti-γ-Al_2O_3 these species may be more uniformly dispersed.

In Chapter 5, it was shown that the 2D D-HMQC experiment is able to provide detailed information on ^{1}H-^{27}Al correlations in γ-Al_2O_3. This approach has been extended to the characterisation of Ti-γ-Al_2O_3 and Ti-Al M50 using fast MAS and short τ_{rec} values (0.3 ms). Figure 6.48(a) displays the ^{1}H-^{27}Al 2D D-HMQC spectrum of Ti-γ-Al_2O_3. Resonances corresponding to Al(IV), Al(V) and Al(VI) in the ^{27}Al dimension are observed, and all correlate with signal in the ^{1}H dimension at $\delta_{iso} \approx 3.5$ ppm. Based on the results reported by Taoufik *et al.*,[33] this resonance can be assigned to Al_3-OH species on the surface of the material. Al(IV) and Al(VI) species are also seen to correlate with ^{1}H $\delta_{iso} \approx 4.5$ ppm, which can be attributed to adsorbed surface water.[22-24] Weak correlations are also observed between this species and Al(V). Figure 6.48(b) shows the D-HMQC spectrum of Ti-Al M50, where correlation between Al(IV) and Al(VI) species and adsorbed H_2O is also observed. A resonance with low sensitivity is tentatively assigned to Al(V) species, although improved S/N is required in order to confirm this finding. In contrast to Ti-γ-Al_2O_3, all ^{27}Al signals only exhibit correlation with ^{1}H $\delta \approx 4.5$ ppm, suggesting that the Al_3-OH functional group may not be present

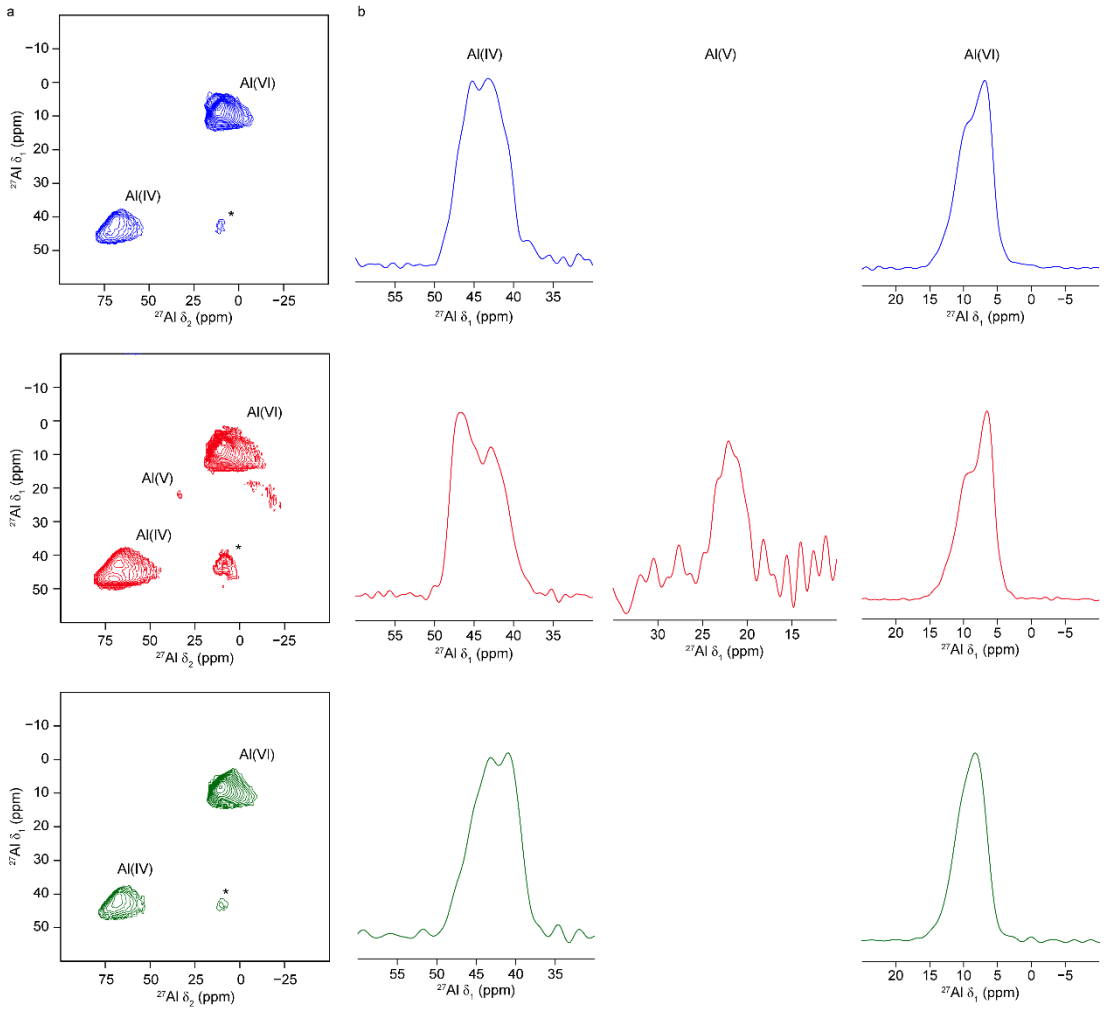

Figure 6.49. *(a) ^{27}Al (14.1 T, 14 kHz MAS) z-filtered 3QMAS NMR spectra of γ-Al_2O_3 (blue), Ti-γ-Al_2O_3 (red) and Ti-Al M50 (green). A shearing transformation has been applied to all spectra. (b) Cross sections parallel to δ_1 extracted from the spectra shown in (a). * denotes a spinning sideband.*

on the surface of Ti-Al M50. These findings, taken together with those discussed earlier in the chapter, indicate two different types of alumina morphology. In Ti-γ-Al_2O_3, the underlying γ-Al_2O_3 structure is maintained, resulting in a material that seems to be the Ti analogue of Si-γ-Al_2O_3, where only the surface has been modified. By contrast, Ti-Al M50 produces a distinctly different structure. Whilst a γ-Al_2O_3-like oxide component has been created, it is one that exhibits discernible local structural differences to a single-phase alumina, implying the formation of a mixed TiO_2-Al_2O_3 material.

Table 6.6. *NMR parameters (average quadrupolar product, $\langle P_Q \rangle$ and average isotropic chemical shift, $\langle \delta_{iso} \rangle$) for the Al sites in γ-$Al_2O_3$, Ti-γ-$Al_2O_3$ and Ti-Al M50, obtained from the z-filtered 3QMAS spectra in Figure 6.49(a).*

Sample	Al(IV)			
	$\langle P_Q \rangle$ / MHz		$\langle \delta_{iso} \rangle$ (ppm)	
	(Site 1)	(Site 2)	(Site 1)	(Site 2)
γ-Al_2O_3	4.8 (3)	5.9 (3)	73 (2)	78 (2)
Ti-γ-Al_2O_3	5.2 (3)	6.2 (3)	74 (2)	80 (2)
Ti-Al M50	4.3 (3)	5.1 (3)	72 (2)	77 (2)
	Al(V)			
	$\langle P_Q \rangle$ / MHz		$\langle \delta_{iso} \rangle$ (ppm)	
	(Site 1)	(Site 2)	(Site 1)	(Site 2)
γ-Al_2O_3	-	-	-	-
Ti-γ-Al_2O_3	4.3 (2)	-	38 (1)	-
Ti-Al M50	-	-	-	-
	Al(VI)			
	$\langle P_Q \rangle$ / MHz		$\langle \delta_{iso} \rangle$ (ppm)	
	(Site 1)	(Site 2)	(Site 1)	(Site 2)
γ-Al_2O_3	2.9 (3)	4.2 (3)	12 (2)	14 (2)
Ti-γ-Al_2O_3	3.3 (3)	3.9 (3)	12 (2)	15 (2)
Ti-Al M50	3.8 (3)	-	13 (2)	-

Figure 6.49(a) shows ^{27}Al z-filtered 3QMAS spectra obtained for γ-Al_2O_3, Ti-γ-Al_2O_3 and Ti-Al M50. By examining the lineshapes, the presence of two distinct Al(IV) sites can be identified. Confirmation of this finding was obtained by extracting cross sections parallel to δ_1 from each 2D spectrum, which are free from the effects of second-order quadrupolar broadening. They are displayed in Figure 6.49(b), revealing that two Al(IV) sites are indeed present in all three materials, and furthermore, in γ-

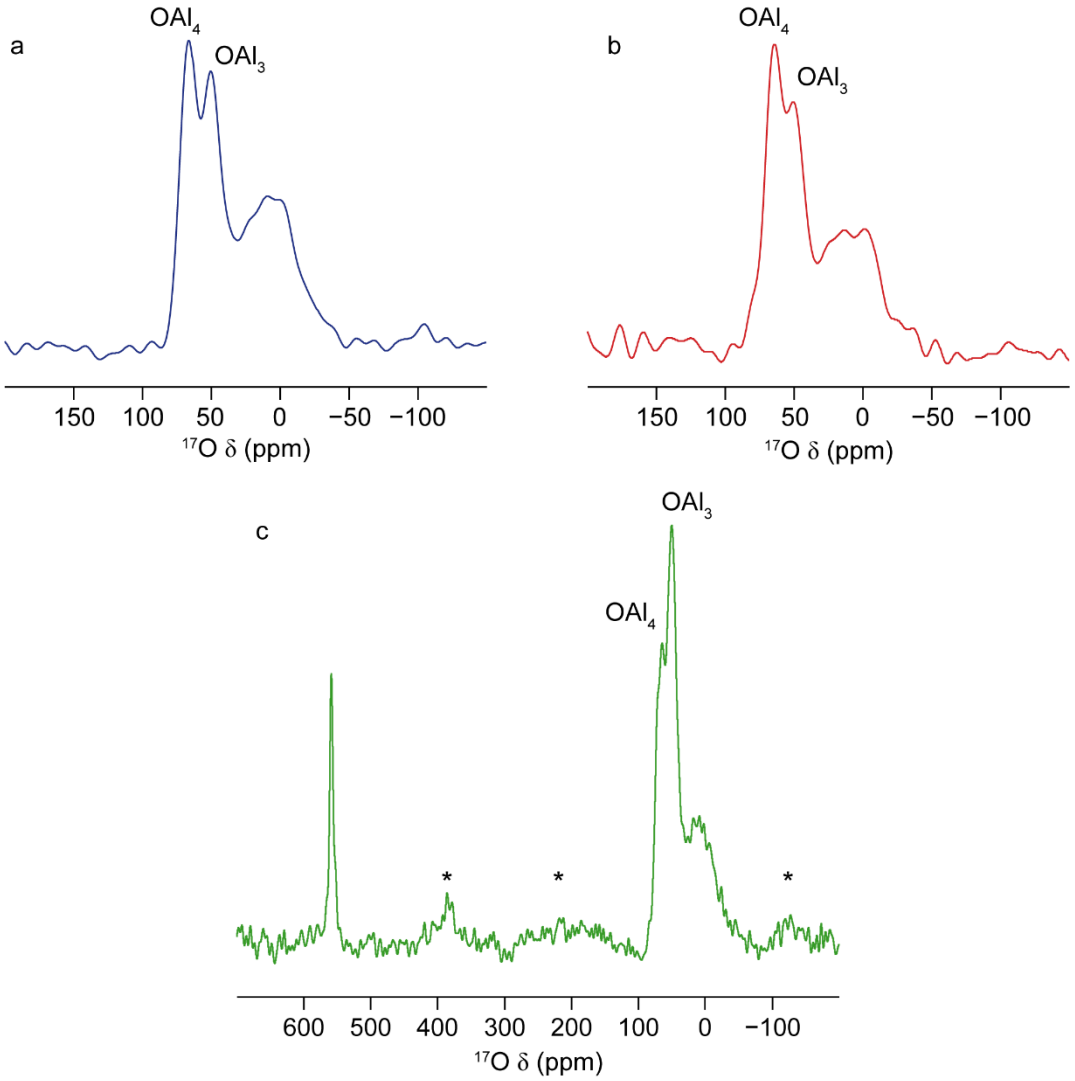

Figure 6.50. *^{17}O (14.1 T, 14 kHz MAS) DP NMR spectra of (a) γ-Al_2O_3 (blue), (b) Ti-γ-Al_2O_3 (red) and (c) Ti-Al M50 (green), ^{17}O-enriched at 500 °C for 12 h. * denotes a spinning sideband.*

Al_2O_3 and Ti-γ-Al_2O_3, two distinct Al(VI) sites are also observed. A resonance attributed to pentahedral Al species is seen only in the spectrum of Ti-γ-Al_2O_3. This is consistent with the results obtained from the ^{1}H-^{27}Al CP and D-HMQC experiments discussed previously. Extraction of NMR parameters for each of the observed Al sites was carried out, and the results are given in Table 6.6. All three samples display an Al(IV) average P_Q value for one site that is higher than the other. A similar finding was reported by Lee *et al.*[34] for γ-Al_2O_3, and they postulated that the tetrahedral site with higher C_Q resides in the disordered subsurface. These authors reported a C_Q value of 7.5 MHz for this second Al(IV) though, which is ~1 MHz larger (accounting for

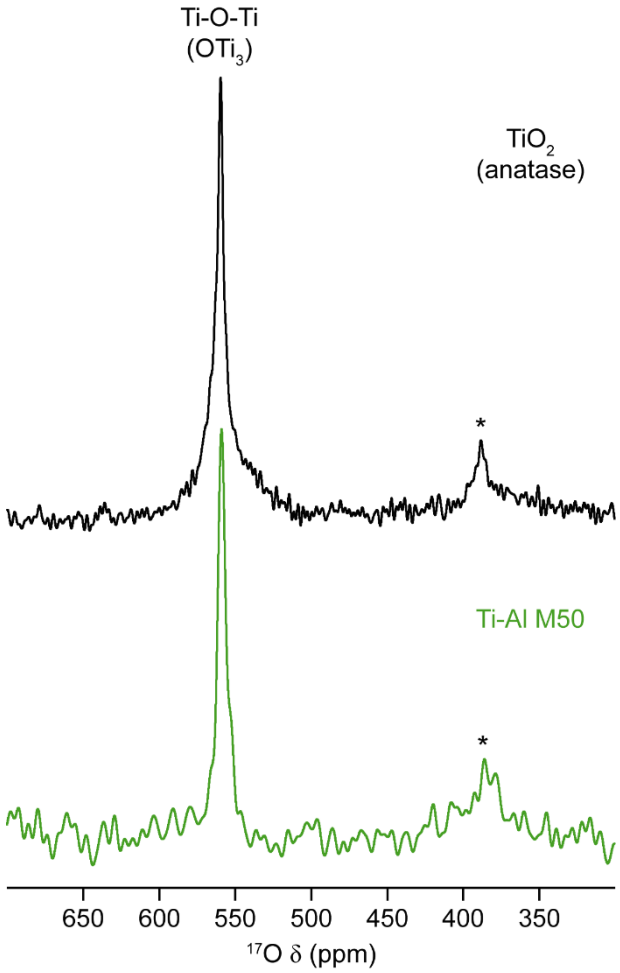

Figure 6.51. *^{17}O (14.1 T, 14 kHz MAS) DP NMR spectra of TiO_2 (anatase) (black) and Ti-Al M50 (green), ^{17}O-enriched at 500 °C for 12 h. * denotes a spinning sideband.*

errors) than those observed here, implying that in the present case, the observed sites may be located further into the bulk of the materials. The same trend can be seen in the Al(VI) values extracted for γ-Al_2O_3 and Ti-γ-Al_2O_3, once again in the same range as previously reported.[34] Lee *et al*. did, however, observe a third octahedral Al site with a higher C_Q (6.6 MHz) that was not seen in the present work, although it is expected that it would significantly overlap with at least one of the other Al(VI) lineshapes. Both the P_Q and δ_{iso} values for Al(V) in Ti-γ-Al_2O_3 are in good agreement with those extracted from dehydrated γ-Al_2O_3, discussed in Chapter 5, confirming that these are surface species. Only one Al(VI) is readily observable in Ti-Al M50, though it does not exhibit a substantially different average P_Q value. This lends support to the earlier assertion that the material formed contains a γ-Al_2O_3-like phase that differs

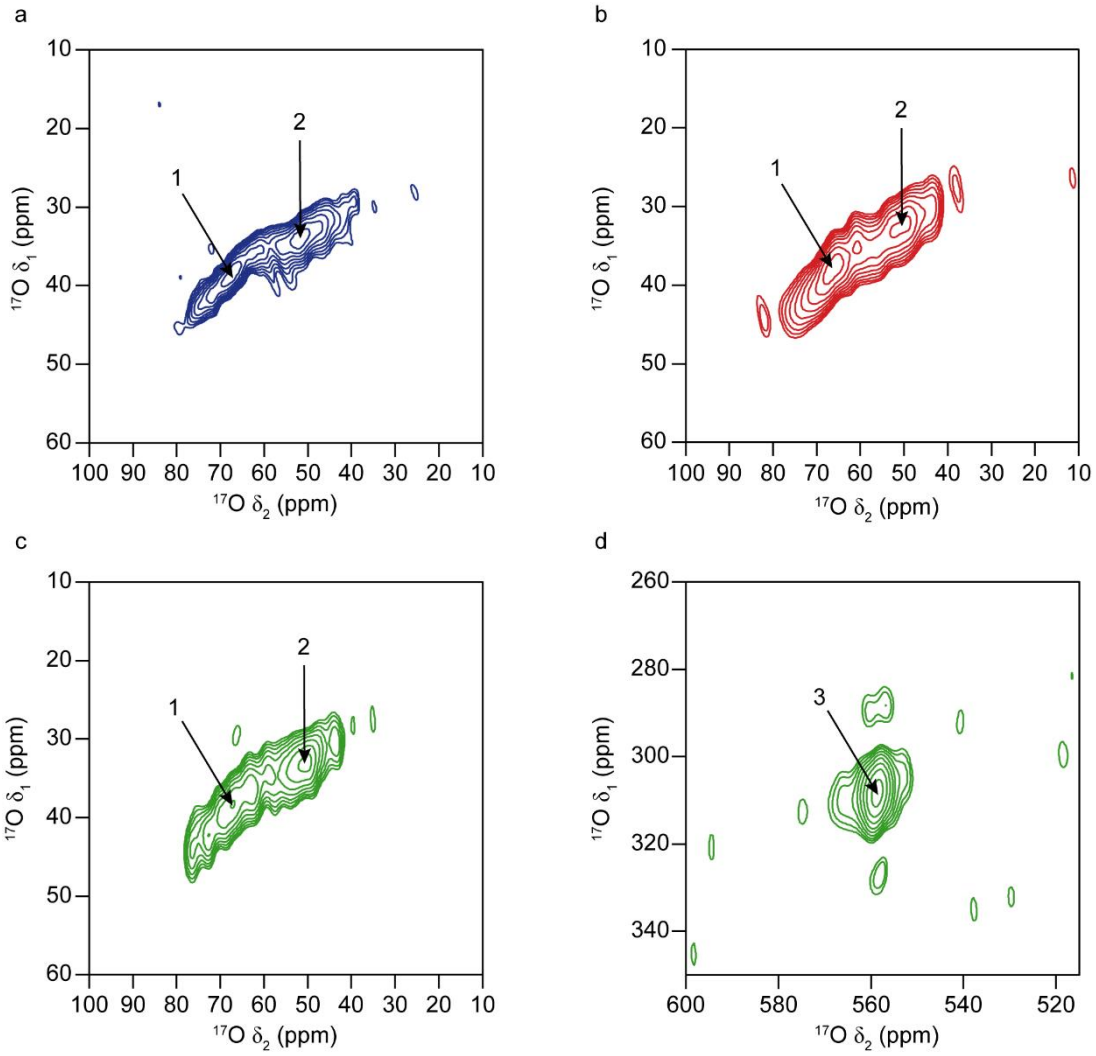

Figure 6.52. *^{17}O z-filtered 3QMAS NMR spectra of γ-Al_2O_3 (blue), Ti-γ-Al_2O_3 (red) and Ti-Al M50 (green), ^{17}O-enriched at 500 °C for 12 h, acquired at (a-c) 14.1 T and 14 kHz MAS and (d) 9.4 T and 14 kHz MAS. A shearing transformation has been applied to all spectra. Peak assignments are as follows: 1 = Al-O-Al (OAl_4); 2 = Al-O-Al (OAl_3); 3 = Ti-O-Ti (OTi_3).*

somewhat from the end member by being part of an Al-Ti mixed material. The presence of a shoulder on this peak suggests that a second Al(VI) site may also be present, but would require high external field strength in order to be resolved. In the previous section of this chapter, ^{17}O gas exchange enrichment and NMR spectroscopy was demonstrated to be an effective approach for characterising γ-Al_2O_3 and Si-γ-Al_2O_3 materials. Therefore, it was decided that this method could be extended to the analysis of Ti-aluminas, and a preliminary study was carried out. Figure 6.50 shows ^{17}O DP NMR spectra acquired for samples of γ-Al_2O_3, Ti-γ-Al_2O_3 and Ti-Al M50, ^{17}O

Table 6.7. *NMR parameters (average quadrupolar product, $\langle P_Q \rangle$ and average isotropic chemical shift, $\langle \delta_{iso} \rangle$) for the O sites in γ-$Al_2O_3$, Ti-γ-$Al_2O_3$ and Ti-Al M50, obtained from the z-filtered 3QMAS spectra in Figure 6.52.*

Site	γ-Al_2O_3		Ti-γ-Al_2O_3		Ti-Al M50	
	$\langle P_Q \rangle$ / MHz	$\langle \delta_{iso} \rangle$ (ppm)	$\langle P_Q \rangle$ / MHz	$\langle \delta_{iso} \rangle$ (ppm)	$\langle P_Q \rangle$ / MHz	$\langle \delta_{iso} \rangle$ (ppm)
OAl_4	1.5 (3)	73 (3)	1.4 (3)	66 (3)	1.5 (3)	69 (3)
OAl_3	2.3 (3)	57 (3)	2.4 (3)	60 (3)	2.3 (3)	60 (3)
OTi_3	-	-	-	-	1.6 (2)	561 (2)

enriched at 500 °C for 12 h. All three spectra display signals in the region from *ca.* −50 to 100 ppm, consistent with those previously identified in γ-Al_2O_3. The relative intensities of the peaks attributed to OAl_4 and OAl_3 environments are seen to vary between the three materials. In particular, in the spectrum of Ti-Al M50, the OAl_3 resonance is comparatively much more intense than that for OAl_4, possibly suggesting that this type of Al-O-Al linkage is more prevalent in this material, although the reason behind this observation is not presently known. Another signal is also present in the spectrum of Ti-Al M50 at ^{17}O $\delta \approx 560$ ppm, which was not detected in the other two materials despite extensive signal averaging. Figure 6.51 shows ^{17}O DP NMR spectra of this spectral region acquired for samples of Ti-Al M50 and TiO_2 (anatase) (both ^{17}O-enriched at 500 °C for 12 h). By comparing these two spectra, it can be determined that the peak at ^{17}O $\delta \approx 560$ ppm corresponds to a bridging Ti-O-Ti oxygen in a OTi_3 arrangement, as in prior studies of TiO_2 (anatase).[134,135] The good agreement between the chemical shifts in each spectrum raises the possibility that Ti-Al M50 may be partly comprised of anatase. Comparison of PXRD patterns of TiO_2 and Ti-Al M50 (shown in Appendix E) demonstrate that a crystalline anatase phase is not seen in the latter material, where primarily peaks from amorphous γ-Al_2O_3 are present.[136-138] However, a peak at low angle (~25°) is also present which may correspond to TiO_2 nanoparticles, as the PXRD pattern of Ti-Al M50 matches well with published data for mixed TiO_2-Al_2O_3 nanoparticle composite materials.[139-141] These results, together with those obtained from solid-state NMR spectroscopy, suggest that Ti-Al M50 may be a two-phase solid composed of nanoparticle TiO_2 (anatase) and γ-Al_2O_3, featuring a poor degree of mixing between the two phases. This latter proposal may explain why no

^{17}O NMR signals from Ti-O-Al species could be identified. Based on the work of O'Dell *et al.*,[142] such resonances are expected to lie in the ^{17}O spectral region between 400 and 450 ppm, but experiments using a Si_3N_4 rotor, variable MAS rates (to avoid the ZrO_2 rotor signal/spinning sidebands obscuring possible peaks) and extensive signal averaging did not yield any detectable resonances.

Figure 6.52 shows ^{17}O z-filtered 3QMAS NMR spectra acquired for γ-Al_2O_3, Ti-γ-Al_2O_3 and Ti-Al M50. For the Ti-modified materials, the presence of two resonances can be identified, and these match well with the position of peaks in the spectrum of γ-Al_2O_3. As discussed in the previous section of this chapter, these can be assigned to OAl_4 and OAl_3 species. NMR parameters extracted for each site in the three spectra in Figure 6.52(a-c) are given in Table 6.7. There is very little variation in either average P_Q or δ_{iso} values between the materials, indicating that a γ-Al_2O_3-type phase is present in both Ti-γ-Al_2O_3 and Ti-Al M50. In the 3QMAS NMR spectrum of Ti-Al M50 obtained at a field strength of 14.1 T, no resonance was detected for the previously identified Ti-O-Ti (OTi_3) site owing to low CQ.[9,10] Figure 6.52(d) presents the ^{17}O z-filtered 3QMAS NMR spectrum of Ti-Al M50, acquired at a lower external field strength of 9.4 T. Under these conditions, a resonance at ^{17}O $\delta_2 \approx 560$ ppm can be observed and NMR parameters extracted. As evidenced from its relatively sharp appearance in the ^{17}O MAS NMR spectrum of Ti-Al M50, this site possesses a relatively small average P_Q value of 1.6 MHz, and an average δ_{iso} value of 561 ppm. These figures are in reasonable agreement with published data for TiO_2 (anatase)[134,135] and titania sol-gel materials containing OTi_3 sites.[143] Furthermore, the average δ_{iso} value agrees very well with prior ^{17}O NMR studies of TiO_2 (anatase) nanoparticles,[144] adding to prior evidence that suggests that this type of phase may be present, along with a γ-Al_2O_3-type phase, in Ti-Al M50. These interesting preliminary findings merit future investigation in this area.

6.11 Conclusions

The work presented in this chapter has demonstrated that multinuclear solid-state NMR spectroscopy is able to offer detailed insights into the structure of silicate

alumina model catalysts. It has shown that a combination of isotopic enrichment and DNP NMR spectroscopy can provide a definitive and fully quantitative description of the surface structure of silica-modified alumina catalysts, even at a silica loading of 1.5 wt%. The combination of the increased amount of information available as a result of the DNP enhancement, and the ability to obtain quantitative spectra using isotopic enrichment, affords a more rigorous quantitative interpretation of ^{29}Si spectra, and a detailed understanding of the nature of the Si-Al interface. Analysis of silicated aluminas prepared by sequential grafting and "single shot" approaches has shown that silica growth on γ-Al_2O_3 can follow two distinct morphologies. The sequential grafting method results in the build-up of 3D silica layers *via* an "island stacking" process, whereas the "single shot" approach results in a mixed growth morphology consisting of 2D islands accompanied by the formation of amorphous SiO_2 "ball" structures. It has also been revealed that long term ageing of the non-calcined analogue of this second sample promotes the formation of a structure with a greater proportion of silicate Q^n species than its calcined counterpart.

Post synthetic enrichment by ^{17}O gas exchange has been demonstrated to be very successful in facilitating ^{17}O solid-state NMR studies of γ-Al_2O_3 and Si-γ-Al_2O_3 materials. Using this method, the presence of two (γ-Al_2O_3) and four (Si-γ-Al_2O_3 (1.5 wt% Si)) distinct oxygen environments has been revealed. The dependence of ^{16}O/^{17}O exchange on heating temperature has also been highlighted, with elevated temperatures found to favour isotopic enrichment of the underlying γ-Al_2O_3 structure in Si-γ-Al_2O_3 (1.5 wt% Si). Preliminary ^{17}O NMR studies on Si-γ-Al_2O_3 4th graft (5.2 wt% Si) have indicated that a Si-O-Si oxygen environment, similar to that found in amorphous silica, is present in the material, consistent with both Si "stacked" islands and amorphous SiO_2 "ball" structures. It has been demonstrated that double (^{29}Si and ^{17}O) enrichment of Si-γ-Al_2O_3 (1.5 wt% Si) is able to facilitate access to ^{29}Si-^{17}O 2D correlation experiments, even at low silica loading. It is found that, although the ^{17}O gas exchange process induces some hydrolysis of Si-O-Si units in the silicated alumina overlayer, it causes no significant overall change to the nature of the silica structure. Notably, Q^4 Si units are seen to primarily correlate with OAl_3 and OAl_4 O species, rather than with Si-O-Si oxygens. This finding has been interpreted in terms of strong

dipolar connectivity between these species, which is observable due to the through-space nature of the ^{29}Si-^{17}O D-HMQC experiment.

A preliminary investigation of Ti-alumina model catalysts has been undertaken using ^{1}H, ^{27}Al and ^{17}O solid-state NMR techniques. It has been revealed that two Al(IV) and Al(VI) sites are present in the structure of γ-Al_2O_3, a finding that was not initially evident. Preliminary results have shown that, whilst Ti-γ-Al_2O_3 can be described as a surface modified γ-Al_2O_3 material, similar to Si-γ-Al_2O_3, Ti-Al M50 may be morphologically distinct. It is tentatively proposed that the latter material is a combined phase TiO_2-Al_2O_3 composed of TiO_2 (anatase) nanoparticle and γ-Al_2O_3-like phases, that could be distinct, exhibiting a low degree of connectivity. Additional investigations into these complex materials are however necessary in order to substantiate these initial findings.

6.12 References

1. G. Busca, *Chem. Rev.*, 2007, **107**, 5366.
2. M. Trombetta, G. Busca, S. Rossini, V. Piccoli, U. Cornaro, A. Guercio, R. Catani and R. J. Willey, *J. Catal.*, 1998, **179**, 581.
3. G. Crépeau, V. Montouillout, A. Vimont, L. Mariey, T. Cseri and F. Maugé, *J. Phys. Chem. B*, 2006, **110**, 15172.
4. C. Chizallet and P. Raybaud, *Angew. Chem. Int. Ed.*, 2010, **48**, 2891.
5. J. H. Lunsford, *Catal. Today*, 2000, **63**, 165.
6. A. C. Sofianos and M. S. Scurrell, *Ind. Eng. Chem. Res.*, 1991, **30**, 2372.
7. R. C. Medrud, in *Industrial Applications of X-Ray Diffraction*., Eds. F. H. Chung and D. K. Smith, CRC Press. Boca Raton, 1999.
8. W. E. Farneth and R. J. Gorte, *Chem. Rev.*, 1995, **95**, 615.
9. K. J. D. MacKenzie and M. E. Smith, *Multinuclear Solid-State NMR of Inorganic Materials*, Pergamon, Oxford, 2002.
10. S. E. Ashbrook, D. M. Dawson and J. M. Griffin, in *Local Structural Characterisation*, Eds. D. W. Bruce, D. O'Hare and R. I. Walton, Wiley, Chichester, 2014.

11. S. E. Ashbrook and S. Sneddon, *J. Am. Chem. Soc.*, 2014, **136**, 15440.
12. K. M. Delak, T. C. Farrar and N. Sahai, *J. Non-Cryst. Solids*, 2005, **351**, 2244.
13. R. Wischert, P. Florian, C. Copéret, D. Massiot and P. Sautet, *J. Phys. Chem. C*., 2014, **118**, 15292.
14. Q. Z. Ni, E. Daviso, T. V. Can, E. Markhasin, S. K. Jawla, T. M. Swager, R. J. Temkin, J. Herzfeld and R. G. Griffin, *Acc. Chem. Res.*, 2013, **46**, 1933.
15. A. J. Rossini, A. Zagdoun, M. Lelli, A. Lesage, C. Copéret and L. Emsley, *Acc. Chem. Res.*, 2013, **46**, 1942.
16. A. Lesage, M. Lelli, D. Gajan, M. A. Caporini, V. Vitzthum, P. Mieville, J. Alazun, A. Roussey, C. Thieuleux, A. Mehdi, G. Bodenhausen, C. Copéret and L. Emsley, *J. Am. Chem. Soc.*, 2010, **132**, 15459.
17. M. Lelli, D. Gajan, A. Lesage, M. A. Caporini, V. Vitzthum, P. Mieville, F. Heroguel, F. Rascon, A. Roussey, C. Thieuleux, M. Boualleg, L. Veyre, G. Bodenhausen, C. Copéret and L. Emsley, *J. Am. Chem. Soc*., 2011, **133**, 2104.
18. M. McMillan, J. S. Brinen, J. D. Carruthers and G. L. Haller, *Colloids Surf.*, 1989, **38**, 133.
19. S. Sato, T. Sodesawa and F. Nozaki, *J. Mol. Catal.*, 1991, **66**, 343.
20. H. Koller and M. Weiß, *Top. Curr. Chem.* 2012, **306**, 189.
21. E. Lippmaa, M. Magi, A. Samoson, G. Engelhardt and A. R. Grimmer, *J. Am. Chem. Soc*., 1980, **102**, 4889.
22. D. R. Kinney, I. S. Chuang and G. E. Maciel, *J. Am. Chem. Soc*., 1993, **115**, 6786.
23. J. Z. Hu, J. H. Kwak, J. E. Herrera, Y. Wang and C. H. F. Peden, *Solid State Nucl. Magn. Reson.*, 2005, **27**, 200.
24. H. N. Kim and S. K. Lee, *Geochim. Cosmochim. Acta*, 2013, **120**, 39.
25. A. Lesage, M. Bardet and L. Emsley, *J. Am. Chem. Soc.*, 1999, **121**, 10987.
26. P. Florian, F. Fayon and D. Massiot, *J. Phys. Chem. C*, 2009, **113**, 2562.
27. P. Florian, E. Veron, T. F. G. Green, J. R. Yates and D. Massiot, *Chem. Mater.*, 2012, **24**, 4068.
28. C. A. Fyfe, K. C. Wong-Moon, Y. Huan and H. Grondey, *J. Am. Chem. Soc.*, 1995, **117**, 10397.
29. E. De Vita and L. Frydman, *J. Magn. Reson.*, 2001, **148**, 327.

30. M. Valla, A. J. Rossini, M. Caillot, C. Chizallet, P. Raybaud, M. Digne, A. Chaumonnot, A. Lesage, L. Emsley, J. A. van Bokhoven and C. Copéret, *J. Am. Chem. Soc.*, 2015, **137**, 10710.
31. T. Guillion and J. Schaefer, *J. Magn. Reson.*, 1989, **81**, 196.
32. B. A. Huggins and P. D. Ellis, *J. Am. Chem. Soc.*, 1992, **114**, 2098.
33. M. Taoufik, K. C. Szeto, N. Merle, I. D. Rosal, L. Maron, J. Trébosc, G. Tricot, R. M. Gauvin and L. Delevoye, *Chem. Eur. J.*, 2014, **20**, 4038.
34. D. Lee, N. T. Duong, O. Lafon and G. De Paëpe, *J. Phys. Chem. C*, 2014, **118**, 25065.
35. Z. Wang, Y. Jiang, O. Lafon, J. Trébosc, K. D. Kim, C. Stampfl, A. Baiker, J.-P. Amoureux and J. Huang, *Nat. Commun.*, 2016, **7:13820**, 1.
36. D. W. Sindorf and G. E. Maciel, *J. Phys. Chem.*, 1983, **87**, 5516.
37. X. S. Zhao, G. Q. Lu, A. K. Whittaker, G. J. Millar and H. Y. Zhu, *J. Phys. Chem. B*, 1997, **101**, 6525.
38. E. Finocchio, G. Busca, S. Rossini, U. Cornaro, V. Piccoli and R. Miglio, *Catal. Today*, 1997, **33**, 335.
39. M. Xu, J. H. Lunsford, D. W. Goodman and A. Bhattacharyya, *Appl. Catal. A*, 1997, **149**, 289.
40. D. Leckel, *Ind. Eng. Chem. Res.*, 2007, **46**, 3505.
41. M. Caillot, A. Chaumonnot, M. Digne and J. A. van Bokhoven, *J. Catal.*, 2014, **316**, 47.
42. M. Caillot, A. Chaumonnot, M. Digne, C. Poleunis, D. P. Debecker and J. A. van Bokhoven, *Micropor. Mesopor. Mater.*, 2014, **185**, 179.
43. A. R. Mouat, C. George, T. Kobayashi, M. Pruski, R. P. van Duyne, T. J. Marks and P. C. Stair, *Angew. Chem. Int. Ed.*, 2015, **54**, 13346.
44. A. R. Mouat, T. Kobayashi, M. Pruski, T. J. Marks and P. C. Stair, *J. Phys. Chem. C*, 2017, **121**, 6060.
45. S. A. Morris, G. P. M. Bignami, Y. Tian, M. Navarro, D. S. Firth, J. Čejka, P. S. Wheatley, D. M. Dawson, W. A. Slawinski, D. S. Wragg, R. E. Morris and S. E. Ashbrook, *Nat. Chem.*, 2017, **9**, 1012.
46. D. R. Modeshia, R. I. Walton, M. R. Mitchell and S. E. Ashbrook, *Dalton Trans.*, 2010, **39**, 6031.

47. A. V. Chadwick, G. Mountjoy, V. M. Nield, I. J. F. Poplett, M. E. Smith, J. H. Strange and M. G. Tucker, *Chem. Mater.*, 2001, **13**, 1219.
48. S. L. P. Savin, A. V. Chadwick, L. A. O'Dell and M. E. Smith, *Solid State Ionics*, 2006, **177**, 2519.
49. M. Baca, E. de la Rochefoucauld, E. Ambroise, J.-M. Krafft, R. Hajjar, P. P. Man, X. Carrier and J. Blanchard, *Micropor. Mesopor. Mater.*, 2008, **110**, 232.
50. J. F. Watts and J. Wolstenholme, *An Introduction to Surface Analysis by XPS and AES*, Wiley, Chichester, 2003.
51. M. Stöcker, *Micropor. Mater.*, 1996, **6**, 235.
52. G. C. Allen, K. R. Hallam, J. R. Eastman, G. J. Graveling, V. K. Ragnarsdottir and D. R. Skuse, *Surf. Interface Anal.*, 1998, **26**, 518.
53. S. Wang, Q. Liu, X. Tan, C. Xu and M. R. Gray, *Energy Fuels*, 2013, **27**, 2465.
54. R. M. Torres Sánchez, E. I. Basaldella and J. F. Marco, *J. Colloid Interface Sci.*, 1999, **215**, 339.
55. T. L. Barr, S. Seal, H. He and J. Klinowski, *Vacuum*, 1995, **46**, 1391.
56. V. K. Kaushik, R. P. Vijayalakshmi, N. V. Choudary and S. G. T. Bhat, *Micropor. Mesopor. Mater.*, 2002, **51**, 139.
57. S. R. Bare, A. Knop-Gericke, D. Teschner, M. Hävacker, R. Blume, T. Rocha, R. Schlögl, A. S. Y. Chan, N. Blackwell, M. E. Charochak, R. ter Veen and H. H. Brongersma, *Surf. Sci.*, 2016, **648**, 376.
58. T. L. Barr, *Zeolites*, 1990, **10**, 760.
59. J. M. Adams, S. Evans, P. I. Reid, J. M. Thomas and M. J. Walters, *Anal. Chem.*, 1977, **49**, 2001.
60. G. G. Biino and P. Gröning, *Eur. J. Mineral.*, 1998, **10**, 423.
61. A. M. Venezia, M. A. Floriano, G. Deganello and A. Rossi, *Surf. Interface Anal.*, 1992, **18**, 532.
62. A. R. González-Elipe, J. P. Espinós, J. G. Munuera, J. Sanz and J. M. Serratosa, *J. Phys. Chem.*, 1988, **92**, 3471.
63. T. Ebina, T. Iwasaki A. Chatterjee, M. Katagiri and G. D. Stucky, *J. Phys. Chem. B*, 1997, **101**, 1125.
64. *US Pat.* US4013589A, 1977.
65. *US Pat.* US4778779A, 1988.

66. C. A. Fyfe, H. Grondey, Y. Feng and G. T. Kokotailo, *J. Am. Chem. Soc.*, 1990, **112**, 8812.
67. C. A. Fyfe, Y. Feng, H. Grondey, G. T. Kokotailo and H. Gies, *Chem. Rev.*, 1991, **91**, 1525.
68. S. Cadars, D. H. Brouwer and B. F. Chmelka, *Phys. Chem. Chem. Phys.*, 2009, **11**, 1825.
69. D. Lee, G. Monin, N. T. Duong, I. Z. Lopez, M. Bardet, V. Mareau, L. Gonon and G. De Paëpe, *J. Am. Chem. Soc.*, 2014, **136**, 13781.
70. E. J. M. Hensen, D. G. Poduval, P. C. M. M. Magusin, A. E. Coumans and J. A. R. van Veen, *J. Catal.*, 2010, **269**, 201.
71. H. Koller, A. Wo1lker, L. A. Villaescusa, M. J. Díaz-Cabanãs, S. Valencia and M. A. Camblor, *J. Am. Chem. Soc.*, 1999, **121**, 3368.
72. S. Senapati, J. Zimdars, J. Ren and H. Koller, *J. Mater. Chem. A*, 2014, **2**, 10470.
73. G. Brinklaus, H. Koller and S. I. Zones, *Angew. Chem. Int. Ed.*, 2016, **55**, 14459.
74. V. Gualandris, F. Babonneau, M. T. Janicke and B. F. Chmelka, *J. Sol-Gel Sci. Technol.*, 1998, **12**, 75.
75. A. Aerts, M. Haouas, T. P. Caremans, L. R. A. Follens, T. S. van Erp, F. Taulelle, J. Vermant, J. A. Martens and C. E. A. Kirschhock, *Chem. Eur. J.*, 2010, **16**, 2764.
76. A. J. Vega and G. W. Scherer, *J. Non-Cryst. Solids*, 1989, **111**, 153.
77. J.-B. d'Espinose de la Caillerie, M. R. Aimeur, Y. El Kortobi and A. P. Legrand, *J. Colloid Interface Sci.* 1997, **194**, 434.
78. C. Jaeger and F. Hemmann, *Solid State Nucl. Magn. Reson.*, 2014, **57-58**, 22.
79. H. Nia, W. J. Simonsick, A. D. Skaja, J. P. Williams and M. D. Soucek, *Prog. Org. Coat.*, 2000, **38**, 97.
80. A. Altube, E. García-Lecina, N. Imaz, J. A. Díez, P. Ferrón, J. M. Aizpurua, *Prog. Org. Coat.*, 2012, **74**, 281.
81. F. Asaro, A. Benedetti, N. Savko, and G. Pellizer, *Langmuir*, 2009, **25**, 3224.
82. S. E. Ashbrook and M. E. Smith, *Chem. Soc. Rev.*, 2006, **35**, 718.

83. S. E. Ashbrook and M. E. Smith, in *Oxygen-17 NMR of Inorganic Materials*, eMagRes, Wiley, Chichester, 2011.
84. S. E. Ashbrook and I. Farnan, *Solid State Nucl. Magn. Reson.*, 2004, **26**, 105.
85. S. Schramm and E. Oldfield, *J. Am. Chem. Soc.*, 1984, **106**, 2502.
86. H. K. C. Timken, G. L. Turner, J.-P. Gilson, L. B. Welsh and E. Oldfield, *J. Am. Chem. Soc.*, 1986, **108**, 7231.
87. N. Janes and E. Oldfield, *J. Am. Chem. Soc.*, 1986, **108**, 5743.
88. T. H. Walter, G. L. Turner and E. Oldfield, *J. Magn. Reson.*, 1988, **76**, 106.
89. E. Oldfield, C. Coretsopoulos, S. Yang, L. Reven, H. C. Lee, J. Shore, O. H. Han, E. Ramli and D. Hinks, *Phys. Rev. B*, 1989, **40**, 6832.
90. T. H. Walter and E. Oldfield, *J. Phys. Chem.*, 1989, **93**, 6744.
91. R. K. Harris, M. J. Leach and D. P. Thompson, *Chem. Mater.*, 1992, **4**, 260.
92. A. V. Chadwick, I. J. F. Poplett, D. T. S. Maitland and M. E. Smith, *Chem. Mater.*, 1998, **10**, 864.
93. B. O. Skadtchenko, Y. Rao, T. F. Kemp, P. Bhattacharya, P. A. Thomas, M. Trudeau, M. E. Smith and D. M. Antonelli, *Angew. Chem. Int. Ed.*, 2007, **46**, 2635.
94. G. P. M. Bignami, D. M. Dawson, V. R. Seymour, P. S. Wheatley, R. E. Morris and S. E. Ashbrook, *J. Am. Chem. Soc.*, 2017, **139**, 5140.
95. J. E. Readman, N. Kim, M. Ziliox and C. P. Grey, *Chem. Commun.*, 2002, **23**, 2808.
96. J. E. Readman, C. P. Grey, M. Ziliox, L. M. Bull and A. Samoson, *Solid State Nucl. Magn. Reson.*, 2004, **26**, 153.
97. L. Peng, Y. Liu, N. Kim, J. E. Readman and C. P. Grey, *Nat. Mater.*, 2005, **4**, 216.
98. L. Peng, H. Huo, Z. Gan and C. P. Grey, *Micropor. Mesopor. Mater.*, 2008, **109**, 156.
99. M. Wang, X.-P. Wu, S. Zheng, L. Zhao, L. Li, L. Shen, Y. Gao, N. Xue, X. Guo, W. Huang, Z. Gan, F. Blanc, Z. Yu, X. Ke, W. Ding, X.-Q. Gong, C. P. Grey and L. Peng, *Sci. Adv.*, 2015, **1**, e1400133.
100. M. A. Hope, D. M. Halat, P. C. M. M. Magusin, S. Paul, L. Peng and C. P. Grey, *Chem. Commun.*, 2017, **53**, 2142.

101. C. A. Klug, S. Kroeker, P. M. Aguiar, M. Zhou, D. F. Stec and I. E. Wachs, *Chem. Mater.*, 2009, **21**, 4127.
102. B. Chen and Y. Huang, *J. Am. Chem. Soc.*, 2006, **128**, 6437.
103. J. V. Oglesby, P. Zhao and J. F. Stebbins, *Geochim. Cosmochim. Acta*, 2002, **66**, 291.
104. S. K. Lee, J. F. Stebbins, C. A. Weiss and R. J. Kirkpatrick, *Chem. Mater.*, 2003, **15**, 2605.
105. N. Merle, J. Trébosc, A. Baudouin, I. Del Rosal, L. Maron, K. Szeto, M. Genelot, A. Mortreux, M. Taoufik, L. Delevoye and R. M. Gauvin, *J. Am. Chem. Soc.*, 2012, **134**, 9263.
106. B. C. Schmidt, F. Gaillard and M. E. Smith, *Solid State Nucl. Magn. Reson.*, 2004, **26**, 197.
107. U.-T. Pingel, J.-P. Amoureux, T. Anupold, F. Bauer, H. Ernst, C. Fernandez, D. Freude and A. Samoson, *Chem. Phys Lett.*, 1998, **294**, 345.
108. A. Lafuma, F. Fayon, D. Massiot, S. Chodorowski-Kimmès and C. Sanchez, *Magn. Reson. Chem.*, 2003, **41**, 944.
109. C. Gervais, M. Profeta, F. Babonneau, C. J. Pickard and F. Mauri, *J. Phys. Chem. B*, 2004, **108**, 13249.
110. J. F. Stebbins, J. V. Oglesby and S. Kroeker, *Am. Mineral.*, 2001, **86**, 1307.
111. P. J. Dirken, S. C. Kohn, M. E. Smith and E. R. H. van Eck, *Chem. Phys. Lett.*, 1997, **266**, 568.
112. A. Ionescu, A. Allouche, J.-P. Aycard, M. Rajzmann and F. Hutschka, *J. Phys. Chem. B*, 2002, **106**, 9359.
113. R. Wischert, P. Laurent, C. Copéret, F. Delbecq and P. Sautet, *J. Am. Chem. Soc.*, 2012, **134**, 14430.
114. C. Pecharromán, I. Sobrados, J. E. Iglesias, T. González-Carreño and J. Sanz, *J. Phys. Chem. B*, 1999, **103**, 6160.
115. L. A. O'Dell, S. L. P. Savin, A. V. Chadwick and M. E. Smith, *Solid State Nucl. Magn. Reson.*, 2007, **31**, 169.
116. E. R. H. van Eck, M. E. Smith and S. C. Kohn, *Solid State Nucl. Magn. Reson.*, 1999, **15**, 181.

117. S. Lamouria, M. Hamidouche, N. Bouaouadja, H. Belhouchet, V. Garnier, G. Fantozzi and J. F. Trelkat, *Bol. Soc. Esp. Ceram. V.*, 2017, **56**, 47.
118. G. Tricot, J. Trébosc, F. Pourpoint, R. Gauvin and L. Delevoye, *Annu. Rep. NMR Spectrosc.*, 2014, **81**, 145.
119. A. Brinkmann and A. P. M. Kentgens, *J. Am. Chem. Soc.*, 2006, **128**, 14758.
120. Z. Gan, P. Gor'kov, T. A. Cross, A. Samoson and D. Massiot, *J. Am. Chem. Soc.*, 2002, **124**, 5634.
121. J.-P. Amoureux, J. Trébosc, L. Delevoye, O. Lafon, B. Hu and Q. Wang, *Solid State Nucl. Magn. Reson.*, 2009, **35**, 12.
122. B. Bouchevreau, C. Martineau, C. Mellot-Draznieks, A. Tuel, M. R. Suchomel, J. Trébosc, O. Lafon, J.-P. Amoureux and F. Taulelle, *Chem. Eur. J.*, 2013, **19**, 5009.
123. B. Bouchevreau, C. Martineau, C. Mellot-Draznieks, A. Tuel, M. R. Suchomel, J. Trébosc, O. Lafon, J.-P. Amoureux and F. Taulelle, *Chem. Mater.*, 2013, **35**, 2227.
124. B. O'Regan and M. Grätzel, *Nature*, 1991, **353**, 737.
125. U. Bach, D. Lupo, P. Comte, J. E. Moser, F. Weissörtel, J. Salbeck, H. Spreitzer and M. Grätzel, *Nature*, 1998, **395**, 583.
126. G. W. Wagner, L. R. Procell and S. Munavalli, *J. Phys. Chem. C*, 2007, **111**, 17564.
127. Q. Wang, W. Ma, Q. Tong, G. Du, J. Wang, M. Zhang, H. Jiang, H. Yang, Y. Liu and M. Cheng, *Sci. Rep.*, 2017, **7:7209**.
128. J. M. Fraile, C. Gil, J. A. Mayoral, B. Muel, L. Roldán, E. Vispe, S. Calderón and F. Puente, *Appl. Catal. B*, 2016, **180**, 680.
129. L. P. Rivoira, V. A. Vallés, B. C. Ledesma, M. V. Ponte, M. L. Martinez, O. A. Anunziata and A. R. Beltramone, *Catal. Today*, 2016, **271**, 102.
130. A. M. Venezia, V. La Parola, L. F. Liotta, G. Pantaleo, M. Lualdi, M. Boutonnet and S. Järås, *Catal. Today*, 2012, **197**, 18.
131. G. M. Dahr, B. N. Srinivas, M. S. Rana, M. Kumar and S. K. Maity, *Catal. Today*, 2003, **86**, 45.
132. J. B. Rosenholm, H. Rahiala, J. Puputti, V. Stathopoulos, P. Pomonis, I. Beurroies and K. Backfolk, *Colloids Surf. A*, 2004, **250**, 289.

133. C. Lahousse, F. Maugé, J. Bachelier and J-C. Lavalley, *J. Chem. Soc. Faraday Trans.*, 1995, **9**, 2907.
134. T. J. Bastow and S. N. Stuart, *Chem. Phys.*, 1990, **143**, 459.
135. X. Sun, M. Dyballa, J. Yan, L. Li, N. Guan and M. Hunger, *Chem. Phys. Lett.*, 2014, **594**, 34.
136. M. Vahtrus, M. Umalas, B. Polyakov, L. Dorogin, R. Saar, M. Tamme, K. Saal, R. Lõhmus and S. Vlassov, *Mater. Charact.*, 2015, **107**, 119.
137. V. P. Pakharukova, D. A. Yatsenko, E. Yu. Gerasimov, A. S. Shalygin, O. N. Martyanov, S. V. Tsybulya, *J. Solid State Chem.*, 2017, **246**, 284.
138. M. Rezaee, S. M. M. Khoie and K. H. Liu, *CrystEngComm*, 2011, **13**, 5055.
139. D. Reyes-Coronado, G. Rodríguez-Gattorno, M. E. Espinosa-Pesqueira, C. Cab, R. de Coss and G. Oskam, *Nanotechnology*, 2008, **19**, 145605.
140. B. M. Reddy, G. K. Reddy, K. N. Rao, I. Ganesh and J. M. F. Ferreira, *J. Mater. Sci.*, 2009, **44**, 4874.
141. M. A. Ahmed and M. F. Abdel-Messih, *J. Alloys Compd.*, 2011, **509**, 2154.
142. L. A. O'Dell, S. L. P. Savin, A. V. Chadwick and M. E. Smith, *J. Phys. Chem. C*, 2007, **111**, 13740.
143. T. J. Bastow, A. F. Moodie, M. E. Smith and H. J. Whitfield, *J. Mater. Chem.*, 1993, **3**, 697.
144. E. Scolan, C. Magnenet, D. Massiot and C. Sanchez, *J. Mater. Chem.*, 1999, **9**, 2467.

Chapter 7. Conclusions

This thesis focussed on the applications of advanced one- and two-dimensional multinuclear solid-state NMR experiments to the characterisation of a variety of industrially-relevant catalyst materials.

In Chapter 5, ^{1}H and ^{27}Al solid-state NMR spectroscopy was utilised for an in-depth investigation of alumina-based supported metal catalysts. ^{1}H-^{27}Al CP and D-HMQC experiments applied on unmodified γ-Al_2O_3 conclusively demonstrated the existence of Al(V) sites on the surface of this material. It was shown that removal of adsorbed H_2O may facilitate a rearrangement effect on the surface of γ-Al_2O_3 that promotes the generation of pentacoordinated Al species. Analysis of Co-γ-Al_2O_3 model catalysts indicated that a metal-support interaction (MSI) does exist in many of these systems, and is strongest for materials that contain small, well dispersed Co_3O_4 crystallites. It was found that methods based on incipient wetness impregnation may promote the formation of a MSI to a far greater extent than colloidal approaches, a preparation route which tends to favour the formation of co-mixtures composed of self-contained Co oxide "nanocubes".[1]

It was shown *via* ^{1}H MAS NMR that, although the deposition of Co_3O_4 onto the surface of γ-Al_2O_3 effectively removes OH functionality, the hygroscopic nature of this system allows the extent of the MSI to be visualised by observing the extent of the proton-metal oxide interaction, *via* the presence of adsorbed H_2O. As a result, in these materials, water was found to be both adventitious and advantageous. Results obtained from ^{1}H-^{27}Al CP and ^{27}Al z-filtered 3QMAS experiments indicated that Al(IV) environments are the preferential binding site for Co oxide crystallites on the surface of γ-Al_2O_3. It was also shown that this was likely to be the case for Co spinel aluminate materials. Additionally, the surface chemistry of the diamagnetic analogue $MgAl_2O_4$ was investigated, with MgOH and AlOH environments being identified. It was also demonstrated that two types of Al(VI) species are present in $MgAl_2O_4$, $CoAl_2O_4$ and Co-$CoAl_2O_4$, one of which may be located closer to the surface of the spinels. These findings, whilst having provided valuable insights into the structures of supported

metal catalysts, demonstrated that additional, detailed investigations will be necessary to fully understand the surface/bulk chemistry of these complex materials.

Chapter 6 presented work using multinuclear solid-state NMR spectroscopy to provide detailed insights into the structure of several silicated alumina model catalysts. It was shown that a combination of isotopic enrichment and DNP NMR spectroscopy can provide a definitive and fully quantitative description of the surface structure of Si-γ-Al_2O_3 (1.5 wt% Si), and the role of adventitious surface H_2O was uncovered. It was found that this H-bonded water forms a sufficiently dense proton network at the silica surface, mediating efficient polarisation transfer to all Si species, regardless of their chemical nature and hydroxyl functionality. It was determined that the combination of the increased amount of information available from the DNP enhancement and the ability to obtain quantitative spectra using isotopic enrichment, affords a more rigorous, quantitative interpretation of ^{29}Si spectra, and a detailed understanding of the nature of the Si-Al interface. Analysis of silicated aluminas prepared by sequential grafting and "single shot" approaches showed that silica growth on γ-Al_2O_3 results in two distinct morphologies. Sequential silica grafting was shown to result in the build-up of 3D layers through an "island stacking" process, whereas the "single shot" approach results in a mixed growth morphology consisting of silica island moieties accompanied by the formation of amorphous SiO_2 "ball" structures. It was also revealed that long term ageing of as-made "single shot" silicated alumina promotes the formation of a structure possessing a greater proportion of silicate Q^n species than the calcined version.

Post-synthetic exchange with ^{17}O gas was demonstrated to be very successful in facilitating ^{17}O solid-state NMR studies of γ-Al_2O_3 and Si-γ-Al_2O_3 materials. Using this method, the presence of two (γ-Al_2O_3) and four (Si-γ-Al_2O_3 (1.5 wt% Si)) distinct oxygen environments was revealed. The dependence of $^{16}O/^{17}O$ exchange on heating temperature has also been highlighted, with conditions of 700 °C for 12 h found to facilitate more uniform isotopic enrichment of the underlying alumina structure in Si-γ-Al_2O_3 (1.5 wt% Si). Preliminary ^{17}O NMR studies on Si-γ-Al_2O_3 4th graft (5.2 wt% Si) indicated that an amorphous silica-type of oxygen environment is present in this

material, consistent with both "stacked" silica islands and amorphous SiO_2 "ball" structures. These results demonstrate that ^{17}O NMR spectroscopy has the potential to be used to investigate other materials in the Si-γ-Al_2O_3 sequential grafting series. It was shown that ^{29}Si and ^{17}O double-enrichment of Si-γ-Al_2O_3 (1.5 wt% Si) can allow access to ^{29}Si-^{17}O 2D correlation experiments, even at low silica loading. It was observed that Q^4(3Al) bridging Si units primarily correlate with OAl_3 and OAl_4 oxygen species, rather than with Si-O-Si oxygens, as might have been expected. This finding was interpreted in terms of strong dipolar connectivity between these Si and O species, which is observable due to the through-space nature of the ^{29}Si-^{17}O D-HMQC experiment. Future work in this area could potentially include additional sequences such as J-HMQC[2] and MQ-INEPT,[3,4] in order to probe through-bond connectivities and provide increased resolution, respectively. It was also discovered that, although the ^{17}O gas exchange enrichment process induces hydrolysis of Si-O-Si units in the silicated alumina overlayer, it causes no overall change to the nature of the surface silica structure.

A preliminary investigation of Ti-alumina model catalysts was also carried out using ^1H, ^{27}Al and ^{17}O solid-state NMR techniques. It was revealed that two Al(IV) and Al(VI) sites are present in the structure of γ-Al_2O_3. Initial results highlighted that, whilst Ti-γ-Al_2O_3 can be described as a surface modified γ-Al_2O_3 structure, (similar to Si-γ-Al_2O_3), Ti-Al M50 may be morphologically distinct. Evidence indicated that the latter material may be a combined phase TiO_2-Al_2O_3 composed of TiO_2 (anatase) nanoparticles and γ-Al_2O_3-like phases exhibiting a poor degree of mixing. These findings showed that additional analysis is necessary to substantiate these initial determinations. Multi-temperature ^{17}O gas exchange enrichment studies, 2D correlation experiments, and potentially $^{47,49}Ti$ solid-state NMR spectroscopy, are proposed as possible avenues for future investigations of these systems. The use of complementary analytical techniques such as PXRD, XPS and electron microscopy would also be highly beneficial to such studies. Additionally, the study of Ti-γ-Al_2O_3 samples with variable Ti loading and TiO_2-Al_2O_3 materials with a high degree of phase-mixing could also be highly informative.

In summary, the work presented in this thesis demonstrated that multinuclear solid-state NMR spectroscopy is an effective, versatile, and robust tool for the characterisation of catalytically-relevant oxide materials, that offers great potential for future investigations of such systems.

7.1 References

1. S. Sadasivan, R. M. Bellabarba and R. P. Tooze, *Nanoscale*, 2013, **5**, 11139.
2. J.-P. Amoureux, J. Trébosc, L. Delevoye, O. Lafon, B. Hu and Q. Wang, *Solid State Nucl. Magn. Reson.*, 2009, **35**, 12.
3. B. Bouchevreau, C. Martineau, C. Mellot-Draznieks, A. Tuel, M. R. Suchomel, J. Trébosc, O. Lafon, J.-P. Amoureux and F. Taulelle, *Chem. Eur. J.*, 2013, **19**, 5009.
4. B. Bouchevreau, C. Martineau, C. Mellot-Draznieks, A. Tuel, M. R. Suchomel, J. Trébosc, O. Lafon, J.-P. Amoureux and F. Taulelle, *Chem. Mater.*, 2013, **35**, 2227.

Appendix A. Extended Figure Captions

The figure captions in this appendix provide full solid-state NMR experimental details for the spectra presented in the relevant figures. The revised Hartman-Hahn match condition for CP experiments, and any pulses or delays used were experimentally optimised prior to spectral acquisition. For 2D experiments, the quadrature detection methods of States *et al.*[1] or Marion *et al.*[2] were used to achieve sign discrimination in the indirect dimension.

Chapter 1

Figure 1.1. ^{1}H (14.1 T, 55 kHz MAS) NMR spectrum of L-alanine (structure shown in figure), with resonance assignments for each of the three H environments. The spectrum was acquired by averaging 16 transients separated by a recycle interval of 1 s. A spin echo pulse sequence was used with τ = 16.95 μs. $\nu_1 \approx$ 100 kHz.

Figure 1.2. ^{1}H-^{29}Si (9.4 T, 10 kHz MAS and τ_{CP} = 1 ms) CP NMR spectrum of powdered octakis(trimethylsiloxy)silsesquioxane (Q8M8) with resonance assignments for each type of Si environment present. The spectrum was acquired by averaging 8 transients separated by a recycle interval of 10 s. The contact pulse was implemented using a ramped pulse (90-100%) applied to ^{1}H. ^{1}H decoupling was carried out using the TPPM-15 decoupling sequence[3] with $\nu_1 \approx$ 100 kHz.

Figure 1.3. ^{29}Si (14.1 T, 18 kHz MAS) NMR spectrum of a silicon phosphate material, accompanied by resonance assignments for the two types of Si coordination environment present. The spectrum was acquired by averaging 752 transients separated by a recycle interval of 15 s. $\nu_1 \approx$ 83 kHz.

Figure 1.4. ^{27}Al (14.1 T, 14 kHz MAS) NMR spectrum of zeolite USY, with resonance assignments for the three types of Al-O coordination environment present. The spectrum was acquired by averaging 512 transients separated by a recycle interval of 1 s. $\nu_1 \approx$ 90 kHz.

Figure 1.5. ^{17}O (14.1 T, 14 kHz MAS) NMR spectra of ^{17}O enriched (a) TiO_2 (anatase) and (b) MgO, along with resonance assignments for the O environments present in each material. In (a), the spectrum was acquired by averaging 2048 transients separated by a recycle interval of 3 s. $\nu_1 \approx 60$ kHz. In (b), the spectrum was acquired by averaging 2 transients separated by a recycle interval of 10 s. A saturation train was used to reduce the recycle interval required. $\nu_1 \approx 56$ kHz.

Chapter 2

Figure 2.4. The effect of signal averaging on the ^{13}C MAS NMR spectrum (9.4 T, 14 kHz MAS) of the CH_3 site ($\delta = 20.5$ ppm) of L-alanine. The left spectrum was acquired by averaging 16 transients separated by a recycle interval of 10 s. The right spectrum was acquired by averaging 128 transients separated by a recycle interval of 10 s. $\nu_1 \approx$ 63 kHz for both spectra. ^1H decoupling was carried out using the TPPM-15 decoupling sequence[3] with $\nu_1 \approx 91$ kHz for both spectra.

Chapter 3

Figure 3.1. (a) Schematic representation of the experimental setup for MAS. (b) Photograph of a 7 mm rotor used for spinning solid samples at a maximum MAS rate of 7 kHz. (c) ^{13}C (9.4 T) NMR spectrum of a static sample of 1[^{13}C]-glycine. (d) ^{13}C (9.4 T, 10 kHz MAS) NMR spectrum of 1[^{13}C]-glycine. * denotes a spinning sideband. In (c) and (d), spectra were acquired by averaging 16 transients separated by a recycle interval of 20 s. $\nu_1 \approx 125$ kHz for both spectra.

Figure 3.2. ^{119}Sn (9.4 T) NMR spectra of SnO_2 acquired at several different MAS rates. The isotropic resonance is broadened by the CSA interaction. $\delta_{iso} = -604$ ppm, $\Omega = 126$ ppm and $\kappa = 1$ ($\delta_{11} = \delta_{22} = -563$ ppm, $\delta_{33} = -687$ ppm). The spectrum of the static sample was acquired by averaging 64 transients separated by a recycle interval of 30 s. A spin echo pulse sequence was used with $\tau = 20$ μs. $\nu_1 \approx 100$ kHz. The spectra of SnO_2 rotated at $\nu_R = 2$-10 kHz were acquired by averaging 16 transients separated by a recycle interval of 30 s. $\nu_1 \approx 125$ kHz for all MAS spectra.

Figure 3.5. (a) ^{13}C (9.4 T, 14 kHz MAS) DP (blue) and CP (red, τ_{CP} = 0.5 ms) MAS NMR spectra of the C=O resonance of glycine (structure also shown). (b) Schematic depicting the pulse sequence for the CP experiment. In (a), the DP NMR spectrum was acquired by averaging 16 transients separated by a recycle interval of 20 s. $\nu_1 \approx 63$ kHz. ^1H decoupling was carried out using the TPPM-15 decoupling sequence[3] with $\nu_1 \approx 91$ kHz. The CP NMR spectrum was acquired by averaging 16 transients separated by a recycle interval of 1 s. The contact pulse was implemented using a ramped pulse (90-100%) applied to ^1H. ^1H decoupling was carried out using the TPPM-15 decoupling sequence[3] with $\nu_1 \approx 91$ kHz.

Figure 3.6. ^{17}O (14.1 T, 14 kHz MAS) (a) DP and (b) CP (from ^1H, τ_{CP} = 0.4 ms) NMR spectra of ^{17}O-enriched γ-Al_2O_3. * denotes a spinning sideband. In (a), the spectrum was acquired by averaging 1024 transients separated by a recycle interval of 3 s. In (b), spectrum was acquired by averaging 4096 transients separated by a recycle interval of 0.5 s. The contact pulse was implemented using a ramped pulse (90-100%) applied to ^1H. ^1H decoupling was carried out using continuous wave decoupling with $\nu_1 \approx 66$ kHz.

Figure 3.7. ^{13}C (9.4 T, 10 kHz MAS) DP NMR spectra of 1[^{13}C]-glycine (a) without ^1H decoupling and (b) with ^1H TPPM decoupling. Expansions of the isotropic resonances are also shown inset. * denotes a spinning sideband. In (a), the spectrum was acquired by averaging 16 transients separated by a recycle interval of 20 s. $\nu_1 \approx$ 125 kHz. In (b), the spectrum was acquired by averaging 16 transients separated by a recycle interval of 20 s. $\nu_1 \approx 125$ kHz. ^1H decoupling was carried out using the TPPM-15 decoupling sequence[3] with $\nu_1 \approx 100$ kHz.

Figure 3.8. ^1H (9.4 T, 9.091 kHz MAS) NMR spectra of L-alanine (a) without and (b) with eDUMBO-1_{22} homonuclear decoupling[4] during acquisition. In (b), a scaling factor of 0.50 has been applied to correct the chemical shift axis. * denotes a spinning sideband. Both spectra were acquired by averaging 32 transients separated by a recycle interval of 5 s. $\nu_1 \approx 100$ kHz. In (b) an eDUMBO-1_{22} shaped pulse of 32 μs was applied with $\nu_1 \approx 100$ kHz and phase angle = 120°.

Figure 3.10. (a) Pulse sequence for a CP HETCOR experiment. (b) ^{1}H-^{27}Al (9.4 T, 14 kHz MAS, τ_{CP} = 0.8 ms) CP HETCOR spectrum of partially dehydrated γ-Al_2O_3. Assignments for Al and H resonances are shown next to the projections of each dimension. In (b), the spectrum is the result of averaging 944 transients separated by a recycle interval of 1 s, for each of 60 t_1 increments of 17.86 μs. The contact pulse was implemented using a ramped pulse (90-100%) applied to ^{1}H. ^{1}H decoupling was carried out using continuous wave decoupling with $\nu_1 \approx 41$ kHz. The spectrum shown was processed with 50 Hz Lorentzian broadening in the ^{27}Al dimension.

Figure 3.12. (a) Pulse sequence and coherence pathway for a refocused INADEQUATE experiment.[5] In this version, CP is used to enhance initial ^{13}C magnetisation. (b) ^{13}C-^{13}C (9.4 T, 10 kHz MAS, τ = 3 ms) refocused INADEQUATE[5] spectrum (with CP from ^{1}H, where τ_{CP} = 0.5 ms) of U[^{13}C]-L-alanine. Solid black lines indicate correlations between directly bonded ^{13}C species. The solid grey line denotes the $\delta_{DQ} = 2\delta_{SQ}$ autocorrelation diagonal. ♦ indicates a relayed anti-phase peak resulting from two nuclei that are not covalently bonded, but share a common coupling partner.[6] * denotes a spinning sideband. In (b), the spectrum is the result of averaging 32 transients separated by a recycle interval of 0.75 s, for each of 480 t_1 increments of 20 μs. The CP contact pulse was implemented using a ramped pulse (90-100%) applied to ^{1}H. ^{1}H decoupling was carried out using the SPINAL-64 decoupling sequence[7] with $\nu_1 \approx 100$ kHz. The FIDs were truncated, even after 38 ms acquisition, and the spectrum shown was processed with 500 Hz Lorentzian broadening in both the direct and indirect dimensions.

Figure 3.13. (a) Pulse sequence and coherence transfer pathway for a generic homonuclear SQ-DQ correlation experiment. (b) The BABA scheme[8,9] employed for excitation and conversion of DQ coherences where τ_r = rotor period and n = number of BABA blocks used. (c) ^{1}H-^{1}H (9.4 T, 40 kHz MAS) SQ-DQ BABA spectrum of L-alanine, where n = 1. Solid black lines denote DQ coherences between two protons of the same type (*e.g.*, CH-CH). Dashed coloured lines indicate DQ coherences between two different types of protons (*e.g.*, CH_3-CH). The solid grey diagonal line denotes the $\delta_{DQ} = 2\delta_{SQ}$ autocorrelation diagonal. The spectrum is the result of averaging 16 transients separated by a recycle interval of 1 s, for each of 120 t_1 increments of 25 μs.

Figure 3.14. (a) Pulse sequence for a CPMG experiment, where N = number of echoes. (b) ^{93}Nb (14.1 T) CPMG spectrum of a static sample of $K_7Na[Nb_6O_{19}]$. The spectrum was acquired by averaging 1024 transients separated by a recycle interval of 2 s. A CPMG pulse sequence[10-12] was used with $1/\tau = 4$ kHz, and 40 pulses were applied in the echo train.

Figure 3.20. (a) ^{87}Rb (9.4 T, 14 kHz MAS) NMR spectrum of $RbNO_3$. (b) ^{87}Rb (9.4 T, 14 kHz MAS) z-filtered 3QMAS NMR spectrum of $RbNO_3$. A shearing transformation has been applied. (c) Cross sections parallel to δ_2 extracted from the spectrum shown in (b). In (a), the spectrum was acquired by averaging 1024 transients separated by a recycle interval of 0.25 s. $\nu_1 \approx 140$ kHz. In (b), the spectrum is the result of averaging 48 transients separated by a recycle interval of 0.2 s, for each of 300 t_1 increments of 50 μs. Excitation and conversion pulses were applied with $\nu_1 \approx 140$ kHz and the CT selective pulse with $\nu_1 \approx 11$ kHz.

Figure 3.22. (a) ^{1}H (9.4 T, 8 kHz MAS) DNP NMR spectrum of a 14 mM solution of TEKPol in 1,1,2,2-tetrachloroethane (TCE), impregnated onto ^{29}Si-γ-Al_2O_3 (1.5 wt% Si). * denotes a spinning sideband. (b) ^{1}H-^{29}Si (9.4 T, 8 kHz MAS, $\tau_{CP} = 3.5$ ms) DNP CP NMR spectrum of ^{29}Si-γ-Al_2O_3. For both sets of spectra, enhancement factors, ε, are given in the top right corner. All spectra were acquired at ~100 K. mw = microwaves. In (a), the spectrum was acquired by averaging 8 transients separated by a recycle interval of 5 s. $\nu_1 \approx 100$ kHz. In (a), the spectrum is the result of averaging 16 transients separated by a recycle interval of 2 s. The CP contact pulse was implemented using a ramped pulse (80-100%) applied to ^{1}H. ^{1}H decoupling was carried out using the SPINAL-64 decoupling sequence[7] with $\nu_1 \approx 100$ kHz.

Chapter 5

Figure 5.1. (a) ^{27}Al (9.4 T, 14 kHz MAS) short flip angle DP NMR spectrum of the CT of aluminium acetylacetonate ($Al(acac)_3$). ♦ denotes the centreband of the inner ($\pm1/2 \leftrightarrow \pm3/2$) satellite transition.[13] (b) Lineshape fit of the experimental spectrum shown in (a). The following NMR parameters were obtained: $C_Q = 3.0$ MHz; $\eta_Q =$

0.16 and δ_{iso} = 0.0 ppm. In (a), The spectrum was acquired by averaging 64 transients separated by a recycle interval of 5 s, using a pulse duration of 0.4 μs with $\nu_1 \approx 110$ kHz. The spectrum shown was processed with 25 Hz Lorentzian broadening.

Figure 5.2. ^{27}Al (9.4 T, 14 kHz MAS) short flip angle DP NMR spectrum of γ-Al_2O_3. * denotes a spinning sideband. The spectrum is the result of averaging 256 transients separated by a recycle interval of 3 s, using a pulse duration of 0.2 μs with $\nu_1 \approx 110$ kHz.

Figure 5.3. (a) ^{27}Al (9.4 T, 14 kHz MAS) z-filtered 3QMAS spectrum of γ-Al_2O_3, with lines indicating distributions of chemical shifts ($dist_{CS}$) and quadrupolar parameters ($dist_Q$). A shearing transformation has been applied. (b) ^{27}Al (9.4 T, 14 kHz MAS) z-filtered 3QMAS spectrum of γ-Al_2O_3, with fits using the Czjzek model for the EFG and a Gaussian distribution of δ_{iso} (black lines) overlaid on each resonance (coloured lines). A shearing transformation has been applied. In (b) referencing in δ_1 was carried out according to the convention proposed by Amoureux and Fernandez,[14] in order for the Czjzek model to be implemented within DMFit.[15,16] Both spectra are the result of averaging 48 transients separated by a recycle interval of 3 s, for each of 104 t_1 increments of 25 μs. Excitation and conversion pulses were applied with $\nu_1 \approx 110$ kHz and the CT selective pulse with $\nu_1 \approx 9$ kHz.

Figure 5.4. ^{27}Al (14.1 T, 20 kHz MAS) short flip angle DP NMR (black) and ^{1}H-^{27}Al (14.1 T, 20 kHz MAS, τ_{CP} = 0.8 ms) CP NMR (red) spectra of γ-Al_2O_3. * denotes a spinning sideband. The DP NMR spectrum was acquired by averaging 128 transients separated by a recycle interval of 3 s, using a pulse duration of 0.2 μs with $\nu_1 \approx 91$ kHz. The CP NMR spectrum is the result of averaging 4096 transients separated by a recycle interval of 1 s. The contact pulse was implemented using a ramped pulse (90-100%) applied to ^{1}H. ^{1}H decoupling was carried out using continuous wave decoupling with $\nu_1 \approx 92$ kHz.

Figure 5.5. ^{1}H-^{27}Al (14.1 T, 14 kHz MAS, τ_{CP} = 0.8 ms) z-filtered CP 3QMAS[17] NMR spectrum of γ-Al_2O_3. A shearing transformation has been applied. Resonances

corresponding to Al(IV) and Al(VI) species are labelled. * denotes a spinning sideband. The spectrum is the result of averaging 2304 transients separated by a recycle interval of 0.75 s, for each of 42 t_1 increments of 25 μs. Excitation and conversion pulses were applied with $\nu_1 \approx 87$ kHz and the CT selective pulse with $\nu_1 \approx 7$ kHz. The CP contact pulse was implemented using a ramped pulse (90-100%) applied to ^{1}H. ^{1}H decoupling was carried out using continuous wave decoupling with $\nu_1 \approx 66$ kHz.

Figure 5.6. ^{1}H-^{27}Al (14.1 T, 40 kHz MAS) D-HMQC spectra of γ-Al_2O_3, acquired with (a) τ_{rec} = 0.3 ms and (b) τ_{rec} = 0.9 ms. In both spectra, annotations have been provided for resonance assignments/chemical shift values. (c) Schematic representations of the functional groups observed in the spectra shown in (a) and (b), along with corresponding ^{1}H δ_{iso} values. (d) Overlaid total projections of the ^{27}Al dimension of the 2D spectra in (a) (blue) and (b) (red), processed with 300 Hz Lorentzian broadening. Both spectra are the result of averaging 2880 transients separated by a recycle interval of 1 s, for each of 18 t_1 increments of 25 μs. Active recoupling of the ^{1}H-^{27}Al dipolar interaction was achieved using the $SR4^2_1$ scheme,[18] with $\nu_1 \approx 2\nu_R$. The spectra shown were processed with 200 Hz Lorentzian broadening in the ^{27}Al dimension.

Figure 5.7. (a) ^{1}H-^{27}Al (9.4 T, 14 kHz MAS, τ_{rec} = 0.43 ms) D-HMQC spectrum of γ-Al_2O_3 dehydrated in vacuo at 300 °C for ~6 h. It is the result of averaging 5120 transients separated by a recycle interval of 1 s, for each of 8 t_1 increments of 71.43 μs. Active recoupling of the ^{1}H-^{27}Al dipolar interaction was achieved using the $SR4^2_1$ scheme,[18] with $\nu_1 \approx 2\nu_R$. The spectrum shown was processed with 100 Hz Lorentzian broadening in the ^{27}Al dimension. Annotations have been provided for resonance assignments/chemical shift values. (b) ^{1}H (9.4 T, 14 kHz MAS) NMR spectrum of the γ-Al_2O_3 sample studied in (a). The spectrum was acquired by averaging 128 transients separated by a recycle interval of 1 s, using the DEPTH pulse sequence for probe background suppression.[19] $\nu_1 \approx 100$ kHz. Chemical shift values for resonances are indicated. (c) Schematic representations of the functional groups observed in the spectra shown in (a) and (b), along with corresponding ^{1}H δ_{iso} values.

Figure 5.8. (a) ^{27}Al (14.1 T, 14 kHz MAS) z-filtered 3QMAS spectrum of γ-Al_2O_3 dehydrated *in vacuo* at 300 °C for 6 h. The spectrum is the result of averaging 144 transients separated by a recycle interval of 1 s, for each of 120 t_1 increments of 17.86 μs. Excitation and conversion pulses were applied with $\nu_1 \approx 87$ kHz and the CT selective pulse with $\nu_1 \approx 7$ kHz. A shearing transformation has been applied. (b) Overlay of ^{27}Al (14.1 T, 14 kHz MAS) short flip angle DP NMR spectra of hydrated (red) and dehydrated γ-Al_2O_3 (300 °C, 6 h) (black). Both spectra are the result of averaging 128 transients separated by a recycle interval of 3 s, using a pulse duration of 0.2 μs with $\nu_1 \approx 87$ kHz. (c) Overlay of ^{27}Al (14.1 T, 14 kHz MAS, black) short flip angle DP and ^{1}H-^{27}Al (14.1 T, 14 kHz MAS, τ_{CP} = 0.8 ms, green) CP NMR spectra of spectrum of dehydrated γ-Al_2O_3 (300 °C, 6 h), where spectra have been scaled with respect to the Al(VI) resonance. In all spectra, * denotes a spinning sideband. The DP NMR spectrum was acquired by averaging 128 transients separated by a recycle interval of 3 s, using a pulse duration of 0.2 μs with $\nu_1 \approx 87$ kHz. The CP NMR spectrum was acquired by averaging 4096 transients separated by a recycle interval of 1 s. The contact pulse was implemented using a ramped pulse (90-100%) applied to ^{1}H. ^{1}H decoupling was carried out using continuous wave decoupling with $\nu_1 \approx 55$ kHz.

Figure 5.9. ^{1}H (9.4 T, 40 kHz MAS) NMR spectra of series one catalysts (a) stacked and (b) overlaid and normalised. Spectra are the result of averaging 16 transients separated by a recycle interval of 0.25 s, using the DEPTH pulse sequence for probe background suppression.[19] $\nu_1 \approx 100$ kHz. The sharp feature at ^{1}H $\delta_{iso} \approx 0$ ppm in the spectra of IWN020 results from background signal.[20,21]

Figure 5.10. ^{1}H-^{1}H (9.4 T, 40 kHz MAS) SQ-DQ spectra of (a) IW5 and (b) COLL10. Both spectra were acquired using one block of BABA excitation/conversion.[8,9] The solid grey line denotes the $\delta_{DQ} = 2\delta_{SQ}$ autocorrelation diagonal. Both spectra are the result of averaging 64 transients separated by a recycle interval of 0.25 s, for each of (a) 50 or (b) 128 t_1 increments of 25 μs. $\nu_1 \approx 100$ kHz.

Figure 5.11. ^{27}Al (9.4 T, 40 kHz MAS) DP NMR spectra overlaid of (a) series one catalysts and (b) γ-Al_2O_3, IW5 and COLL10. Spectra have been normalised with respect to the Al(VI) resonance. All spectra were acquired by averaging 1024 transients separated by a recycle interval of 3 s. A spin echo pulse sequence was used with a rotor synchronised τ delay of 25 μs. $\nu_1 \approx 110$ kHz.

Figure 5.12. (a) ^{1}H (14.1 T, 20 kHz MAS) NMR spectra of γ-Al_2O_3 and series two catalysts overlaid. Intensities have been normalised with respect to the maximum point of the γ-Al_2O_3 lineshape. ♦ denotes background signal. All spectra were acquired by averaging 512 (128 for γ-Al_2O_3) transients separated by a recycle interval of 5 s, using the DEPTH pulse sequence for probe background suppression.[19] $\nu_1 \approx 100$ kHz. (b) ^{27}Al (9.4 T, 14 kHz MAS) short flip angle DP NMR spectra of the samples studied in (a). Spectra have been scaled with respect to the number of transients and the mass of sample contained within each 4 mm rotor. All spectra were acquired by averaging 512 (256 for γ-Al_2O_3) transients separated by a recycle interval of 3 s, using a pulse duration of 0.2 μs with $\nu_1 \approx 110$ kHz. In both (a) and (b), * denotes a spinning sideband.

Figure 5.13. ^{27}Al (14.1 T, 14 kHz MAS) z-filtered 3QMAS spectra of (a) γ-Al_2O_3, (b) IWN020, (c) IWN010 and (d) IWN05. A shearing transformation has been applied to all spectra. Resonances corresponding to Al(IV) and Al(VI) species are labelled. * denotes a spinning sideband. In (a), the spectrum is the result of averaging 48 transients separated by a recycle interval of 2 s, for each of 130 t_1 increments of 25 μs. Excitation and conversion pulses were applied with $\nu_1 \approx 91$ kHz and the CT selective pulse with $\nu_1 \approx 6$ kHz. In (b)-(d), spectra are the result of averaging 144 transients separated by a recycle interval of 1 s, for each of 50 t_1 increments of 35.71 μs. Excitation and conversion pulses were applied with $\nu_1 \approx 87$ kHz and the CT selective pulse with $\nu_1 \approx$ 7 kHz.

Figure 5.14. ^{1}H-^{27}Al (9.4 T, 14 kHz MAS, $\tau_{CP} = 0.8$ ms) CP NMR spectra of series two catalyst materials. The mass of sample in each rotor and the number of transients in each experiment were the same for all samples. All spectra were acquired by averaging 106208 transients separated by a recycle interval of 0.5 s. The contact pulse

was implemented using a ramped pulse (90-100%) applied to ^{1}H. ^{1}H decoupling was carried out using continuous wave decoupling with $\nu_1 \approx 52$ kHz.

Figure 5.15. (a) ^{1}H (14.1 T, 20 kHz MAS) NMR spectra of IWN020, γ-Al_2O_3 and IWN020:γ-Al_2O_3 ground mixtures overlaid. Spectra have been normalised to give equal intensities at 4.7 ppm. The sharp peaks at ^{1}H $\delta_{iso} \approx 2$ ppm are attributed to residual solvent.[22] The sharp feature at ^{1}H $\delta_{iso} \approx 0$ ppm in the spectra of IWN020 results from background signal.[20,21] All spectra were acquired by averaging 128 transients separated by a recycle interval of 5 s, using the DEPTH pulse sequence for probe background suppression.[19] $\nu_1 \approx 100$ kHz. (b) ^{27}Al (9.4 T, 14 kHz MAS) short flip angle DP NMR spectra of the same samples studied in (a). Spectra were acquired by averaging 512 (256 for γ-Al_2O_3) transients separated by a recycle interval of 3 s, using a pulse duration of 0.2 μs with $\nu_1 \approx 110$ kHz. Spectra have been normalised with respect to the Al(VI) resonance.

Figure 5.16. ^{1}H (9.4 T, 14 kHz MAS) NMR spectra of $MgAl_2O_4$ (blue), $CoAl_2O_4$ (red) and Co-$CoAl_2O_4$ (green). Spectra have been scaled with respect to the centre of the $MgAl_2O_4$ resonace at ^{1}H $\delta \approx 4.2$ ppm. Expansions of the upfield resonances in the spectrum of $MgAl_2O_4$ are also shown inset. ♦ denotes background signal. All spectra were acquired by averaging 1024 transients separated by a recycle interval of 0.2 s, using the DEPTH pulse sequence for probe background suppression.[19] $\nu_1 \approx 100$ kHz.

Figure 5.17. (a) ^{27}Al (9.4 T, 14 kHz MAS) short flip angle DP NMR spectra of $MgAl_2O_4$ (blue), $CoAl_2O_4$ (red) and Co-$CoAl_2O_4$ (green). Spectra have been scaled with respect to the Al(VI) resonance. Spectra were acquired by averaging 512 transients separated by a recycle interval of 5 s, using a pulse duration of 0.2 μs with $\nu_1 \approx 110$ kHz. (b) ^{27}Al (14.1 T, 14 kHz MAS (blue) and 20 kHz MAS (red and green)) DP NMR spectra of $MgAl_2O_4$ (blue), $CoAl_2O_4$ (red) and Co-$CoAl_2O_4$ (green). Spectra were acquired by averaging 128 ($CoAl_2O_4$ (red) and Co-$CoAl_2O_4$ (green)) or 64 ($MgAl_2O_4$ (blue)) transients separated by a recycle interval of 30 ($CoAl_2O_4$ (red) and Co-$CoAl_2O_4$ (green)) or 20 ($MgAl_2O_4$ (blue)) s. $\nu_1 \approx 91$ ($CoAl_2O_4$ (red) and Co-

$CoAl_2O_4$ (green)) or 87 kHz ($MgAl_2O_4$ (blue)). In both (a) and (b), * denotes a spinning sideband.

Figure 5.18. ^{27}Al (14. 1 T, 14 kHz MAS (a) and 20 kHz MAS (b and c)) z-filtered 3QMAS spectra of (a) $MgAl_2O_4$, (b) $CoAl_2O_4$ and (c) Co-$CoAl_2O_4$. A shearing transformation has been applied to all spectra. Resonances corresponding to Al(IV) and Al(VI) species are labelled. * denotes a spinning sideband. In (a), the spectrum is the result of averaging 144 transients separated by a recycle interval of 1 s, for each of 50 t_1 increments of 35.71 μs. Excitation and conversion pulses were applied with $\nu_1 \approx$ 87 kHz and the CT selective pulse with $\nu_1 \approx 7$ kHz. In (b) and (c), spectra are the result of averaging 48 transients separated by a recycle interval of 5 s, for each of 115 (b) or 100 (c) t_1 increments of 25 μs. Excitation and conversion pulses were applied with ν_1 ≈ 91 kHz and the CT selective pulse with $\nu_1 \approx 6$ kHz. In (a), the spectrum shown was processed with 100 Hz Lorentzian broadening in both the direct and indirect dimensions. In (b), the spectrum shown was processed with 25 Hz Lorentzian broadening in the direct dimension. In (c), the spectrum shown was processed with 100 Hz Lorentzian broadening in the direct dimension.

Figure 5.19. ^{1}H-^{27}Al (9.4 T, 14 kHz MAS, $\tau_{CP} = 0.8$ ms) CP NMR spectra of $MgAl_2O_4$ (blue) and $CoAl_2O_4$ (red). Spectra are the result of averaging 4096 ($MgAl_2O_4$ (blue)) or 10240 transients ($CoAl_2O_4$ (red)) separated by a recycle interval of 1 ($MgAl_2O_4$ (blue)) or 0.5 s ($CoAl_2O_4$ (red)). The contact pulse was implemented using a ramped pulse (90-100%) applied to ^{1}H. ^{1}H decoupling was carried out using continuous wave decoupling with $\nu_1 \approx 91$ ($MgAl_2O_4$ (blue)) or 52 kHz ($CoAl_2O_4$ (red)).

Chapter 6

Spectra were acquired using $\nu_1 \approx$ ~90-100 kHz for ^{1}H, ~110 kHz for ^{27}Al, and ~80 kHz for ^{29}Si, unless otherwise indicated. ^{29}Si spectra were acquired using either single pulse excitation (DP), DEPTH[19] pulse sequences, or cross polarisation (CP). ^{1}H spectra were acquired using the DEPTH pulse sequence for probe background suppression.[19] For CP spectra, transverse magnetisation was obtained from ^{1}H using a using a ramped

contact pulse (90-100% or 80-100%) applied to ^{1}H. TPPM-15[3] ($\nu_1 \approx$ 90-100 kHz), SPINAL-64[7] ($\nu_1 \approx$ 90-100 kHz) or continuous wave ^{1}H decoupling ($\nu_1 \approx$ 50 kHz) was applied during acquisition. All DP and CP experiments were carried out at room temperature (298 K) on samples with no radical added, while DNP experiments were carried out at low temperature (100 K) on samples impregnated with the nitroxide biradical polarising agent TEKPol, as outlined in Chapter 4.

Figure 6.2. ^{29}Si and ^{1}H-^{29}Si (9.4 T, 10-14 kHz MAS) NMR spectra of 99% ^{29}Si-enriched Si-γ-Al_2O_3 (1.5 wt% Si), acquired using DP (black), CP (red) and DNP (blue). Spectra are shown (a) stacked and (b) overlaid. DP and CP spectra were acquired at room temperature on samples that had no radical added. The DNP spectrum was performed at 100 K. For CP and DNP spectra, τ_{CP} = 3 ms. In (b), spectral intensities have been normalised with respect to the centre of the lineshape in the DP NMR spectrum. For the DNP NMR spectrum, ε ^{29}Si CP = ~92. Spectra are the result of averaging 504 (DP), 14400 (CP), and 32 (DNP) transients with recycle intervals of 120 (DP), 1 (CP), and 3 s (DNP).

Figure 6.3. ^{1}H-^{29}Si (9.4 T, 10 kHz MAS) CP NMR spectra of 99% ^{29}Si-enriched Si-γ-Al_2O_3 (1.5 wt% Si) overlaid, acquired by averaging 14400 transients separated by a recycle interval of 1 s, using τ_{CP} values between 0.1 and 10 ms. Spectral intensities have been normalised with respect to the centre of the lineshape.

Figure 6.4. ^{1}H (9.4 T, 14 kHz MAS) NMR spectra of (a) hydrated and (b) dehydrated ^{29}Si-enriched Si-γ-Al_2O_3 (1.5 wt% Si). Spectra are the result of averaging 4000 transients separated by a recycle interval of 1 s.

Figure 6.5. (a) Comparison of ^{1}H-^{29}Si (9.4 T, 10 kHz MAS, τ_{CP} = 3 ms) CP NMR spectra of hydrated (black) and dehydrated (red) 99% ^{29}Si-enriched Si-γ-Al_2O_3 (1.5 wt% Si). Spectral intensities have been normalised with respect to the centre of the lineshape in the spectrum of the hydrated material. Spectra are the result of averaging 14400 (hydrated) and 34000 (dehydrated) transients separated by a recycle interval of 1 s. (b) ^{29}Si (9.4 T, 10-14 kHz MAS) NMR spectra of dehydrated ^{29}Si-enriched Si-γ-

Al_2O_3 (1.5 wt% Si), acquired directly (blue) and using CP (red). Spectra are the result of averaging 2896 (DP) and 34000 (CP) transients with recycle intervals of 120 s (DP) and 1 s (CP). For the CP MAS NMR spectrum, polarisation transfer (from ^1H) was achieved using a τ_{CP} value of 3 ms. Spectral intensities have been normalised with respect to the centre of the lineshape in the DP NMR spectrum.

Figure 6.6. ^{29}Si (9.4 T, 14 kHz MAS) DP NMR spectra of hydrated (blue) and dehydrated (red) ^{29}Si-enriched Si-γ-Al_2O_3 (1.5 wt% Si). Spectral intensities have been normalised with respect to the centre of the lineshape in the spectrum of the hydrated material. Spectra are the result of averaging 504 (hydrated) and 2896 (dehydrated) transients with a recycle interval of 120 s.

Figure 6.7. ^1H-^{29}Si (9.4 T, 10 kHz MAS, τ_{CP} = 0.5 or 3 ms) CP HETCOR NMR spectra of ^{29}Si-enriched Si-γ-Al_2O_3 (1.5 wt% Si), demonstrating the effect of (a) the hydration level of the sample and (b) τ_{CP} on the dehydrated material. In (a), the spectrum of the hydrated material is the result of averaging 880 transients separated by a recycle interval of 1 s, for each of 20 t_1 increments of 100 μs. The spectrum of the dehydrated material is the result of averaging 1600 transients separated by a recycle interval of 1 s, for each of 18 t_1 increments of 50 μs. A CP contact time of 0.5 ms was employed in both instances. In (b), both spectra were acquired by averaging 1600 transients separated by a recycle interval of 1 s, for each of 18 t_1 increments of 50 μs.

Figure 6.8. ^{29}Si (9.4 T, 12.5 kHz MAS) refocused CP INADEQUATE[5] DNP NMR spectra of ^{29}Si-enriched Si-γ-Al_2O_3 (1.5 wt% Si), acquired using τ_J values of (a) 3.2 ms, (b) 6.4 ms, (c) 9.6 ms and (d) 16 ms. The solid grey line in each spectrum denotes the $\delta_{DQ} = 2\delta_{SQ}$ autocorrelation diagonal. Spectra are the result of averaging between 96 and 256 transients with a recycle interval of 3 s, for each of 48 t_1 increments of 80 μs. The CP contact time, τ_{CP} = 3 ms.

Figure 6.9. Overlay of δ_2 projections of two-dimensional refocused INADEQUATE[5] DNP NMR spectra, shown in Figure 6.8, as a function of τ_J. The ^1H-^{29}Si CP DNP NMR spectrum is also shown for comparison (τ_{CP} = 3 ms) (orange).

Figure 6.10. ^{29}Si-^{27}Al (9.4 T, 10 kHz MAS) dipolar CP INEPT[24] DNP NMR spectrum of hydrated ^{29}Si-enriched Si-γ-Al_2O_3 (1.5 wt% Si). The spectrum is the result of averaging 48 transients separated by a recycle interval of 2 s for each of 32 t_1 increments of 100 μs. Recoupling of the dipolar interaction was carried out using 4 REDOR[23] blocks of 8 rotor cycles (of 100 μs) in duration. Polarisation transfer was achieved using a τ_{CP} value of 3 ms.

Figure 6.11. ^{27}Al (14 kHz MAS) spectra of 99% ^{29}Si-enriched Si-γ-Al_2O_3 (1.5 wt% Si), acquired at (a, b) 9.4 T and (c, d) 14.1 T, with (a, c) DP and (b, d) CP (τ_{CP} = 0.8 ms). * denotes a spinning sideband. Spectra are the result of averaging (a, c) 128 and (b, d) 8192 transients with recycle intervals of 3 s (DP) and 1 s (CP).

Figure 6.12. ^{29}Si-^{27}Al (9.4 T, 10 kHz MAS) scalar CP INEPT[25] DNP NMR spectrum of hydrated ^{29}Si-enriched Si-γ-Al_2O_3 (1.5 wt% Si). The spectrum is the result of averaging 224 transients separated by a recycle interval of 2 s for each of 32 t_1 increments of 100 μs. τ_J = 6 ms.

Figure 6.13. (a) ^{29}Si (9.4 T, 14 kHz MAS) experimental (blue) and simulated (red) NMR spectra of hydrated ^{29}Si-enriched Si-γ-Al_2O_3 (1.5 wt% Si). Also shown are the individual components of the fit (green). The experimental spectrum is the result of averaging 504 transients separated by a recycle interval of 120 s. (b) Simplified structural representations of the species assigned to each of the components shown in (a).

Figure 6.14. (a) ^{1}H-^{29}Si (9.4 T, 10 kHz MAS) CP NMR spectra of ^{29}Si-enriched Si-γ-Al_2O_3 (1.5 wt% Si) and Si-γ-Al_2O_3 materials prepared by a sequential grafting approach. (b) ^{1}H-^{29}Si (9.4 T, 10 kHz MAS) CP NMR spectra of Si-γ-Al_2O_3 2nd graft (2.8 wt% Si) and ^{29}Si-enriched Si-γ-Al_2O_3 (~8 wt% Si) prepared by a "single shot" approach. For all spectra, τ_{CP} = 3 ms. Spectral intensities have been normalised. Spectra are the result of averaging 14400 ("1st graft" and high loading), 76600 (2nd and 3rd graft) or 54000 (4th graft) transients separated by a recycle interval of 1 s.

Figure 6.15. ^{29}Si (9.4 T, 14 kHz MAS) DP NMR (blue) and ^{1}H-^{29}Si (9.4 T, 10 kHz MAS, τ_{CP} = 3 ms) CP NMR (red) spectra of (a) 2nd, (b) 3rd and (c) 4th graft Si-γ-Al_2O_3 materials. Spectral intensities have been normalised. DP NMR spectra are the result of averaging (a) 2840, (b) 1608 or (c) 2128 transients separated by a recycle interval of 120 s. CP NMR spectra are the result of averaging (a) 76600, (b) 76600 or (c) 54000 transients separated by a recycle interval of 1 s.

Figure 6.16. ^{29}Si (9.4 T, 14 kHz MAS) DP NMR and ^{1}H-^{29}Si (9.4 T, 10 kHz MAS, τ_{CP} = 0.5-10 ms) CP NMR spectra of "single shot" ^{29}Si-enriched Si-γ-Al_2O_3 (~8 wt% Si). Spectral intensities have been normalised. The DP NMR spectrum is the result of averaging 504 transients separated by a recycle interval of 120 s. CP NMR spectra are the result of averaging 14400 (0.5, 1.5 and 3 ms) or 3200 transients (10 ms), separated by a recycle interval of 1 s.

Figure 6.19. ^{27}Al (14.1 T, 20 kHz MAS) DP NMR spectra of γ-Al_2O_3, Si-γ-Al_2O_3 materials prepared by a sequential grafting approach, and Si-γ-Al_2O_3 (8 wt% Si) prepared via a "single shot" method. Spectra have been normalised with respect to the Al(VI) resonance. * denotes a spinning sideband. Spectra are the result of averaging 32 (high loading) or 128 transients (all others), separated by a recycle interval of 3 s.

Figure 6.20. (a) ^{1}H-^{27}Al (14.1 T, 20 kHz MAS, τ_{CP} = 0.8 ms) CP NMR spectra of γ-Al_2O_3 and Si-γ-Al_2O_3 materials prepared by a sequential grafting approach. Spectra are the result of averaging 8192 (4th graft) or 4096 (all others) transients separated by a recycle interval of 1 s. (b) ^{1}H-^{27}Al (9.4 T, 10 kHz MAS, τ_{CP} = 0.8 ms) DNP CP NMR spectra of Si-γ-Al_2O_3 2nd graft, 3rd graft and high loading materials. Spectra are the result of averaging 32 transients separated by a recycle interval of 3 s. In both (a) and (b), Spectra have been normalised with respect to the Al(VI) resonance. * denotes a spinning sideband.

Figure 6.21. ^{29}Si (9.4 T, 12.5 kHz MAS) refocused CP INADEQUATE DNP NMR spectra of ^{29}Si-enriched Si-γ-Al_2O_3 (8 wt% Si), acquired using τ_J values of (a) 3.2 ms,

(b) 6.4 ms, (c) 9.6 ms and (d) 16 ms. The solid grey line in each spectrum denotes the $\delta_{DQ} = 2\delta_{SQ}$ autocorrelation diagonal. Spectra are the result of averaging (a) 128 transients for each of 48 t_1 increments separated by a recycle interval of 3 s, (b), (c) and (d) 96 transients for each of 48 t_1 increments separated by a recycle interval of 3 s.

Figure 6.22. Overlay of δ_2 projections of two-dimensional refocused INADEQUATE DNP NMR spectra, shown in Figure 6.21, as a function of τ_J. The ^{1}H-^{29}Si CP DNP NMR spectrum is also shown for comparison (τ_{CP} = 3 ms) (cyan), and was acquired by averaging 32 transients separated by a recycle interval of 3 s.

Figure 6.23. ^{29}Si-^{27}Al (9.4 T, 10 kHz MAS) CP INEPT DNP NMR spectrum of ^{29}Si-enriched high silica loading Si-γ-Al_2O_3 (8 wt% Si), with transfer *via* the (a) dipolar[24] and (b) scalar coupling.[25] In (a), the spectrum is the result of averaging 48 transients with a recycle interval of 3 s, for each of 80 t_1 increments of 100 μs. Recoupling of the dipolar interaction was carried out using 4 REDOR[23] blocks of 8 rotor cycles (of 100 μs) in duration. In (b), the spectrum is the result of averaging 48 transients with a recycle interval of 3 s, for each of 30 t_1 increments of 100 μs. τ_J = 6 ms. In both experiments the CP contact time, τ_{CP} = 3 ms.

Figure 6.24. ^{1}H (9.4 T, 10 kHz MAS) NMR spectra of as-made high silica loading Si-γ-Al_2O_3 (8 wt% Si) acquired (a) directly after synthesis and after ageing for (b) ~2 weeks, (c) ~1 year and (d) ~1 year and 1 month. ♦ denotes a peak from the rotor cap.[21] In (b) an expansion of the spectrum is also shown inset. Spectra are the result of averaging 16 transients separated by a recycle interval of 5 s.

Figure 6.25. ^{1}H-^{13}C (9.4 T, 10 kHz MAS,τ_{CP} = 3 ms) CP NMR spectra of as-made high silica loading Si-γ-Al_2O_3 (8 wt% Si) acquired after ageing for (a) ~2 weeks and (b) ~1 year. The same experimental parameters were used to acquire both spectra. Spectra are the result of averaging 1600 transients separated by a recycle interval of 5 s. The contact pulse was implemented using a ramped pulse (90-100%) applied to ^{1}H. ^{1}H decoupling was carried out using TPPM-15 decoupling[3] with $\nu_1 \approx 100$ kHz.

Figure 6.26. ^{29}Si (9.4 T, 14 kHz MAS) DP NMR (black) and ^{1}H-^{29}Si (9.4 T, 10 kHz MAS,τ_{CP} = 3 ms) CP NMR spectra (red) of as-made ^{29}Si-enriched high silica loading Si-γ-Al_2O_3 (8 wt% Si). Spectra were acquired (a) directly after synthesis and after ageing for (b) ~2 weeks, (c) ~1 year and (d) ~1 year and 1 month. In (a) an expansion of part of the spectrum is shown inset. DP NMR spectra were acquired by averaging (a) 504, (b) 470, and (c) and (d) 40 transients separated by a recycle interval of 120 s. CP NMR spectra were acquired by averaging (a) 3200, (b) 800 and (c) and (d) 400 transients separated by a recycle interval of 5 s.

Figure 6.27. (a) ^{29}Si (9.4 T, 14 kHz MAS) DP (black) and CP (red) NMR spectra of as-made high silica loading Si-γ-Al_2O_3 (8 wt% Si) aged for ~1 year. Spectra are the result of averaging 40 transients separated by a recycle interval of 120 s (DP), or 400 transients separated by a recycle interval of 5 s (CP). (b) ^{29}Si (9.4 T, 14 kHz MAS) DP NMR spectra of as-made high silica loading Si-γ-Al_2O_3 (8 wt% Si) aged for ~1 year (blue) and calcined high silica loading Si-γ-Al_2O_3 (8 wt% Si) (green). Spectral intensities have been normalised. Spectra are the result of averaging 40 transients separated by a recycle interval of 120 s (as-made), or 504 transients separated by a recycle interval of 120 s (calcined).

Figure 6.28. ^{27}Al (14.1 T, 20 kHz MAS) short flip angle DP NMR spectra of γ-Al_2O_3 (blue), calcined high silica loading Si-γ-Al_2O_3 (8 wt% Si) (green), and as-made high silica loading Si-γ-Al_2O_3 (8 wt% Si) aged for ~1 year and 4 months (red). * denotes a spinning sideband. Spectral intensities have been normalised with respect to the Al(VI) resonance. Spectra are the result of averaging 256 transients separated by a recycle interval of 3 s, using a pulse duration of 0.2 μs with $\nu_1 \approx 91$ kHz.

Figure 6.29. ^{17}O (14.1 T, 14 kHz MAS) short flip angle DP NMR spectra of (a) γ-Al_2O_3 and (b) Si-γ-Al_2O_3 (1.5 wt% Si), ^{17}O-enriched for heating times of 12 (blue), 24 (red) and 48 h (green). Spectra have been scaled with respect to the number of transients and the mass of sample contained within each 4 mm rotor. * denotes a spinning sideband. In both (a) and (b), spectra are the result of averaging 2048

transients separated by a recycle interval of 3 s, using a pulse duration of 0.4 μs with $\nu_1 \approx 63$ kHz.

Figure 6.30. ^{17}O (20.0 T, 20 kHz MAS) DP NMR spectra of ^{17}O-enriched (a) γ-Al_2O_3, (500 °C for 24 h) (b) Si-γ-Al_2O_3 (500 °C for 24 h) and (c) amorphous SiO_2 (enriched during synthesis). * denotes a spinning sideband. In (a) and (b), spectra are the result of averaging 4096 transients separated by a recycle interval of 0.5 s, with $\nu_1 \approx 63$ kHz. In (c), the spectrum is the result of averaging 4096 transients separated by a recycle interval of 0.5 s, with $\nu_1 \approx 50$ kHz.

Figure 6.31. ^{17}O z-filtered 3QMAS NMR spectra of (a) and (c) γ-Al_2O_3, and (b) and (d) Si-γ-Al_2O_3 (1.5 wt% Si) ^{17}O-enriched at 500 °C for 24 h. Spectra were acquired at (a) and (b) 14.1 T and 14 kHz MAS, and (c) and (d) 20.0 T and 20 kHz MAS. In all spectra shearing transformations have been applied. Peak assignments are as follows: 1 = Al-O-Al (OAl_4); 2 = Al-O-Al (OAl_3); 3 = Si-O-Al; 4 = Si-O-Si. In (a), the spectrum is the result of averaging 360 transients separated by a recycle interval of 1 s, for each of 160 t_1 increments of 17.86 μs. Excitation and conversion pulses were applied with $\nu_1 \approx 63$ kHz and the CT selective pulse with $\nu_1 \approx 11$ kHz. ^1H decoupling was carried out using continuous wave decoupling with $\nu_1 \approx 55$ kHz. In (b), the spectrum is the result of averaging 816 transients separated by a recycle interval of 1 s, for each of 88 t_1 increments of 17.86 μs. Excitation and conversion pulses were applied with $\nu_1 \approx 63$ kHz and the CT selective pulse with $\nu_1 \approx 11$ kHz. The spectrum shown was processed with 50 Hz Lorentzian broadening in the direct dimension. In (c), the spectrum is the result of averaging 1128 transients separated by a recycle interval of 0.5 s, for each of 60 t_1 increments of 25 μs. Excitation and conversion pulses were applied with $\nu_1 \approx 63$ kHz and the CT selective pulse with $\nu_1 \approx 10$ kHz. The spectrum shown was processed with 100 Hz Lorentzian broadening in the direct dimension. In (d), the spectrum is the result of averaging 1320 transients separated by a recycle interval of 0.5 s, for each of 50 t_1 increments of 25 μs. Excitation and conversion pulses were applied with $\nu_1 \approx 63$ kHz and the CT selective pulse with $\nu_1 \approx 10$ kHz. The spectrum shown was processed with 50 Hz Lorentzian broadening in both the direct and indirect dimension.

Figure 6.32. ^{17}O (14.1 T, 14 kHz MAS) z-filtered 3QMAS NMR spectrum of ^{17}O-enriched amorphous SiO_2. A shearing transformation has been applied. The spectrum is the result of averaging 576 transients separated by a recycle interval of 1 s, for each of 120 t_1 increments of 17.86 μs. Excitation and conversion pulses were applied with $\nu_1 \approx 63$ kHz and the CT selective pulse with $\nu_1 \approx 11$ kHz.

Figure 6.33. ^{1}H-^{17}O (14.1 T, 14 kHz MAS) CP NMR spectra of ^{17}O-enriched amorphous SiO_2, (pink), γ-Al_2O_3 (500 °C for 12 h) (green) and Si-γ-Al_2O_3 (1.5 wt% Si) (500 °C for 12 h) (blue). τ_{CP} = 0.4 (blue) or 0.5 ms (pink and green). Spectra are the result of averaging 8192 (amorphous SiO_2), 2048 (γ-Al_2O_3) or 4096 (Si-γ-Al_2O_3 (1.5 wt% Si)) transients separated by a recycle interval of 1 (amorphous SiO_2) or 0.5 s (γ-Al_2O_3 and Si-γ-Al_2O_3 (1.5 wt% Si)). For all spectra, transverse magnetisation was obtained from ^{1}H using a using a ramped contact pulse (90-100%) applied to ^{1}H. ^{1}H decoupling was carried out using continuous wave decoupling with $\nu_1 \approx 55$ kHz.

Figure 6.34. ^{1}H-^{17}O (14.1 T, 20 and 14 kHz MAS) CP HETCOR NMR spectra of (a) ^{17}O-enriched γ-Al_2O_3 (500 °C for 12 h) (green, τ_{CP} = 0.5 ms) and (b) ^{17}O-enriched Si-γ-Al_2O_3 (1.5 wt% Si) (500 °C for 12 h) (blue, τ_{CP} = 0.4 ms). In (a), the spectrum is the result of averaging 800 transients separated by a recycle interval of 0.5 s, for each of 20 t_1 increments of 50 μs. Transverse magnetisation was obtained from ^{1}H using a using a ramped contact pulse (90-100%) applied to ^{1}H. ^{1}H decoupling was carried out using continuous wave decoupling with $\nu_1 \approx 100$ kHz. In (b), the spectrum is the result of averaging 944 transients separated by a recycle interval of 1 s, for each of 50 t_1 increments of 17.86 μs. Transverse magnetisation was obtained from ^{1}H using a using a ramped contact pulse (90-100%) applied to ^{1}H. ^{1}H decoupling was carried out using continuous wave decoupling with $\nu_1 \approx 65$ kHz.

Figure 6.35. ^{17}O (14.1 T, 14 kHz MAS) (a) DP NMR and (b) z-filtered 3QMAS NMR spectra of Si-γ-Al_2O_3 (1.5 wt% Si), ^{17}O-enriched for 12 h at temperatures of 500 (blue) and 700 °C (red). In (b), a shearing transformation has been applied to both spectra. In (a), spectra have been normalised, and * denotes a spinning sideband. In (a) the DP NMR spectra are the result of averaging 128 transients separated by a recycle interval

of 3 s. The spectra shown were processed with 50 Hz Lorentzian broadening. In (b) the spectrum in blue was obtained by averaging 1032 transients separated by a recycle interval of 2 s, for each of 118 t_1 increments of 17.86 μs. Excitation and conversion pulses were applied with $\nu_1 \approx 63$ kHz and the CT selective pulse with $\nu_1 \approx 10$ kHz. The spectrum in red was obtained by averaging 264 transients separated by a recycle interval of 3 s, for each of 82 t_1 increments of 17.86 μs. Excitation and conversion pulses were applied with $\nu_1 \approx 63$ kHz and the CT selective pulse with $\nu_1 \approx 10$ kHz.

Figure 6.36. (a) ^{29}Si (9.4 T, 14 kHz MAS) DP NMR and (b) ^{1}H-^{29}Si (9.4 T, 10 kHz MAS, τ_{CP} = 0.5 ms) CP HETCOR NMR spectra of ^{29}Si-enriched Si-γ-Al_2O_3 (1.5 wt% Si) before (black) and after (red) ^{17}O gas exchange enrichment at 500 °C for 24 h. In (a) spectra have been normalised. In (a), the spectrum in black was obtained by averaging 504 transients separated by a recycle interval of 120 s, and the spectrum in red was obtained by averaging 496 transients separated by a recycle interval of 120 s. In (b), the spectrum in red was obtained by averaging 1576 transients separated by a recycle interval of 1 s, for each of 34 t_1 increments of 100 μs. The spectrum in red was obtained by averaging 880 transients separated by a recycle interval of 1 s, for each of 20 t_1 increments of 100 μs.

Figure 6.37. ^{1}H-^{29}Si (9.4 T, 10 kHz MAS) CP NMR spectra of (a) dehydrated ^{29}Si-enriched Si-γ-Al_2O_3 (1.5 wt% Si) (τ_{CP} = 1.5 ms) and (b) hydrated ^{29}Si- and ^{17}O-enriched Si-γ-Al_2O_3 (1.5 wt% Si) (500 °C for 24 h) (τ_{CP} = 0.1, 1.5, or 10 ms). In (b) spectra have been normalised. The spectrum was obtained by averaging 14400 (1.5 ms) or 18000 transients (0.1 and 10 ms) separated by a recycle interval of 1 s.

Figure 6.38. ^{1}H (9.4 T, 10 kHz MAS) NMR spectra of (a) partially dehydrated ^{29}Si-enriched Si-γ-Al_2O_3 (1.5 wt% Si) and (b) hydrated ^{29}Si- and ^{17}O-enriched Si-γ-Al_2O_3 (1.5 wt% Si) (^{17}O-enriched at 500 °C for 24 h). In (b), ♦ denotes a peak from the rotor cap.[21] In (a), the spectrum is the result of averaging 4000 transients separated by a recycle interval of 1 s. In (b), the spectrum is the result of averaging 128 transients separated by a recycle interval of 1 s.

Figure 6.39. ^{17}O (20.0 T, 20 kHz MAS) DP NMR spectra of ^{17}O-enriched (a) γ-Al_2O_3, (500 °C for 24 h) (b) Si-γ-Al_2O_3 (500 °C for 24 h) and (c) doubly-enriched (^{29}Si and ^{17}O) Si-γ-Al_2O_3 (^{17}O-enriched at 500 °C for 24 h). * denotes a spinning sideband. Spectra are the result of averaging 4096 transients separated by a recycle interval of 0.5 s, with $\nu_1 \approx 63$ (a) and (b) or 50 kHz (c).

Figure 6.40. ^{17}O (14.1 T, 14 kHz MAS) z-filtered 3QMAS NMR spectrum of doubly-enriched (^{29}Si and ^{17}O) Si-γ-Al_2O_3 (1.5 wt% Si) (500 °C for 24 h). A shearing transformation has been applied. Peak assignments are as follows: 1 = Al-O-Al (OAl_4); 2 = Al-O-Al (OAl_3); 3 = Si-O-Al; 4 = Si-O-Si. The spectrum was obtained by averaging 504 transients separated by a recycle interval of 1 s, for each of 100 t_1 increments of 17.86 μs. Excitation and conversion pulses were applied with $\nu_1 \approx 70$ kHz and the CT selective pulse with $\nu_1 \approx 9$ kHz.

Figure 6.41. ^{29}Si-^{17}O (20.0 T, 20 kHz MAS) D-HMQC spectra of doubly enriched (^{29}Si and ^{17}O) Si-γ-Al_2O_3 (^{17}O-enriched at 500 °C for 24 h), acquired with (a) τ_{rec} = 0.6 ms, (b) τ_{rec} = 1.2 ms and (c) τ_{rec} = 1.8 ms. In (a), the spectrum was obtained by averaging 10240 transients separated by a recycle interval of 0.5 s, for each of 8 t_1 increments of 50 μs. In (b), the spectrum was obtained by averaging 19200 transients separated by a recycle interval of 0.5 s, for each of 8 t_1 increments of 50 μs. In (c), the spectrum was obtained by averaging 12352 transients separated by a recycle interval of 0.5 s, for each of 12 t_1 increments of 50 μs. In all experiments, active recoupling of the ^{29}Si-^{17}O dipolar interaction was achieved using the $SR4^2_1$ scheme,[18] with $\nu_1 \approx 2\nu_R$. All spectra shown were processed with 300 Hz Lorentzian broadening in the direct (^{17}O) dimension.

Figure 6.43. ^{17}O (20.0 T, 20 kHz MAS) DP NMR spectra of ^{17}O-enriched (a) Si-γ-Al_2O_3 4th graft (5.2 wt% Si) (700 °C for 12 h) (b) Si-γ-Al_2O_3 (500 °C for 24 h) and (c) amorphous SiO_2 (^{17}O-enriched during synthesis). * denotes a spinning sideband. Spectra are the result of averaging 4096 transients separated by a recycle interval of 0.5 s, with $\nu_1 \approx 63$ (a) and (b) or 50 kHz (c).

Figure 6.44. ^{17}O z-filtered 3QMAS NMR spectra of Si-γ-Al_2O_3 (1.5 wt% Si) (^{17}O-enriched at 500 °C for 24 h) (black), Si-γ-Al_2O_3 4th graft (5.2 wt% Si) (^{17}O-enriched at 700 °C for 12 h) (blue) and ^{17}O-enriched amorphous SiO_2, (pink). Spectra were acquired at (a) 20.0 T and 20 kHz MAS and (b) 14.1 T and 14 kHz MAS. A shearing transformation has been applied in all spectra. In (a), the black spectrum is the result of averaging 1320 transients separated by a recycle interval of 0.5 s, for each of 50 t_1 increments of 25 μs. Excitation and conversion pulses were applied with $\nu_1 \approx 63$ kHz and the CT selective pulse with $\nu_1 \approx 10$ kHz. The spectrum shown was processed with 50 Hz Lorentzian broadening in both the direct and indirect dimension. The blue spectrum is the result of averaging 1128 transients separated by a recycle interval of 0.5 s, for each of 60 t_1 increments of 25 μs. Excitation and conversion pulses were applied with $\nu_1 \approx 63$ kHz and the CT selective pulse with $\nu_1 \approx 10$ kHz. In (b), The blue spectrum is the result of averaging 3456 transients separated by a recycle interval of 0.5 s, for each of 80 t_1 increments of 17.86 μs. The pink spectrum is the result of averaging 576 transients separated by a recycle interval of 1 s, for each of 120 t_1 increments of 17.86 μs. For both spectra, excitation and conversion pulses were applied with $\nu_1 \approx 63$ kHz and the CT selective pulse with $\nu_1 \approx 11$ kHz.

Figure 6.45. ^{1}H (14.1 T, 20 kHz MAS) NMR spectra of γ-Al_2O_3 (blue), Ti-γ-Al_2O_3 (red) and Ti-Al M50 (green). ♦ denotes a peak from the rotor cap.[21] Spectra were obtained by averaging 16 transients separated by a recycle interval of 0.5 s.

Figure 6.46. (a) ^{27}Al (14.1 T, 20 kHz MAS) DP NMR spectra and (b) ^{1}H-^{27}Al (14.1 T, 14 kHz MAS, τ_{CP} = 0.8 ms) CP NMR spectra of of γ-Al_2O_3 (blue), Ti-γ-Al_2O_3 (red) and Ti-Al M50 (green). In (b) spectra have been normalised with respect to the Al(VI) resonance. * denotes a spinning sideband. In (a), spectra were obtained by averaging 512 transients separated by a recycle interval of 3 s. In (b), spectra were obtained by averaging 4096 (γ-Al_2O_3 (blue)) or 8192 (Ti-γ-Al_2O_3 (red) and Ti-Al M50 (green)) transients separated by a recycle interval of 1 s.

Figure 6.47. ^{1}H-^{27}Al (9.4 T, 14 kHz MAS) D-HQMC 1D NMR spectra of (a) Ti-γ-Al_2O_3 and (b) Ti-Al M50, acquired using τ_{rec} = 0.43 (blue), 0.86 (red) or 1.72 ms (green). In both (a) and (b) spectra have been scaled with respect to the number of

transients averaged in each experiment. In (a), spectra are the result of averaging 17280 (0.43 ms) or 20736 transients (0.86 and 1.72 ms) separated by a recycle interval of 1 s. In (b), spectra are the result of averaging 20736 transients separated by a recycle interval of 1 s. In all experiments, active recoupling of the ^{1}H-^{27}Al dipolar interaction was achieved using the $SR4^2_1$ scheme,[18] with $\nu_1 \approx 2\nu_R$.

Figure 6.48. ^{1}H-^{27}Al (14.1 T, 40 kHz MAS) D-HMQC spectra of (a) Ti-γ-Al_2O_3, and (b) Ti-Al M50, acquired with τ_{rec} = 0.3 ms. (c) Schematic representations of the functional groups observed in the spectra shown in (a) and (b), along with corresponding ^{1}H δ_{iso} values. In (a), the spectrum is the result of averaging 2432 transients separated by a recycle interval of 1 s, for each of 18 t_1 increments of 50 μs. In (b), the spectrum is the result of averaging 2560 transients separated by a recycle interval of 1 s, for each of 20 t_1 increments of 50 μs. In both experiments, active recoupling of the ^{1}H-^{27}Al dipolar interaction was achieved using the $SR4^2_1$ scheme,[18] with $\nu_1 \approx 2\nu_R$.

Figure 6.49. (a) ^{27}Al (14.1 T, 14 kHz MAS) z-filtered 3QMAS NMR spectra of γ-Al_2O_3 (blue), Ti-γ-Al_2O_3 (red) and Ti-Al M50 (green). A shearing transformation has been applied in all spectra. (b) Cross sections parallel to δ_1 extracted from the spectra shown in (a). * denotes a spinning sideband. In (a), the spectrum is the result of averaging 48 transients separated by a recycle interval of 3 s, for each of 130 t_1 increments of 25 μs. In (b) and (c), spectra are the result of averaging 48 transients separated by a recycle interval of 2 s, for each of 100 t_1 increments of 25 μs. In all experiments, excitation and conversion pulses were applied with $\nu_1 \approx 110$ kHz and the CT selective pulse with $\nu_1 \approx 9$ kHz.

Figure 6.50. ^{17}O (14.1 T, 14 kHz MAS) DP NMR spectra of (a) γ-Al_2O_3 (blue), (b) Ti-γ-Al_2O_3 (red) and (c) Ti-Al M50 (green). * denotes a spinning sideband. the spectrum is the result of averaging (a) and (b) 4096 or (c) 10000 transients separated by a recycle interval of (a) and (b) 0.5 or (c) 3 s. A spin echo pulse sequence was used with a rotor synchronised τ delay of 71.43 μs. $\nu_1 \approx 63$ kHz.

Figure 6.51. ^{17}O (14.1 T, 14 kHz MAS) DP NMR spectra of TiO_2 (anatase) (black) and Ti-Al M50 (green), ^{17}O-enriched at 500 °C for 12 h. * denotes a spinning sideband. Spectra are the result of averaging 2048 (black) or 10000 transients (green) separated by a recycle interval of 3 s. $\nu_1 \approx 63$ kHz.

Figure 6.52. ^{17}O z-filtered 3QMAS NMR spectra of γ-Al_2O_3 (blue), Ti-γ-Al_2O_3 (red) and Ti-Al M50 (green), ^{17}O-enriched at 500 °C for 12 h, acquired at (a-c) 14.1 T and 14 kHz MAS and (d) 9.4 T and 14 kHz MAS. A shearing transformation has been applied in all spectra. Peak assignments are as follows: 1 = Al-O-Al (OAl_4); 2 = Al-O-Al (OAl_3); 3 = Ti-O-Ti (OTi_3). In (a), the spectrum is the result of averaging 360 transients separated by a recycle interval of 1 s, for each of 160 t_1 increments of 17.86 μs. Excitation and conversion pulses were applied with $\nu_1 \approx 63$ kHz and the CT selective pulse with $\nu_1 \approx 11$ kHz. ^1H decoupling was carried out using continuous wave decoupling with $\nu_1 \approx 55$ kHz. In (b), the spectrum is the result of averaging 2280 transients separated by a recycle interval of 0.5 s, for each of 54 t_1 increments of 17.86 μs. Excitation and conversion pulses were applied with $\nu_1 \approx 63$ kHz and the CT selective pulse with $\nu_1 \approx 11$ kHz. In (c), the spectrum is the result of averaging 1680 transients separated by a recycle interval of 2 s, for each of 50 t_1 increments of 17.86 μs. Excitation and conversion pulses were applied with $\nu_1 \approx 63$ kHz and the CT selective pulse with $\nu_1 \approx 11$ kHz. In (d), the spectrum is the result of averaging 8400 transients separated by a recycle interval of 1 s, for each of 30 t_1 increments of 17.86 μs. Excitation and conversion pulses were applied with $\nu_1 \approx 71$ kHz and the CT selective pulse with $\nu_1 \approx 13$ kHz. The spectrum shown was processed with 100 Hz Lorentzian broadening in the direct dimension.

References

1. D. J. States, R. A. Haberkorn and D. J. Ruben, *J. Magn. Reson.*, 1982, **48**, 286.
2. D. Marion, M. Ikura, R. Tschudin and A. Bax, *J. Magn. Reson.*, 1989, **85**, 393.
3. A. E. Bennett, C. M. Rienstra, M. Auger, K. V. Lakshmi and R. G. Griffin, *J. Chem. Phys.*, 1995, **103**, 6951.
4. B. Elena, G. De Paëpe and L. Emsley, *Chem. Phys. Lett.*, 2004, **398**, 532.

5. A. Lesage, M. Bardet and L. Emsley, *J. Am. Chem. Soc.*, 1999, **121**, 10987.
6. S. Cadars, J. Sein, L. Duma, A. Lesage, T. N. Pham, J. H. Baltisberger, S. P. Brown and L. Emsley, *J. Magn. Reson.*, 2007, **188**, 24.
7. B. M. Fung, A. K. Khitrin and K. Ermolaev, *J. Magn. Reson.*, 2000, **142**, 97.
8. W. Sommer, J. Gottwald, D. E. Demco and H. W. Spiess, *J. Magn. Reson. A*, 1995, **113**, 131.
9. M. Feike, D. E. Demco, R. Graf, J. Gottwald, S. Hafner and H. W. Spiess, *J. Magn. Reson. A*, 1996, **122**, 214.
10. H. Y. Carr and E. M. Purcell, *Phys. Rev.*, 1954, **94**, 630.
11. S. Meiboom and D. Gill, *Rev. Sci. Instrum.*, 1958, **29**, 688.
12. K. K. Dey, J. T. Ash, N. M. Trease and P. J. Grandinetti, *J. Chem. Phys.*, 2010, **133**, 054501.
13. A. Wong, M. E. Smith, V. Terskikh and G. Wu, *Can. J. Chem.*, 2011, **89**, 1087.
14. J.-P. Amoureux and C. Fernandez, *Solid State Nucl. Magn. Reson.*, 1998, **10**, 211.
15. D. R. Neuville, L. Cormier and D. Massiot, *Geochim. Cosmochim. Acta*, 2004, **68**, 5071.
16. D. Massiot, F. Fayon, M. Capron, I. King, S. Le Calvé, B. Alonso, J.-O. Durand, B. Bujoli, Z. Gan and G. Hoatson, *Magn. Reson. Chem.*, 2002, **40**, 70.
17. S. E. Ashbrook and S. Wimperis, *Chem. Phys. Lett.*, 2001, **340**, 500.
18. A. Brinkmann and A. P. M. Kentgens, *J. Am. Chem. Soc.*, 2006, **128**, 14758.
19. D. G. Cory and W. M. Ritchey, *J. Magn. Reson.*, 1988, **80**, 128.
20. J. Feng and J. A. Reimer, *J. Magn. Reson.*, 2011, **209**, 300.
21. C. Jaeger and F. Hemmann, *Solid State Nucl. Magn. Reson.*, 2014, **57-58**, 22.
22. H. E. Gottlieb, V. Kotlyar and A. Nudelman, *J. Org. Chem.*, 1997, **62**, 7512.
23. T. Guillion and J. Schaefer, *J. Magn. Reson.*, 1989, **81**, 196.
24. E. De Vita and L. Frydman, *J. Magn. Reson.*, 2001, **148**, 327.
25. C. A. Fyfe, K. C. Wong-Moon, Y. Huang and H. Grondey, *J. Am. Chem. Soc.*, 1995, **117**, 10397.

Appendix B. Primary and Secondary Chemical Shift References

Unless otherwise specified, all spectra presented in this thesis were referenced relative to a primary reference compound ($\delta = 0$) using the secondary reference compounds detailed in the table below.

Table B1. *Primary and secondary chemical shift references used in this work.*[1-8]

Nucleus	Primary Reference (δ_{iso} = 0 ppm)	Secondary Reference (ppm)
^{1}H	$(CH_3)_4Si$	L-alanine: NH_3 δ_{iso} = 8.5 Adamantane: δ_{iso} = 1.9
^{13}C	$(CH_3)_4Si$	L-alanine: CH_3 δ_{iso} = 20.5
^{17}O	H_2O	-
^{27}Al	1 M $Al(NO_3)_3$ (aq)	Aluminium acetylacetonate ($Al(acac)_3$): downfield singularity $\delta = -1.1$ (14.1 T); centre of gravity $\delta = -4.2$ (9.4 T)[a]
^{29}Si	$(CH_3)_4Si$	Octakis(trimethylsiloxy)silsesquioxane **(**Q8M8): $OSi(CH_3)_3$ δ_{iso} = 11.5
^{87}Rb	1 M $RbNO_3$ (aq)[b]	RbCl (s): δ = 128[b]
^{93}Nb	Saturated solution of $NbCl_5$ in wet acetonitrile	$LiNbO_3$: downfield singularity $\delta = -1018$ (14.1 T)[c]

a. δ_{iso} = 0.0 ppm, C_Q = 3.0 MHz, η_Q = 0.16[5]
b. ^{87}Rb has been demonstrated by Skibsted and Jakobsen to have temperature-dependent NMR parameters (*i.e.*, δ_{iso}, C_Q).[7]
c. δ_{iso} = 1004.0 ppm, C_Q = 22.1 MHz, η_Q = 0.0[8]

References

21. R. K. Harris, E. D. Becker, S. M. C. de Menezes, R. Goodfellow and P. Granger, *Pure Appl. Chem.*, 2001, **73**, 1795.
22. R. K. Harris, E. D. Becker, S. M. C. de Menezes, P. Granger, R. E. Hoffman and K. W. Zilm, *Pure Appl. Chem.*, 2008, **80**, 59.
23. D. C. Apperley, R. K. Harris and P. Hodgkinson, *Solid-State NMR: Basic Principles & Practice*, Momentum Press, New York, 2012.
24. E. Lippmaa, M. Magi, A. Samoson, G. Engelhardt and A. R. Grimmer, *J. Am. Chem. Soc.*, 1980, **102**, 4889.
25. A. Wong, M. E. Smith, V. Terskikh and G. Wu, *Can. J. Chem.*, 2011, **89**, 1087.
26. J. T. Cheng, J. C. Edwards and P. D. Ellis, *J. Phys. Chem.*, 1990, **94**, 553.
27. J. Skibsted and H. J. Jakobsen, *J. Phys. Chem. A*, 1999, **103**, 7958.
28. S. Prasad, P. Zhao, J. Huang, J. J. Fitzgerald and J. S. Shore, *Solid State Nucl. Magn. Reson.*, 2001, **19**, 45.

Appendix C. Coefficients for Second-Order Quadrupolar Perturbation Theory

Table C1. *Coefficients $A^n(I,m_I)$ for nuclei with half-integer spin.*

Spin I	m_I	$A^0(I,m_I)$	$A^2(I,m_I)$	$A^4(I,m_I)$
3/2	1/2	−2/5	−8/7	54/35
	3/2	6/5	0	−6/5
5/2	1/2	−16/15	−64/21	144/35
	3/2	−4/5	−40/7	228/35
	5/2	20/3	40/21	−60/7
7/2	1/2	−30/15	−120/21	270/35
	3/2	−54/15	−96/7	606/35
	5/2	30/15	−240/21	330/35
	7/2	294/15	168/21	−966/35
9/2	1/2	−48/15	−192/21	432/35
	3/2	−108/15	−168/7	1092/35
	5/2	−60/15	−600/21	1140/35
	7/2	168/15	−336/21	168/35
	9/2	648/15	432/21	−2332/35

References

1. K. J. D. MacKenzie and M. E. Smith, *Multinuclear Solid-State NMR of Inorganic Materials*, Pergamon, Oxford, 2002.
2. S. E. Ashbrook and S. Wimperis, “Quadrupolar Coupling: An Introduction and Crystallographic Aspects”, in *NMR of Quadrupolar Nuclei in Solid Materials*, Eds. R. E. Wasylishen, S. E. Ashbrook and S. Wimperis, Wiley, Chichester, 2012.

Appendix D. Gradients for MQMAS Experiments

Table D1. *Gradients for R ($A^4(I,m_I)/A^4(I,1/2)$), $dist_{CS}$ and $dist_Q$ in an unsheared MQMAS experiment.*

Spin I	m_I	R	$dist_{CS}$	$dist_Q$
3/2	1/2			
	3/2	−7/9	3	−3
5/2	1/2			
	3/2	19/12	3	3/4
	5/2	−25/12	5	−25/4
7/2	1/2			
	3/2	101/45	3	9/5
	5/2	11/9	5	−1
	7/2	−161/45	7	49/5
9/2	1/2			
	3/2	91/36	3	9/4
	5/2	95/36	5	5/4
	7/2	7/18	7	−5/2
	9/2	−31/6	9	−15/2

Table D2. *Gradients for R ($A^4(I,m_I)/A^4(I,1/2)$), $dist_{CS}$ and $dist_Q$ in sheared z-filtered or split-t_1 experiments.*

Spin I	m_I	R	$dist_{CS}$	$dist_Q$
3/2	1/2			
	3/2	−7/9	17/8	−5/4
5/2	1/2			
	3/2	19/12	17/31	−10/31
	5/2	−25/12	85/37	−50/37
7/2	1/2			
	3/2	101/45	17/73	−10/73
	5/2	11/9	17/10	−1
	7/2	−161/45	238/103	−140/103
9/2	1/2			
	3/2	91/36	17/127	−10/127
	5/2	95/36	85/131	−50/131
	7/2	7/18	119/35	−14/5
	9/2	−31/6	85/37	−50/37

References

1. L. Frydman and J. S. Harwood, *J. Am. Chem. Soc.*, 1995, **117**, 5367.
2. J.-P. Amoureux, C. Fernandez and S. Steuernagel, *J. Magn. Reson. A*, 1996, **123**, 116.
3. S. P. Brown and S. Wimperis, *J. Magn. Reson.*, 1997, **124**, 279.
4. J.-P. Amoureux and C. Fernandez, *Solid State Nucl. Magn. Reson.*, 1998, **10**, 211.
5. K. J. Pike, R. P. Malde, S. E. Ashbrook, J. McManus and S. Wimperis, *Solid State Nucl. Magn. Reson.*, 2000, **16**, 203.
6. K. J. D. MacKenzie and M. E. Smith, *Multinuclear Solid-State NMR of Inorganic Materials*, Pergamon, Oxford, 2002.

Appendix E. Powder XRD Patterns

Powder XRD patterns shown below were acquired with PANalytical Empyrean or STOE STADIP diffractometers. PANalytical Empyrean diffractometers were operated in reflection, Bragg–Brentano, θ-2θ mode, and equipped with Cu X-ray tube, primary beam monochromator ($CuK_{\alpha 1}$, $\lambda = 1.5406$ Å) and X'celerator RTMS detector. STOE STADIP diffractometers were operated with powdered samples sealed in capillaries, in Debye–Scherrer mode, equipped with a Cu X-ray tube, primary beam monochromator ($CuK_{\alpha 1}$, $\lambda = 1.5406$ Å) and scintillation position-sensitive linear detector. 2θ ranges and scan durations are provided in figure captions. Offline processing of PXRD data was performed using Profex.[1] The assistance of Miss Giulia Bignami (St Andrews) with mounting of sample capillaries is gratefully acknowledged.

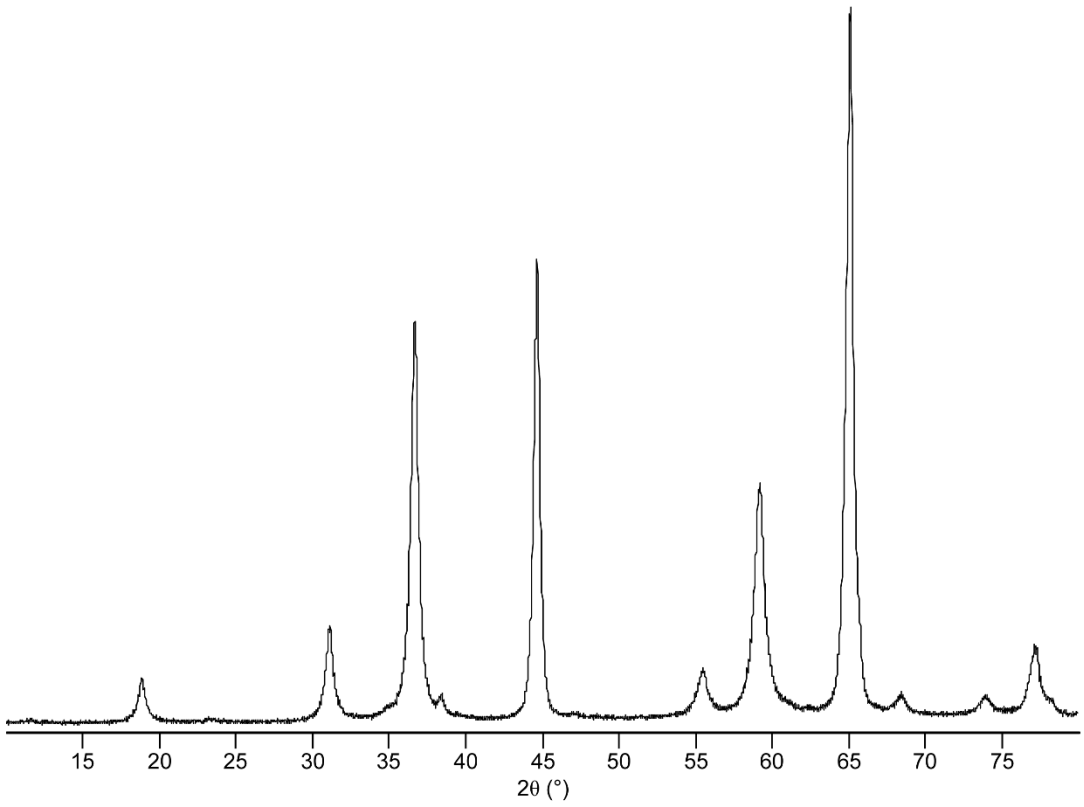

Figure E1. *PXRD pattern of commercially obtained $MgAl_2O_4$. 2θ range = 10-80° and scan duration = 1 h.*

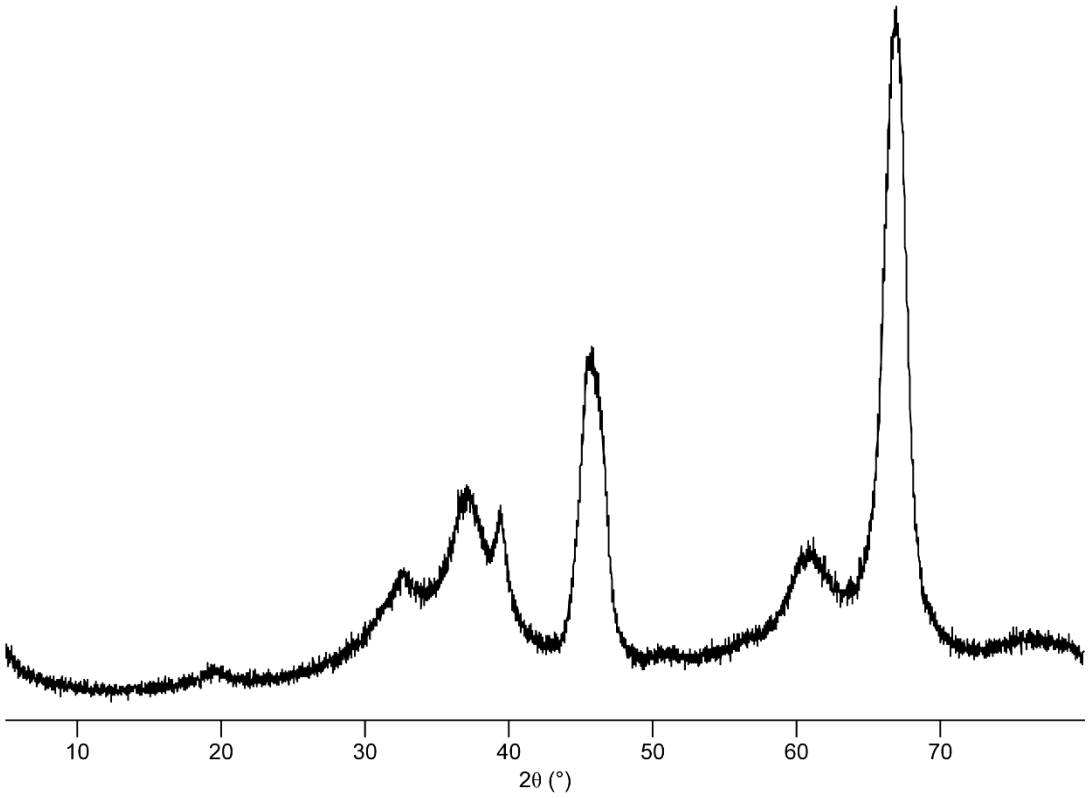

Figure E2. *PXRD pattern of commercially obtained γ-Al_2O_3. 2θ range = 5-80° and scan duration = 1 h.*

Figure E1 shows the PXRD pattern of commercially obtained $MgAl_2O_4$. Phase identity was confirmed by comparison with published data.[2,3]

Figure E2 shows the PXRD pattern of commercially obtained γ-Al_2O_3. Phase identity was verified by comparing the acquired pattern against published data.[4,5]

Figure E3 shows the PXRD pattern of commercially obtained Si-γ-Al_2O_3 (1.5 wt% Si).

Figure E4 shows the PXRD pattern of commercially obtained TiO_2. Confirmation of phase-pure anatase was obtained *via* comparison with published powder patterns of this form of TiO_2.[6,7]

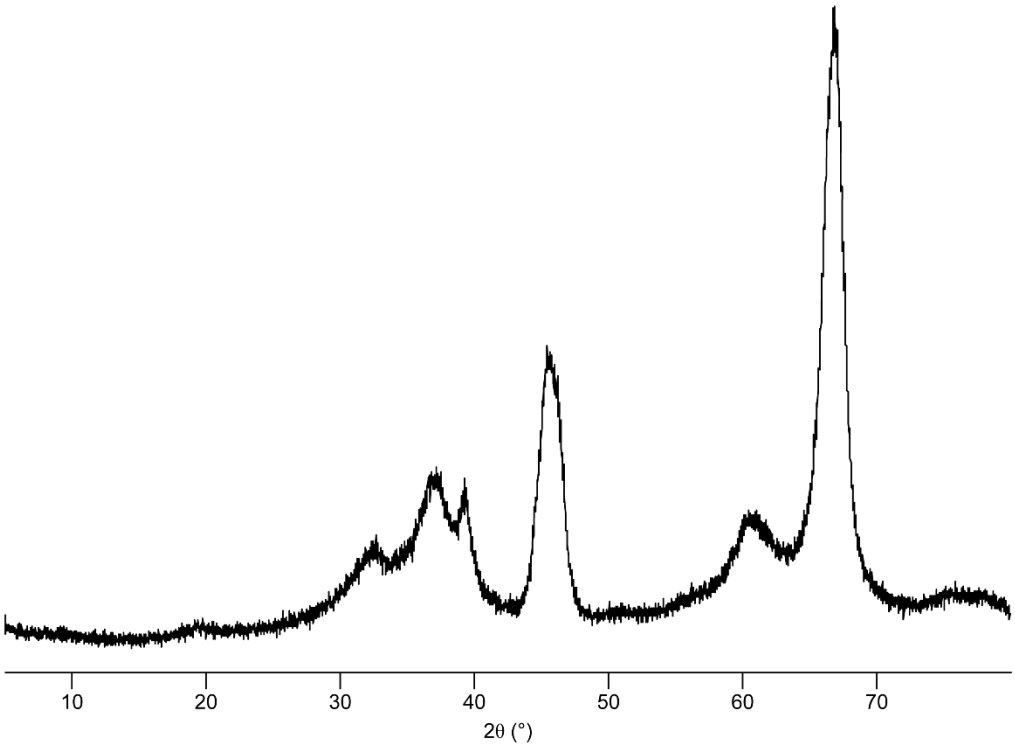

Figure E3. *PXRD pattern of commercially obtained Si-γ-Al_2O_3 (1.5 wt% Si). 2θ range = 5-80° and scan duration = 1 h.*

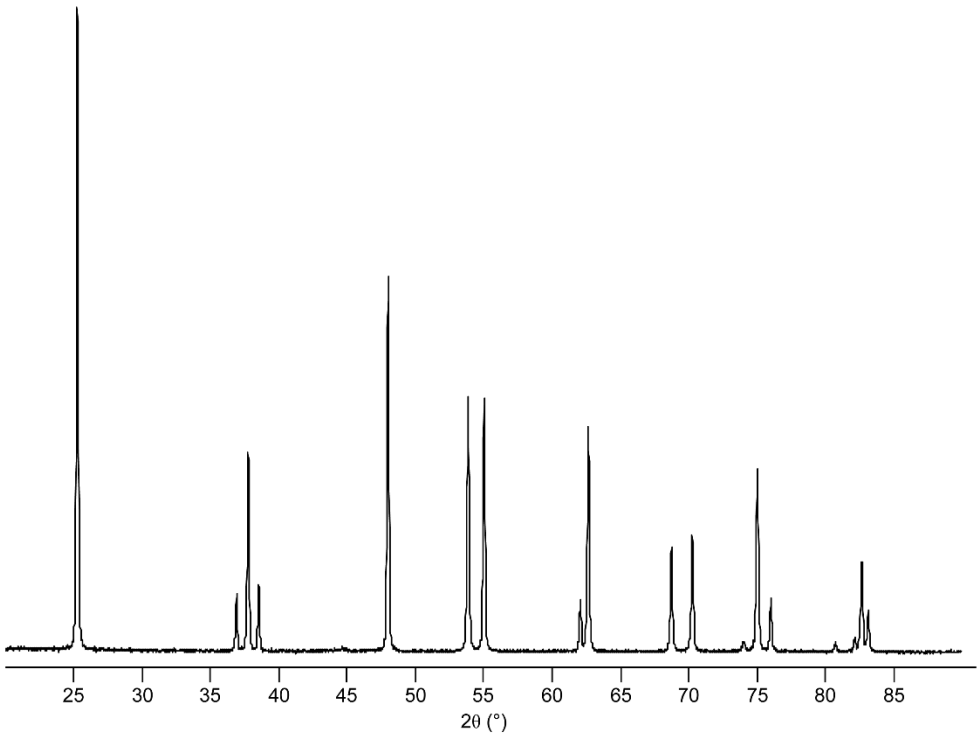

Figure E4. *PXRD pattern of commercially obtained TiO_2. 2θ range = 20-90° and scan duration = 1 h.*

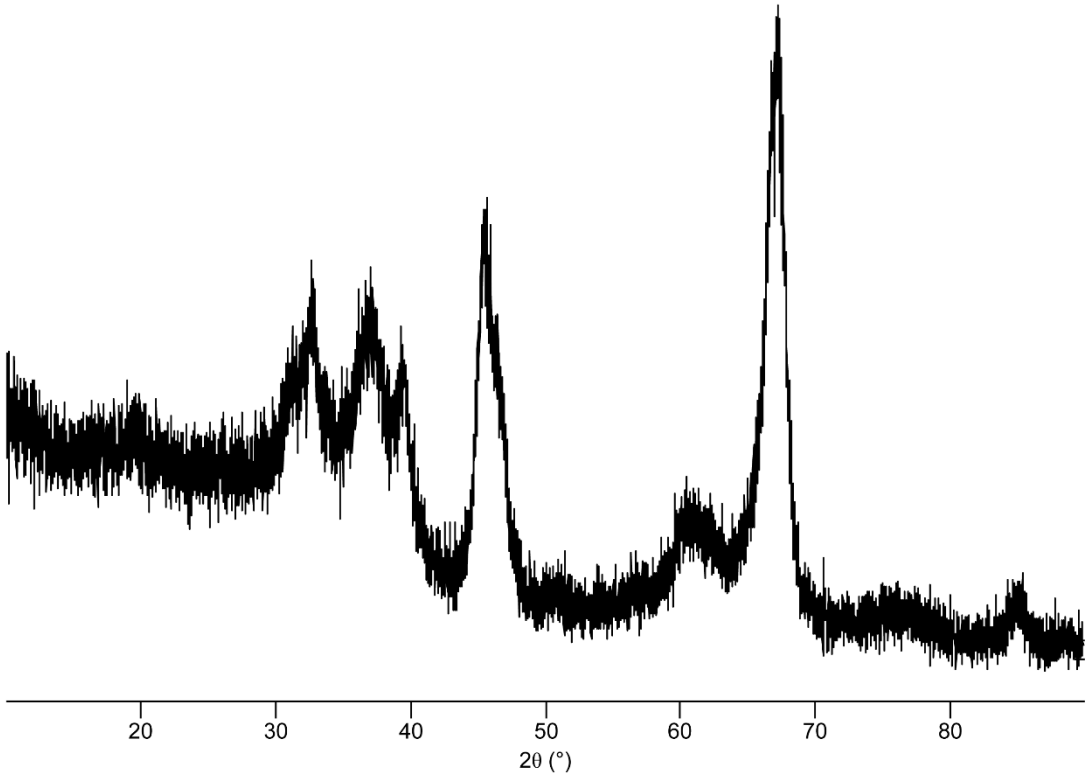

Figure E5. *PXRD pattern of Ti-γ-Al_2O_3. 2θ range = 10-90° and scan duration = overnight.*

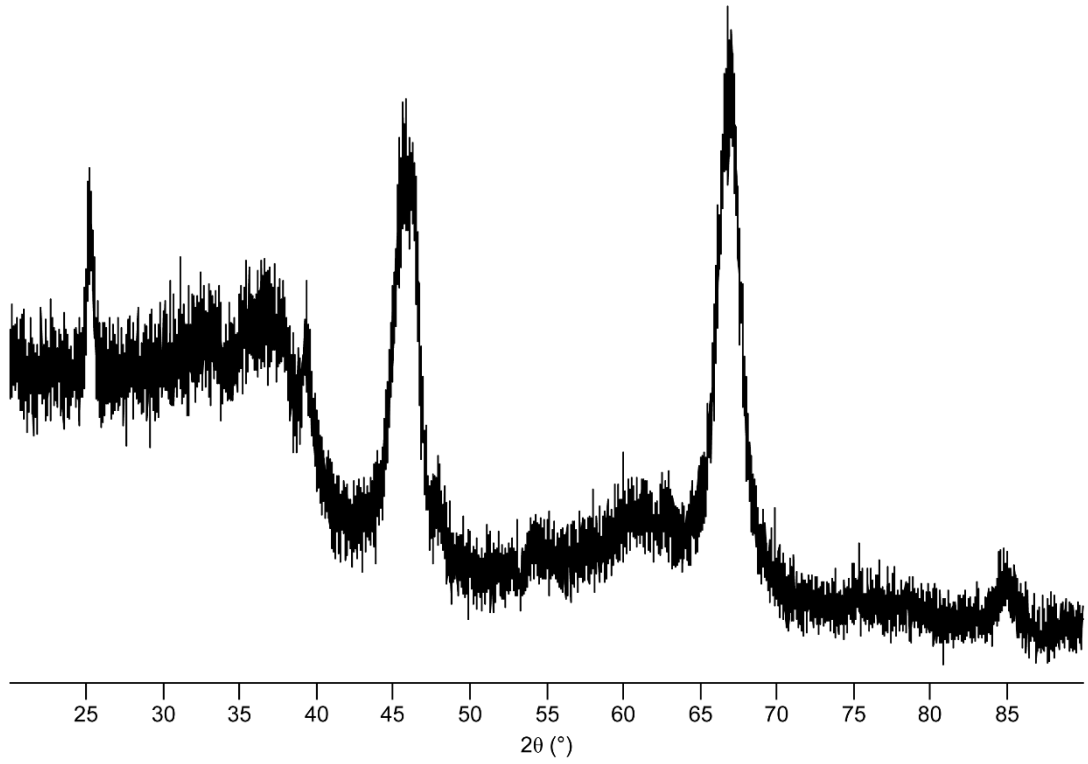

Figure E6. *PXRD pattern of Ti-Al M50. 2θ range = 20-90° and scan duration = overnight.*

Figure E5 shows the PXRD pattern of Ti-γ-Al_2O_3.

Figure E6 shows the PXRD pattern of Ti-Al M50. Comparison with published studies[4-10] and solid-state NMR data suggests that this is a two-phase solid composed of nanoparticle anatase TiO_2 and γ-Al_2O_3, as discussed in Chapter 6.

References

1. N. Doebelina and R. Kleeberg, *J. Appl. Crystallogr.*, 2015, **48**, 1573.
2. D. Dwibedi, M. Avdeev and P. Barpanda, *J. Am. Ceram. Soc.*, 2015, **98**, 2908.
3. I. Ganesh, B. Srinivas, R. Johnson, B. P. Saha and Y. R. Mahajan, *J. Eur. Ceram. Soc*., 2004, **24**, 201.
4. M. Vahtrus, M. Umalas, B. Polyakov, L. Dorogin, R. Saar, M. Tamme, K. Saal, R. Lõhmus and S. Vlassov, *Mater. Charact.*, 2015, **107**, 119.
5. V. P. Pakharukova, D. A. Yatsenko, E. Yu. Gerasimov, A. S. Shalygin, O. N. Martyanov, S. V. Tsybulya, *J. Solid State Chem.*, 2017, **246**, 284.
6. M. Rezaee, S. M. M. Khoie and K. H. Liu, *CrystEngComm*, 2011, **13**, 5055.
7. X. Sun, M. Dyballa, J. Yan, L. Li, N. Guan and M. Hunger, *Chem. Phys. Lett.*, 2014, **594**, 34.
8. D. Reyes-Coronado, G. Rodríguez-Gattorno, M. E. Espinosa-Pesqueira, C. Cab, R. de Coss and G. Oskam, *Nanotechnology*, 2008, **19**, 145605.
9. B. M. Reddy, G. K. Reddy, K. N. Rao, I. Ganesh and J. M. F. Ferreira, *J. Mater. Sci.*, 2009, **44**, 4874.
10. M. A. Ahmed and M. F. Abdel-Messih, *J. Alloys Compd.*, 2011, **509**, 2154.

Appendix F. D-HMQC Pulse Sequence

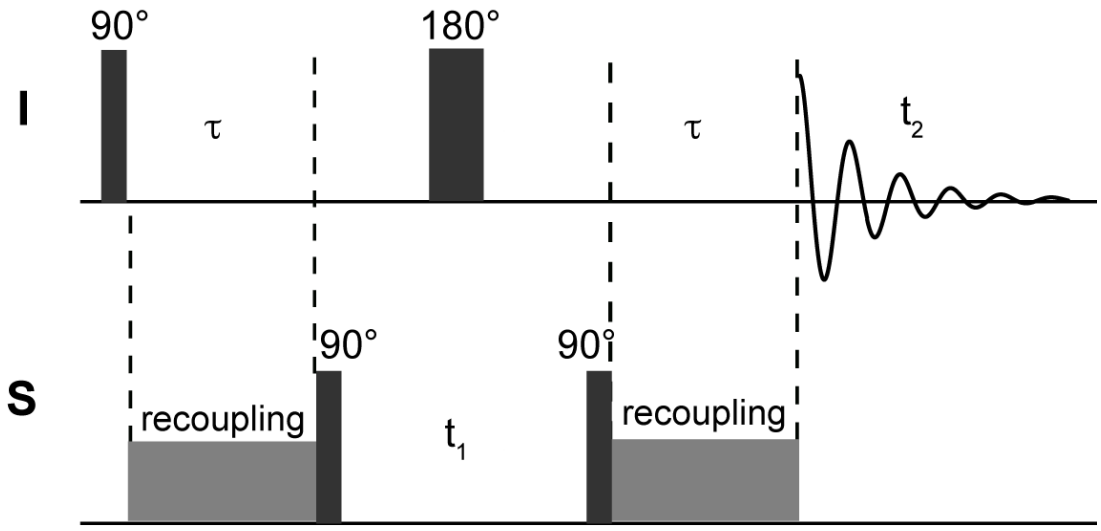

Figure F1. *Pulse sequence for the D-HMQC experiment.[1,2] In this work, the $SR4^2_1$ dipolar recoupling scheme[3] was used.*

References

1. J.-P. Amoureux, J. Trébosc, L. Delevoye, O. Lafon, B. Hu and Q. Wang, *Solid State Nucl. Magn. Reson.*, 2009, **35**, 12.
2. G. Tricot, J. Trébosc, F. Pourpoint, R. Gauvin and L. Delevoye, *Annu. Rep. NMR Spectrosc.*, 2014, **81**, 145.
3. A. Brinkmann and A. P. M. Kentgens, *J. Am. Chem. Soc.*, 2006, **128**, 14758.

Appendix G. List of Abbreviations and Symbols

1D	One-Dimensional
2D	Two-Dimensional
3D	Three-Dimensional
3QMAS	Triple-Quantum Magic Angle Spinning
ASR	Absolute Sensitivity Ratio
B	Magnetic Field
B_0	Strength of Applied Magnetic Field
B_1	Strength of Applied Pulse
BABA	Back-to-Back
BMS	Bulk Magnetic Susceptibility
CE	Cross Effect
CP	Cross Polarisation
CPMG	Carr-Purcell Meiboom-Gill
C_Q	Quadrupolar Coupling Constant
CRAMPS	Combined Rotation and Multiple-Pulse Spectroscopy
CSA	Chemical Shift Anisotropy
CT	Central Transition
CW	Continuous Wave
DAS	Dynamic Angle Spinning
DFT	Density Functional Theory
D-HMQC	Dipolar HMQC
$dist_{CS}$	Distribution of Chemical Shifts
$dist_Q$	Distribution of Quadrupolar Parameters
DME	Dimethyl Ether
DNP	Dynamic Nuclear Polarisation
DOR	Double Rotation
DP	Direct Polarisation
DQ	Double Quantum
DUMBO	Decoupling Using Mind-Boggling Optimisation
E	Energy

eDROOPY	Experimental Decoupling is Robust for Offset or Power Inhomogeneity
EFG	Electric Field Gradient
FCC	Fluid Catalytic Cracking
FID	Free Induction Decay
F-T	Fischer-Tropsch
FT	Fourier Transform
h	Planck's Constant
ħ	Reduced Planck's Constant
HETCOR	Heteronuclear Correlation
HMQC	Heteronuclear Multiple-Quantum Correlation
HTF-T	High Temperature Fischer-Tropsch
I	Intrinsic Spin Angular Momentum Vector
I	Spin Quantum Number
ICP OES	Inductively Coupled Plasma Optical Emission Spectroscopy
INADEQUATE	Incredible Natural Abundance Double Quantum Transfer Experiment
INEPT	Insensitive Nuclei Enhanced by Polarisation Transfer
LT MAS	Low Temperature Magic Angle Spinning
LTF-T	Low Temperature Fischer-Tropsch
$\mathbf{M}_0$	Bulk Magnetisation Vector
MAS	Magic Angle Spinning
m_I	Magnetic Quantum Number
MQMAS	Multiple-Quantum Magic Angle Spinning
MSI	Metal-Support Interaction
NMR	Nuclear Magnetic Resonance
p	Coherence Order
PAS	Principle Axis System
PISSARRO	Phase-Inverted Supercycled Sequence for Attenuation of Rotary Resonance
ppm	Parts Per Million
P_Q	Quadrupolar Product

PXRD	Powder X-ray Diffraction
Q8M8	Octakis(trimethylsiloxy)silsesquioxane
REDOR	Rotational Echo Double Resonance
rf	Radiofrequency
R-INEPT	Refocused INEPT
RSS	Residual Sum of Squares
RT	Room Temperature
SE	Solid Effect
SENS	Surface Enhanced NMR Spectroscopy
SIMPSON	A General Simulation Program for Solid-State NMR Spectroscopy
SMSI	Strong Metal Support Interaction
SOLA	Solid Lineshape Analysis
SPINAL	Small Phase Incremental Alternation
SQ	Single Quantum
ST	Satellite Transition
STMAS	Satellite-Transition Magic Angle Spinning
t_1	Evolution Period
T_1	Longitudinal Relaxation (Spin-Lattice Relaxation)
t_2	Detection Period
T_2	Transverse Relaxation (Spin-Spin Relaxation)
TPPM	Two Pulse Phase Modulation
USY	“Ultrastable” Zeolite Y
VT	Variable Temperature
XiX	X-inverse-X
XPS	X-ray Photoelectron Spectroscopy
XRD	X-ray Diffraction
β	Flip Angle
γ	Gyromagnetic Ratio
δ	Chemical Shift
δ_{iso}	Isotropic Chemical Shift
η_Q	Quadrupolar Asymmetry Parameter

τ_{CP}	CP Contact Time
τ_D	Dead Time
τ_J	J Evolution Time
τ_P	Pulse Duration
τ_{rec}	Dipolar Recoupling Time
ν	Temporal Frequency
ω	Angular Frequency
Ω	Offset Frequency
ρ	Density Operator
σ	Shielding Tensor
μ	Magnetic Dipole Moment